NOTTINGHAM TRENT UNIVERSITY

# Developing a Neural Implant to Enable Controlled Alterations to Brain Architecture

**Nicholas J. Weir**
**(N0389094)**

A thesis submitted in partial fulfilment of the requirements of Nottingham Trent University for the degree of Doctor of Philosophy

**December 2019**

# Copyright Statement

**Acknowledgements**

First, I would like to thank my Director of Studies, Chris Tinsley, for his support and encouragement throughout the course of the PhD. His kind words and ability to find the silver lining in any situation made the past few years that much easier. Thanks also to my supervisory team, Alan Hargreaves, Bob Stevens and Martin McGinnity for their advice and thoughts on experiments and data that helped shape the PhD. Whilst not on my supervisory team, I'm also grateful to Amanda Miles for her help with mass spectrometry and endless technical knowledge and to Rich Hulse for his advice and support throughout.

Special thanks go to my colleagues. Notably, to Awais and Jordan for their ability to distract and take my mind out of the lab during stressful times and to Charlotte for being a role model of scientific rigour and discipline. To Fal, Giulia, Joe, Henry, Elisa and Dan, you all helped me find my feet when I started and helped me make it to the end. To Lydia, Chris, Eden and Max, the four of you made the day that much better by putting up with me venting about whatever issue seemed important on the day. My work would also not have been possible without the support of Sarah with her brutal honesty and patient teaching.

Last but not least, I owe my thanks to my partner Nic, who has put up with late nights and weekend work for several years to get to this stage. I wouldn't have tolerated me but Nic has been as supportive as anyone could wish for and understanding in difficult times, constantly pushing me to better myself.

I owe you all my gratitude.

**Abstract**

Neuroscientific research frequently utilises loss of function experiments to attribute function to a brain region. Gain of function experiments via cortical re-wiring would aid in validation of these studies and could allow the repair of damaged neural circuitry or the creation of novel neural structures. Research into neuronal re-wiring within the central nervous system demonstrates insufficient neurite extension upon implantation and highlights the need for similarity between exogenous and endogenous neurons. An aligned poly-L-lactic acid (PLLA) nanofibre scaffold was developed that induced the three dimensional aggregation of primary cortical neurons into a physiological structure of clustered soma and aligned, fasciculated neurites in a controlled way. Due to the self-assembling and physiological architecture of these 3D structures and subsequent detection of electrophysiological activities, these 3D structures were classified as "organoids". Cerebral cortical organoids generated using the nanofibre based methodology were demonstrated to be more developmentally advanced than their two-dimensional counterparts and mechanisms were elucidated for the aggregation of the neurons and the development that occurred post-aggregation. Analysis of gene expression suggested that the organoids were also undergoing advanced developmental processes and proposed a mechanism by which this occurs. Optogenetic depolarisation of the implanted neurons and detection of downstream electrophysiological activity was selected as the means of confirming integration of exogenous neurons into endogenous circuitry post-implantation. Methods were optimised to facilitate efficient viral transfection of the optogenetic protein (Channelrhodopsin-2). Aligned PLLA nanofibres were found to significantly enhance transfection rates relative to the 2D control and the process by which this occurs was investigated. The work presented within suggests that aligned PLLA nanofibres may be used to generate a cerebral cortical organoid that is suited to implantation and cortical re-wiring and may have additional *in vitro* applications within diverse fields such as high throughput pharmacology, computational neuroscience and bioengineering.

**Abbreviations**

AAV; adeno-associated virus

AIDA; advanced image data analyser

AMPA; α-amino-3-hydroxy-5-methyl-4-isoxazolepropionic acid

ANN; artificial neural network

ANNI; artificial neural network inference

BSA; bovine serum albumin

CAM; cell adhesion molecule

Chr2; channelrhodopsin-2

CNS; central nervous system

DAPI; 4',6-diamidino-2-phenylindole

DCM; dichloromethane

DIV; days in vitro

DMEM; Dulbecco's modified Eagle's medium

DMF; dimethylformamide

DMSO; dimethyl sulfoxide

ECM; extracellular matrix

ES; electrospun

FBS; fetal bovine serum

FGF; fibroblast growth factor

fMRI; functional magnetic resonance imaging

FOV; field of vision

GABA; γ-aminobutyric acid

HBSS; Hanks' balanced salt solution

HEB; Hibernate-EB

HFIP; hexafluoroisopropanol

LDH; lactate dehydrogenase

LED; light emitting diode

MEA; microelectrode array

MOI; multiplicity of infection

MRI; magnetic resonance imaging

MS; mass spectrometry

MTT; thiazolyl blue tetrazolium bromide

NSC; neural stem cell

ofMRI; optogenetic functional magnetic resonance imaging

PAN; polyacrylonitrile

PBS; phosphate buffered saline

PCA; principal components analysis

PD; Parkinson’s disease

PDLO; poly-DL-ornithine

PFA; paraformaldehyde

PLA; poly-lactic acid

PLL; poly-L-lysine

PLLA; poly-L-lactic acid

PLO; poly-L-ornithine

PNS; peripheral nervous system

PVC; polyvinyl chloride

ROI; region of interest

Rq; roughness

TENN; tissue engineered neural network

UV; ultraviolet

w/v; weight/volume

w/w; weight/weight

# Table of Contents

# Chapter 1: Literature Review

## 1.1 Introduction

The study of the central nervous system (CNS) and the treatment of neurological disorders is dependent on the ability to alter or replace neural circuitry. Despite extensive study, the CNS remains poorly understood and limitations in knowledge hamper attempts to change the brain's architecture. Lesion studies are a staple of neuroscience to gain understanding of brain regions, yet they are inherently flawed (Vaidya et al, 2019). Neuroengineering and biomaterial approaches have advanced our ability to manipulate neurons and thus counter some of the limitations of lesion studies and in doing so, have opened other avenues of research relating to the manipulation of neurons *in vivo*. While studies aiming to repair neural circuitry have been met with little success thus far, recurring observations in these studies highlight several key aspects that must be considered to achieve successful rewiring/repair.

## 1.2 Lesion studies

Connectivity is key in the computational processes of the brain, where functions arise from the emergent properties of ensembles of neurons and synapses; the typical form of connection within the brain (Bettencourt et al, 2007; Yuste, 2015). The importance of connectivity within the brain is illustrated by studies in brain architecture. Neurons receive many inputs whilst sending outputs to many other neuronal cells. Most excitatory connections are weakly able to induce action potentials in order to facilitate integration of as many inputs as possible prior to summating to an output whilst inhibitory neurons synapse to nearly 100% of neighbouring excitatory neurons (Yuste, 2015). Alterations to connectivity have been documented to correlate with multiple pathophysiological changes, reinforcing the role of connectivity in function (DeKosky et al, 1990; Shimada et al, 2003). Thus, lesions which induce changes in connectivity through alterations to brain architecture induce functional changes, allowing

causal relationships to be uncovered. However, lesion studies can only be performed for loss of function experiments; inhibition of neural circuits through alterations to structure. Conversely, gain of function (whether that be restoring lost capacity via repair or integration of new structures and thus functionality) has yet to be achieved to a significant degree (Harris et al, 2016). In essence, structures can be destroyed but cannot yet be added to the brain. Lesion studies also introduce additional complications. The loss of cells that occurs within a lesion study adds to the complication of confounding causality; is the observed change due to a loss of connectivity of the network, perturbances in surviving cells' electrophysiological activity or due to non-electrophysiological alterations to the neural network due to the loss of cells?

### 1.3.1 Limitations to lesion studies

Lesion studies induce loss of function through targeted destruction of specific neuronal populations and remain an essential tool within the neuroscience community, as they can be used to demonstrate a causal relationship between brain structures and function. Advances in neuroimaging methodologies such as functional magnetic resonance imaging (fMRI) and electrophysiological methods have enabled a significant volume of non-invasive work to be performed. However as the techniques can only observe regions that are more or less active during a behaviour, they can only demonstrate correlation between brain structures and behaviour, they cannot demonstrate that neural activity in specific regions causes specific behaviours (Adolphs, 2016). In addition, the temporal resolution for fMRI is limited; the haemodynamic response to a stimulus peaks 4-8 seconds after the initial stimulus, a limitation in correlating relatively rapid behaviours with particular neural networks (Nicolas et al, 2017). In contrast, electrophysiological studies using techniques such as electrodes or patch clamping take rapid temporal readings but suffer from the limitation of spatial resolution over long time periods. Additionally, invasive electrodes can record with high spatial resolution for relatively short periods of time prior to neurodegeneration, whilst non-invasive recordings have poorer

spatial resolution (Hochberg and Donoghue, 2006). Thus, lesion studies remain a useful tool for studying the connectome, albeit with their own limitations.

Electrophysiological perturbances and non-electrophysiological mechanisms occurring post-lesion play a role in disturbing functionality, although to what degree remains unclear. Functional impairment does not always correlate with the number of cells lost, suggesting that alterations to the electrophysiology of the remaining network play a role in observed changes (Cohen et al, 2007). Surviving neurons exhibit altered electrophysiological behaviours post-injury; cortical neurons have been demonstrated to exhibit depressed synapse induced calcium ($Ca^{2+}$) oscillations and excitatory postsynaptic currents with reduced amplitude up to 2 days after the injury (Goforth et al, 2011). At a more distal location to the injury, electrophysiological suppression is present but for a shorter period prior to the onset of hyperexcitability of the network (Ding et al, 2011). These alterations to the surviving neural network may be involved in alterations to behaviour, limiting the ability to ascribe function to a region.

Lesions inherently induce changes to connectivity due to the loss of synapses resulting from a loss of neurons but non-synaptic connectivity is rarely considered in lesion studies. Neurons possess several non-synaptic mechanisms that can influence their electrophysiological activity and thus the loss of neurons in a lesion would cause the loss of these non-synaptic methods of connectivity and induce changes to behaviour via loss of these mechanisms. These non-synaptic connections can influence the afferent (upstream neuronal networks) and efferent networks (downstream neuronal networks) and neighbouring neurons, affecting the connectome at the scale of synapses (nanoscale connectome), individual neurons (the microscale connectome), neuronal sub-populations (the mesoscale connectome) and between

regions (the macroscale connectome) (Swanson and Lichtman, 2016). Lesion studies fail to take these factors in to account when inhibiting the neural circuitry.

Non-synaptic mechanisms used by neurons to communicate intercellularly are ephaptic signalling, volume transmission and gap junctions (figure 1.1) (Bentley, 2017). Ephaptic signalling is a contactless, electrical mechanism with limited range (Bentley, 2017). Action potentials in neuron A induce influx of $Ca^{2+}$ and efflux of $K^{+}$ ions which then can alter the likelihood of neuron B firing. Ephaptic signalling is thought to be a result of the summation of all variables involved in determining the extracellular field potential such as synaptic currents and astrocytic ion waves (Martinez-Banaclocha, 2018).

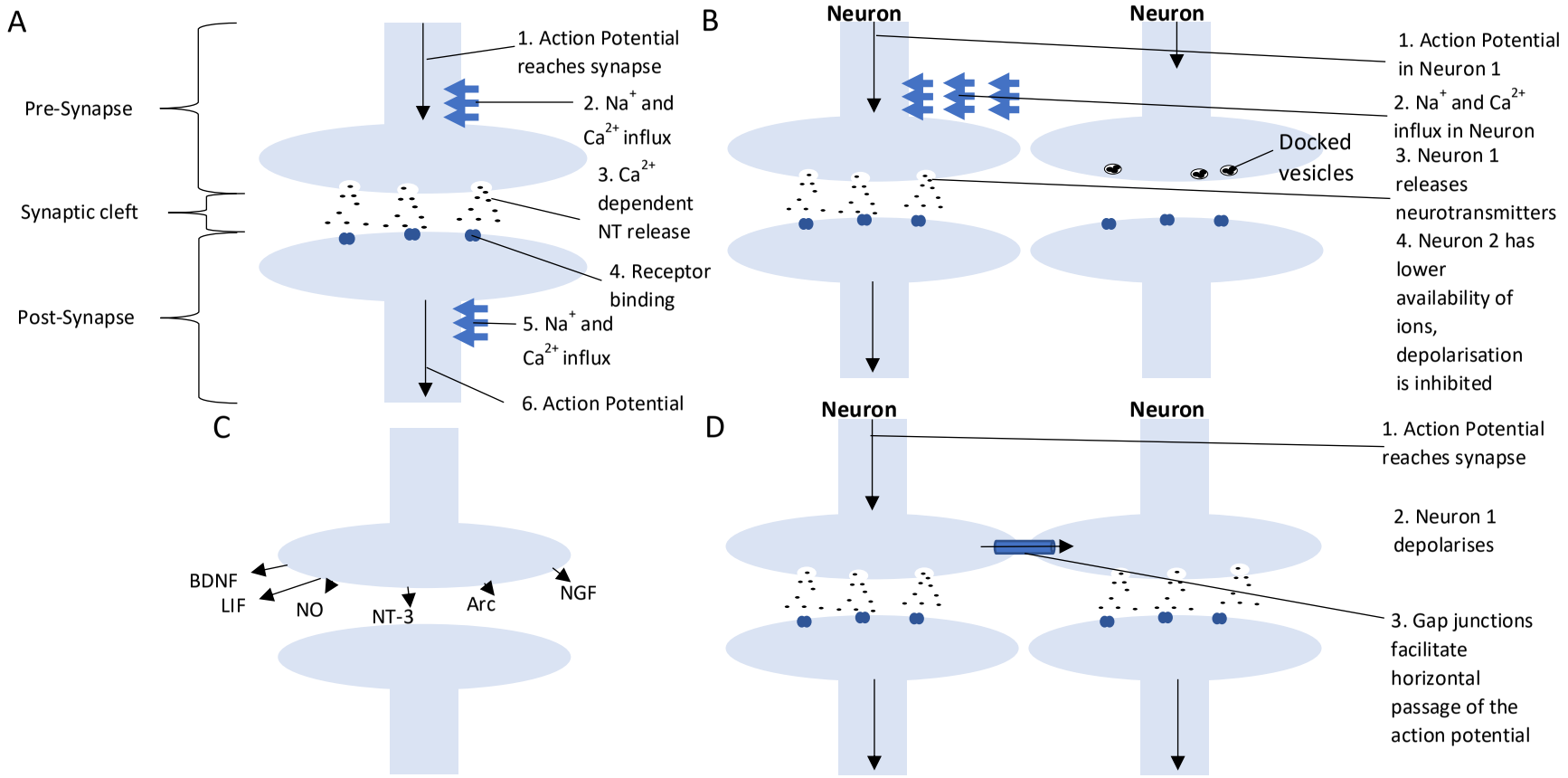


Figure 1.1: Methods of inter-neuronal communication (A) Excitatory synaptic communication. An action potential arrives at a chemical synapse. The influx of $Ca^{2+}$ causes membrane tethered vesicles to fuse with the membrane, releasing neurotransmitters in to the synaptic cleft. Neurotransmitters diffuse across the synaptic cleft and stimulate metabotropic and ionotropic receptors on the post-synaptic neuron, inducing an influx of ions and continuing the action potential, successfully converting an action potential from electrical signal to chemical and back to electrical signal. Inhibitory synapses utilise the same mechanism but induce an influx of hyperpolarising $Cl^-$ rather than the depolarising $Na^+$ and $Ca^{2+}$, inhibiting action potentials in the post-synapse. (B-E) Non-synaptic methods of inter-neuronal communication. (B) Ephaptic signalling. Depolarisation of one neuron can induce hyperpolarisation of a neighbouring neuron by decreasing the local concentration of ions. (C) Volume transmission. The secretion of soluble and membrane bound molecules in to the surrounding environment which can be constitutive or activity-dependent, from the pre- or post-synapse (D) Gap junctions. Neuron 1 depolarises and due to the gap junction, the action potential can be transferred to a neighbouring neuron, allowing both to depolarise.

Ephaptic signalling cannot independently induce action potentials when neurons are at resting potential but is capable of modulating the timing of spikes receiving suprathreshold inputs (Anastassiou et al, 2011). Volume transmission is the communication between neurons through secreted molecules, peptides and gases that can influence neighbouring cells (Bentley, 2017). Volume transmission can regulate the survival of surrounding neurons, a property that can affect the functionality of the network. Neurotrophic factors such as nerve growth factor (NGF), brain derived neurotrophic factor (BDNF), neurotrophin-3 (NT-3) and leukaemia inhibitory factor (LIF) are capable of promoting neuronal survival in a diverse array of brain regions (Korsching, 1993) and are secreted by neurons (Matsumoto et al, 2008; Thoenon, 1995; Houlgatte et al, 1989). Glutamate has been demonstrated to be a trophic factor in the adult brain thus, lesioning excitatory cells in one network would additionally cause cell death in the efferent neurons (Balazs, 2006); lesioning one region may induce death in another. Thus, removal of neurons from a network through lesioning may impact function by reducing afferent and efferent network survival, affecting networks beyond the one that was originally lesioned. Extracellular vesicles are also classified as a means of volume transmission and have exhibited secretion of proteins involved in regulating synaptic activity. Proteins such as L1CAM, GluR2/3, MAP1b and activity-related miRNAs are secreted in response to synaptic activity (Budnik et al, 2016; Zappulli et al, 2016; Pastuzyn et al, 2018) whilst the *Arc* protein, a protein essential for synaptic plasticity has also demonstrated functionality through exosomes (Pastuzyn et al, 2018).

Gap junctions are intercellular channels that link adjacent cells; they facilitate exchange of ions and small molecules, forming a low-resistance path, enabling synchronisation of neuronal electrophysiology. Gap junctions are comprised of connexins that form hexameric structures on each cellular membrane prior to docking with adjacent cells (Goodenough and Paul, 2009).

Typically, a neuron will form gap junctions with multiple other neurons, facilitating the spread of an action potential to a horizontal neuronal ensemble rather than a single neuron (Traub et al, 2018).

The role of the three non-synaptic mechanisms of intercellular communication in behaviour is unclear. Lesioning of one neuronal pathway abolishes all of the mechanisms of intercellular communication, both synaptic and non-synaptic. Whilst the role of gap junctions can be studied with relative ease through the use of connexin knockout or knockdown animal models (Lo et al, 1999), the role of ephaptic signalling and volume transmission on neural network functionality compared to synaptic neurotransmission is more difficult to quantify due to their diffuse effects and influence on afferent and efferent networks.

Thus, clarification for lesion studies is needed. Are alterations in functionality due to a loss of synaptic connectivity as a result of lesions within the network or are they due to changes in the surviving neural network as a result of the injury? How much of an effect do non-synaptic communicative mechanisms have on the function of the network as a whole? Lesion studies have enabled the study of the synaptic connectome for over a century but as knowledge of how information is encoded within the brain has advanced, so too should lesion studies, through gain of function experiments. The rebuilding of lost neural architectures and subsequent re-gain of function with sufficient accuracy would further validate any functions that have been ascribed to a particular brain region.

### 1.3.2 Use of an implant to overcome these limitations

Tissue engineered neural networks (TENNs) represent a potential method of clarifying the causal relationship by allowing (re)gain of structure (and thus potentially function)

experiments. Previously, attempts to integrate exogenous neurons into the brain caused integration of exogenous neurons into existing neural networks in a relatively random manner (Chen et al, 2016). Upon implantation into the brain, neuronal cell bodies do not cluster to form nodes, as is usually observed physiologically while neurites extend at random to a distance that is insufficient for brain repair (Harris et al, 2016). TENNs are biomaterial-based implants formulated externally to the body and have generated physiological architectures *in vitro*; clustered soma, interconnected by fasciculated neurite bundles (Tang-Schomer et al, 2014). Due to the ability to generate physiological structures and exhibit their electrophysiological properties and morphologies *in vitro,* TENNs are an appealing methodology for rewiring the lesioned brain to study functionality.

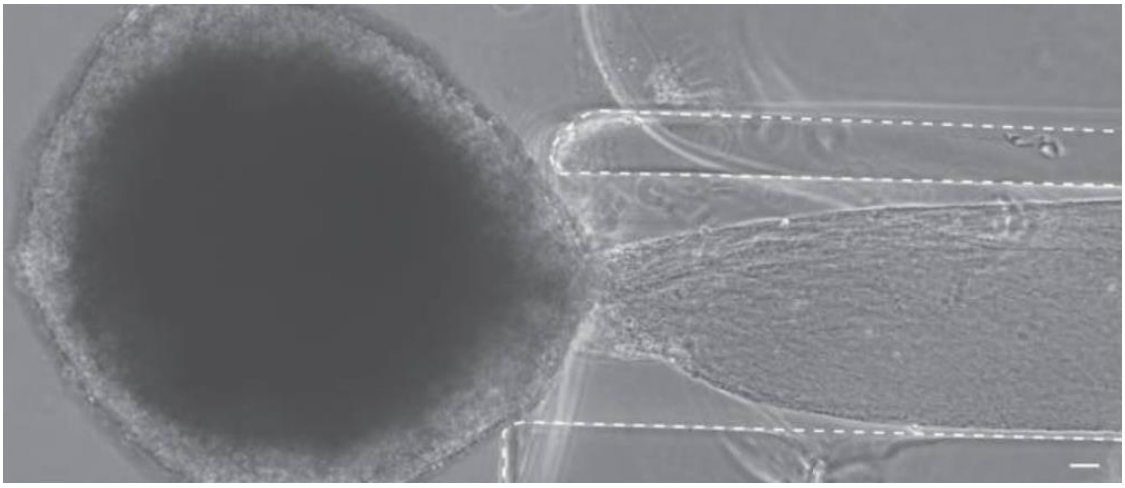

Figure 1.2: The Cullen group TENN. The dotted line marks the agarose shell that encapsulates the neurites and hydrogel. Adapted from Harris et al, 2016. Scale bar = 100µm

Implantation of a TENN along an ablated axonal pathway of the cortex could potentially restore the neuronal architecture to its pre-injury state. This has the potential to facilitate ephaptic signalling and volume transmission upon implantation, whereas studies typically report synaptic integration of exogenous neurons into the CNS several months after implantation (Pothayee et al, 2018; Tornero et al, 2013; Falkner et al, 2016). This ability to ablate and restore the non-synaptic connectivity within a neural network should aid in elucidating the roles of

both synaptic and non-synaptic communication within a network. Integrating a TENN with primary neurons transfected with fluorescent proteins modulated by a promoter that is synaptic activity dependent (such as the synaptic activity response element (SARE) promoter) (Kawashima et al, 2013) and implanting along the ablated pathway would allow for the degree of integration of exogenous neurons into the existing circuitry to be tracked. This would determine the role of connectivity or electrophysiological perturbances in functional impairment, removing a key limitation of lesion studies. Attributing function to architecture is fundamentally flawed if the act of ablation is the cause of the functional change via electrophysiological perturbance. Currently, few TENNs fulfil the criteria of generating the desired neural architecture of clustered cell bodies and aligned neurites projecting from node to node whilst retaining the ability to be implanted. The TENNs generated by the Cullen group (figure 1.2) (Harris et al, 2016; Struzyna et al, 2018; Adewole et al, 2018) are currently the only ones that fulfil the criteria of being an implantable, pre-fabricated structure that exhibits clustered cell bodies and aligned, fasciculated neurites. The structure designed by the Cullen group is an agarose based cylindrical shell that has an extracellular matrix (ECM) hydrogel within the lumen of the agarose shell. Cells are then seeded to a single end of the structure, creating a unidirectional TENN. However, due to the agarose shell of the structure, ephaptic signalling and volume transmission are limited. Thus, whilst the model may serve to reconnect disconnected regions synaptically, elements of non-synaptic neuronal communication are ignored until the agarose shell has been degraded. A TENN that allows for non-synaptic connectivity in addition to synaptic connectivity is needed in order to overcome the limitations that are inherent to lesion studies.

## 1.4 Additional uses for an implant capable of re-wiring the cortex

In addition to the use of implants to overcome limitations of lesion studies, implants that are capable of re-wiring the cortex could be utilised for (i) repairing damaged neural circuitry for

therapeutic purposes; (ii) integrating non-physiological brain architectures in order to allow gains of non-physiological functions; and (iii) to study the temporal dynamics of neural networks by altering degrees of myelination within the TENN.

### 1.4.1 Integration of physiological neural circuit components into the cerebral cortex as a therapy

To facilitate the re-wiring of lesioned pathways, an implant must be capable of restoring damaged pathways and restoring functionality. For many neurodegenerative diseases or injuries, loss of neurons induces disruption of neural circuitry and thus functionality, leading to development of the symptoms associated with the disease. Whilst neurodegenerative diseases are increasingly associated with disruptions to the temporal dynamics of whole brain electrophysiology (Jones et al, 2012), white matter pathways (Hattori et al, 2011; Rieckmann et al, 2016) and the electrophysiology of individual afflicted neurons (Amin et al, 2017), neuronal loss remains a key causative factor. This neuronal loss could be corrected by replacing lost neurons with implanted exogenous neurons highlighting how an implant that can rewire the cerebral cortex can be used therapeutically to rebuild damaged pathways.

Research on the repair of neural circuitry for therapeutic purposes typically focuses on conditions such as Parkinson's disease (PD) (Steinbeck et al, 2015; Lindvall and Kokaia, 2010; Wang et al, 2016; Wernig et al, 2008; Kim et al, 2011; Hargus et al, 2010) but serves as a model for limitations to therapeutic re-wiring of the cerebral cortex. PD is frequently used as a model for neural circuitry restoration studies due to the targeted nature of the disease; only one subset of neurons are damaged and reinnervate one target, the striatum. Whilst studies on re-wiring of the striatum (introduction of exogenous neurons that integrate into striatal neural circuitry) frequently observe benefits and functional recovery upon implantation of neurons and other CNS-derived cells, these observed effects can be induced through mechanisms other

than integration of neurons into the endogenous neural circuitry (Table 1). Few studies demonstrate full integration of a significant number of implanted neurons into the endogenous circuitry due to a lack of guidance of the neurite outgrowths (Harris et al, 2016). Thus, if an implant can be generated that promotes integration of a significant number of exogenous neurons into endogenous circuitry, it could facilitate the rebuilding of injured endogenous neural circuits, thus allowing functional recovery from neurodegenerative diseases. Whilst the rebuilding of neural circuitry would not combat the β-amyloid plaques, cellular prion protein and neurofibrillary tangles of Alzheimer's disease or the mutant Huntingtin gene of Huntingdon's disease (Manoharan et al, 2016), it would counter the loss of neuronal populations that are common to these diseases. Re-wiring would aid in the amelioration of the symptoms of these diseases but not the underlying cause.

| **Mechanism of beneficial effects induced by the introduction of exogenous neurons** | **Overview of the mechanism** |
|---|---|
| Positive effects of surgical intervention | The act of surgery may stimulate endogenous neuroregenerative mechanisms or lesion pathways that were overactive |
| "Bystander effects" | Mitigation of neurodegeneration through the modulation of support cell activity rather than neurons. |
| Trophic support | Exogenous cells deliver trophic factors that aid in survival or regeneration of endogenous neural circuitry |
| Support of efferent endogenous neurons | Provide a replacement target for endogenous neurons, preventing atrophy of endogenous neurons due to lack of targets. |

| | |
|---|---|
| Replacement of neuroprotective glial cells | Glial cells provide mechanical, metabolic and homeostatic support; restoring glial populations restores this support. |
| Pharmacological support | Implanted neurons release deficient neurotransmitters that diffuse to nearby synapses, restoring some functionality at a tonic level to downstream targets. |
| Diffuse reinnervation | Implanted neurons release deficient neurotransmitters at a physiological concentration to downstream targets. |
| Passive bridging | Passive bridges act as guidance for regenerating endogenous neurons to rebuild lost neural circuitry. |
| Active bridging | Neurons connect two host targets and relay electrical signals but do not contribute to information processing. |
| Reciprocal graft-host reinnervation | Implanted neurons integrate into host neural circuitry fully and contribute to information processing. |
| Full reconstruction of neural circuitry | Full integration of exogenous neurons into the host neural circuitry and restoration of the properties of the circuit to pre-injury levels. |

Table 1.1: Possible outcomes from transplantation of neurons and glial cells in to the CNS (adapted from Dunnett and Bjorklund, 2017)

### 1.4.2 Integrating non-physiological components into the cerebral cortex

Loss of function studies are one of the primary tools used to study the connectome. These approaches typically target neuronal populations, silence them and monitor alterations to the connectome, observing changes to function caused by altered structure. Gain of function experiments have been conducted by teaching a behaviour to an animal model and monitoring

the effects on the macroscale connectome (Table 1.2; Bennett et al, 2018); altering the function and then observing changes to the connectome. Whilst lesion studies/loss of function experiments demonstrate causality, the gain of function experiments indicate a correlation between behaviours and subsequent changes to structures.

| **Authors** | **Paradigm** | **Evidence of rewiring** |
|---|---|---|
| Boyke et al (2008) | Motor learning | Increased grey matter in regions associated with task |
| Scholz et al (2009) | Motor learning | Increased grey matter and alterations to white matter microstructure in regions associated with task |
| Oberlaender et al (2015) | Sensory stimulation | Restructuring of axons in the thalamocortical projection |
| Hihara et al (2006) | Motor learning | Conversion of unimodally to bimodally responsive neurons due to the formation of new connections |
| Boele et al (2013) | Associative learning | Axonal sprouting and terminal formation in the cerebellum |

Table 1.2: Induced architectural rewiring at the macroscale

Rewiring of the physiological connectome at the macroscale level has been demonstrated in the cerebral cortex of several animal models and each is associated with a gain of function; the animal could perform behaviours that they were not previously able to. For example, Japanese monkeys trained in tool use demonstrated novel connections from the high level visual cortex to the parietal cortex that were absent in the untrained control (Hihara et al, 2006); the architecture supported the function. What was previously a unimodal input from the somatosensory cortex became a bimodal input from both somatosensory and visual cortex, allowing the animal to perceive the tool at hand as an extension of their body and use the tool. Wistar rats exposed to the Morris water maze task exhibited structural changes in the dentate

gyrus and several regions of the limbic system whilst the swimming only control group exhibited structural changes in the primary and secondary somatosensory cortices, highlighting the role of attention on the task for inducing structural changes (Blumenfeld-Katzir et al, 2011). Each of these physiological macroscale rewiring events occurred in line with the acquisition of new skills or behaviours that were not present previously. This raises the possibility that successful non-physiological rewiring of the brain could be performed, enabling the acquisition of skills/capabilities that may not have been physiologically possible even with training, as the brain lacked the structure to allow for function. This could lead to the integration of non-physiological modules of neural tissue or prosthetics. At least one group has considered using a TENN as a biological brain-machine interface (BMI) (Serruya et al, 2017); a non-physiological gain of function, due to integration of a structure that did not previously exist within the brain.

While non-physiological modules of neural tissue with specified function have been explored in a limited way to date, brain-machine interfaces (BMIs) are a developing aspect of neuroscience and can be utilised for repair, such as the cochlear implant for hearing loss or deep brain stimulation for movement disorders (Serruya et al, 2017) or eventually, enhancement; the gain of non-physiological functionalities. BMIs require 3 components: a sensor capable of recording from a neuron population, a decoder to interpret the electrophysiological signals in to commands and actuators to induce the effects (Hochberg et al, 2006). TENNs represent one strategy for a stable, long term sensor capable of recording/stimulating activity with high resolution within the cortex. Intracortical electrodes have several benefits over extra-cranial systems, e.g. higher resolution of neuronal signal recordings and the ability to directly interface with the substrate that controlled activities prior to injury/disease, reducing the amount of time between input and output (Hochberg and Donoghue, 2006). However, chronic implantation of invasive electrodes typically results in progressive loss of signal. Due to the mismatch between the elastic modulus of the brain and

the electrode, chronic shear and differential motion occurs, resulting in microtraumas and chronic inflammation (Harris et al, 2011), which is inherently neurodegenerative to the local neuronal population (McConnell et al, 2009). Methods of reducing the elastic modulus or reducing the shear stress/movement of the implant are being developed (Wu et al, 2015; Sohal et al, 2016; Sridharan et al, 2015) and a variety of methods of delivery that do not require needles, insertion shuttles or catheters are also being trialled such as flexible electrodes and microfluidic delivery devices (Harris et al, 2016; Vitale et al, 2017).

Implanted intracortical electrodes attain their high resolution through their close contact to the neuron from which the signal originates, in contrast to tools such as electroencephalography, which has low spatial resolution due to the large distance between the origin and the point of signal recording (Hochberg and Donoghue, 2006). Due to the potential role for TENNs in re-wiring the brain as a long-term implant, TENNs used to rewire must by necessity be non-inflammatory and possess a low elastic modulus to minimise glial scarring. As a result, TENNs could theoretically be used to reroute outputs to the surface of the brain, allowing for greater spatial resolution with a less invasive technique. The re-routing of connections could be achieved by inserting a unipolar TENN through the cortex, with the seeded end acting as a “biological electrode” and neurites extending within the niche of the TENN to the surface of the brain. Non-invasive, previously low-resolution recording techniques could then be used to detect neural signals from relatively deep regions of the cortex with a higher degree of resolution. Currently, only the Cullen research group (Harris et al, 2016; Adewole et al, 2017; Struzyna et al, 2018) has developed a TENN that possesses the pre-requisites to perform the rewiring.

### 1.4.3 Temporal dynamics of neural networks

Whilst re-wiring of the brain is predominantly an effort to alter the existing spatial architecture, for information to be processed physiologically, the temporal aspects of computation within the brain should also be considered. Connectivity can occur at specific spatial nodes, specific temporal intervals or both (Köse-Dunn et al, 2017). The encoding of information through spatially distributed networks within the brain has been extensively studied through investigations of the brain's structure but increasingly, function is attributed to temporally dynamic, spatially distributed neural networks. Temporally dynamic fluctuations of electrophysiological activity have been extensively documented in single cell recordings and local fields but only recently in fMRI studies (Allen et al, 2014). Global temporal dynamics have also been observed; fMRI utilising non-stationary correlation methods, such as sliding window correlation have illustrated transient activation of regions during behaviours that would not have been detected if only the spatial activation had been considered (Hindricks et al, 2016). The importance of the temporal dynamics of neural networks is further illustrated through the neurological conditions that feature disruption of temporal connectivity such as schizophrenia (Sakoglu et al, 2010) and Alzheimer's disease (Jones et al, 2012). Thus, temporal aspects of functional connectivity should be considered when attempting to re-wire the brain.

In order to study the temporal dynamics of neural networks, attempts to re-wire the cortex should consider two factors in particular: path length and myelination. The laminar architecture of the brain was theorised to maximise efficiency of spatial organisation and ensure consistent path length to synchronise action potentials that originate and terminate at the same point. However, *Reeler* mutant mice have no laminar architecture and suffer from no behavioural or functional deficits (Guy and Staiger, 2017). Thus, ensuring that the neurites of implanted exogenous neurons all possess a similar length may not aid in the synchronisation and temporal dynamics of exogenous neurons. In contrast, myelination facilitates saltatory

conduction, a process that can increase the speed of action potentials by 300-fold (Purves et al, 2001). The degree of myelination of axons is a factor that could be manipulated by seeding varying densities of oligodendrocytes to the structure, influencing the degree of myelination and saltatory conduction and action potential speed. Theoretically, this may be a method for manipulating the temporal dynamics of action potentials and thus study the temporal dynamics of networks. Cortical maps have been theorised to expand through exposure of latent connections rather than through the creation of novel connections (Albieri et al, 2014); by reducing the temporal dynamics within a network, latent connection may be revealed as the neural circuit utilises a more efficient path, shedding light on the connectome of the brain.

## 1.5 How can the cortex be re-wired: considerations and existing methodologies

The reasons for developing a method of rewiring the cortex are diverse, yet evidence of significant rewiring of the cerebral cortex is limited within the literature. However, substantial progress has been made in the field, which can be drawn upon to inform the work moving forward. The following considerations must be made for any implant that aims to facilitate re-wiring.

### 1.5.1 Cellular sub-populations

To facilitate the re-wiring of the cortex, the biological architecture must be restored. The cerebral cortex is composed of a diverse population of cell types and subtypes. Forty-seven molecularly distinct subclasses of cells have thus far been described within the rodent cortex (Zeisel et al, 2015) but they can be broadly divided in to two categories; glia and neurons.

Glial cells are divided into two dominant subclasses; astrocytes and oligodendrocytes.

Astrocytes were historically viewed as maintenance cells, the purpose of which was to regulate pH and osmolarity, provide metabolic substrates and clear neurotransmitters from the synaptic cleft (Kandel, 2012). However, in recent years, astrocytes have been attributed with further vital roles within the CNS. Lactate is shuttled from the astrocyte to neurons that require metabolic support, astrocytes control the diameter of blood vessels and thus blood flow within the brain and astrocytes are even capable of modulating neuronal activity (Brown and Ransom, 2015; Teschemacher and Kasparov, 2015). Similar to astrocytes, oligodendrocytes have traditionally been attributed with one major role, the myelination of axons. However, in recent years, an increasing number of functions have been attributed to them. Myelination of axons reduces the capacitance of the axon membrane whilst increasing the electrical resistance, facilitating faster conduction speed of action potentials and altering the overall dynamics of the neural network (Kandel, 2012). Oligodendrocytes are also thought to provide metabolic and trophic support to axons and aberrant oligodendrocytes are associated with numerous psychiatric disorders (Edgar and Sibille, 2012).

Neurons are the effectors of the CNS: computation is performed through the activity-dependent release of neurotransmitters targeted towards a downstream neuron (Teschemacher and Kasparov, 2015). The *Neuron Doctrine* (Ramon y Cajal, 1888) suggested that neurons were the smallest functional unit of the brain. This hypothesis was supported by the techniques that dominated the field of neuroscience for almost a century and a half; single-cell techniques such as Golgi staining and microelectrodes were used to study individual cells of neural circuits to elucidate the structure of the brain. The discovery of receptive fields, specific stimuli that activate individual neurons, further cemented neurons as the smallest functional units of the CNS (Yuste, 2015). However, in contrast to the *Neuron Doctrine*, neural network models propose that the smallest functional units of the CNS are networked neurons (Yuste et al, 2015). Anatomically, distributed connectivity is evident in the structure of the

brain. Neurons receive inputs from numerous other neurons, each of the excitatory inputs possibly being significantly below the threshold for depolarisation; this feature allows the integration of numerous excitatory signals prior to depolarisation without saturation (Abeles, 1991). Inhibitory neurons utilise gap junctions as a form of connectivity, reinforcing their ability to act as a single unit whilst dendritic spines increase connectivity between excitatory neurons via the axons (Kandel, 2012). By increasing connectivity between neurons, each individual neuron within a circuit becomes less important; thus function is likely to arise from the composite interactions of ensembles of neurons rather than any one individual neuron (Yuste, 2015). This is also evident pathologically. Clinical symptoms of PD appear when approximately 50-60% of the dopaminergic neurons in the *substantia nigra* are lost, suggesting that the network can adapt to the loss of single neurons to a point, contradicting the *Neuron Doctrine* (Gorman, 2008).

To facilitate re-wiring, the cellular sub-populations of the brain should be accounted for rather than using the reductionist approach of solely replacing neurons.

### 1.5.2 Tissue-wide organisation

Neurons in the cerebral cortex display distinctive cellular and tissue-wide architectures to support brain function. The cellular architectures of a neuron of the cerebral cortex are shared with the architecture of the majority of other neurons within the CNS. Cerebral cortical neurons have a soma (cell body), containing the nucleus, and from the soma extends the axon, the output component of a neuron, and dendrites, the input component of neurons (Kandel, 2012). Within the CNS, neural circuits are comprised of cell bodies, typically clustered together (grey matter), that are interconnected by fasciculated, myelinated bundles of axons (Kandel, 2012; Tang-Schomer et al, 2014). In order for a network of neurons to be generated, synapses form. Synapses are the point of electro-chemical communication between neurons within the CNS and serve to convert an electrical signal in the pre-synaptic neuron to a chemical signal

that is converted back to an electrical signal by the post-synaptic neuron. Synapses can form between axons-dendrites, axons-somas, axons-axons, axons-dendritic spines and dendrites-dendrites (Bear et al, 2016). Non-synaptic communication between cells can occur but synapses are the predominant method of information flow within the CNS (Bentley et al, 2017). Notable non-synaptic manners of communication between adjacent neurons are ephaptic transmission (communication through extracellular electric fields) (Su et al, 2012), through secretion of extracellular vesicles containing proteins and RNA (Pastuzyn et al, 2018) and even through quantum entanglement via calcium phosphate molecules (Fisher, 2015). Of note is the importance of proximity for each method of communication; structure leads to function. The close proximity that results from the clustering of cell bodies and bundling of axons is fundamental to each of the methods of communication that neurons employ to process information.

Within the cerebral cortex, cells are also arranged into a laminar structure (Table 3). The laminar structure of the cortex is theorised to enhance the computational abilities of the brain. The cerebral cortex has demonstrated the ability to process top-down information from higher cortical areas, bottom-up information from sensory organs and lateral signals from neighbouring neurons, all within the same region. The laminar architecture has been theorised to facilitate this function (Raizada and Grossberg, 2003) however, evidence suggests a simpler role for the lamination of the cerebral cortex. The reelin protein plays a role in the development of the laminar structure of the cortex; loss of the reelin protein from a mouse model results in loss of lamination, yet functional connectivity within the brain is unaffected. Furthermore, in various studies, reeler mutant mice were found to have unaltered cortical function or behaviours (Guy and Staiger, 2017). The authors hypothesise that the laminar structure serves to optimise neuronal placement thus minimising neuronal length, saving space and the metabolic cost of maintaining the network. In addition, they note a lack of layers

and organisation generates more variable neurite lengths to reach the downstream target; if conduction velocity is consistent, a lack of lamination may lead to temporal desynchrony, limiting summation of action potentials.

| **Layer** | **Properties** |
|---|---|
| I – the molecular layer | Acellular layer, mainly comprised of apical dendritic tufts of neurons originating in deeper layers and horizontal axons that pass through or form connections within the layer |
| II – the external granular layer | Composed predominantly of granule cells, small spherical morphology. Contains the apical dendrites of cells within layers V and VI. |
| III – the external pyramidal layer | Contains vertically orientated small and medium sized pyramidal neurons, typically larger than cells of the more superficial layers. Contains the apical dendrites of cells within layers V and VI. |
| IV – the internal granular layer | Similar to layer II, comprising of predominantly granular cells. |
| V – the internal pyramidal layer | Composed mainly of pyramidal neuronal cell, typically larger than the pyramidal neurons of layer III. Contains the basal dendrites of cells within layers III and IV. |
| VI – the polymorphic/multiform layer | Contains a diverse cellular population; few pyramidal neurons, many multiform neurons and small spindle-like pyramidal neurons. Contains the basal dendrites of cells within layers III and IV. |

Table 1.3: The diverse properties of the layers. Layer I is the most superficial layer, whilst layer VI is the deepest. It is important to note that these are general observations, not all cortical regions follow this organisation; the primary visual cortex has a prominent layer IV which has subdivisions, whilst the perirhinal cortex lacks layer IV and has no clear border between layers II and III. The layering of the cortex allows the efficient organisation of inputs and outputs to and from the cortex; the main projections of layer VI are to the thalamus, for layer V, the midbrain, hindbrain and spinal cord whilst layers II and III and some cells of layer V form the majority of intracortical connections (Kandel et al, 2000; Furtak et al, 2007; Espuny-Carmacho et al, 2013).

### 1.5.3 Existing methods of re-wiring the cerebral cortex

Literature on re-wiring of the brain in a manner that is not directly related to repair of damaged pathways are limited. However, the aims of repair and re-wiring are analogous; to implant exogenous neurons into a host brain and integrate neurons into the existing host circuitry. Due to the analogous nature of the aims, publications on the repair of lost connectivity within the brain using exogenous neurons make an excellent source for information regarding strategies to facilitate brain re-wiring. Key concepts identified in these studies are applicable to work within the cortex such as areal identity, integration of exogenous neurons in to the existing neural circuitry, survival of cells upon implantation and failure to extend neurites in a targeted way to a significant degree.

#### 1.5.3.1 Areal Identity

Areal identity is the concept that neurons of different areas have different molecular, electrophysiological and laminar profiles. Studies that utilise stem cells illustrate this concept well. For example, stem cells to be utilised to re-wire the striatum are consistently differentiated to a midbrain dopaminergic fate prior to implantation (Steinbeck et al, 2015; Hargus et al, 2010; Wang et al, 2016). Only ventral mesencephalon dopaminergic neurons are capable of reinnervating the striatum whilst neurons isolated from other dopaminergic regions lack this property. Interestingly, dopaminergic neurons within the ventral mesencephalon are comprised of two populations; *substantia nigra pars compacta* neurons and ventral tegmental area neurons. Only neurons of the nigral subtype can reinnervate the striatum, demonstrating the need to match areal identity for successful rewiring (Thompson et al, 2005). Studies take care to ensure ventral mesencephalon identity of implanted neurons (Steinbeck et al, 2015; Hargus et al, 2010; Wang et al, 2016). The concept of areal identity has also been demonstrated within the cortex. Pyramidal neurons with an occipital areal identity implanted within the visual cortex show significant integration whilst implantation of pyramidal neurons with an

occipital identity within the motor cortex exhibited negligible integration (Michelson et al, 2015). However, several studies provide evidence of limited area plasticity within the cortex (Gaspard et al, 2008; Hansen et al, 2011; Ideguchi et al, 2010) although greater areal plasticity was noted for neurons isolated from younger embryos. Interestingly, areal matching of implant to implanted region is conserved across species; Espuny-Carmacho et al (2013) implanted human cells into a mouse host and observed integration in the occipital cortex by occipital-identity human neurons but not within the motor cortex. Thus, in order to maximise integration of exogenous neurons, matching the areal identity of exogenous neurons is key. This represents a crucial distinction between repair of damaged endogenous neural networks and re-wiring to create entirely new neural architectures. Due to the need to match the areal identity of implanted neurons and the region to be innervated, it may be difficult to force integration of neurons that physiologically should not form synapses, limiting construction of non-physiological neuronal networks.

### 1.5.3.2 Cell Survival

Survival of implanted neurons is another hurdle identified by previous studies. Attrition of cells upon implantation is high. A number of factors play a role in this, namely anoikis (apoptosis due to lack of ECM), ischaemia and withdrawal of trophic factors (Sortwell et al, 2000; Pires, 2013). The attrition of cells typically occurs within the first week of implantation but beyond this point, studies have shown exceedingly high survival (Falkner et al, 2016). Biomaterial scaffolds are frequently used to ameliorate anoikis. Cells are implanted attached to a scaffold rather than implantation as a cell suspension (Wang et al, 2016; Vaysse et al, 2015; Cooke et al, 2010; Wang et al, 2012) although it should be noted that not all the named studies used scaffolds that were solid, as in some cases hydrogels that gelate in response to light or heat were employed instead. The mechanical support of the scaffold limits the level of cell death

due to anoikis. By implanting on a scaffold, detachment of cells from a surface is not necessary and thus, anoikis is limited with a greater number of cells able to integrate. This effect can be further enhanced by coating the scaffold with ECM proteins such as a fibronectin or laminin (Cooke et al, 2010), although it should be noted that survival as high as 76±11% has been noted for primary neurons cultured on glass beads and implanted in to the CNS in the absence of ECM coatings (Jgamadze et al, 2012).

### 1.5.3.3 Neurite Extension

However, implanted neurons that survive do not extend neurites to a significant degree in the correct direction, preventing effective repair (Harris et al, 2016). Oki et al (2012) induced neural stem cells (NSCs) (derived from induced pluripotent stem cells) towards a cortical neuronal fate prior to implantation and observed differentiation into the correct phenotype, axonal extension to the correct target and electrophysiological activity characteristic of mature neurons. However, axonal extension to the correct appropriate target was only noted for cells implanted into the striatum and not for those implanted into the cortex. The study utilised human cells in a rodent brain; human derived neurons extend axons to a greater degree than rodent derived neurons upon implantation into a rodent brain, likely due to the degree of axonal extension within the native species' brain (Hurelbrink and Barker, 2005) and thus, an allograft may not have seen the same degree of neurite extension. Oki et al (2012) highlight the need for axonal guidance for restoring neural circuitry within the cortex. Human cells fail to extend axons to distant targets and migrate to a greater degree than rodent cells in a rodent model, hence translating to a clinical setting (human cells in human model) will require a great deal more work on guidance of axon extension towards distant targets.

### 1.5.3.4 Integration into existing neural circuitry

Current research into neural circuitry replacement for PD has demonstrated rapid reinnervation of the striatum by the implant to a great extent, yet this is less true of cells implanted within the cortex. Early retrograde labelling studies indicate that only 1 in 3 cortical neurons grows axons into an implant of fetal tissue, although these fibres do form synapses with the implanted neurons that have been demonstrated as functionally active via electrophysiology (Peschanski et al, 1995). Innervation is not limited to host afferents, implanted neuron-derived efferents have also been observed for fetal neurons. Studies have demonstrated fetal implants within the cortex extending axons towards the *globus pallidus*; structural analysis confirmed functional synapses were established with the correct targets but axon extension towards more distant areas was more limited. Human xenografts in a similar study did demonstrate distant projections, but again this may be due to the size of the brain that the NSCs were derived from; if the brain of the donor species was larger than that of the host species, greater axonal extension is often observed (Peschanski et al, 1995; Hurelbrink and Barker, 2005). These studies suggest that one of the reasons cortical implants fail is due to a lack of axonal guidance/extension resulting in a lack of integration rather than an inherent inability to integrate into existing neural circuitry. Studies also suggest that utilising human cells in animal models may have limitations with respect to axon extension; allografts demonstrate poor axonal extension whilst human xenografts demonstrate axonal extension. As clinical implants will utilise human cells as an implant within human patients (allografting), poor axonal extension is likely to be observed.

## 1.6 Biomaterials and nanofibres

Scaffolds have demonstrated multiple properties beneficial to implanted cells. The ideal scaffold should be capable of guiding organisation and growth of exogenous neurons, allowing diffusion of oxygen and nutrients whilst also allowing vascular infiltration, limiting the extent

of ischaemia (Park et al, 2002). The ideal scaffold for a neural implant is biocompatible (during culture, implantation or degradation), promotes beneficial biological activities (such as enhanced survival) (Chen et al, 2011), enhances neurite outgrowth (Yang et al, 2005), degrades at a similar rate to tissue growth of the cells within the implant, possesses a 3D porous structure facilitating infiltration and diffusion of nutrients, reproducible structure and similar mechanical "stiffness" to the brain to prevent microtraumas upon movement (Pettikiriarachchi et al, 2010). The choice of material for the scaffold is heavily dependent on the aims of the implant. Different materials induce different effects on various cellular populations: Polycaprolactone promotes oligodendrocyte differentiation at the expense of neuronal and astrocytic differentiation in NSCs (Nisbet et al, 2007), ideal for studies working on remyelination for a multiple sclerosis therapy but less than suitable for studies into cellular replacement of neurons for PD or Huntington's disease. Scaffolds can be used to guide axonal extension of the cells; facilitating targeted reinnervation that is lacking in their absence (Harris et al, 2016). Whilst studies have focused on increasing the rate of axon growth either by direct stimulation of the neuronal growth (Yip et al, 2010; Liu et al, 2010) or by engineering the environment to be more permissive for axon outgrowth (Tang et al, 2007). Neither method ensures axonal extension to the correct target; however, scaffolds can be used to direct axon extension to the desired region (Yang et al, 2005).

Neuronal cells have been grown on nanofibres in an attempt to mimic the topographical features of the ECM. Aligned nanofibre structures promote guidance of axon extension and rate of growth due to "contact guidance", beneficial to neural tissue engineering as cell replacement strategies often lack directionality (Harris et al, 2016). Upon random nanofibres, neurite extension can be observed to be random, whilst on aligned nanofibres, neurite extension demonstrates increased directionality and rate of growth (Yang et al, 2005; Corey et al, 2007; Lee et al, 2011).

Thus, aligned nanofibres are able to counter two of the key hurdles that are expected to hinder re-wiring; cell death upon implantation due to anoikis and failure to extend targeted neurites from point A to point B. Of the ideal properties for a tissue engineering scaffold that were previously mentioned (biocompatible, promotes beneficial behaviour, enhanced neurite outgrowth, degrades, porous structure for diffusion and cellular infiltration, reproducible and similar elastic modulus to the brain (Pettikiriarachchi et al, 2010)), aligned nanofibre membranes satisfy two of the criteria; porosity and reproducibility. Nanofibres can be electrospun from a variety of materials that can promote the other ideal properties.

## 1.7 Goals of the PhD project

In order to develop an implant capable of re-wiring the brain, several aims were established:

1. Development of a method of inducing cellular aggregation of primary cortical neurons and aligned neurite extension through use of a biocompatible nanofibre scaffold
2. Characterisation of the resultant cellular structures to ensure that they are sufficiently viable and developed for implantation
3. Elucidation of the mechanism through which aggregation occurs
4. Development of a method to detect successful integration of exogenous cortical neurons in to endogenous neural circuitry

# Chapter 2: Materials and methods

## 2.1 Methods common to all chapters

### 2.1.1 Isolation of E18 Sprague Dawley rat cortex

Timed pregnant CD Sprague Dawley rats were killed on embryonic day 18 by overdose of inhaled isoflurane in accordance with the UK Animals (Scientific Procedures) Act 1986 by Nottingham Trent Barrier Unit. Death was confirmed by cervical dislocation. Embryos were removed rapidly and decerebrated on ice. Microdissection was performed under sterile conditions. Briefly, the meninges were removed and the hemispheres of the brains were separated. The olfactory bulb, midbrain, hindbrain and hippocampus were removed. The isolated cortex was then placed in Hibernate EB (HEB) medium and stored at 4°C until use.

### 2.1.2 Dissociation of primary cortical neurons

E18 Sprague Dawley rat cortex was stored in HEB prior to dissociation. Using a silanised Pasteur pipette, HEB solution was removed, leaving only the tissue with minimal HEB. Papain (2mg/ml) in Hibernate-E without $Ca^{2+}$ was kept on ice prior to use. Tissue was transferred in to the papain and incubated in a water bath for 10 minutes at 30°C. The tissue with minimal medium was then transferred back in to HEB medium and triturated (approximately 8 passes were needed to disperse the tissue); undispersed pieces were allowed to settle for 1 minute prior to removal of the supernatant. Supernatant was then centrifuged for 1 minute at 200g. The supernatant was then discarded and the pellet resuspended in 1ml of NbActiv1 prior to cell counting using a Biorad TC20 cell counter and a 1:1 dilution in Trypan Blue to assess cell viability.

### 2.1.3 Maintenance of primary cortical neurons

Primary cortical neurons were cultured in NbActiv1 supplemented with gentamicin to a final concentration of 50µg/ml. Flasks were maintained at 37°C in a humidified chamber of 5% v/v $CO_2$ and 95% air v/v. Half medium changes were performed on alternate days. Cells were

plated out at a density of 25,000 cells/$cm^2$ and were not subcultured due to the post-mitotic nature of primary neurons.

### 2.1.4 Cryopreservation

Cells were cryopreserved in the vapour phase of liquid nitrogen. After dissociation of the tissue, primary neurons were resuspended in cryopreservation medium (90% v/v NbActiv1 and 10% v/v DMSO) and placed in a -80°C freezer overnight prior to being moved to liquid nitrogen storage.

### 2.1.5 Thawing

Cryopreserved cells in cryovials were retrieved from the liquid nitrogen storage. Cryovials were then placed in a water bath at 37°C for 1-2 minutes and their thawed contents transferred to a sterile tube. Growth medium (10ml) was then added dropwise to the cells to dilute the DMSO. The tube was then centrifuged for 5 minutes at 300g, after which the supernatant was discarded and the pellet was re-suspended in 1ml of NbActiv1 medium prior to seeding.

### 2.1.6 Electrospinning of nanofibres

A custom electrospinning rig was employed and a patented method was used to generate aligned nanofibres (UK patent application number GB2553316A). Briefly, nanofibres were collected on non-conductive polyester collecting sheets that were cut in to the design used to generate aligned nanofibres (figure 2.1) using a Trotec $CO_2$ laser cutter. For non-conductive collecting sheets that are sufficiently thin, electrostatic attraction is capable of drawing the nanofibres between the two rectangles of the aligned nanofibre design on the collecting sheets. Polyester sheets were 600mm x 300mm x 0.075mm and cutting parameters were: 100% speed, 28% power and 1000 pulses per inch. Poly-L-lactic acid (MW 40,000) was dissolved overnight at 50°C in the solvent hexafluoroisopropanol (HFIP) to a concentration of 30% (w/v). This solution was delivered at a controlled rate of 1ml/hr to a needle (21 gauge, stainless steel) which was subjected to an electrical potential of 25kV. The needle was separated from the

grounded collector by 15cm. The grounded collector was a rotating polystyrene drum wrapped in an aluminium sheet. The high voltage applied to the electrospinning solution decreases the surface tension at the tip of the needle and as the charge density exceeds the surface tension, a Taylor cone forms and the solution is drawn in the direction of the grounded collector. Desolvation occurs as the electrospinning solution is in the air, entangling high molecular weight molecules in order to form a nanofibre which is attracted by the collector. The process is non-sterile; prior to use for cell culture, sterilisation of the nanofibres was achieved by exposure to ultraviolet (UV) light at 256nm for 20 minutes.

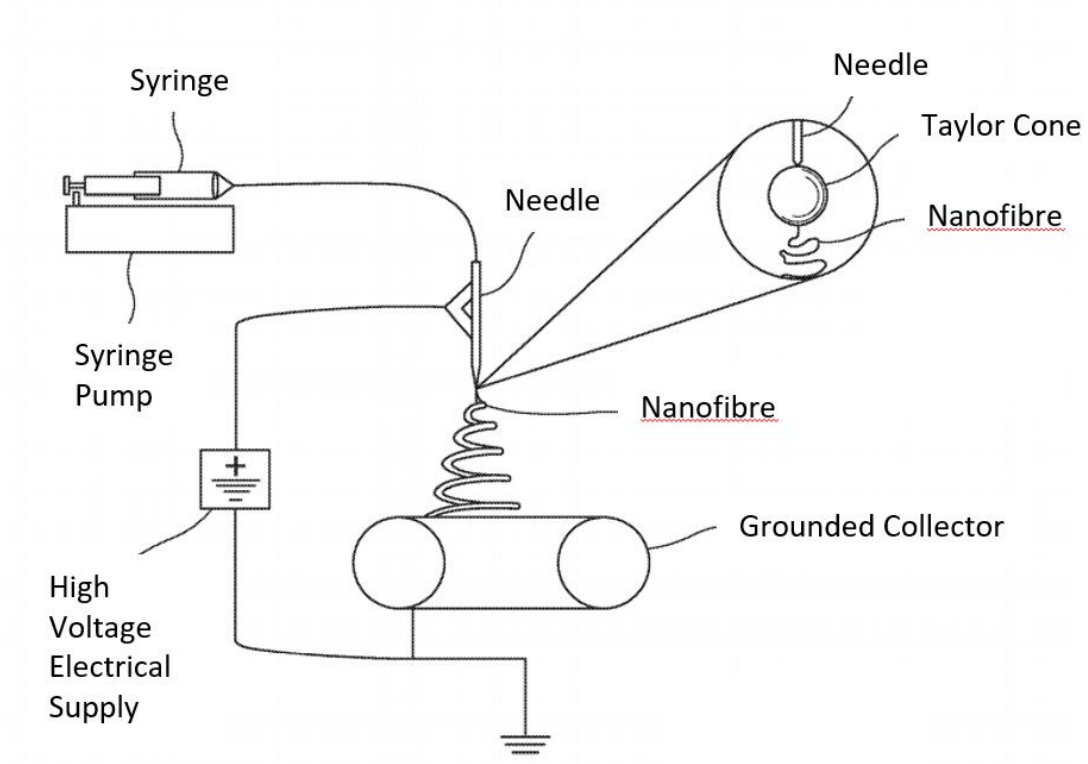


Figure 2.1: The experimental set up for electrospinning of aligned nanofibres. A high voltage power supply is used to apply an electric field to the polymer solution which is ejected in the direction of the grounded, rotating collector.

### 2.1.7 Preparation of samples for fluorescence microscopy

Cells were fixed in 4% w/v paraformaldehyde (PFA) and permeabilised using 0.1% v/v Triton X-100 for twenty minutes each. Cells were then incubated in blocking buffer (3% w/v bovine serum albumin in PBS) for 1 hour at room temperature prior to overnight incubation in primary antibody (concentration stated for each specific antibody alongside the images) at 4°C on an orbital shaker. Incubation in secondary antibody (concentration stated in the antibody sub-section) was performed at room temperature for 2 hours. Subsequent nuclear staining was performed with DAPI. Visualisation was performed using a Leica SP5 microscope. Between each stage, three 5 minutes washes were performed using phosphate buffered saline (PBS).

# Chapter 3: Method optimisation

## 3.1 Introduction

### 3.1.1 Choosing a cellular model for use in rewiring studies

Research into repair of the CNS thus far has highlighted the need for similarity between the implanted neurons and the region of implantation for successful synaptic integration and thus, rewiring. In order to rewire the cerebral cortex, implanted cells should be cortical neurons. Even within the cortex, mismatch of cortical areas between exogenous and endogenous neurons limits synaptic integration (Michelsen et al, 2015). Earlier developmental stages of neurons appear to be more plastic and more easily integrated into existing synaptic circuitry than later developmental stages (Ideguchi et al, 2010; Gaspard et al, 2008; Espuny-Carmacho et al, 2013). This may circumvent the areal identity issue (lack of integration for mismatching cortical areas between host and exogenous neurons) raised by Michelsen et al (2015), therefore, neurons at an early developmental stage are more desirable for rewiring studies. The physiological architecture of the brain is composed of clustered cell bodies and projections of aligned neurites (Tang-Schomer et al, 2014); thus the neurons of the implant should be arranged into this cytoarchitecture. Full reconstruction of neural circuitry requires integration of neurons and restoration of electrophysiological properties of the circuit; therefore, electrically active cells must be employed (Dunnett and Bjorklund, 2017).

Stem cell technology is the gold standard for cellularised biomedical implants into the CNS. Due to the easily scalable nature of mitotic stem cells and the advent of induced pluripotent stem cell technology and personalised medicine, many studies make use of stem cells (Forbes and Andrews, 2019). Embryonic stem cells (ESCs) are totipotent and can be used to generate mixed neural populations composed of neurons, astrocytes and oligodendrocytes; however, they are no longer implanted due to their ability to form teratomas (Brustle et al, 1997). They

are currently used as a source of generating neural stem cells that are subsequently differentiated into neurons and implanted into the CNS (Daadi et al, 2016; Boehm-Sturm et al, 2014; Mezzanotte et al, 2013). In contrast to the pluripotency of ESCs, neural stem cells are lineage restricted and can only generate neurons, oligodendrocytes and astrocytes, limiting their ability to form teratomas (Bonnamain et al, 2012). However, for targeted repair of the central nervous system, neural stem cells (NSCs) have some key limitations. NSCs are capable of migrating towards a site of injury (Tamaki et al, 2002) and thus to retain the desired neurite guidance that is induced by aligned nanofibres and key to this research, the migration of NSCs away from the nanofibres would have to be curbed. NSCs have also demonstrated the ability to undergo fusion events; rather than differentiate into neurons capable of rewiring *in vivo*, they may instead fuse with existing neurons (Brilli et al, 2012; Cusulin et al, 2012). Differentiation may not even occur; studies have reported large percentages of undifferentiated NSCs post-implantation (Aboody et al, 2000; Chaubey and Wolfe, 2013; Weerakkody et al, 2013). Large populations of undifferentiated NSCs can inhibit cortical excitability, neuronal death and microgliosis (Weerakoddy, 2014). Thus, differentiation of NSCs *in vitro* is required to curtail migration away from the nanofibres and the targeted region of rewiring, to limit the undifferentiated NSC population and to prevent fusion events that may obfuscate data.

Whilst neuronal cell lines are extensively utilised for *in vitro* neurobiology studies, they are poorly suited to *in vivo* usage and rewiring the cerebral cortex. The NT2 cell line can be used to generate electrically active neurons that are capable of integrating but possesses an abnormal karyotype (Le Friec et al, 2017) and are legally barred from use in clinical trials as a result. The SH-SY5Y cell can also be differentiated to a dopaminergic neuron phenotype but the neuronal cell line possess two distinct sub-types, epithelial and neuronal; implantation may

result in teratoma formation within the CNS. One cell line (CTX0E03) has been approved for a clinical trial in humans (Le Friec et al, 2017) although these are neural stem cells (NSCs) rather than neurons and suffer the same differentiation concerns (fusion, failure to differentiate, migration from target region) as primary NSCs. Upon implantation during human clinical trials, amelioration of cognitive deficits in stroke patients was observed, although this is not necessarily evidence of rewiring as NSCs can exert a range of beneficial effects that result in a degree of functional recovery (table 1.1, Chapter 1; Ottoboni et al, 2017). Post-mortem analysis would be required to confirm synaptic integration and rewiring rather than behavioural restoration. The CTX0E03 cell line therefore represents a potential candidate for cellular implantation.

Whilst stem cells (both clonal and primary) have the benefits of multipotency and the ability to be sub-cultured to generate cellular stocks, the process of differentiation of stem cells to a neuronal fate is the greatest limitation of the cells for biomaterials-based research. Wettability, elastic modulus, conductivity, nanofibre diameter, nanoroughness and cell density have all been demonstrated to influence differentiation of stem cells (Saha et al, 2008; Christopherson et al, 2009; Blumenthal et al, 2014; Lee and Arinzeh, 2012; Moon et al, 2012). Subtle changes in the environment may induce changes to the proportion of each neural sub-population (neurons, oligodendrocytes, astrocytes, etc) as a result of changes to the implant or environment and thus result in the need for re-optimisation of the differentiation process. Primary neurons were selected as the cellular model despite their finite, post-mitotic nature. Whilst all of the listed cell types are capable of rewiring neural circuitry through the generation of neurons, primary neurons have no capacity to differentiate to any population other than neurons, eliminating the potential for negative interactions between the biomaterials and the intrinsic differentiation programmes of stem cells. Primary cortical neurons can be used from

embryonic day 18; prior to terminal differentiation but far enough through the developmental programme to be lineage restricted to neurons (Semple et al, 2013). A potential limitation to using primary neurons as the cellular model for the research is the non-physiological homogeneity of the culture; a mix of cell types are found within the cerebral cortex (Kandel, 2012). Future work should focus on the use of stem cells to develop the model further as stem cells have the ability to generate heterogeneous neural cultures (neurons, oligodendrocytes and astrocytes), can be scaled up due to their mitotic nature and eventually, to personalise the treatments using induced pluripotent stem cells.

### 3.1.2 Generation of physiologically relevant cytoarchitectures

The use of embryonic primary cortical neurons ensures that cells are plastic and as similar as possible to the desired area for implantation and are an electrically active cell type. It should be noted, however, that use of the whole embryonic cortex to generate primary cortical neurons overlooks the areal identity issue highlighted previously but the early developmental stage may circumvent this. The use of nanofibres to promote aligned neurite extension was discussed in Chapter 1 and allows the targeted outgrowth necessary for rewiring to take place but this is only one half of the desired cytoarchitecture. The brain has grey and white matter structures composed of clustered cell bodies and tracts of myelinated axon interconnections respectively (Kandel et al, 2012). Nanofibres promote the targeted neurite extensions that can be used to mimic the white matter. Aggregation of cell bodies is fundamental to mimicry of the grey matter.

Generation of neuronal aggregates has been performed using several methods previously. Studies have used stem cells to generate neurospheres and differentiated the cells from these to generate the desired cytoarchitectures (Lancaster and Knoblich, 2014), whereas others have

seeded cells to pre-cast molds to generate aggregates (Kato-Negishi et al, 2013; Harris et al, 2016). Generation of aggregates from neurospheres is precluded by the use of primary cortical neurons as a choice of cell. Whilst the use of pre-cast molds is a relatively simple method of generating aggregates, extracellular environments that have a high elastic modulus relative to the native tissue can negatively influence terminal neuronal differentiation. One notable example is yes-activated protein (Yap) expression. Yap protein levels are negatively correlated with neuronal differentiation (Hindley et al, 2016; Zhang et al, 2011) and its expression can be influenced by the extracellular environment. Cells cultured on surfaces with high elastic modulus have demonstrated a transient increase in Yap and after a threshold "mechanical dose", demonstrate constitutive expression (Yang et al, 2014). Similarly, culture of neurons on harder surfaces was associated with inhibition of differentiation relative to a soft, hydrogel surface (Ali et al, 2015). Thus, whilst molds are an attractive method of generating aggregates due to their simplicity, the non-physiological properties of the molds may negatively influence the cells.

Hydrophilicity of cell culture substrates is typically employed by cell biologists to ensure cells adhere to a surface in a homogenous manner (Ryan et al, 2008). In contrast, hydrophobicity limits cellular adhesion (Ishizaki et al, 2010) and often results in the formation of cellular aggregates. Through use of highly hydrophobic nanofibre surface, aggregates with aligned neurite projections should be generated; thus, hydrophobicity is proposed as a method of generating self-assembling aggregates.

Aligned nanofibres are easily generated through electrospinning using a defined process. Electrospinning dissolves polymers in a solvent, exposes the solution to a high electrical charge and directs the solution towards a grounded collector. The attraction of the solution to the

collector draws the solution from point A to point B, stretching the solution in to an elongated fiber with nano-dimensions and causing rapid evaporation of the solvent, solidifying the polymer into this fibrous form (Leach et al, 2011). However, electrospinning affords a great degree of flexibility through tailoring of the parameters used (kV, rate of flow, temperature, etc) and choice of polymers. Different polymers and polymer blends have been used to tailor the properties of the nanofibre to the desired function such as conductivity, piezoelectricity, bioactivity or antibiotic properties (Son et al, 2006; Chang et al, 2012; Zhang et al, 2007). Nanofibre diameters can be tailored through alterations to the voltage, distance between charged solution and grounded collector or polymer concentration to induce greater or smaller air-surface interfaces to decrease/increase the wettability (Hekmati et al, 2014; Wu et al, 2008). Alterations to the temperature (cryogenic electrospinning; Leong et al, 2009) or the grounded collector (airgap electrospinning; Jha et al, 2011) can be used to influence the porosity. Thus, aligned nanofibre structures with desired material chemistries can be created using electrospinning. Optimisation aims to maximise alignment of the nanofibres to enhance the guidance of neurites that are grown upon the fibres whilst retaining the small diameter of the nanofibres to attain the desired wettability and ehance guidance, polarity and growth.

Poly lactic acid (PLA) is a hydrophobic polymer that is one of the most widely used materials within the biomedical sciences (Santoro et al, 2016). It is FDA-approved for *in vivo* uses (Jung et al, 2005) and has found use as a material for drug delivery and scaffolds for tissue engineering, often in the form of nanofibres (Wang et al, 2016; Evans et al, 2000; Hwang et al, 2014; Koh et al, 2010). The poly-L-lactic acid (PLLA) isomer is favourable for tissue engineering purposes due to its tunability as a material, biocompatibility and degradability. Several mechanical properties such as degradation rate, mechanical strength and solubility can be adjusted (Lopes et al, 2012). Degradation and mechanical strength can be adjusted through

stereocomplexing, blends of polymers, crystallinity or altering the molecular weight (Lopes et al, 2012; Ishii et al, 2009; Weir et al, 2004). Additionally, the only by-product of PLLA degradation is the physiological metabolite lactic acid (Santoro et al, 2016). Biocompatibility has been demonstrated in rodent models with a range of different PLLA based structures and limited inflammation and immune response has been observed (Jaiswal et al, 2013; Koh et al, 2010; Evans et al, 2000; Evans et al, 1999), including those implanted in the CNS (Wang et al, 2016; Hwang et al, 2014; Rivet et al, 2015). Thus, PLLA was selected as the polymer for the fabrication of nanofibres in the current work.

In summary, aligned nanofibres are capable of inducing aligned neurite outgrowth from primary neurons whilst hydrophobic structures can be used to induce aggregation of cells. This chapter describes efforts to optimise a system that can be used to generate 3D cell clusters with aligned neurites, spanning hundreds of microns that will comprise the cellular aspect of the implant. The ability to control the dimensions of the cell clusters that can be generated is ideal. Poly-L-lactic acid was selected as it is a hydrophobic polymer that can be electrospun and is FDA-approved for implantation studies (Jung et al, 2005).

## 3.2 Methods

### 3.2.1 Electrospinning of aligned PLLA nanofibre scaffolds

This was achieved as described previously (Chapter 2)

### 3.2.2 Dissociation and maintenance of primary cortical neurons

This was performed as described previously (Chapter 2)

### 3.2.3 Adherence time course assays

The iCelligence E-Plate L8s were loaded with NbActiv1 medium and a background cellular impedance reading was taken for medium alone at 37°C in a humidified incubator. Primary

cortical neurons were isolated and dissociated as previously described (Chapter 2) and seeded to iCelligence E-plate L8s at a density of 25,000 cells/cm$^2$. Electrical impedance was measured every minute for 4 hours and the values for 4 replicates were averaged. Non-linear regression was used to determine the time of plateau, half-time and rate constant (K).

### 3.2.4 Optimising electrospinning parameters

Aligned PLLA nanofibres were electrospun with a custom electrospinning rig as described previously (Chapter 2). Chapter 2 describes the optimised protocol common to all experiments. Initially, aligned PLLA nanofibres were electrospun using the following parameters; 25kV electrical voltage, 15cm needle tip to collector distance and 1ml/hr flow rate. These parameters were established by troubleshooting using the protocol of Leach et al (2011). Optimisation was performed through modulation of the polymer concentration whilst these parameters remained constant. Several polymer concentrations were tested to optimise the alignment while retaining the low diameter. PLLA was dissolved overnight at 50°C to a concentration of 26, 28, 30, and 32% w/w in HFIP. These were spun using the existing parameters, sputter coated with 5nm of gold using a sputter coater and visualised using a Jeol scanning electron microscope (JSM-7100F). Nanofibre diameter was measured using ImageJ. Ten nanofibre diameters were measured per field of vision, with 3 fields of vision used per independent replicate.

Hydrophobicity was measured using a Kruss Drop Shape Analyzer 10 MK2. A 5 µL droplet was placed on the nanofibre membrane and the contact angle between the droplet and the surface was measured using a polynomial fit. Each replicate used 3 nanofibre membrane and 3 independent electrospins were used to generate membranes for the 3 independent replicates.

### 3.2.5 Primary optimisation – medium changes and suspension culture

A multifactorial experimental design was used in the design of the optimisation experiments. Primary cortical neurons were seeded to nanofibres and exposed to 1 of four conditions: “Normal medium change/non-suspended”, “normal medium change/suspended”, “alternate day medium change/non-suspended” or “alternate day medium change/suspended”. Neurons within the suspended conditions were elevated from the base of the well using custom PDMS rings; the aligned nanofibre membrane extended across the negative space of the ring, ensuring that the medium could access the basal aspect of the nanofibre membrane. Neurons of the non-suspended conditions were seeded to nanofibre membranes that rested on the basal surface of the well. Neurons within “normal medium change” subcategory had 50% medium changes performed based on the recommended procedure of Brainbits LLC (Brainbits LLC, 2017), once every 4 days. Neurons within the “alternate day medium change” conditions had 50% medium changes performed every other day.

After 11 days in vitro (DIV), neurons were fixed, permeabilised, incubated with primary and secondary antibody and nuclear stained with DAPI, as described in Chapter 2. The primary antibody for immunostaining was anti-βIII-tubulin (1:100) and the secondary was FITC-labelled anti-mouse IgG (1:50). Samples were visualised using a Leica SP5 fluorescence microscope. Neuronal morphology (cell cluster diameter, neurite length, neurite bundle diameter and dispersion) was then quantified using ImageJ. Cell cluster diameter, neurite length and neurite bundle diameter were measured using basic functionalities within ImageJ; the distances of 10 clusters/neurites/neurite bundles was measured for 3 fields of vision per replicate, with 3 replicates employed. Dispersion is a measure of neurite alignment; decreasing dispersion indicates increasing neurite alignment. Dispersion was measured using the Directionality plugin on ImageJ. To quantify dispersion, whole fields of vision were analysed for their dispersion, 3 fields of vision were used per replicate with 3 replicates employed.

Statistical analysis was performed using Graphpad Prism 7 and IBM SPSS Statistics software 24. Initially, one-way ANOVA and Tukey's post hoc test were used in Graphpad Prism to determine if any condition significantly enhanced neuronal morphologies. Multifactorial ANOVA was utilised in SPSS to investigate the interaction between factors. If interactions between factors were confirmed to be significant ($p = <0.05$), interaction plots were generated within the software to visualise the interactions.

### 3.2.6 Secondary optimisation – controlled seeding

Secondary optimisation focused on optimising the seeding procedures. Seeding thus far had entailed applying the cells as a droplet on to the hydrophobic surface, allowing adhesion for 60 minutes. The size of droplet was determined by the cell count after dissociation. For this optimisation, cells were seeded in this manner for the control. The experimental conditions utilised droplets of controlled sizes. For the experimental conditions, after a cell count was performed, cells were centrifuged again and resuspended in either 3µL or 30µL, ensuring that the number of cells seeded to the surface was 25,000 cells/$cm^2$.

Cell culture, preparation for immunofluorescence visualisation and visualisation was performed in an identical manner to that employed for the primary optimisation. As only one factor was optimised in this optimisation, one way ANOVA and Tukey's post hoc test were employed for statistical analysis.

## 3.3 Results

### 3.3.1 Establishing a control cell culture condition

Primary neuronal culture using Brainbits protocol yielded poor results initially. Cells attached poorly, failed to survive longer than 24 hours and a negligible percentage extended neurites (figure 3.1A). After optimisation of the density of the cell culture (data not shown), cells adhered properly, a greater percentage were extending neurites after 24 hours and less visible

debris were present (figure 3.1B). After 13 DIV, cells exhibited random networked morphologies. Little alignment of neurites can be observed and cells have a stellate morphology (figure 3.1C). Staining for a neuron-specific marker (βIII-tubulin) confirmed that the cultured cells were neuronal (figure 3.1D) although some cultures exhibited a negligible percentage of cells that were non-neuronal (data not shown).

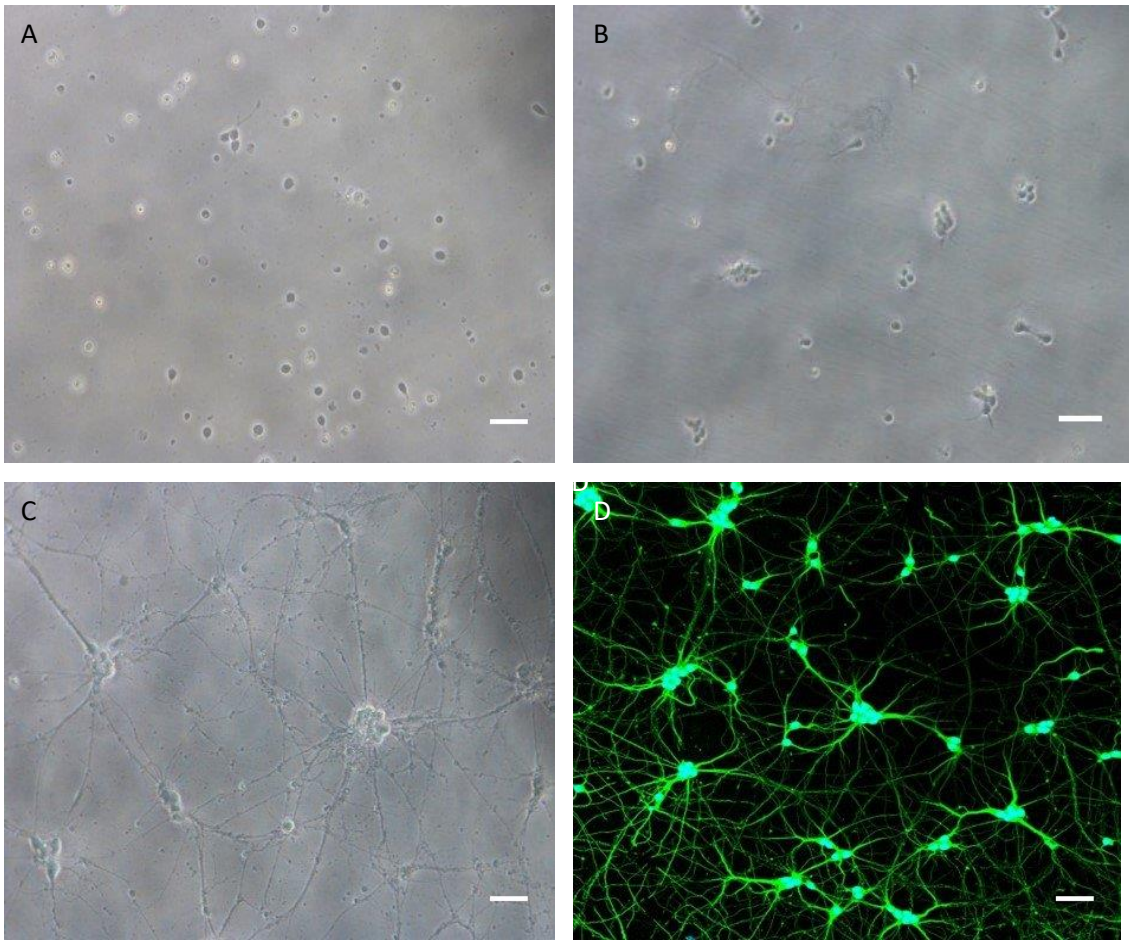


Figure 3.1: E18 primary cortical neurons from Sprague-Dawley rats. Scale bar = 50µm (A) Cortical neurons 24 hours after seeding using Brainbits protocol. Apoptotic cell bodies can be seen to make up the majority of the culture with relatively few cells extending neurites. The quantity of cellular debris is also notable. (B) Cortical neurons 24 hours after seeding using an optimised protocol. A higher proportion of cells are extending neurites and clusters of cell bodies can be observed (C) 13 DIV of culture of primary cortical neurons using the updated protocol. Network formation, neurite fasciculation and cell clustering are all present. (D) Cells stained for a neuron specific antigen (βIII-tubulin), demonstrating that cells were predominantly neuronal

## 3.3.2 Electrospinning PLLA nanofibres with the desired material properties

The electrospinning protocol was optimised in order to maximise the alignment of the nanofibres. Only one parameter, the polymer concentration, was altered in order to do so. Increasing the polymer concentration from 28% to 30% was observed to significantly increase the alignment (figure 3.2A) without significantly affecting the diameter of the nanofibres (figure 3.2B). Aligned PLLA nanofibre membrane exhibited a high degree of hydrophobicity; 131±4° (figure 3.2C).

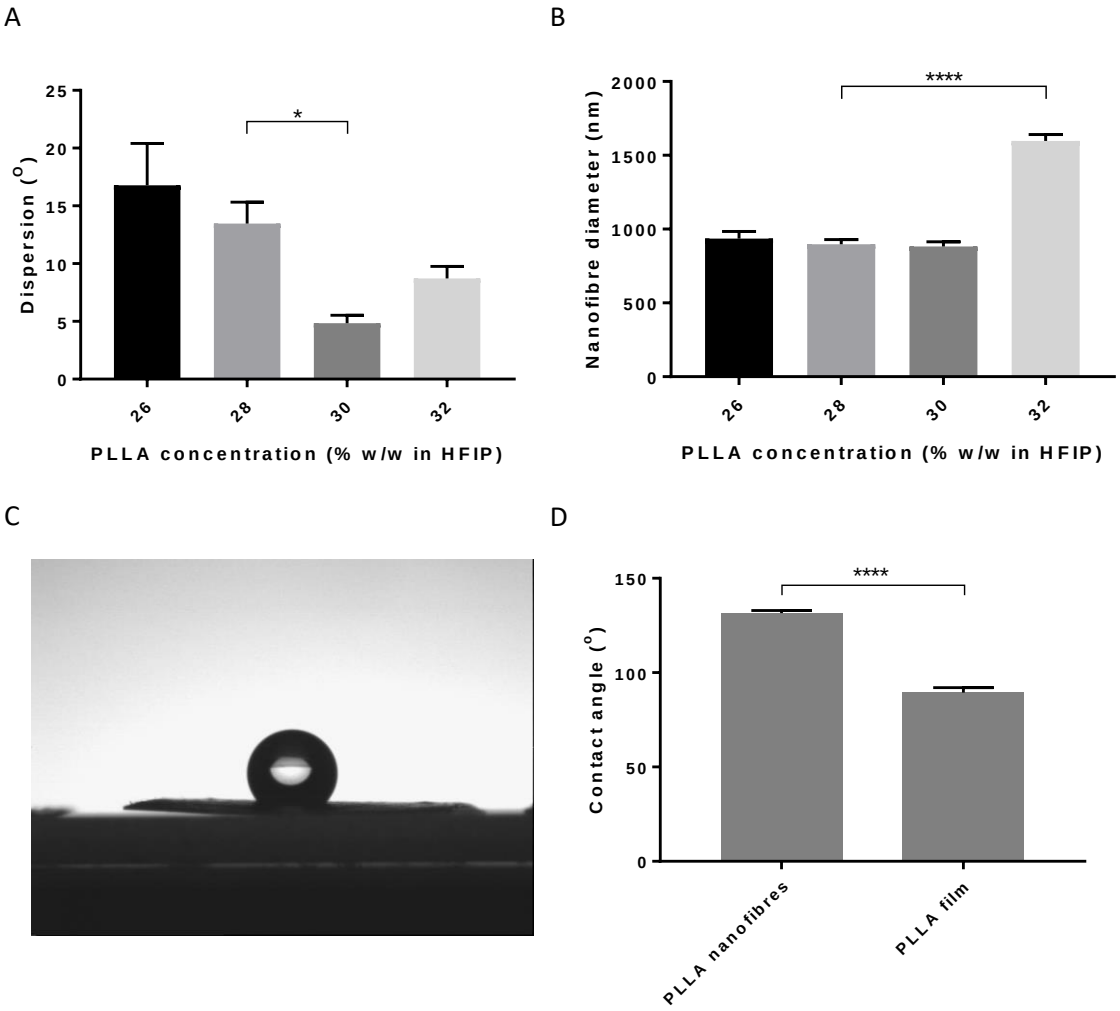


Figure 3.2: Optimisation of electrospinning PLLA nanofibres. (A) Alignment of nanofibres; decreasing dispersion indicates increasing alignment. 30% PLLA (w/w) in HFIP had the greatest alignment. Significant difference was detected by one-way ANOVA (F = 6.046, p = 0.0022). Tukey's post hoc test was applied; significant difference was observed between 26% and 30% (q = 5.595,p = 0.0021) and 28% and 30% (q = 4.043, p = 0.0355) (B) Nanofibre diameter. Significant difference was detected by one-way ANOVA (F = 76.69, p = <0.0001). Tukey's post hoc test

was applied; significant difference was observed between 32% and all other conditions (p = <0.0001 for all, q = 16.7, 17.68 and 18.05 for 26%, 28% and 30% respectively) (C) Aligned PLLA nanofibres electrospun at 30% w/w in HFIP demonstrating hydrophobicity and a high contact angle (D) PLLA nanofibres demonstrated a high degree of hydrophobicity (131° ± 1.35) that was significantly elevated relative to the control, a PLLA film (89.42° ± 2.61) (unpaired t-test; t = 15.98, df = 16, p = <0.0001)

## 3.3.4 Adherence assays

Cells were found to maximally adhere to the surface at 72 minutes whilst the half time of the adherence was 9.94 minutes (figure 3.3). As a result, to ensure that neurons attached to the nanofibres, they were seeded as a single droplet to the membrane, allowed to attach for 60 minutes prior to the addition of the medium required to fill the well.

A

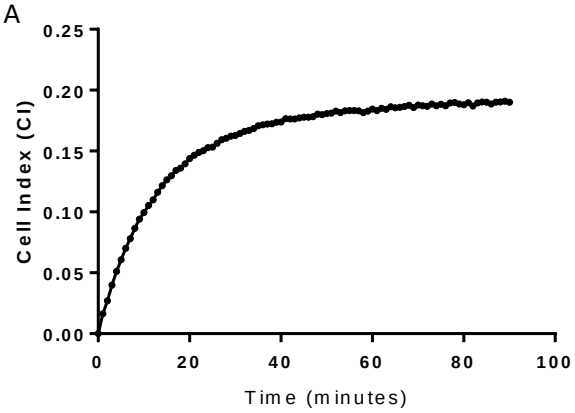


B

| Measurement | Observed value |
|---|---|
| Time of Plateau (minutes) | 72 ± 7.8 |
| Half-time (minutes) | 9.94 ± 0.19 |
| K (minutes$^{-1}$) | 0.06972 ± 0.001 |

Figure 3.3: Adherence behaviours of E18 Sprague Dawley primary cortical neurons using the iCelligence. N = 4. (A) Cell attachment was quantified using electrical impedance; one phase association to the surface was observed (B) Non-linear regression was performed in Graphpad Prism using the equation for one phase association.

## 3.3.5 Initial optimisation

Initial optimisation used a multi-factorial optimisation experiment which focused on two factors; the frequency of medium changes ("normal medium change" and "alternate medium change") and suspension cultures. Only one of the initial conditions demonstrated properties that were suitable for further experiments – non-suspended nanofibres with alternate medium changes. Whilst each of the conditions tested had cells that stained for DAPI and βIII-tubulin and were quantified for their cell cluster diameter, single cells were typically observed (figure

3.4A). These cells did not extend neurites (figure 3.4B) and thus did not fasciculate (figure 3.4C). One-way ANOVA and subsequent Tukey's post hoc test demonstrated that non-suspended neurons that received a medium change on alternate days significantly outperformed all conditions on every quantified assessment (one-way ANOVA; cell clustering - F = 74.53, p = <0.0001 , neurite length - F = 100.4, p = <0.0001, neurite diameter - F = 271.2, p = <0.0001, neurite alignment - F = 2514305, p = <0.0001).

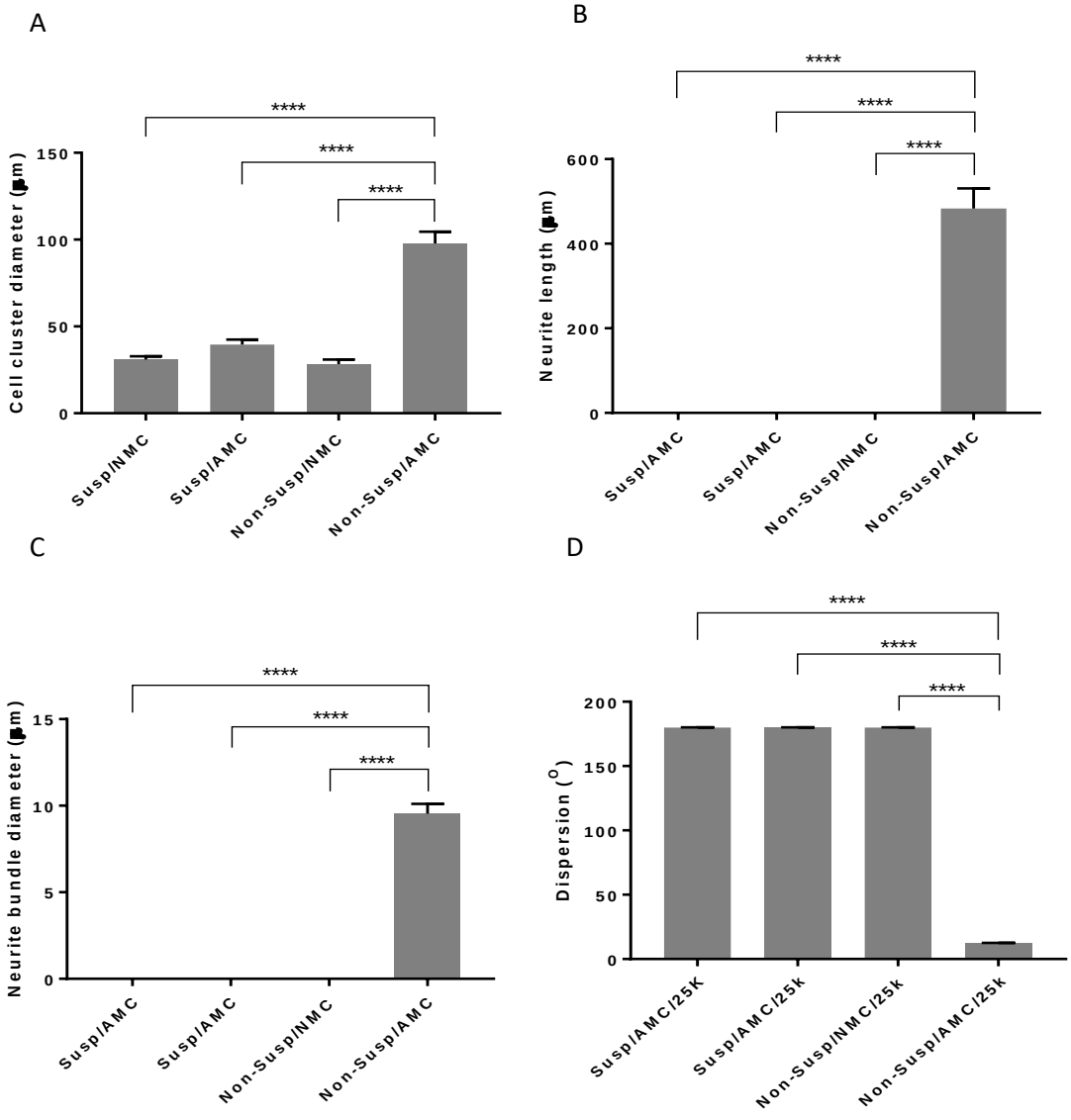


Figure 3.4: Initial multi-factorial optimisation of 3D cell cluster formation. Of the 4 tested conditions, only non-suspended cultures with alternate medium changes allowed for long-term survival, clustering and neurite growth/fasciculation. Susp = suspended nanofibre membranes, Non-Susp = non-suspended nanofibre membranes, NMC = normal medium change, AMC = alternate day medium change. N = 3.(A) Diameter of the 3D cell clusters grown in the separate conditions. Cells clustered significantly more on the non-suspended, alternate medium day

medium change condition (one-way ANOVA; F = 74.53, p = <0.0001) (B) Neurite length. Non-susp/AMC resulted in significantly greater neurite outgrowth (one-way ANOVA; F = 100.4, p = <0.0001) (C) Neurite bundle diameter. Neurites were significantly more fasciculated in the non-susp/AMC condition (one-way ANOVA; F = 271.2, p = <0.0001) (D) Neurite alignment. (one-way ANOVA; F = 2514305, p = <0.0001). Statistical analysis was performed by one-way ANOVA and Tukey's post hoc test.

Alternate day medium changes for neurons grown on non-suspended nanofibre membranes was the optimal condition of those tested. Due to the multifactorial design, the ability of factors to influence each other was investigated using a multifactor ANOVA. A significant interaction was detected between medium change frequency and suspension of the nanofibre membranes for cell cluster diameter, neurite length and neurite bundle diameter (figure 3.5A-C). Whilst culture of primary cultured neurons on the uncoated aligned PLLA nanofibres appeared to kill the cultured neurons, this could be ameliorated by two out of the four conditions. The condition with "normal medium changes" in non-suspended culture exhibited greater clustering than the suspended cultures but the comparative culture with alternate day medium changes exhibited greater clustering (figure 3.4A). Whilst the alternate day medium change was beneficial enough to the culture to allow some clustering in the suspension culture, it was not sufficient to allow the cells to survive, blunting the cell clustering and inhibiting the neurite extension (figure 3.4A, 3.4B and 3.4C).

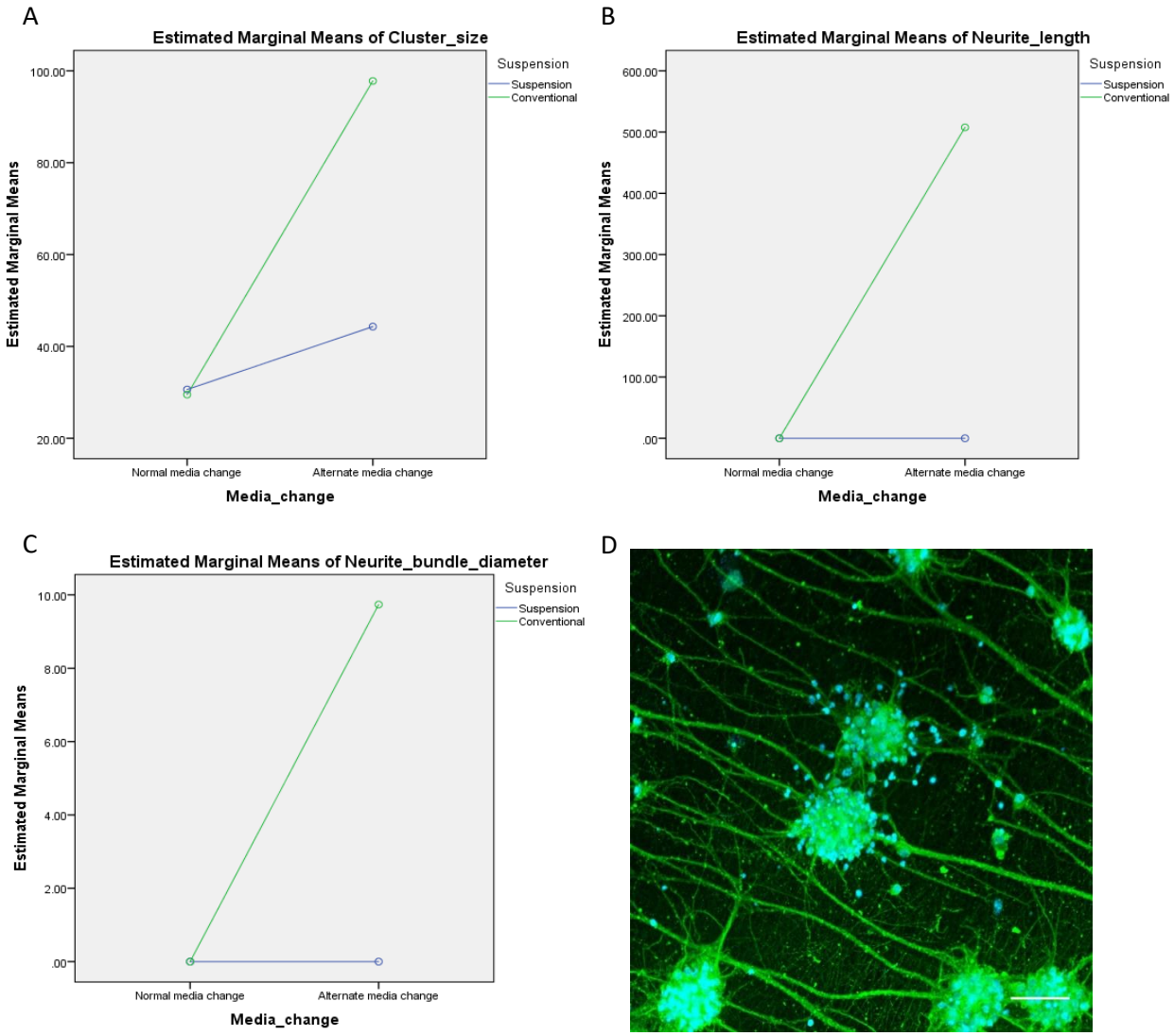


Figure 3.5: Multifactorial ANOVA of the data generated in the primary optimisation. N = 3 (A) Whilst medium changes on alternate days significantly increase clustering, this effect is enhanced by conventional culture/reduced by suspension culture ($p = <0.0001$) (B) Neurite extension shows an interaction between factors; only the combination of alternate medium changes and conventional culture is capable of inducing neurite outgrowth from neurons cultured on uncoated PLLA nanofibres ($p = <0.001$) (C) Neurite bundle diameter shows an interaction between factors; only the combination of alternate medium changes and conventional culture is capable of inducing fasciculation of neurites from neurons grown on the uncoated PLLA nanofibres ($p = <0.001$) (D) Primary cortical neurons at 11 DIV, cultured on aligned PLLA nanofibres in the non-suspended, alternate day medium change condition.

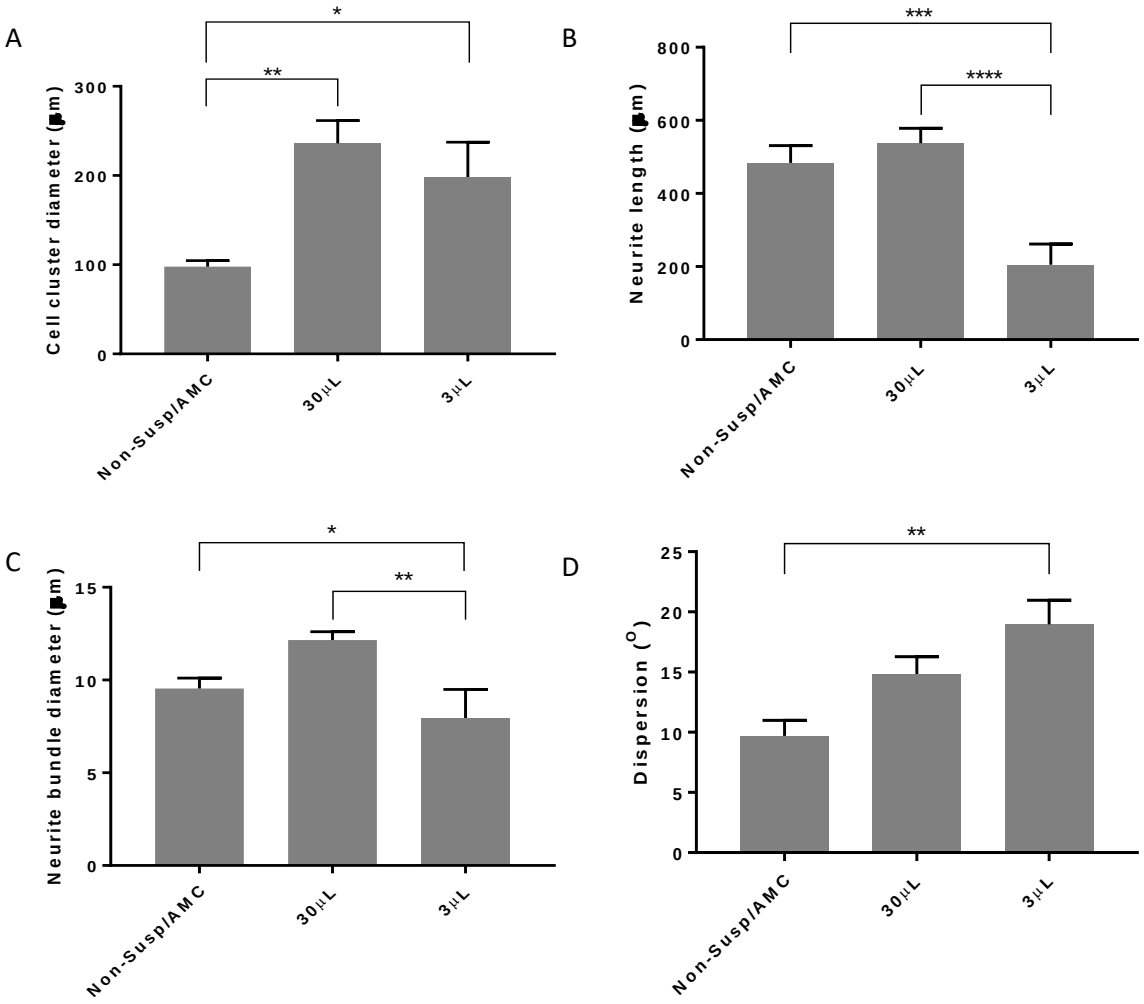


Figure 3.6: Secondary optimisation of cell cluster formation. Cells were delivered in either 3 or 30µL of medium and allowed to attach for 1 hour whilst the control (Non-susp/AMC) were delivered in a randomly sized droplet dependent on the cell count. Statistical testing was performed using one-way ANOVA and Tukey's post hoc test. Delivery of cells in a controlled 30µL droplet resulted in greater cell cluster size, neurite length and neurite bundle diameter. No significant change in alignment of neurites was observed. N = 3 (A) Diameter of the 3D cell clusters in the 3 optimisation conditions (B) Neurite length in the 3 optimisation conditions (C) Neurite bundle diameter in the 3 optimisation conditions (D) Neurite alignment in the 3 optimisation conditions

The seeding process was also identified as a part of the process that could be optimised. Cells were initially delivered as a droplet that was between 15-25µL depending on the cell count that was attained upon dissociation of the tissue. A single droplet was placed on the nanofibre membrane, allowed to attach for 60 minutes before addition of the remaining media to the

well. Through changing the volume of the droplet, the size of the area that cells could adhere to would also be altered. Cells were delivered in either a 3 or 30µL drop and compared to the control; the previously identified optimal condition. Cells delivered in controlled volumes of medium (3 and 30µL) both displayed a significant increase in clustering (one way ANOVA; $F = 7.072$, $p = 0.0018$. Tukey's multiple comparison; $q = 3.832$ and 5.054 for 3 and 30 µl respectively, $p = 0.0237$ and 0.002 respectively) with an approximately 2-fold increase in clustering for the 3 µL droplet and a 2.4-fold increase for the 30 µL drop delivery. However, whilst both conditions increased the cell cluster diameter, decreasing the size of the droplet had a significantly negatively effect on the neurite length, neurite bundle diameter and the alignment (positively affected the dispersion) of the neurons (figure 3.6B, 3.6C and 3.6D).

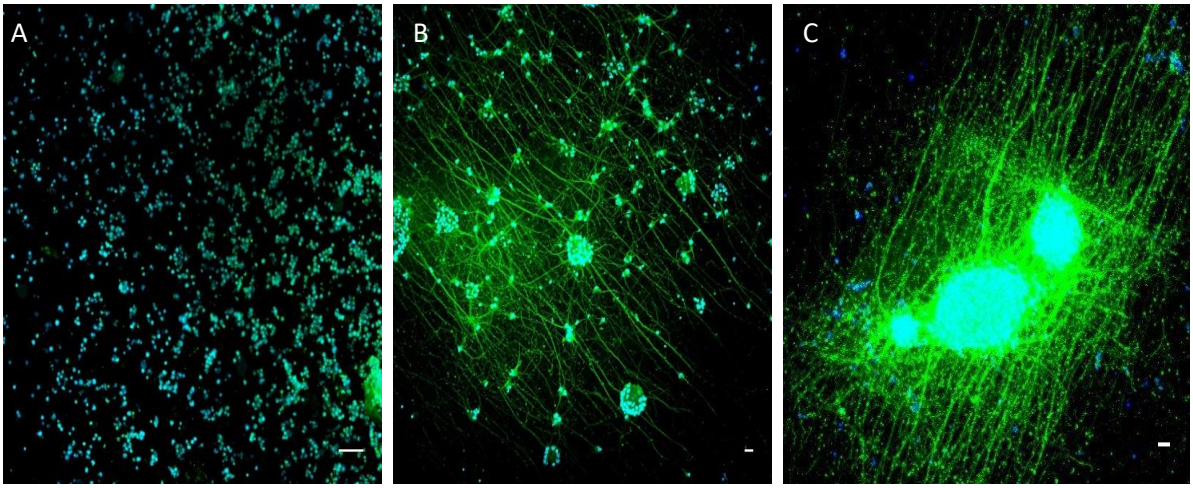


Figure 3.7: Representative images used for quantification of neuronal morphologies for primary cortical neurons grown on aligned PLLA nanofibres under different conditions at 11 DIV (A) Primary cortical neurons grown in suspension conditions with alternate day medium changes. Some clustering is observed but neurites are absent within the culture (B) Neurons grown in a non-suspension culture, seeded within a 3µL droplet. Clustering is observed with extensive neurite outgrowth but relative to the 30µL seeding conditions, clustering is limited (C) Neurons grown under the ideal condition: non-suspension cultures with alternate day medium changes and seeded within a 30µL droplet

## 3.4 Discussion

### 3.4.1 Optimisation of the generation of cellular architectures

Once cell culture conditions that allowed survival of neurons on a 2D surface had been established, culture work transitioned to the 3D aligned PLLA nanofibres. Initial optimisation for generating clustered cellular architectures investigated the influence of factors known to inhibit/aid the growth of neurons in three dimensions. The need for an external homeostatic mechanism is a common problem in the generation of 3D cellular architectures, whether this is for maintenance of oxygen and nutrients or the removal of waste (McMurtrey, 2016). In this experiment, regulation of these diffusible molecules was performed through manual means via medium changes, maximising the concentration gradient of nutrients diffusing into the aggregates while maximising the gradient of waste diffusing out. Primary cortical neurons typically undergo a 50% medium change every 3-4 days whereas alternate day medium changes were performed during the optimisation. In the absence of alternate day medium changes, neurons failed to cluster or extend neurites and had poor viability (figure 3.4). This contrasts with the 2D control; cells were cultured for up to 13 DIV with half media changes every 4 days and remained healthy (figure 3.1). Due to the ability to mitigate the cell death with medium changes, it is likely that the nanofibres produce a diffusible factor in to the medium that accumulates and induces cell death. PLLA degrades to lactic acid (Garlotta, 2002) and neurons are sensitive to lactic acid accumulation (Goldman et al, 1989; Nedergaard et al, 1991). Whilst the degradation of the nanofibres to an acidic by-product is hypothesised to be the cause of cell death, experiments to elucidate the mechanism of cell death were not performed as the aim was to find only the optimal conditions for aggregation and aligned neurite outgrowth. Suspension cultures are often used to generate and maintain neuronal aggregates to promote basolateral access of the aggregates to nutrients/waste disposal (Paşca et al, 2015; Knoblich and Lancaster, 2015; Kadoshima et al, 2013). These cultures are not true

suspension cultures, they utilise spinning bioreactors or ultra-low adherence plates to limit the contact of the cell with the substrate. Maximisation of basolateral access of nutrients is key to the generation of neuronal aggregates. Thus, one of the optimised conditions was the suspension of the nanofibre membranes within the well whilst the other was conventional (membrane resting against the base of the well). However, suspension had a negative effect on the cells with suspension cultures demonstrating poor viability and minimal clustering even in the presence of medium changes on alternate days (figure 3.4A-D). This may occur due to the acidification of the medium due to the degradation of PLLA. By suspending the nanofibres across a space, the porosity of the nanofibres allows greater access of the neurons to the medium through the basal membrane. The increased exposure to the medium may facilitate a greater exposure to and thus, uptake of lactic acid. Alternately, the suspension of the nanofibres exposes more surface area of the fibres to the medium, accelerating the degradation and subsequent acidification, exposing the neurons to harsher conditions, resulting in their reduced viability. Further elucidation was not performed due to time constraints.

Subsequent optimisation was performed in order to enhance the growth of the desired cellular architectures. Cells were initially seeded at a known density in volumes determined by the cell count after dissociation of the tissue. It was theorised that by reducing the size of the droplet used to seed to the nanofibres, the seeded neurons would adhere within a smaller area and thus, due to the close proximity of cells, aggregation would be enhanced. Additionally, controlled seeding and the ability to localise where a cell cluster formed was desirable for the later developmental stages of the implant to facilitate re-wiring. At the current stage, aggregates form on a nanofibre membrane of large surface area that cannot be implanted. This structure would need to be refined to make a deliverable structure and control over the

aggregation aids in facilitating that. Controlling the volume that neurons were seeded into significantly increased the size of the cell clusters produced, both increasing the droplet size (30µL) and decreasing the droplet size (3µL) ($p = 0.0237$ and 0.002 respectively). However, despite the ability of the smaller droplet (3µL) to increase cell cluster size relative to the control ($p = 0.0237$), the neurite length, diameter and alignment were all significantly reduced by seeding in a smaller, controlled volume (figure 3.6B, 3.6C and 3.6D; $p = 0.0007$, 0.003 and 0.0027 respectively). The increase in cell cluster size is likely to be due to restricting the area of adherence caused by the reduction in droplet size. The decrease in neurite length, diameter and alignment may be due to the density of the cells at the point of seeding. To seed cells at 25,000 cells/$cm^2$ on the surface, cells seeded in a 3 µL droplet have a density of 16 million cells/mL whilst those seeded within a 30 µL droplet have a seeding density of 1.6 million cells/mL. Harris et al (2016) achieved better neural network topologies at low plating densities and observed "acute neuronal survival and neurite outgrowth" at 3.6-7.2 million cells/mL. Whilst it is not directly stated, the implication is that above 7.2 million cells/mL resulted in poor survival and neurite outgrowth, which was observed in the current study when plating neurons on the nanofibres in a 3 µL droplet (16 million cells/mL). In contrast, no significant change was induced by seeding the cells in a larger droplet (30µL).

## 3.4.2 Future directions

A method of generating the desired architecture was established but further improvements can be made. Whilst alternative day medium changes had positive effects on the aggregation and viability of the neuronal culture, a potential alternative to alternate medium changes that could be employed in future experiments would be to utilise a microfluidic systems (Kelava et al, 2016). Microfluidic systems would take on the role of *in vitro* vasculature and ensure a dynamic removal of waste products/supply of fresh nutrients/gases, potentially enhancing the

formation further or to provide targeted spatiotemporal cues to the aggregate to manipulate cellular behaviours (Millet and Gillette, 2012). Additionally, a mixed culture could be produced by using a chamber filled with glial cells that is upstream of the neurons, allowing for the supply of soluble neurotrophic factors to the developing neurons (Gao et al, 2016).

Currently, neurons aggregate on the surface at a random location, although typically the cellular structures were relatively centralised on the nanofibre membrane. In order to facilitate the assembly of an implant for rewiring, a greater degree of control is needed over where the aggregates form. The prepared nanofibre membranes form a large elliptical structure, which is not suited to being drawn up into a needle and injected along a damaged axonal pathway to facilitate rewiring. The current membrane would have to be cut in to a linear format before or after seeding of the neurons. Preliminary data suggest that laser ablation of acellular nanofibre membranes into a linear format significantly influences the hydrophobicity of the surface and thus, may limit the aggregation behaviours of the cell (figure 3.8C). Whilst the reduction in hydrophobicity is limited, it is significant. This may not be a great enough reduction in hydrophobicity to influence the aggregation behaviours but it is possible that cells may need to be delivered on to the membrane as an aggregate or the membrane should be cut, post self-assembly. Cutting the membrane post-assembly would require accurate knowledge of where the neuronal clusters form to avoid damage to the cellular structures, thus, greater control over location of aggregate formation is needed. However, the alterations to hydrophobicity induced by laser ablation may be beneficial in another context. Anchor points, highly adhesive regions on an otherwise poorly adhesive surface, have been used to provide neurons with a location on a surface to adhere to and act as “hot spots” for the formation of clusters (Limongi et al, 2015; Gabay et al, 2005). Anchor points can be produced using nanotopography, changing the surface wettability or chemical modification (Gabay et al, 2005). By introducing these

elements on to the surface, migration of cells can be controlled; limited in “hot spots” and promoted everywhere else, inducing the formation of aggregates in a controlled manner. Laser treatment of the nanofibres could be used to generate these hot spots and facilitate controlled aggregation in a desired location. Conversely, due to the abilities of bioactive extracellular matrix (ECM) proteins such as laminin to induce adhesion, inhibit anoikis, stimulate neurite outgrowth and its hydrophilic properties (Yamada and Sekiguchi, 2015), laminin would make an appealing treatment to create these hotspots.

An alternative to allowing cells to self-assemble on the surface of the nanofibres, either in a specified location or by limiting the place they can form, would be to place pre-assembled neuronal clusters onto the surface and allowing them to extend neurites from the clusters. The model of Harris et al (2016) utilises pre-assembled cell clusters that are placed onto the surface of the implant. Previously discussed was the use of molds and the negative impact that could have on cellular biology. However, alternate methods exist for the mechanical assembly of cellular structures in the absence of molds. Studies have employed holographic optical tweezers that allowed cells to be assembled in to complex 3D architectures without manual handling (Kirkham et al, 2015). Additionally, hanging drop culture has demonstrated the ability to induce aggregation of cells at the base of the droplet upon inversion of the culture surface and subsequent culture (Fennema et al, 2013). This method could be used to induce aggregation into small, cellular clusters. These could then be pipetted on to the aligned nanofibre surface and allowed to grow along the surface.

## 3.5 Summary

A method for generating clustered neuronal cell bodies extending aligned neurites has been described in this chapter. These clustered cell bodies grow along an engineered biomaterial structure that may be used for rewiring and repair within the CNS. Further characterisation of the cellular effect of clustering and culture on the 3D surface is required before consideration of its insertion into the brain. Optimisation was relatively limited due to time constraints but many avenues exist for developing the neuronal aggregation in to 3D architectures using hydrophobic aligned nanofibres further.

# Chapter 4: Characterisation of the organoid

## 4.1 Introduction

In Chapter 3, a method of generating the characteristic clustered cell bodies and aligned neurites of the cerebral cortex was developed. However, characterisation was required to determine any functional changes in the cells that occurred as a result of the aggregation and the cell culture process. Characterisation was also employed to determine the mechanism that induces the formation of the organoids which could facilitate future work to manipulate parameters of the cell culture to generate desirable cellular behaviours.

*In vivo*, cells are arranged in three dimensional matrices with cell-cell and cell-extra cellular matrix (ECM) interactions and complex transport dynamics into, out of and throughout the cell (Antoni et al, 2015). In conventional cell culture, cells do not grow in three dimensions; they are homogenously distributed across a surface and, with the exception of suspension cells, attached using charged molecules or bioactive ligands (Ryan et al, 2008). This divergence between cells *in vivo* and *in vitro* leads to altered cellular properties (table 4.1).

| **Advantages** | **Limitations** |
|---|---|
| Physiological cell phenotype | Scaffolds will not be perfectly reproducible, introducing variability |
| Physiological cell genotype | Extracting cells for molecular characterisation becomes more complicated |
| Increased viability | Scaling experiments up |
| Enhanced differentiation | Imaging 3D cultures can be difficult depending on the scaffold transparency, autofluorescence, and depth |
| Physiological response to stimuli | Integration of 3D cell culture into high-throughput techniques |
| Increased cell-cell communication | Control of cell culture conditions such as pH and temperature |
| Cell polarisation | |
| 2D cultures demonstrated decreased sensitivity to apoptotic signals | |
| More physiological drug susceptibilities | |

Table 4.1: Advantages and limitations of three dimensional cell culture relative to conventional two dimensional cell culture. Adapted from Antoni et al, 2015 and Ravi et al, 2014.

Additionally, cell aggregation results in heterogeneous distribution of cells, which in turn results in changes to cell density. The electrophysiological activity of neurons can be altered by different densities of cells (Biffi et al, 2013). Electrical activity in turn can also influence the expression of genes. Numerous transcription factors are directly activated by $Ca^{2+}$ but calcium driven intracellular signalling cascades can result in post-translational modification and activation/inactivation of transcription factors or transcriptional co-regulators as well (West and Greenberg, 2011). Calcium influx as a result of depolarisation can induce alterations to the morphology and cellular behaviours such as altered axon pathfinding, neurite outgrowth, migration, synapse maturation and neurotransmitter phenotype (West and Greenberg, 2011).

Organoids are cellular structures that more accurately recapitulate the tissue of origin than conventional cultures and are extensively used in the pharmaceutical industry although typically, they take a much longer period of time to assemble than the 3D structures presented in Chapter 3 (Lancaster and Knoblich, 2016). Organoids are defined as 3D cellular clusters that are derived from primary tissues or induced pluripotent/embryonic stem cells that demonstrate self-renewal and self-assembly and exhibit similar functionality to the tissue of origin (Fatehullah et al, 2016). For neuronal cultures, due to the post-mitotic nature of mature neurons, self-renewing organoids would require a mixed culture including multipotent neural stem cells. However, within the adult brain, neurogenesis is limited to the olfactory bulb, rostral migratory stream, the subventricular zone and the subgranular zone (Yamagishi et al, 2015); thus, a self-renewing organoid would not accurately recapitulate the cerebral cortex. Thus in order to recapitulate cerebral cortical organoids, the cellular structures must self-assemble in such as a way as to mimic the architecture of the cerebral cortex and they should also demonstrate electrophysiological activity and responsiveness to appropriate neurotransmitters. Due to the nature of the 3D cellular structures that are generated using the previously defined methodology (Chapter 3), further work will also focus on the potential to

use aligned PLLA nanofibres for the generation of organoids for high-throughput pharmaceutical purposes.

In summary, alterations to the conditions of cell culture can significantly affect cellular behaviours. Whilst the desired cellular architectures have been generated from the work present in Chapter 3, other cellular behaviours remained an unknown. The aim of this chapter was to quantify the characteristics of the culture during organoid formation, to form hypotheses for the molecular mechanism involved and to determine if these cellular clusters can be considered to be “organoids”.

## 4.2 Methods

### 4.2.1 Quantification of morphological features and sub-cellular populations within the organoid cultures

Aligned PLLA nanofibres were fabricated as described in Chapter 2. Primary cortical neurons were dissociated and maintained as described in Chapter 2. Neurons were seeded to aligned PLLA nanofibres or to PDL and laminin coated tissue culture plastic, prepared as described in Chapter 2. Neurons were cultured for 11 days and on 1, 3, 7 and 11 days in vitro (DIV), cells were prepared for immunofluorescence staining as described in Chapter 2. The primary antibody used was anti-βIII-tubulin (1:100). Imaging was performed using a Leica SP5 fluorescence microscope.

Quantification was performed using ImageJ. Quantification was identical for each of the time points. Neurite length was quantified by measuring the length of 10 neurites in each field of vision, with 3 fields of vision used for each of 3 replicates. The same method of quantification was used for neurite bundle diameter and cell cluster diameter. At later time points, fewer cell cluster diameter measurements were performed as fewer cell clusters could be visualised per field of vision. Non-neuronal cells were defined as cells that stained for DAPI, indicating nuclear

DNA, in the absence of staining for βIII-tubulin. These cells were counted manually. Dispersion was measured using the Directionality plugin for ImageJ. A region of interest that was 100 x 100 microns (L x W) was placed within the neurite arbor of the forming organoid and quantified. Three measurements were performed for each field of vision and 3 fields of vision were used for each of 3 replicates. For each time point, the average value was used for each quantitative measure. Normalisation was performed to the value of the first measurement for each measure.

Correlation analysis was performed using Graphpad Prism. Data for each of the time points were used individually before repeating with the pooled data. Heatmaps and scatterplots were generated using the Graphpad Prism or Morpheus Heatmap software.

Sholl analysis was employed to investigate differences in neurite morphologies. Images of primary cortical neurons cultured on both the control and aligned PLLA nanofibres for 11 days were converted into 8-bit and thresholded to produce black and white images for Sholl analysis. Using the neurite tracer plugin of ImageJ, the arbors were drawn. The Sholl analysis plugin for ImageJ was employed for quantification with a step size of 0.01µm. The arbors of 3 neuronal clusters were employed for 3 independent replicates, results were pooled and quadratic non-linear regression was performed using Graphpad Prism 7.

### 4.2.2 Cell viability assay

A lactate dehydrogenase (LDH) assay was performed to determine the cell viability of the organoid over time. The LDH assay was performed according to manufacturer's protocols (Thermofisher Scientific). Briefly, neurons were dissociated, seeded and cultured as described previously for 28 days. On 1, 7, 14, 21 and 28 DIV, 50µL of supernatant were removed from the cultures and frozen at -80°C until usage. For use in assays, samples were thawed at room temperature and transferred to a 96 well plate. To each 50µL aliquot of supernatant, 50µL of LDH reaction mix were added. The solution was then incubated for 30 minutes at room

temperature before addition of 50µL of LDH stop solution was added. Absorbance was measured in a BMG Labtech Clariostar plate reader at 680nm. Blanks were subtracted and values were normalised to the control; the amount of LDH activity that was detected at 0 DIV.

### 4.2.3 Plasma treatment of aligned PLLA nanofibres

Aligned PLLA nanofibres were prepared as described previously. To plasma treat nanofibres, a Tegal Plasmaline 415 Asher was used. Nanofibres were exposed to argon/oxygen plasma at 200W for 5 minutes at 200 mTorr pressure.

The wettability of the nanofibre membranes was measured using a Kruss Drop Shape Analyser 10 MK2. Deionised water (5 µL) was applied onto untreated and plasma treated nanofibre membranes and the contact angle between the liquid and surface was measured using a polynomial fit. For each determination of contact angles, 3 measurements were performed per membrane and 3 independent electrospins were used to generate each of the replicates for the membranes.

Neurons were cultured on the plasma treated nanofibres as described previously for untreated nanofibres. Cells were fixed for immunostaining with anti-βIII-tubulin (1:100) as described previously (Chapter 2). Neurite length, neurite bundle diameter, neurite dispersion and cell cluster diameter quantification was performed as described in the section "Section 4.2.1: Quantification of morphological features and sub-cellular populations within the organoid cultures".

### 4.2.4 Quantifying electrical activity from the organoid

To determine whether the cortical neurons of the organoid were responsive to pharmacologically relevant compounds, a voltage sensitive dye was used. Primary cortical neurons were dissociated and cultured for 14 days as described previously. At 14 DIV, the supernatant was removed from the organoids, which were then washed with Hank's buffered saline solution (HBSS) twice. Fluovolt loading solution was added to the cells which were then

incubated at 37°C for 30 minutes. The Fluovolt loading solution was then removed and cells were washed twice in HBSS. Fluovolt-loaded cells were maintained in HBSS with a 1:10 dilution of Neuro Backdrop Background Suppressor. During fluorescence quantification, cells were maintained in 5% $CO_2$ at 37°C. Fluorescence intensity readings were taken at 488nm.

For recordings of elicited activity of neurons, fluorescence readings were performed using a BMG Labtech Clariostar plate reader to a temporal resolution of 1 value every 60 milliseconds. Drugs were administered automatically by the plate reader, AMPA was administered to a final concentration of 10µM whilst GABA was administered to a final concentration of 25µM. Fluorescence was normalised using equation 1.

$$\frac{\Delta F}{F} = \frac{Fluorescence}{Fluorescence\ at\ time\ point\ 0}$$

Equation 1: Normalisation of global fluorescence intensity

For recordings of spontaneous activity from neurons, fluorescence readings were performed using a Leica SP5 confocal microscope to a temporal resolution of one value per 12 milliseconds. Recordings were taken for 60 seconds and normalised using equation 2.

$$\frac{\Delta F}{F} = \frac{(Fluorescence\ Intensity - Background\ Fluorescence\ Intensity)}{Background\ Fluorescence\ Intensity}$$

Equation 2: Normalisation of fluorescence intensity using the Leica SP5 confocal microscope

Spiking events were then identified within the dataset using thresholding. Briefly, the root mean square was calculated for the dataset and values that exceeded 4 times the root mean square were labelled as spiking events.

## 4.3 Results

Primary cortical neurons were fixed and immunostained with anti-βIII-tubulin (1:100) at 1, 3, 7 and 11 DIV (figure 4.1). Over the time period assessed, the organoid can be seen to form; from initial homogenous distribution to increasingly aggregated, demonstrating that the observed results are not due to a failure to disaggregate.

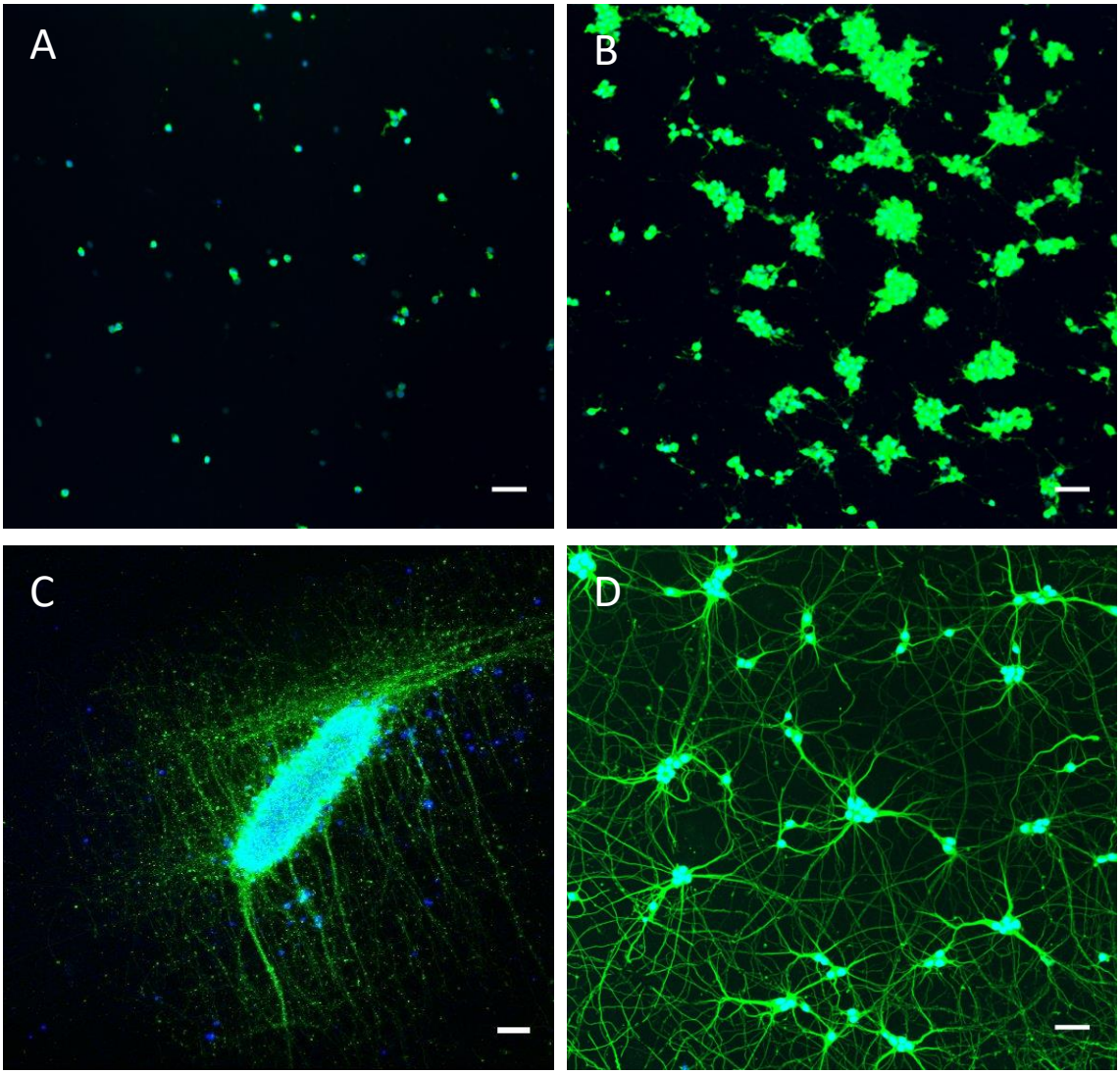


Figure 4.1: Growth of primary cortical neurons over a period of 11 days. A-C: Primary cortical neurons grown on nanofibres. D: Primary cortical neurons grown in 2D (A) At 1 DIV, neurons exhibit homogenous distribution across the nanofibre scaffold. Neurites can be observed from a negligible percentage of neurons and some non-neuronal cells (DAPI stained, non-βIII tubulin stained) have been detected. Scale bar = 50µm (B) At 5 DIV, neuron clustering can be observed although neurite extension is still somewhat random with neurons extending towards other clusters rather than with any alignment Scale bar = 50µm (C) By 11 DIV, cell clusters are fully formed and extending highly aligned, fasciculated neurites. Scale bar = 100µm (D) Primary cortical neurons grown on conventional 2D

tissue culture plastic. Neurites extend at random over relatively short distances. Minimal clustering can be observed. Scale bar = 50µm

Initial morphological analysis of the neuronal cultures demonstrated that neurons cultured on the nanofibres were significantly more clustered (figure 4.2A) and extended longer (figure 4.2A), thicker (figure 4.2B) and less branched neurites (figure 4.2C).

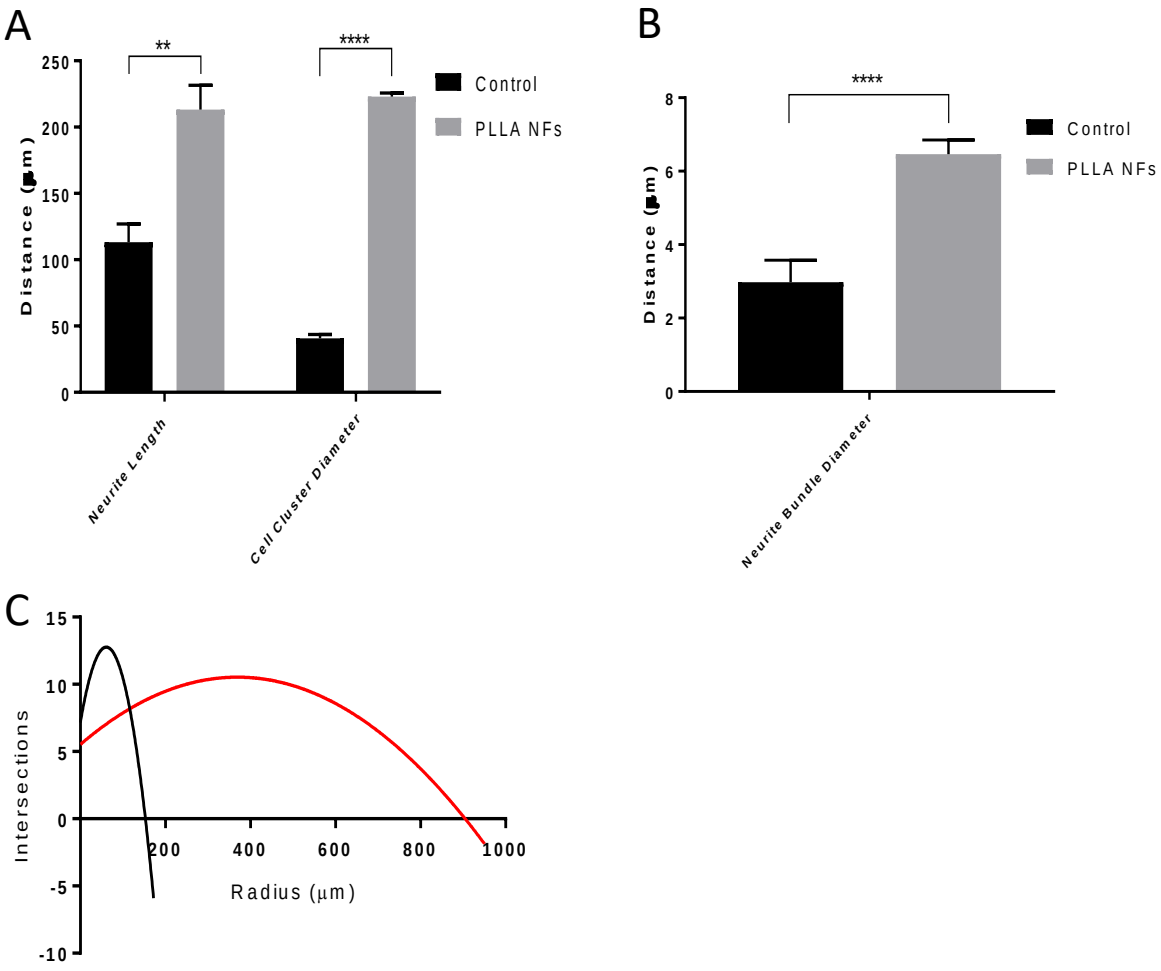


Figure 4.2: Quantification of morphological features of neurons at 11 DIV for the control and nanofibre surfaces (A) Neurites and cell clusters are significantly shorter and less smaller respectively in the 2D culture conditions (unpaired t-test: $p$ = <0.0001, $t(6)$ = 7.178) (B) Neurites are significantly less fasciculated within the 2D cultures (unpaired t-test: $p$ = 0.0014, $t(148)$ = 3.266) (C) Sholl analysis of neurites indicates that neurites cultured on nanofibres are less branched and extend over further distances. Black - control, red = primary cortical neurons cultured on aligned PLLA nanofibres

Subsequent quantitative analysis of the neuronal cultures on nanofibres was then performed at each of the described time points (1, 3, 7 and 11 DIV) using ImageJ. Neurite length, neurite bundle diameter, cell cluster diameter and the percentage of non-neuronal cells were all quantified. Neurite length and neurite bundle diameter exhibited linear growth for the initial 7 days before exhibiting an exponential increase (figure 4.3A and 4.3B). Cell cluster diameter exhibited a more gradual increase but still appeared to be in the early lag phase of an exponential curve (figure 4.3C). In contrast, the percentage of the culture identified as non-neuronal cells decreased early on and then progressively increased, achieving levels that were observed at the beginning of the culture by 11 DIV (figure 4.3D). Normalisation of the data against the values for 1 DIV demonstrates that relative to the control, neurite length exhibited the greatest increase, closely followed by the cell cluster diameter (figure 4.4A). The viability of the culture remained stable through this time period with a significant increase in LDH only appearing at 14 DIV, although this remained consistent until 28 DIV (figure 4.4B).

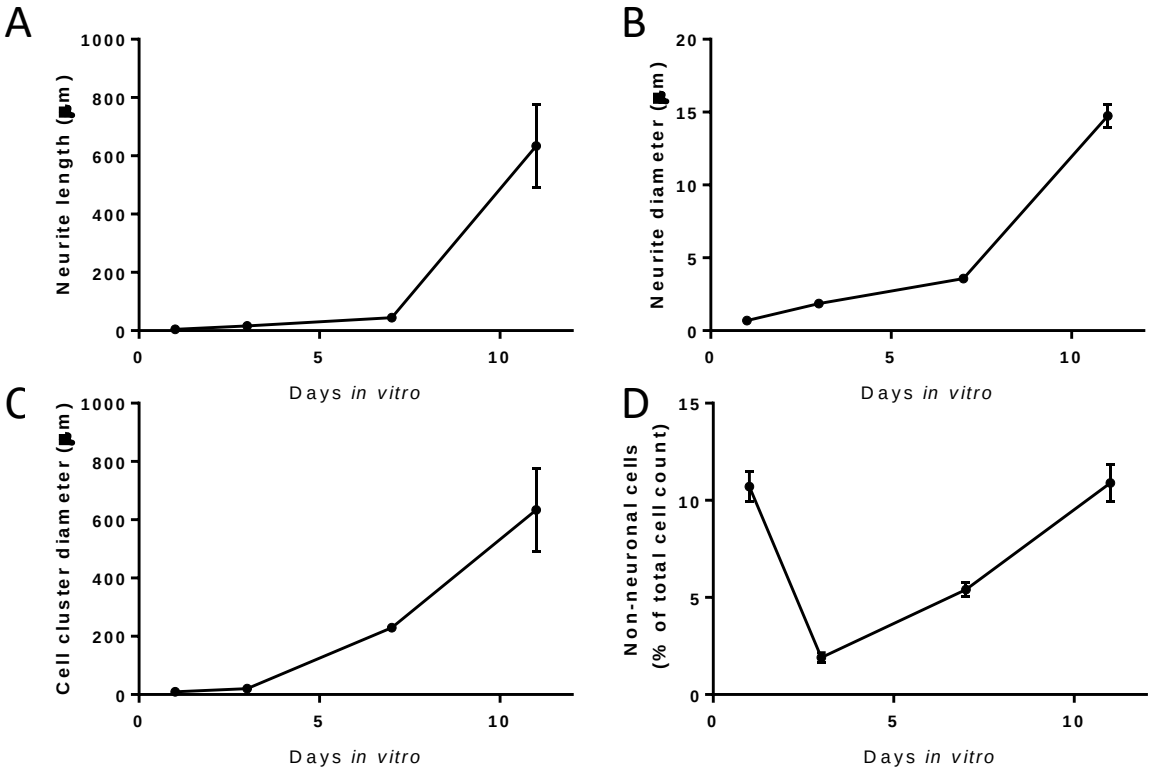


Figure 4.3: Time course for absolute changes to morphology and sub-cellular populations for primary cortical neurons grown on aligned PLLA nanofibres (A) Neurite length (B) Neurite diameter (C) Cell cluster diameter (D) Percentage of the total cell count that were non-neuronal

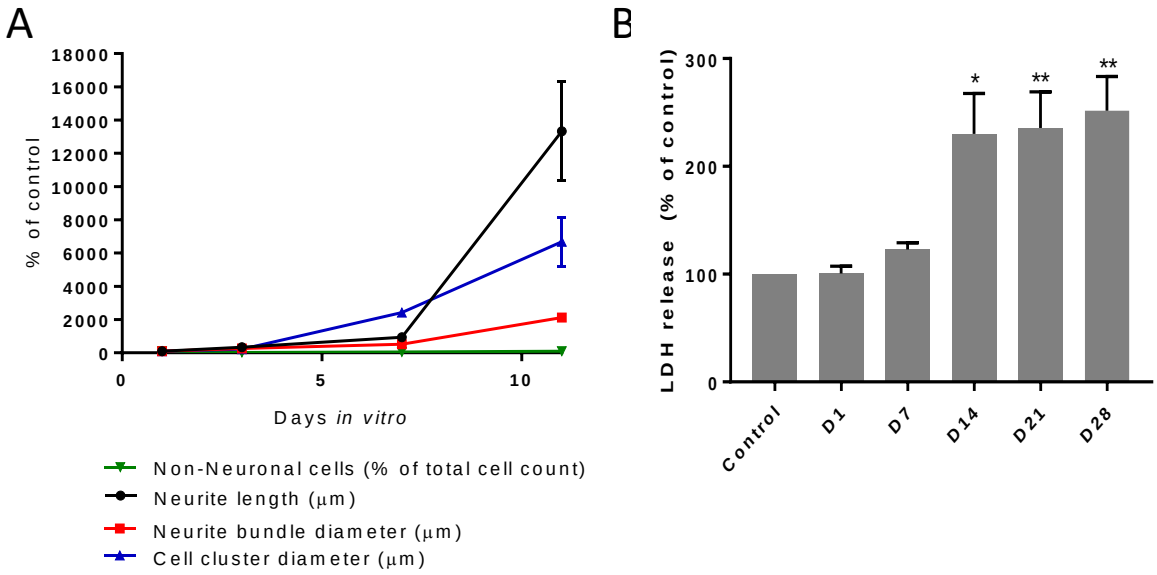


Figure 4.4: Time course for normalised changes to primary cortical neurons grown on aligned PLLA nanofibres (A) Analysis of cell morphology and sub-cellular populations. Data for each category were normalised to the value of 1 DIV. (B) Cell viability was significantly decreased relative to the control after 14 days although remained stable up until 28 DIV (One-way ANOVA: $p = 0.0011$, $F(5,12) = 8.738$. Dunnett's multiple comparisons test was used for post-

hoc testing. Control vs D1: $p$ = 0.9999. Control vs D7: $p$ = 0.9429. Control vs D14: $p$ = 0.0114. Control vs D21: $p$ = 0.0086. Control vs D28: $p$ = 0.0039.

Correlation analysis was used to investigate relationships between factors at different time points (figure 4.5). At 1 DIV, neurite length was significantly positively correlated with every other factor (figure 4.5A and 4.5B). By 3 DIV, only the neurite bundle diameter and cell cluster diameter correlated with neurite length significantly (figure 4.5A and 4.5C. By 7 DIV, no significant correlations were observed (figure 4.5A and 4.5D). At 11 DIV, neurite length significantly correlated with neurite bundle diameter and cell cluster diameter; however, whilst neurite length positively correlated with neurite bundle diameter, a significant negative interaction was observed for neurite length and cell cluster diameter (Figure 4.5A and 4.5E).

The significant correlations for neurite bundle diameter were identical for neurite bundle diameter as they were for neurite length with the exception of 11 DIV; neurite bundle diameter was significantly positively correlated with cell cluster diameter whereas for neurite length, the relationship was negative (figure 4.5A and 4.5E)

The cell cluster diameter was significantly negatively correlated with the percentage of the culture comprised of non-neuronal cells at the majority of time points (figure 4.4A, 4.4B, 4.4C, 4.4E). The relationship between cell cluster diameter and neurite length and neurite bundle diameter has been described in the previous points.

The percentage of the culture that was made up of non-neuronal cells had only significant negative effects on the other factors examined at all time points although this negative influence was mitigated at later time points (figure 4.5A-E).

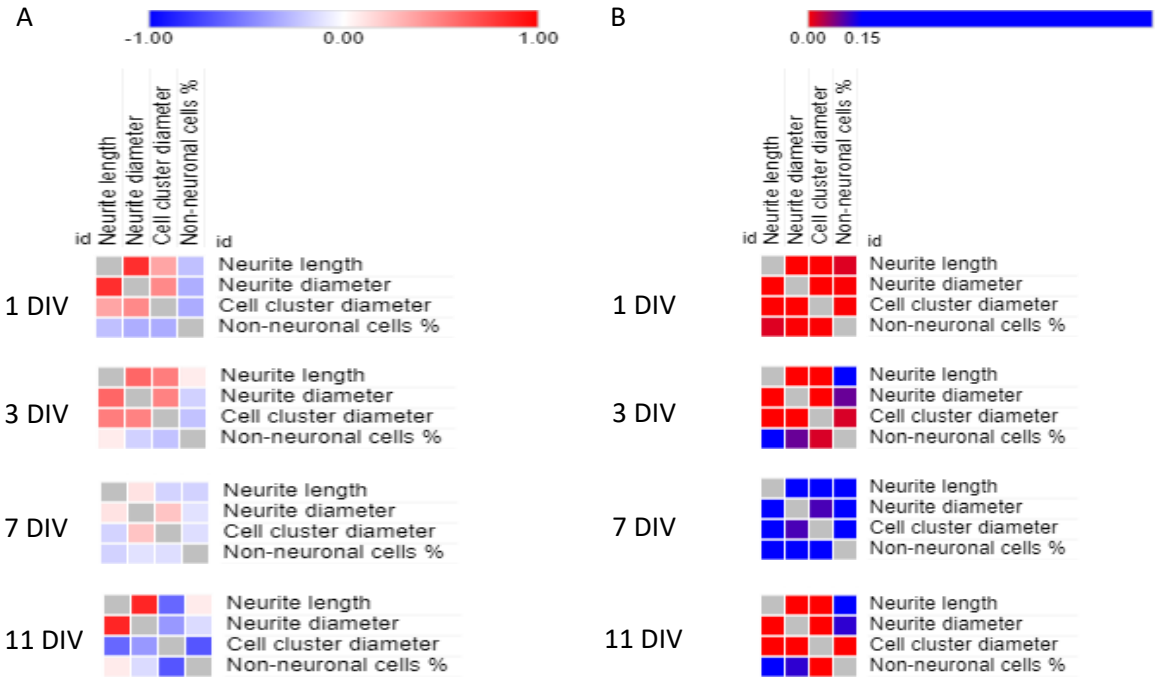


Figure 4.5: Correlation analysis for various morphological properties of cortical neurons grown on aligned PLLA nanofibres at different time points (A) Heat map visualisation of $R^2$ values for neurite length, neurite bundle diameter, cell cluster diameter and the percentage of cells that were non-neuronal. Red = positive correlation, blue = negative correlation (B) Heat map visualisation of *p* values for the correlation analysis. Red = significant, blue = non-significant, purple = borderline significant

A regression analysis was performed using the data from all time points to determine whether factors could be used to consistently predict the values of other factors and potentially infer a mechanism of formation for the organoids (figure 4.6A-F). Regression analysis revealed that the strongest correlation was between neurite length and neurite diameter (figure 4.6D; $R^2$ = 0.7599), closely followed by cell cluster diameter/neurite length (figure 4.6C; $R^2$ = 0.5301) and cell cluster diameter/neurite bundle diameter (figure 4.6B; $R^2$ = 0.3171). Alignment of neurites (dispersion) was found to be a poor predictor of any other factor (figures 4.6A, 4.6E, 4.6F).

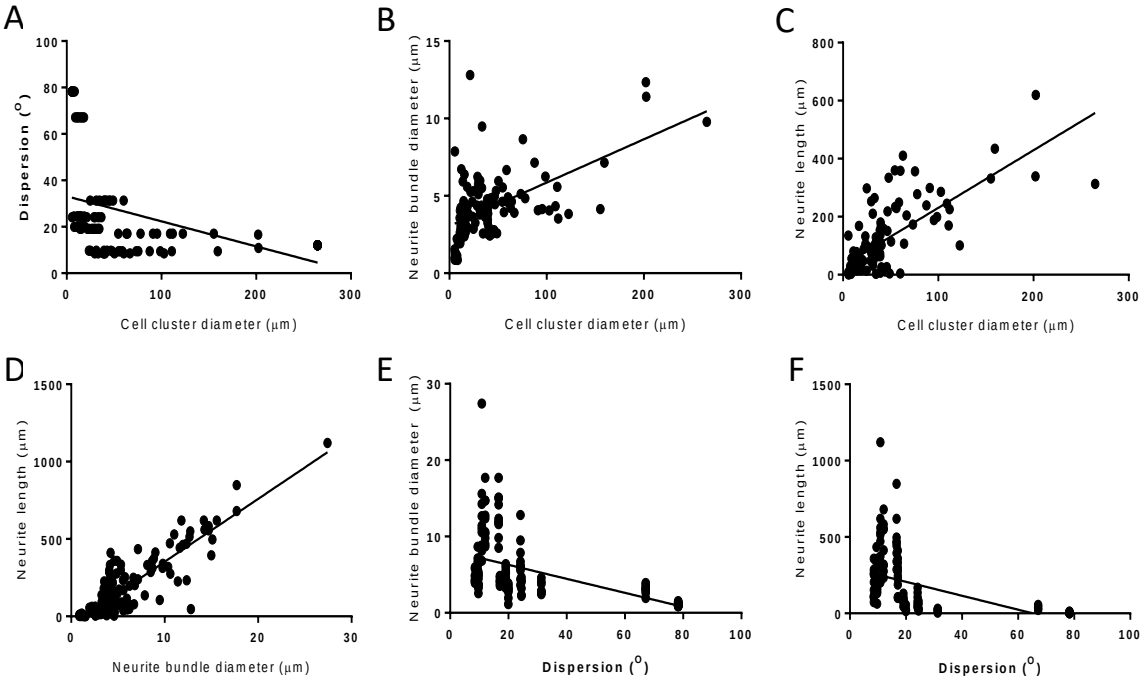


Figure 4.6: Regression analysis for morphological features of primary cortical neurons grown on aligned PLLA nanofibres. For all figures, significance was confirmed at p = <0.0001. (A) Cell cluster diameter and neurite dispersion exhibited a negative correlation; increasing cell cluster diameter correlated with decreasing dispersion ($R^2$ = 0.1876). (B) Cell cluster diameter and the diameter of neurite bundles exhibited positive correlation ($R^2$ = 0.3171). (C) Cell cluster diameter and neurite length exhibited positive correlation ($R^2$ = 0.5301). (D) Neurite bundle diameter and neurite length exhibited positive correlation ($R^2$ = 0.7599). (E) Neurite dispersion and neurite bundle diameter exhibited negative correlation; with decreasing dispersion/increasing alignment of neurites, neurite bundle diameter increased ($R^2$ = 0.1983). (F) Neurite dispersion and neurite length exhibited a negative correlation; decreasing dispersion/increasing alignment correlate with increasing neurite length ($R^2$ = 0.2251).

Plasma treatment of aligned PLLA nanofibre membranes was utilised to alter the wettability of the surface. Plasma treatment resulted in pitting of individual nanofibres (figure 4.7A) and a significant reduction in the hydrophobicity (figure 4.7B). Culture of primary cortical neurons on the hydrophilic plasma treated nanofibres significantly altered cellular morphologies (figure 4.7C). Relative to the neurons grown on untreated PLLA nanofibres, neurons grown on plasma

treated PLLA nanofibres generated significantly smaller cell clusters with shorter, less fasciculated and less aligned neurites (figure 4.8A-D).

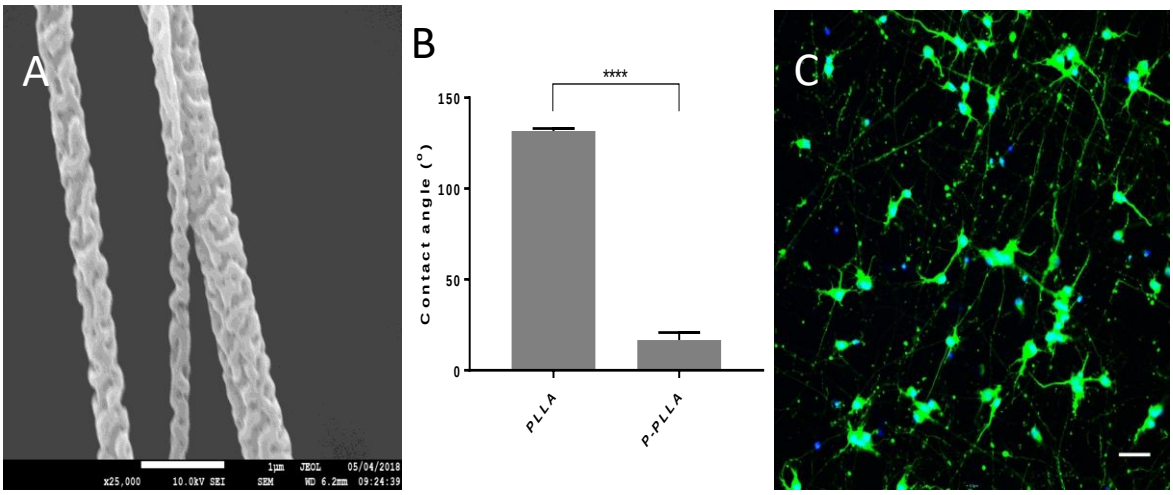


Figure 4.7: Plasma treatment induces significant changes to nanofibre wettability and cellular behaviours. (A) Plasma treated PLLA nanofibres (B) Significant reduction in contact angle was observed for plasma treated PLLA (p-PLLA) (Unpaired t-test: $p$ = 0.0001, $t(16)$ = 26.44) (C) Primary cortical neurons grown on plasma treated PLLA nanofibres; a reduction in clustering, neurite extension and neurite alignment is observed.

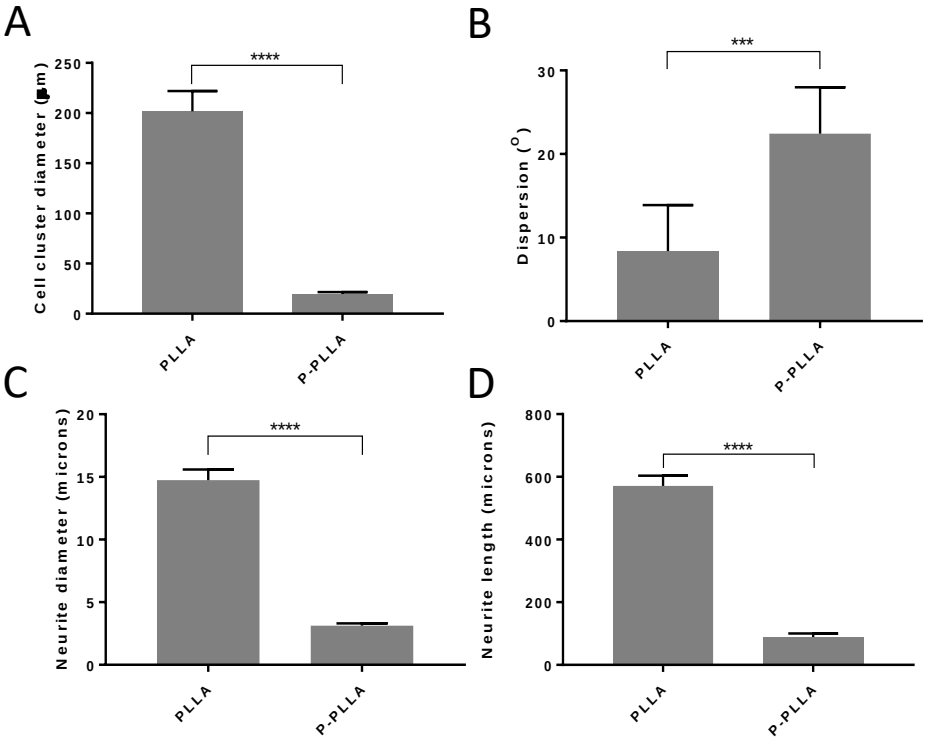


Figure 4.8: Morphological changes to primary cortical neurons induced by nanofibres cultured on untreated and plasma-treated PLLA nanofibres. (A) Cell cluster diameter was significantly reduced by plasma treatment (Unpaired t-test: $p$ = <0.0001, $t(21)$ = 23.38) (B) Alignment of the neurites was significantly reduced by plasma treatment of

the nanofibres; low dispersion indicates highly aligned neurites (Unpaired t-test: $p$ = 0.0007, $t$(12) = 4.56) (C) Diameter of the neurite bundles was significantly reduced by plasma treatment of the nanofibres (Unpaired t-test: $p$ = <0.0001, $t$(18) = 13.37) (D) Neurites were significantly shorter on plasma treated nanofibres (Unpaired t-test: $p$ = <0.0001, $t$(18) = 14.12)

Stimulation of the organoid with pharmacologically relevant compounds elicited responses from the organoid. Using a Clariostar plate reader to measure changes in fluorescence in voltage-sensitive dye-loaded neurons revealed that in response to an glutamatergic agonist to excitatory cortical neurons (AMPA, 10µM), the membrane potential of cells increased. This increase in membrane potential could then be significantly reduced through administration of the inhibitory neuron agonist, GABA (25µM) (figure 4.9A and B).

Spontaneous activity was detected using confocal microscopy of voltage sensitive dye loaded cells. Root mean square was used as a measure of noise within the system and the threshold for spike detection was set at 3 times the root mean square. For each of the repeats used, spontaneous spikes were detected from the organoids (figure 4.9C).

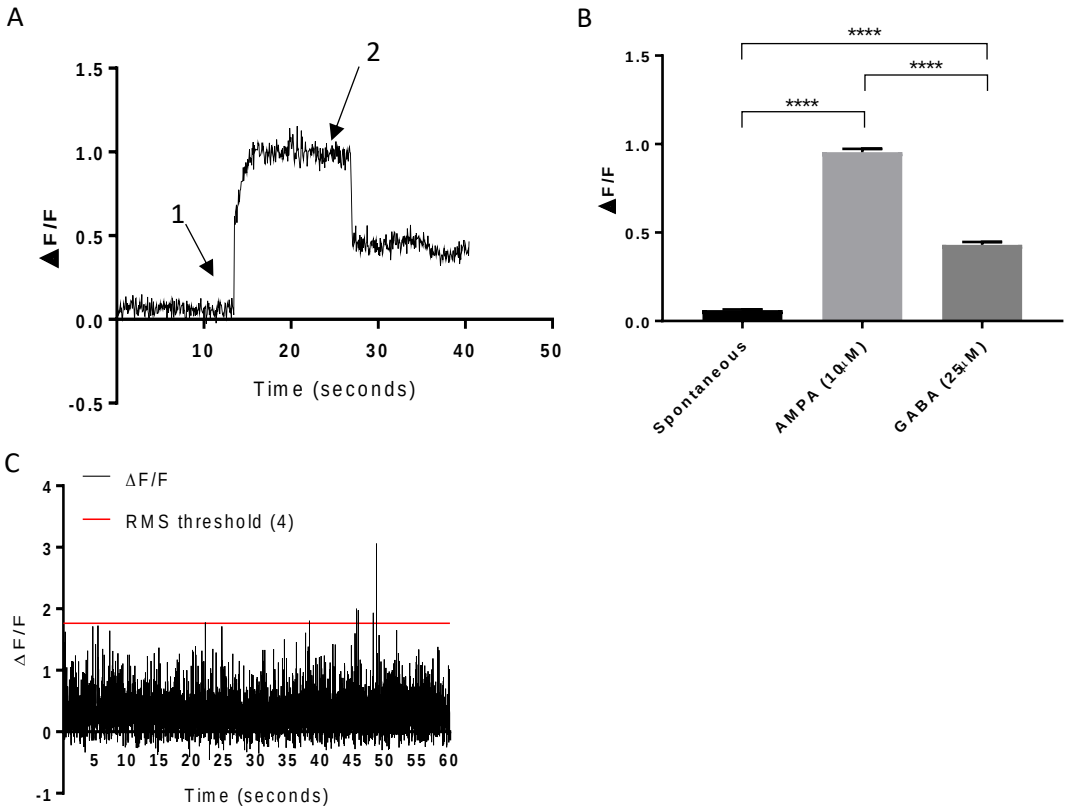


Figure 4.9: Fluovolt-loaded organoids exhibit changes in membrane potential spontaneously or when exposed to pharmacological ligands. Recordings were taken using a Clariostar fluorescent plate reader with a sampling rate of 60 milliseconds (A-B) or an SP5 Leica confocal microscope (C) with a sample rate of 6 milliseconds (A) Pharmacologically induced changes in global fluorescence in fluovolt loaded organoids. AMPA (10µM) (1) was administered at 12 seconds whilst GABA (25 µM) (2) was administered at 26 seconds. An increase in membrane potential is observed after stimulation with an excitatory ligand (AMPA) whilst a decrease is observed after the addition of an inhibitory ligand (GABA) (B) Mean ΔF/F for each of the three time points; significant changes were induced by each of the treatments (One-way ANOVA; $p$ = <0.0001, $F$(1.968,1348) = 1432. Tukey's multiple comparisons test was performed as a post-hoc test. Spontaneous vs AMPA: $p$ = <0.0001. Spontaneous vs GABA: $p$ = <0.0001. AMPA vs GABA: $p$ = <0.0001) (C) Spontaneous spiking events were observed in the organoids; spikes were identified as datapoints that exceed four times the value of the root mean square

## 4.4 Discussion

### 4.4.1 Mechanistic hypotheses for the aggregation of neurons

Neuronal aggregation occurs on the aligned PLLA nanofibres (figure 4.1A-C). The self-assembly behaviour is attributed to the hydrophobicity of the nanofibres. From a physical perspective, adhesive forces are likely to be a factor that promotes aggregation. Hydrophilic surfaces are

typically used to adhere cells and generate homogenous cultures on the culture surface (Ryan, 2008) whereas the PLLA nanofibres are hydrophobic and thus inhibit adhesion. Neurons are capable of generating approximately 150 μdyn of force through the neurites (Segev et al, 2003). When neurites extending from the soma come into contact with other neurites, they exert this force on each other. When the force exerted on the soma is greater than the force of adhesion holding the cell in place, the cells will migrate towards each other to form cell clusters (Segev et al, 2003). By inhibiting the physical adhesion of the cells to the surface, the ability of neurons to form clusters is enhanced. Biologically, the cell-cell and cell surface adhesion have been suggested to be inversely proportional (Limongi et al, 2012; McCain et al, 2012). Through inhibition of adhesion of cells to the surface, decreased expression of cell-substrate adhesion proteins and upregulation of cell-cell adhesion proteins may have occurred, compounding the lack of adhesion induced by the alterations to the wettability of the surface.

The hypothesis that the surface wettability of the PLLA nanofibres aided the formation of the organoids was tested by altering the wettability of the nanofibres through plasma treatment (figure 4.7). Plasma treated PLLA nanofibres were observed to have a lower contact angle than untreated PLLA nanofibres (figure 4.7B) and cellular aggregation was attenuated (figure 4.7C). Quantification of the neuronal morphologies demonstrated a significant decrease in cell cluster diameter (figure 4.8A), neurite alignment (figure 4.8B), neurite bundle diameter (figure 4.8C) and neurite length (figure 4.8D). Therefore, surface wettability is an influencing factor in the formation of the cellular aggregates that are observed.

### 4.4.2 Molecular hypotheses for generation of altered cellular morphologies

The consistent significant positive correlation between cell cluster diameter, neurite bundle diameter and neurite length (figure 4.5) may be indicative of the mechanism that induced the significant alterations relative to the control 2D culture (figure 4.2). Whilst the mechanism behind the clustering of cells is theorised to be due to reduced adhesion and consistent mechanical tension within the neurites, the increase in neurite length and diameter is hypothesised to be due to the aggregation of neurons. Increasing cell cluster diameter is positively correlated with neurite bundle diameter and length; proximity of cells appears to induce an increase in these cellular features. Neurons express cell adhesion molecules (CAMs) on their membranes which are capable of inducing an increase in neurite outgrowth and cell-cell adhesion (Missaire and Hindges, 2015). The theorised mechanism is that through increased clustering of cell bodies, neurites are in closer proximity and more probable to come into contact with other neurites and allow for ligand-receptor interactions between CAM and CAM-receptor. Signalling molecules downstream of CAMs have roles in differentiation, gene transcription, metabolism, morphogenesis and cellular migration (Kleene et al, 2010; Shima et al, 2007; Noren et al, 2000); thus, further molecular characterisation is warranted as a means of establishing those changes that result from the increased proximity of neurons.

### 4.4.3 Avenues for further optimisation of the cell culture conditions for promoting cerebral cortical organoid formation

The choice of medium (NbActiv1) selects for neuronal cells while inhibiting proliferation/survival of non-neuronal cells. A small percentage of cells within the culture were stained with DAPI while not staining for βIII-tubulin, suggesting that they were non-neuronal cells. The percentage of non-neuronal cells was found to be consistently negatively correlated with all other factors at all time-points (figure 4.5). The main non-neuronal cells that comprise

the cerebral cortex are the astrocytes and oligodendrocytes (Kandel, 2012). Whilst astrocytes enhance the extension of neurites (Kanemaru et al, 2007), oligodendrocytes are inhibitory (Ma et al, 2009). The inhibition of neurite growth that is observed due to the increasing percentage of non-neuronal cells is suggestive that these cells are oligodendrocytes and therefore, removing the non-neuronal cells may increase the growth of the organoids. However, the mechanism of formation is theorised to be dependent on the force that neurites exert on each other during the formation of a neural network (Segev et al, 2000). Probabilistically, the greater the number of non-neuronal cells, the lower the chance of neurites coming in to contact with a neuron that can generate force and thus form a cluster, decreasing the size of the average aggregate. Smaller clusters correlate with lower neurite length and neurite bundle diameters. Thus, it is also possible that non-neuronal cells negatively correlate with other factors by virtue of being non-neuronal rather than a specific cellular sub-type (oligodendrocytes). Whilst the distinction appears minor, it has implications with respect to potential methods of optimising cluster formation. If oligodendrocytes are inhibitory to organoid formation, then removal of this specific sub-set of cells would yield larger organoids whilst retaining the beneficial growth-promoting properties of astrocytes. If the non-neuronal cells are inhibitory cells because they are non-neuronal then purification could be performed more easily with fluorescence assisted cell sorting using a neuronal marker alone although the beneficial properties of the astrocytes would also be lost. Medium conditioned with primary cortical astrocytes could potentially be used to promote growth and survival in the absence of glia (Mena et al, 1996) although the use of conditioned medium precludes feedback loops between the organoids and the astrocytes.

### 4.4.5 Classification as an organoid

Organoids are classified as 3D cell clusters that recapitulate the *in vivo* behaviours of the target organ (Fatehullah et al, 2016). Thus far, the cellular clusters formed in the current work have demonstrated self-assembly into 3D clusters and more representative morphologies but a key

aspect of the central nervous system is the electrophysiological aspect. Assemblies of neurons are the basis of computation within the central nervous system (Yuste, 2015) and within the cerebral cortex, neurons are typically excitatory (e.g. glutamatergic) or inhibitory (e.g. GABAergic) (Kandel, 2012). Putative organoids were stimulated with AMPA and GABA, a glutamatergic and GABAergic agonist respectively to confirm that the cell clusters were responsive to physiologically relevant compounds.

AMPA is a non-physiological agonist of the AMPA glutamate receptor and has demonstrated an $EC_{50}$ of approximately 5 µM in cortical neurons (Di Angelantonio et al, 2015), although several studies have utilised concentrations as high as 100 µM to stimulate the tissue (Rojas et al, 2012; Carunchio et al, 2007). To elicit a response, 10 µM was selected for this study. In contrast to AMPA, GABA is a physiological agonist. At the synapse, concentrations of GABA upon neurotransmission are relatively broad dependent on the region of the cortex and the study that was performed; studies estimate peak concentrations ranging from 0.3mM to 3mM with constitutive GABAergic concentrations at approximately 0.2-2.5µM (Roth and Draguhn, 2012). In 2D culture, 10 µM GABA alone was sufficient to abolish neuronal activity in cortical cultures (Han et al, 2017); in the current work, 25 µM GABA was selected as a concentration that would be capable of attenuating the increased activity induced by the previously administered AMPA. Pharmacological stimulation of the organoid with AMPA and GABA induced an increase and decrease in activity respectively (figure 4.9A and 4.9B), confirming that the cell cluster expresses receptors that are typical of physiological neurons. In the absence of pharmacological stimulation, spiking behaviours were also observed.

Within the cerebral cortex, neurons are capable of spontaneous depolarisation. To recapitulate behaviours of the organ in question, cerebral cortical organoids should be capable

of generating spontaneous depolarisation. Whilst the voltage sensitive dye exhibits kinetics that are quick enough to capture the action potentials of cortical neurons (2ms/action potential; Kandel, 2012), the temporal resolution of the confocal fluorescence microscope (12ms) does not; thus these spikes within the recorded data set are referred to as "spiking events" rather than true spikes. For each of the tested organoids, numerous spiking events were detected using thresholding as a means of spike detection (figure 4.9C). A limitation of RMS as a thresholding method for spike detection is the susceptibility to bias that results in failure to detect low-amplitude spikes due to high amplitude, high frequency spike trains; due to their inclusion in the signal-noise ratio, the RMS will subsequently be increased, thus generating false negatives. This limitation has lead on to the use of the more sophisticated techniques. However, this experiment aimed to determine whether or not the organoids were capable of generating spikes at all rather than accurately characterising the electrophysiology of the organoids. Due to the ease of implementation, low computational cost and the predisposition towards false negatives rather than false positives, RMS was selected as a means of detecting spiking behaviours.

## 4.5 Conclusion

The 3D cellular structures that are generated through primary culture of cortical neurons on aligned PLLA nanofibres fulfil the criteria to be considered as organoids (Fatehullah et al, 2016). The organoids self-assemble, exhibit electrical activity, recapitulate structures of the organ in question through the segregation of neurite and soma and possess a mixed culture. Multiple avenues to develop the sophistication of the organoid have been discussed, but more in-depth characterisation is needed.

# Chapter 5: Proteomic Characterisation of the Cerebral Cortical Organoids

## 5.1 Introduction

Initial characterisation of the organoid focused on the behaviours of the whole cell or even networks of cells through morphological or electrophysiological quantification. Mass spectrometry can be employed as a high-throughput method for molecular elucidation of biological systems. Within this chapter, mass spectrometry will be used to perform broad characterisation of the organoid to gain insight into developmental aspects of it and to probe for potential upregulation of various markers of plasticity that may have implications for the potential integration of the organoids into endogenous circuitry upon implantation.

The shotgun approach of mass spectrometry-based quantification of the proteome allows an increase in the depth and breadth of the data collection of the system in question relative to targeted tools such as western blotting or qPCR (Angel et al, 2012). Using the mass of data that can be generated by mass spectrometry, bioinformatic analyses was employed to characterise the system. Bioinformatics evolved as a means of analysing the extensive gene sequence data that could be collected as a result of genome sequencing but has since evolved into a means of computationally analysing a wide range of data from genomics to metabolomics to proteomics (Ramsden, 2015), therefore, bioinformatic analyses shall be used to enrich the "proto-data" generated by mass spectrometry to a usable form that can be used to examine the responses of various systems and biological processes in a meaningful way.

Artificial neural network inference (ANNI) was used to characterise the interactome of the organoids as a means of probing the protein network as a whole rather than fixating on the fold changes of individual proteins. Whilst mass spectrometry provided a list of proteins that

were differentially expressed and provided a global image of the changes to the cell, it did not indicate which proteins are key influencers within the system. Proteins that are greatly up- or down-regulated are frequently treated as causative factors of pathologies and targeted, resulting in therapeutic failure (Tong et al, 2014) as this approach fails to understand the system as a whole, instead focusing on the most deregulated protein. The most deregulated protein may be downstream of a potent transcription factor, signalling cascade initiator or synergistic inhibitory/excitatory protein that is causative rather than symptomatic. ANNI modelling allows the discovery of influential proteins within the interactome, regardless of whether the fold-change of expression is high or low, facilitating increasingly accurate characterisation of the system. Regression analysis performed in chapter 4 suggests that the mechanism of cerebral cortical organoid formation on the PLLA nanofibres is due to the clustering of cells on a hydrophobic surface, inducing neurite bundling and subsequent guided outgrowth. The molecular mechanism proposed for this in chapter 4 is that the close proximity of neurons allows neuronal cell adhesion molecules (NCAMs) expressed on the surface of one neuron to stimulate neighbouring neurons. NCAMs have demonstrated growth promoting abilities for neurites through alterations to gene expression or modulation of the cytoskeleton, in addition to neurite guidance properties (Missaire and Hindges, 2015). Alternate models of organoids within the CNS and the physiological architecture of the CNS highlight the importance of close proximity of cell bodies (Lancaster and Knoblich,2014; Harris et al, 2016; Kato-Negishi et al, 2013) and support the NCAM hypothesis as all previous models have demonstrated clustered cell bodies as a necessity for the formation and differentiation of their respective organoids. Lancaster and Knoblich (2014) note that neural rosettes (clusters of neural stem cells) are capable of recapitulating the radial organisation that is typical of the neuroepithelium upon differentiation. Harris et al (2016) and Kato-Negishi et al (2013) pre-assemble clusters of embryonic neurons prior to seeding and note the extensive generation of thick, fasciculated axons and the formation of synapses. Whether the neuronal clustering is

induced through proliferation of neural stem cells into a rosette or mechanical clustering, close proximity of the soma appears to be a necessity for forming cerebral cortical organoids.

## 5.2 Methods

### 5.2.1 Generation of cell lysates for mass spectrometry

To attain lysates for proteomic analysis, primary cortical neurons were seeded to aligned PLLA nanofibres as described previously for 11 days. Cells were then incubated in lysis buffer (1% protease inhibitor, 9.5mM Urea, 130mM dithiothreitol and 34mM octyl-beta-glycopyranoside in dd$H_2O$) for 2 minutes at 37°C. The lysate was then collected and sonicated in an iced water bath, 3 times for 5 minutes. Between each 5 minute sonication, the lysates were chilled on ice for 5 minutes. Samples were centrifuged at 12,000g for 10 minutes. The supernatant was removed and stored at -80°C until protein quantification and mass spectrometry was performed. Protein quantification was performed using a Lowry assay according to the manufacturer's protocols. Briefly, BSA protein standards were prepared at a range of concentrations, diluted to a final volume of 100µL with distilled water and Western Blot lysis buffer. Samples were diluted using distilled water. Working Lowry solution (1ml; 2% $Na_2CO_3$, 0.1M NaOH, 1% $CuSO_4$, 2.7% $Na^+K^+$-Tartrate) was added to each of the samples and standards which were subsequently vortexed and incubated for 15 minutes at room temperature. Folin-Ciocalteau reagent was diluted at a 1:1 ratio with distilled water and 100µL was added to each sample. After 30 minutes of incubation at room temperature, samples were then transferred in to a 96 well plate and the absorbance was read at 750nm using a Clariostar fluorescent plate reader. Standards were then used to generate a standard curve to calculate the protein concentration of the lysates.

## 5.2.2 Mass spectrometry sample preparation

**Performed by Dr. Amanda Miles**

Cell lysates were diluted in tri-ethyl ammonium bicarbonate (TEAB, Sigma Aldrich UK; 50mM) before being reduced in DTT (5mM, 56°C for 20 min) and alkylated in iodoacetamide (15 mM , room temperature for 15 min in the absence of light) and then digested for 16 hours using Trypsin (Promega, UK) at 37°C at a 20:1 protein:protease ratio (w/w) in a thermomixer (650 rpm). Samples were then de-salted and HyperSep C18 spin tips (10-200 µL size) (Thermo Scientific) were used according to the manufacturers protocol to concentrate. A vacuum concentrator was then used to concentrate the samples before resuspension in 5 % acetonitrile + 0.1 % formic acid.

## 5.2.3 Mass Spectrometry

**Performed by Dr. Amanda Miles**

Lysates were analysed on a Sciex TripleTOF 6600 mass spectrometer coupled in line with a eksigent ekspert nano LC 425 system utilising micro flow. Samples (4 µL) were injected and trapped onto a YMC Triart-$C_{18}$ pre-column (0.3 x 5 mm, 300 µm ID) (mobile phase A; 0.1 % formic acid, B; acetonitrile with 0.1 % formic acid) at a flow rate of 10 µL/min mobile phase A (2 minutes) prior to gradient elution onto the YMC Triart-$C_{18}$ analytical column (15 cm, 3 µm, 300 µm ID) in line to a Sciex TripleTOF 6600 Duospray Source using a 50 µm electrode, positive mode +5500V. Lysates underwent information dependent acquisition (IDA) to generate a spectral library and Data Independent Acquisition (SWATH) to quantify the spectra. The parameters for the linear gradients for IDA were: mobile phase B increasing from 3 %-30 % for 68 minutes; 40 % B at 73 minutes. A column wash was performed at 80 % B and re-equilibrated (total run time = 87 minutes). The parameters for the linear gradients for SWATH MS were: 3-30 % B for 38 minutes; 40 % B at 43 minutes, re-equilibration was performed as before after a

wash stage (total run time = 57 minutes). IDA acquisition mode was utilised to generate the spectral library, with a top 30 ion fragmentation (TOFMS *m/z* 400-1250; product ion 100-1500). Subsequently, exclusion using rolling collision energy was performed for 15 seconds, 50 ms accumulation time; 1.8 s cycle. For SWATH acquisition 100 variable windows were used with an accumulation time of 25 ms and a 2.6 s cycle (*m/z* 400-1250) (Mele et al, 2018). ProteinPilot 5.0.2 was used to search the spectral library generated by IDA (Swissprot rat database June 2018). Sciex OneOmics software was used to analyse the SWATH data (Lambert et al, 2013) extracted against the locally generated library (false discovery rate filtering of 1 % and excluding shared peptides). Parameters used within the OneOmics software were: 12 peptides/protein, 6 transitions/peptide, XIC width 30 ppm and a retention time window of 5 minutes.

## 5.2.4 Principal Component Analysis

Principal component analysis (PCA) was performed on the mass spectrometry data. ClustVis was used to perform the PCA and generate the subsequent figures. Pareto scaling was used to normalise the data. The Pareto scaling factor was identified using equation 3 and all fold changes were subsequently divided by the scale factor to normalise them.

$$\tilde{X}ij = \frac{Xij - \overline{Xi}}{\sqrt{Si}}$$

Equation 3: Pareto scaling using to normalise data for Principal Component Analysis

## 5.2.5 Artificial neural network inference (ANNI) modelling

Artificial neural network inference modelling was used to simulate protein-protein interactions *in silico.* Proteins that were significantly de-regulated and above 50% confidence (186 proteins total) were uploaded to the artificial neural network (ANN). Confidence value cutoffs were

relaxed for the ANNI modelling to allow a larger and more robust network to be generated. The ANN used was a 3-layered multilayer perceptron with back-propagation learning and utilised a sigmoidal activation function (Lancashire et al, 2009). For each protein, the interaction between it and every other protein was calculated based off the mass spectrometry data and through this, negative and positive influences were calculated, generating 35,000 total interactions for the list of proteins. Monte Carlo cross validation was used to prevent overfitting with a 60:20:20 ratio used for training, testing and validation.

### 5.2.6 Network analysis

To identify processes that were significantly overrepresented within the network generated by mapping the interactome in cytoscape, the BiNGO plugin was used (Maere et al, 2005). To identify proteins that were vital to the process, the network was analysed using Cytoscape's in-built analytical tools ("Network Analyzer") and betweenness centrality was used to determine key proteins within the network. Proteins that were identified to have high betweenness centrality were isolated in to their own sub-network and the BiNGO plugin was used again to determine enriched gene ontologies within the sub-network. Sub-networks were also created for the influence of the top 10 highest betweenness centrality proteins on ribosomal and developmental proteins.

To gain insight in to the mechanism behind formation and organoid development, the top 100 influencers were then mapped using Cytoscape. Three key proteins (Snp25, Rtn4 and Dpysl2) were highlighted by the ANNI as key nodes of influence within the protein-protein interactions. The mechanism that these 3 proteins exerted their effects on the proteome was investigated further. An average interaction value and standard deviation was found for the total 35,000 interactions. This was performed by investigating the strongest negative and positive

interactions up and downstream from the key nodes (SNAP-25, RTN4 and Dpyl2). For each of the 3 key nodes, the 3 strongest negative and positive interactions of the 185 possible interactions were listed (generation 1 of interactions). From each of these 3 upstream and 3 downstream proteins, the 3 strongest positive and negative interactions was listed (generation 2 of interactions), generating a layered network. For each of these generation 2 proteins, 2 further positive and negative interactions were generated (generation 3 of interactions). This process was also repeated for the "median protein" – CISY which had the median interaction strength. At each generation of interactions, the strengths of the key nodes interactions were compared to the average and tested for significance using an unpaired t test.

### 5.2.7 Bioinformatic analysis

Proteins that were identified by mass spectrometry with a confidence value of greater than 70% were used for bioinformatic analysis. Proteins that were uniquely expressed by the neurons cultured upon nanofibres were identified by generating a Venn diagram of total proteins detected in all replicates of the lysates of the control and the nanofibre condition. 24 proteins were detected that were unique to the nanofibre condition. The function of these proteins was determined through the STRING bioinformatics database.

Data enrichment was also performed to process the data in to a more usable format. Several gene ontologies of interest were present within the list and were selected for further analysis. The 5 gene ontologies were: "Synaptic", "Developmental", "Adhesion", "Adherens junctions" and "Mitochondrial". Markers for lamination were manually searched for using the Uniprot database and a literature search. For each of these gene ontologies, the proteins associated with the process were extracted from Metacore. The normalised mass spectrometry data for each protein was grouped and run through Morpheus visualisation software to generate heatmaps of up- or down-regulation. Furthermore, the lists of up- and down-regulated

proteins was also uploaded in to Venny visualisation software to generate Venn diagrams of each gene ontology to determine multi-functional proteins and infer causative mechanisms for the development of organoids.

### 5.2.8 Transcription factor analysis

The 186 proteins identified by mass spectrometry were uploaded to Metacore and a network analysis was performed. The transcription factors for each of the identified proteins were examined and those that were more common than were mathematically predicted were highlighted with P values. The only transcription factor highlighted was the ARX transcription factor. A network was generated *in silico* using Metacore to map possible protein-protein interactions that were not detected by mass spectrometry but were predicted due to the activity of the ARX transcription factor.

### 5.2.9 Comparisons to an existing epithelial-mesenchymal transition (EMT) dataset

The mass spectrometry dataset output by OneOmics software was compared with an unpublished EMT dataset, generated by RNA-seq, provided by Sarah Wagner. The DU145 prostate cancer cell line was used and treated with TGF-β, an inducer of EMT. Genes/proteins that were present in both datasets were compared initially for directionality of fold change to determine similarities within the datasets. Several identified genes were disqualified from quantification as they were detected in the RNA-seq but present at levels low enough that fold change data was unreliable. Data was then normalised using equation 4 and used to generate scatterplots and perform regression analysis using Graphpad Prism 7. Graphpad was also used to check normality of distribution.

$$x' = \frac{x - \min(x)}{\max(x) - \min(x)}$$

Equation 4: Min-Max scaling used for normalising RNA-seq data for comparison with mass spectrometry data

## 5.2.10 Preparation of lysates for Western Blotting

Primary cortical neurons were dissected from embryonic rats on embryonic day 18, seeded and cultured on PLL/laminin surfaces and aligned PLLA nanofibres as described previously (Chapter 2; section 2.2.2, 2.2.3, 2.2.6). On 11 DIV, cultures were washed three times in PBS and exposed to boiling Western Blot lysis buffer (500nM TRIS, pH 6.8, 5mM EDTA, 1% SDS, 1% v/v protease inhibitor cocktail) for 2-3 minutes. Cells were then scraped and lysis buffer was collected and boiled at 100$^{o}$C for a further 5 minutes. Lysates were then stored on ice, sonicated in a water bath with ice for 15 minutes, centrifuged at 13,000 RPM and the supernatant was then removed and stored at -80 $^{o}$C until protein estimation.

Protein estimation was performed using a mini-Lowry assay, following the manufacturer's protocol, as described in a previous section

## 5.2.11 Sodium dodecyl sulphate-polyacrylamide gel electrophoresis (SDS-PAGE)

Prior to SDS-PAGE, resolving and stacking gels were prepared. For each resolving gel, resolving gel solution ($H_2O$ – 6.1ml, 30% acrylamide – 1.3ml, Tris-HCl, 0.5M, pH 6.8 – 2.5ml, 10% SDS – 100ul, TEMED – 10ul, 10% ammonium persulphate – 100ul) was prepared, cast between two glass plates and allowed to set. Once the resolving gel had set, the stacking gel ($H_2O$ – 4.1ml, 30% acrylamide – 3.3ml, Tris-HCl, 1.5M, pH 8.8 – 2.5ml, 10% SDS – 100ul, TEMED – 10ul, 10% ammonium persulphate – 32ul) was added, a comb was inserted to form the wells and the stacking gel was then allowed to set. Combs were withdrawn, the completed SDS-PAGE gel

was inserted in to the electrophoretic tank and submerged in running buffer (25mM Tris buffer, 192mM glycine, and 0.1% SDS, pH 8.5).

### 5.2.12 Western Blotting

Lysates were diluted 1:1 with 2x reducing Laemmli buffer, boiled for 5 minutes to denature the proteins. For each of the samples, an equal amount of protein was used. Samples were then loaded in to the wells of the stacking gel alongside 1µL molecular weight ladder. Gels were run at 140V for 90 minutes to separate the proteins.

After electrophoresis, proteins were transferred to a nitrocellulose membrane by wet blotting. A blotting sandwich was prepared with the gel and nitrocellulose membrane sandwiched between filter paper. The blotting sandwich was soaked in ice cold transfer buffer (25mM Tris buffer, 192mM glycine, pH 8.3 and 20% v/v methanol), bubbles were removed from the blot using a roller and the blotting sandwich was moved to a western blot cassette. The cassette was then loaded in to the electrophoretic tank with the nitrocellulose membrane on the side of the anode. Transfer was performed for 16 hours at 40V and copper staining was used to assess transfer success. Copper staining was performed by soaking the nitrocellulose membrane in 0.05% (w/v) copper phthalocyanine 3, 4', 4'', 4''' tetrasuphonic acid terasodium salt in 12mM HCl. Copper staining was then imaged using an ImageQuant Las 4000. Following imaging, copper staining was removed with 12mM NaOH.

Immunostaining was performed by initially blocking the membrane with blocking buffer (3% BSA in TBS-Tween) for 1 hour at room temperature. The blot was then incubated in primary antibody (VDAC2; 1:1000, VDAC1; 1:1000, HSP60; 1:1000) overnight on a roller at 4°C, at a concentration stated by each of the blots. Four 15 minute washes were performed in TBS-Tween before staining with the secondary antibody. Secondary antibody was prepared to a dilution of 1:1000 in marvel milk (3% w/v in TBS-Tween). Blots were washed for 4 times for 15

minutes before addition of ECL Western Blotting substrate. Blots were than imaged using an ImageQuant Las 4000. Quantification was performed using Aida image analyser v4.03. Band intensity was quantified for equal areas for each of the bands. Intensities were normalised against the housekeeper protein and results were expressed as a fold change against the control.

## 5.3 Results

### 5.3.1 Validation of the mass spectrometry data

Principal component analysis was run on the mass spectrometry data for proteins that were detected at a confidence value above 70% and were significantly deregulated; a significant change within the proteome was observed. The generated heatmap and cluster analysis demonstrated significant differences between the proteome of the control and the nanofibre-cultured neurons (figure 5.1A and 5.1B). Cluster analysis reveals precise clustering of the control data whilst heterogeneity is evident within the data of the nanofibre-culture neuronal proteome (figure 5.1B).

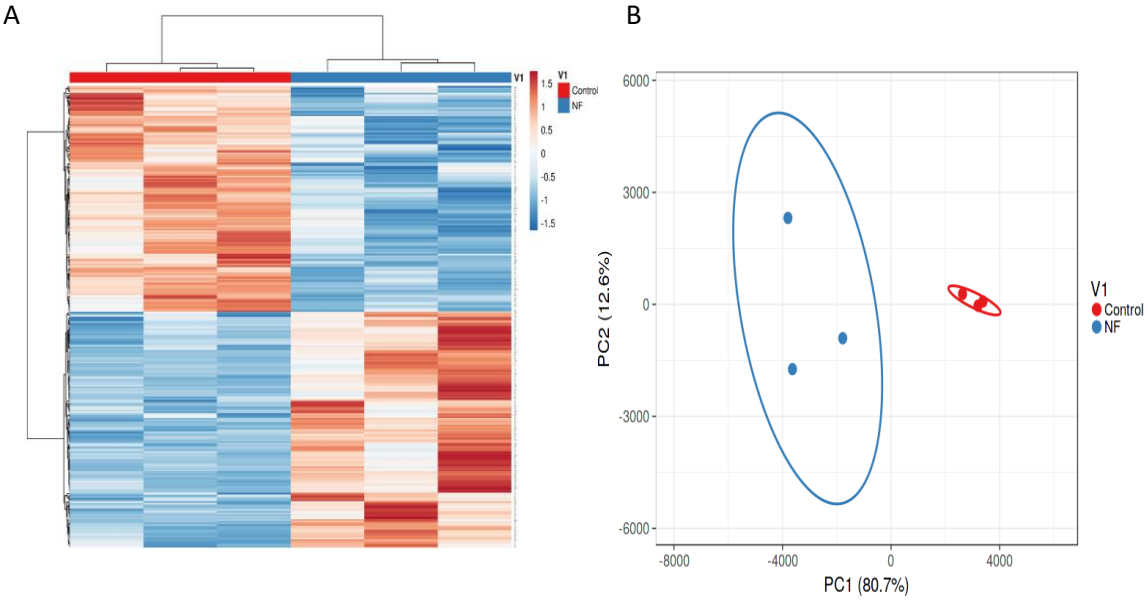


Figure 5.1: Overview of mass spectrometry (A) Heatmap of the results of a principal component analysis of the results of mass spectrometry. Each row of the heatmap represents the

quantified expression of a protein while each column is an independent replicate (B) Cluster analysis of the mass spectrometry data; significant difference is observed between the control and the proteome of neurons cultured on aligned PLLA nanofibres.

Western blots were used to validate the mass spectrometry data. Vdac2 and HSP60 were selected as target proteins. Vdac1 was used as a housekeeper due to its consistent expression within the ProteinQuant data. Commonly used housekeepers such as GAPDH, lamin, vinculin, various actins and tubulins were judged to be inappropriate due to the extensive deregulation that was observed within the mass spectrometry dataset. For HSP60 and VDAC2, deregulation was observed in the same direction for both the western blot and the mass spectrometry, with relatively little difference between the fold changes observed between the two techniques (figure 5.2A and 5.2B).

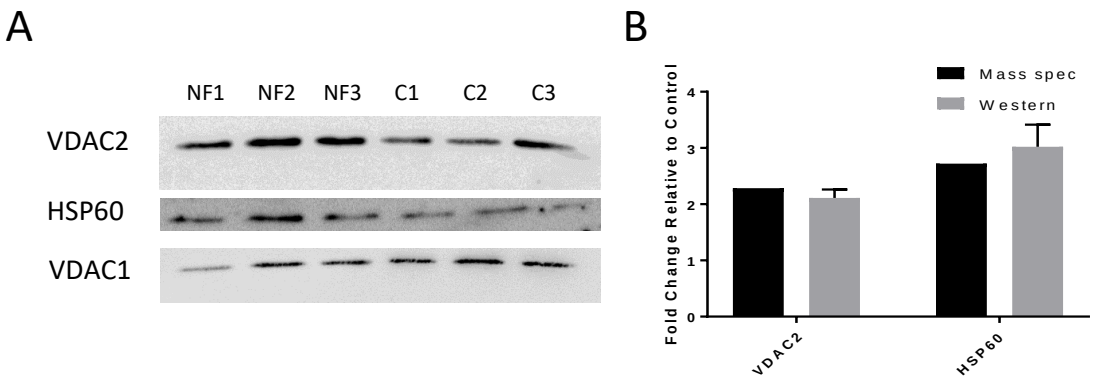


Figure 5.2: Validation of the mass spectrometry dataset. (A) Western blots for VDAC2 (1:1000), HSP60 (1:1000) and VDAC1 (1:1000). NF1-3 are independent replicates for lysates of neurons grown on aligned PLLA nanofibres while C1-3 are lysates of neurons grown on the control surface (B) Comparison of fold changes relative to the control observed for the selected proteins using mass spectrometry and western blots. No significant difference was detected between the fold changes for VDAC2 or HSP60.

### 5.3.2 Protein interactions inferred by the artificial neural network

Using an artificial neural network, a network comprised of 186 proteins was generated with each protein linked to every other protein. Each protein was omitted from the network in turn and the change in expression of each of the 185 proteins was quantified, generating 35,000 interaction data points; significant interactions were mapped (figure 5.3).

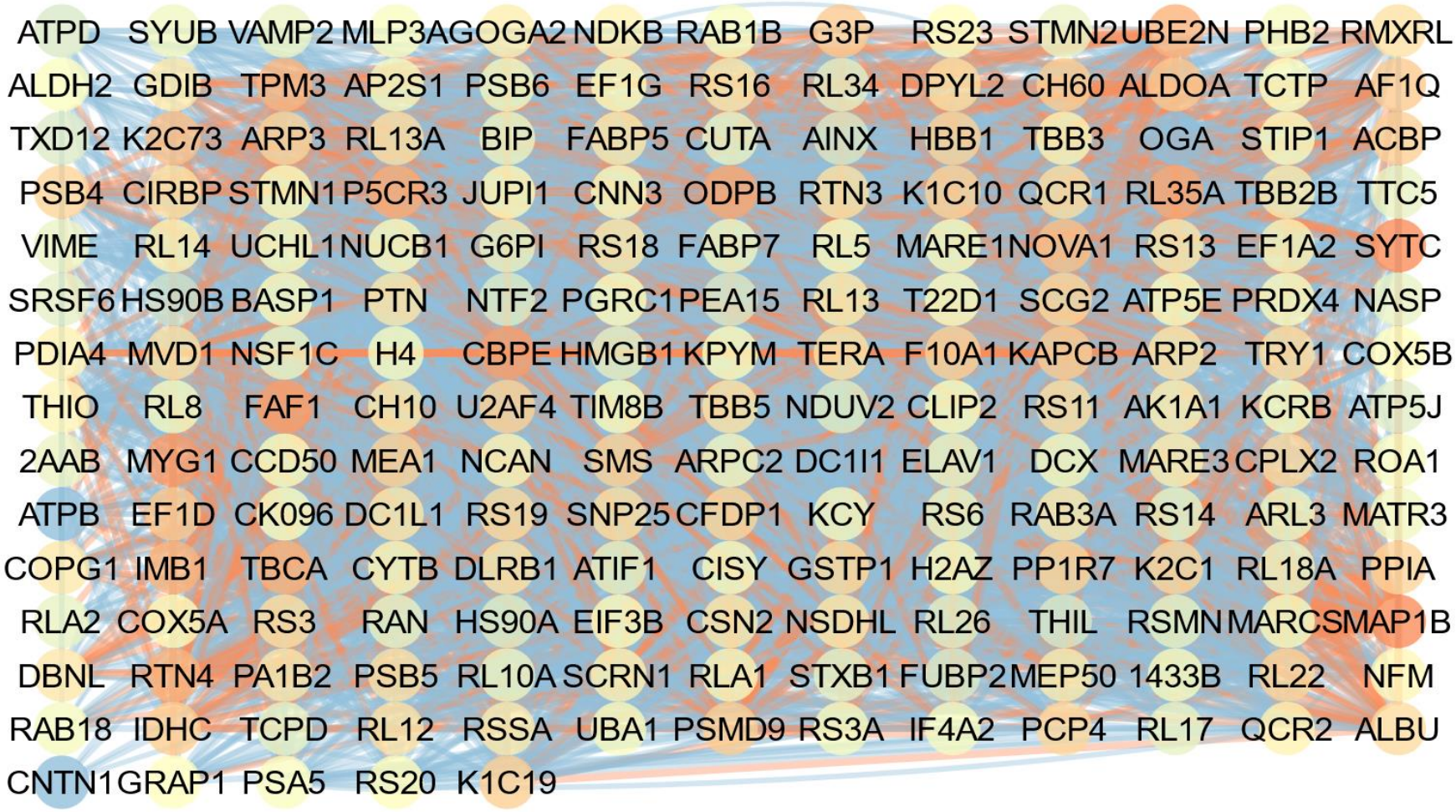


Figure 5.3: Visual representation of the complexity of the interactome of primary cortical neurons cultured on aligned PLLA nanofibres. The significant interactions attained from the ANNI were mapped using Cytoscape. Nodes = proteins, lines/edges = interactions. Edge colour indicates the directionality of the interaction, red = positive, blue = negative. Node colour indicates the closeness centrality, blue = low closeness centrality, red = high closeness centrality.

Network analysis of the function of the proteins within the interactome revealed that within the interactome of the nanofibre cultured neurons, distinct gene ontologies were significantly overrepresented (figure 5.4). Within these overrepresented gene ontologies, developmental gene ontologies were most frequently observed (table 5.1). For the interactome itself, betweenness centrality was used to identify key proteins, listed in table 5.2.

| Enriched Gene Ontology | Corrected *p* Value |
|---|---|
| Regulation of cellular component organization | 0.0000516 |
| Nervous system development | 0.000585 |
| Anatomical structure development | 0.000661 |
| Multicellular organismal development | 0.000661 |
| Neurogenesis | 0.000661 |
| Regulation of protein complex assembly | 0.000706 |
| Developmental process | 0.000925 |
| System development | 0.00109 |
| Positive regulation of protein complex assembly | 0.00180 |
| Regulation of neuron projection development | 0.00308 |

Table 5.1: The ten most significantly overrepresented gene ontologies within the interactome and associated p values. Analysis run through the BiNGO plugin of Cytoscape.

Proteins associated with protein synthesis were observed to decrease (SYTC, -6.36; RL35a, -24.08) while proteins involved with migration/motility (NSDHL, 2.71; NOVA1, 2.53; TPM3, 4.02; GOGA2, 3.63), synaptic plasticity (Map1B, 2.19; NOVA1, 2.53; TPM3, 4.02; PSMD9, 2.98) and morphological regulation (Map1b, 2.19; ODPB, 4.57; TPM3, 4.02; GOGA2, 3.63) exhibited increased expression.

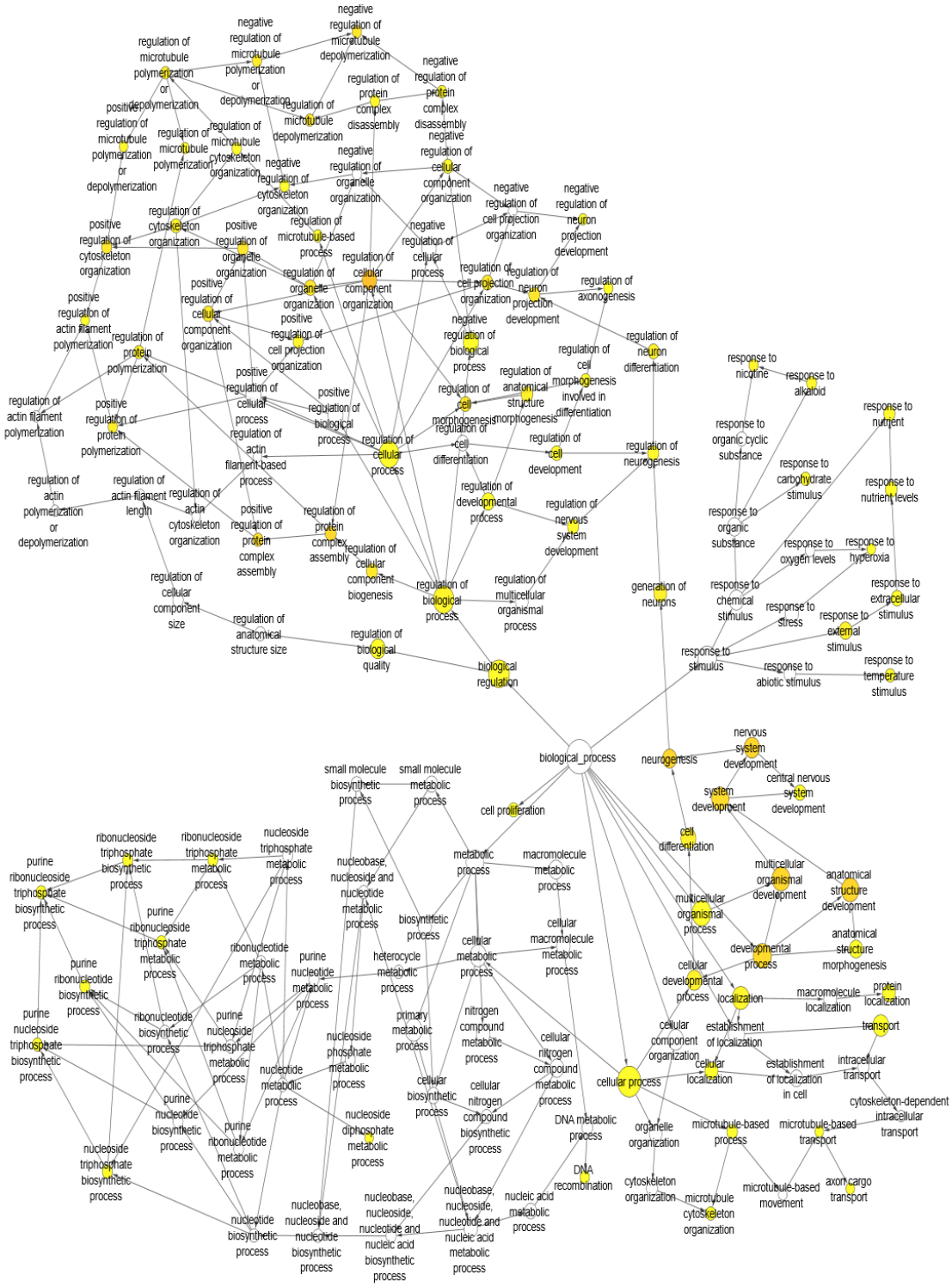


Figure 5.4: Significantly overrepresented gene ontologies within the interactome. White = non-significant, yellow = significant, intensity is proportional to significance

| Protein | Function | Fold Change in Mass Spectrometry dataset | Betweenness Centrality | Reference |
|---|---|---|---|---|
| ODPB (Pyruvate dehydrogenase E1 component subunit beta) | Produces N-acetyl aspartate; an indicator for neuronal health, axonal integrity and modulator of neurotransmission | 4.57 | 0.062805 | Mofett et al, 2007; Chornyy et al, 2017 |
| NSDHL (Sterol-4-alpha-carboxylate 3-dehydrogenase) | Role in cholesterol biosynthesis. Role in cortical migration, defeicits induce microcephaly and cortical deformation. High levels are observed during differentiation and are maintained until adult life. | 2.71 | 0.055534 | Hu et al, 2018; Cunningham et al, 2009 |
| NOVA1 (Neuro-oncological ventral antigen 1) | Elevated expression during development and neural repair, plays a role in synaptic plasticity, positively influences dendritic spine formation. Implicated role in migration/lamination; mutation induces microcephaly | 2.53 | 0.055361 | Störchel et al, 2015; Xin et al, 2017 |
| MAP1B (Microtubule-associated protein 1B) | Establishing cell polarity, cell elongation, closure of the neural tube, dendritic spine formation, synaptic plasticity, axonogenesis and suppression of neurite branching | 2.19 | 0.055155 | Jayachandran et al, 2016; Tortosa et al, 2011; Tymanskyj et al, 2012 |
| MYG1 (Melanocyte proliferating gene 1) | Function unknown. Highly expressed during neuronal development, knockdown experiments indicate role in development | 4.19 | 0.053038 | Philips et al, 2009 |
| RL35A (60s ribosomal protein L35a) | Ribosomal protein expression decreases during forebrain development | -24.08 | 0.052393 | Chau et al, 2018 |
| TPM3 (Tropomyosin-3) | Upregulated during differentiation, role in neuronal migration. Increased expression increases dendritic and axonal length, implied in synaptic plasticity. | 4.02 | 0.043328 | Ryu et al, 2018; Stefen et al, 2016 |
| PSMD9 (26S proteasome non-ATPase regulatory subunit 1) | Enriched in synapses, role in synaptic plasticity | 2.98 | 0.03912 | Tai et al, 2010 |
| SYTC (Threonine-tRNA ligase) | Protein synthesis machinery is downregulated during neuronal development | -6.36 | 0.030367 | Chau et al, 2018 |
| GOGA2 (Golgin A2) | Role in cortical lamination and cell polarity, loss results in microcephaly. | 3.63 | 0.023123 | Shamseldin et al, 2016; Liu et al, 2016 |

Table 5.2: Centrally located proteins. Highlighted proteins exhibit the highest Betweeness Centrality within the network. Average betweenness centrality = 0.007005, standard deviation = 0.0112255

The betweenness centrality was expanded to the top 25 proteins to build a larger, more robust network (figure 5.5); hypergeometric testing within the BiNGO plugin allowed the detection of significantly overrepresented gene ontologies (figure 5.6).

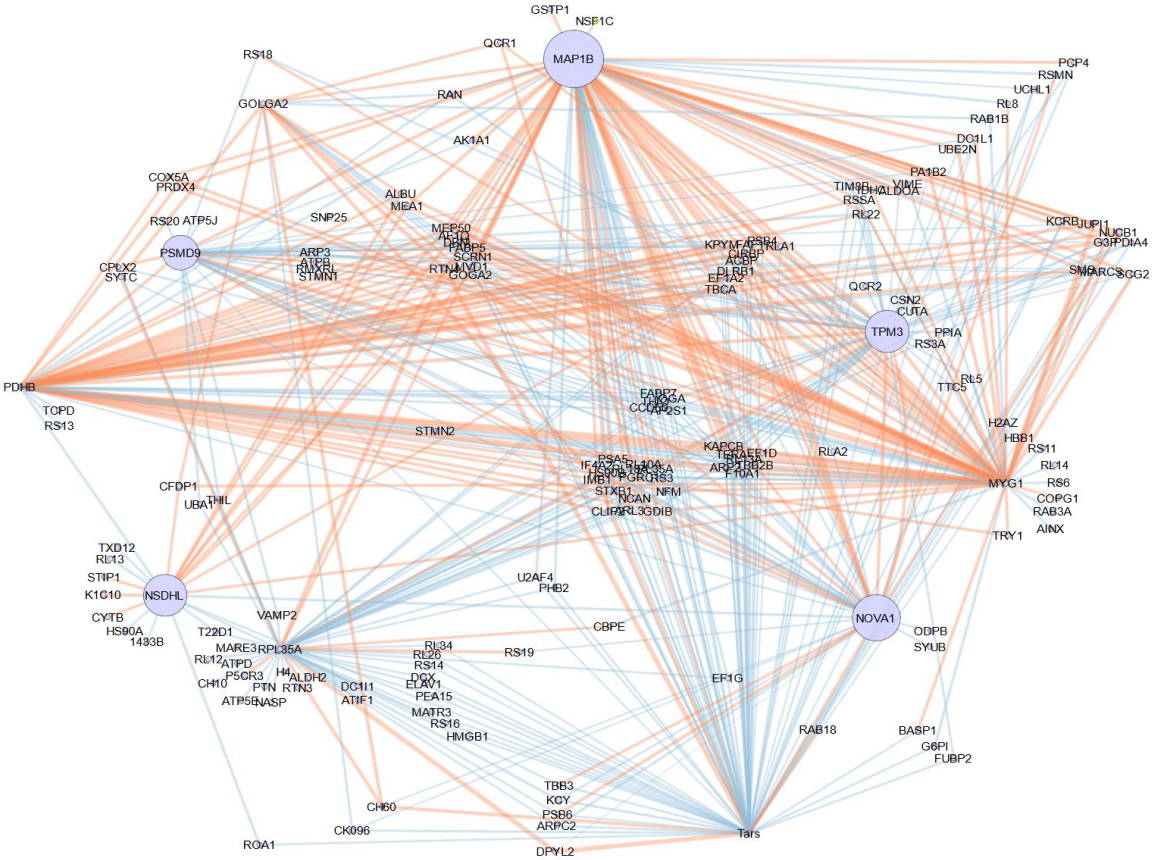


Figure 5.5: The interactome of the 25 proteins with the highest betweenness centrality. The significant interactions attained from the ANNI were mapped using Cytoscape. Nodes = proteins, lines/edges = interactions. Edge colour indicates the directionality of the interaction, red = positive, blue = negative. Node size indicates the betweenness centrality, blue = low betweenness centrality, red = high betweenness centrality.

Similar to the full interactome, the interactome for the proteins with the highest betweenness centralities exhibited significant overrepresentation of developmental gene ontologies (table 5.3).

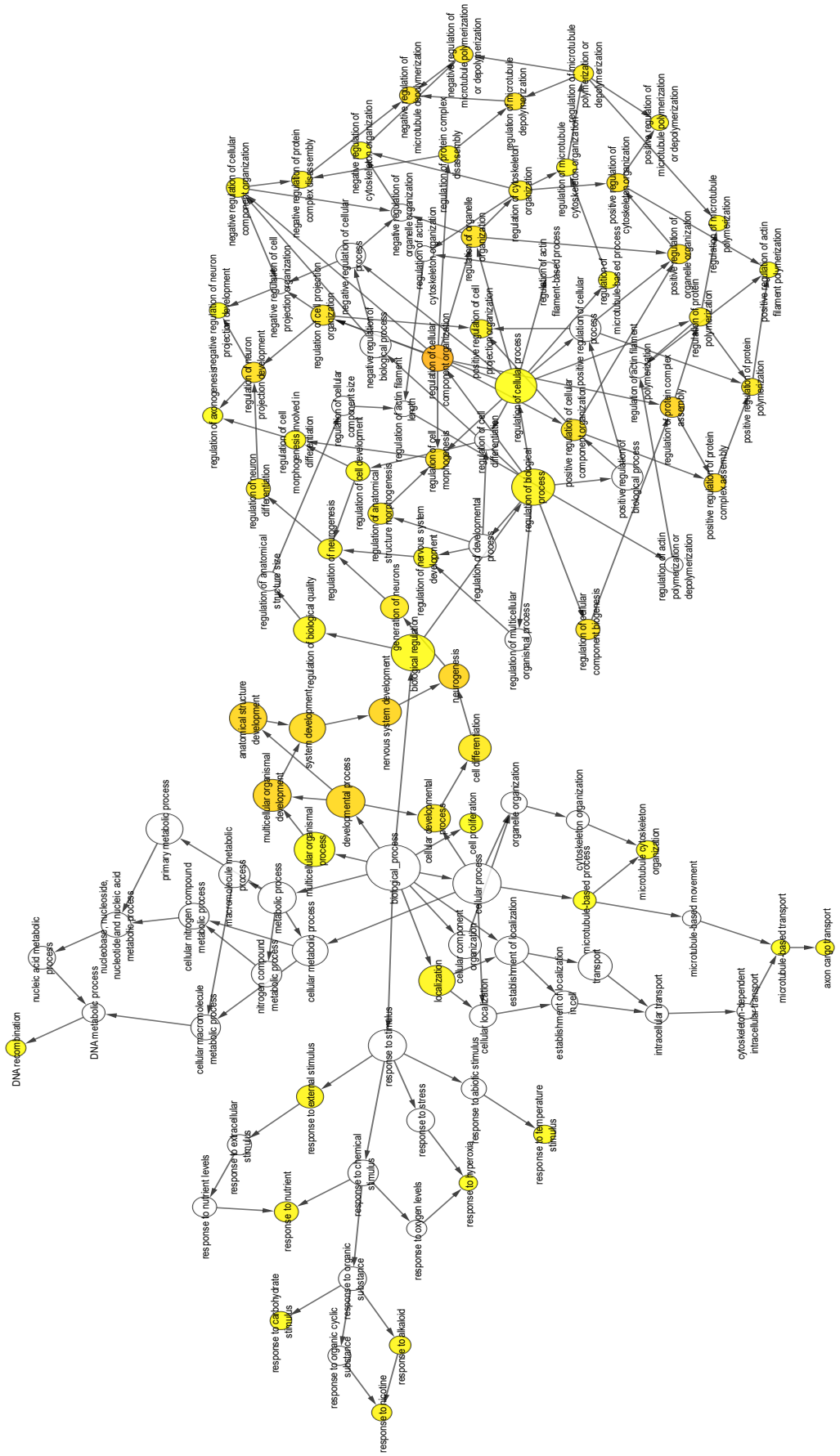


Figure 5.6: Significantly overrepresented gene ontologies within the sub-networks of the proteins with the highest betweenness centralities.

| Enriched Gene Ontology | Corrected *p* Value |
|---|---|
| Regulation of Cellular Component Organization | 0.000026 |
| Neurogenesis | 0.00070 |
| Nervous System Development | 0.00070 |
| Regulation of Protein Complex Assembly | 0.00070 |
| Multicellular Organismal Development | 0.00070 |
| Anatomical Structure Development | 0.00070 |
| Developmental Process | 0.001077 |
| System Development | 0.001420 |
| Positive Regulation of Protein Complex Assembly | 0.001420 |
| Regulation of Neuron Projection Development0 | 0.002233 |

Table 5.3: The ten most significantly overrepresented gene ontologies within the interactome of proteins with the highest betweenness centrality and associated Benjamini-corrected *p* values. Hypergeometic analysis run through the BiNGO plugin of Cytoscape.

Developmental proteins were frequent targets of the proteins with the highest betweenness centralities (figure 5.7) with MAP1B, NOVA1, MYG1 and PDHB displaying notably high degrees of positive influence on developmental proteins. In contrast, Tars and RPL35a demonstrate a high degree of negative influence on developmental proteins.

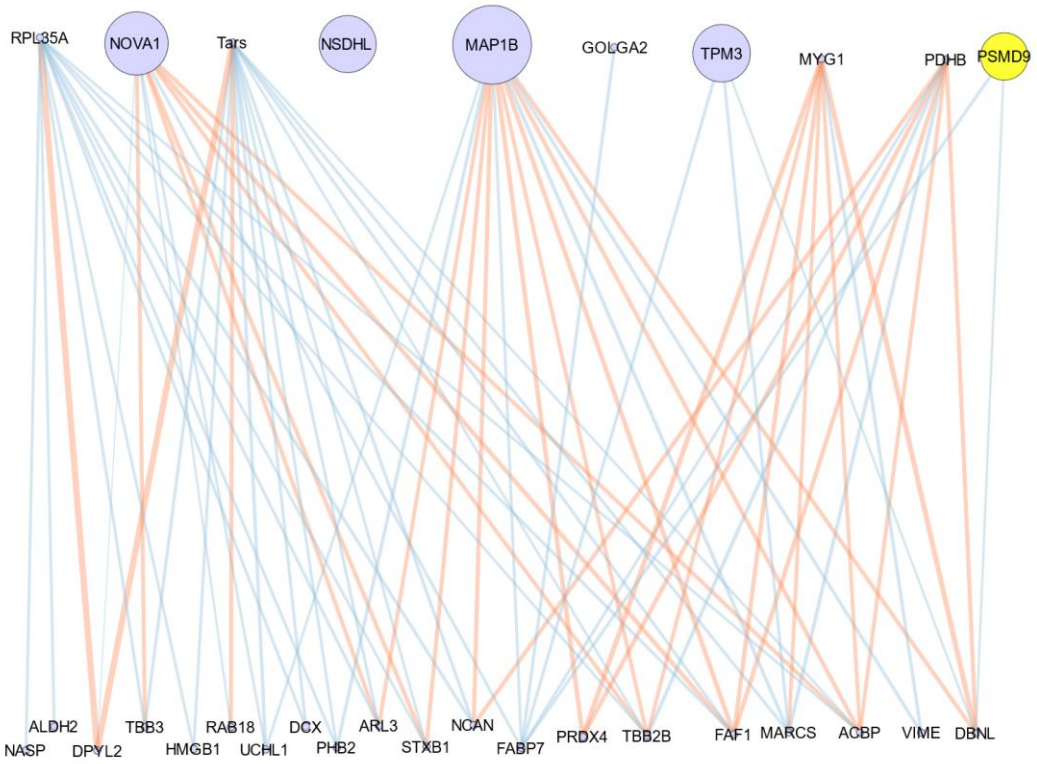


Figure 5.7: Developmental sub-networks of the top 10 betweenness centrality proteins. The significant interactions attained from the ANNI were mapped using Cytoscape. Nodes = proteins, lines/edges = interactions. Edge colour indicates the directionality of the interaction, red = positive, blue = negative. Node size indicates the betweenness centrality, blue = low betweenness centrality, red = high betweenness centrality.

Ribosomal proteins were classified as developmental proteins but were processed separately. The majority of proteins with high betweenness centrality exhibit strong negative influence on ribosomal proteins (figure 5.8).

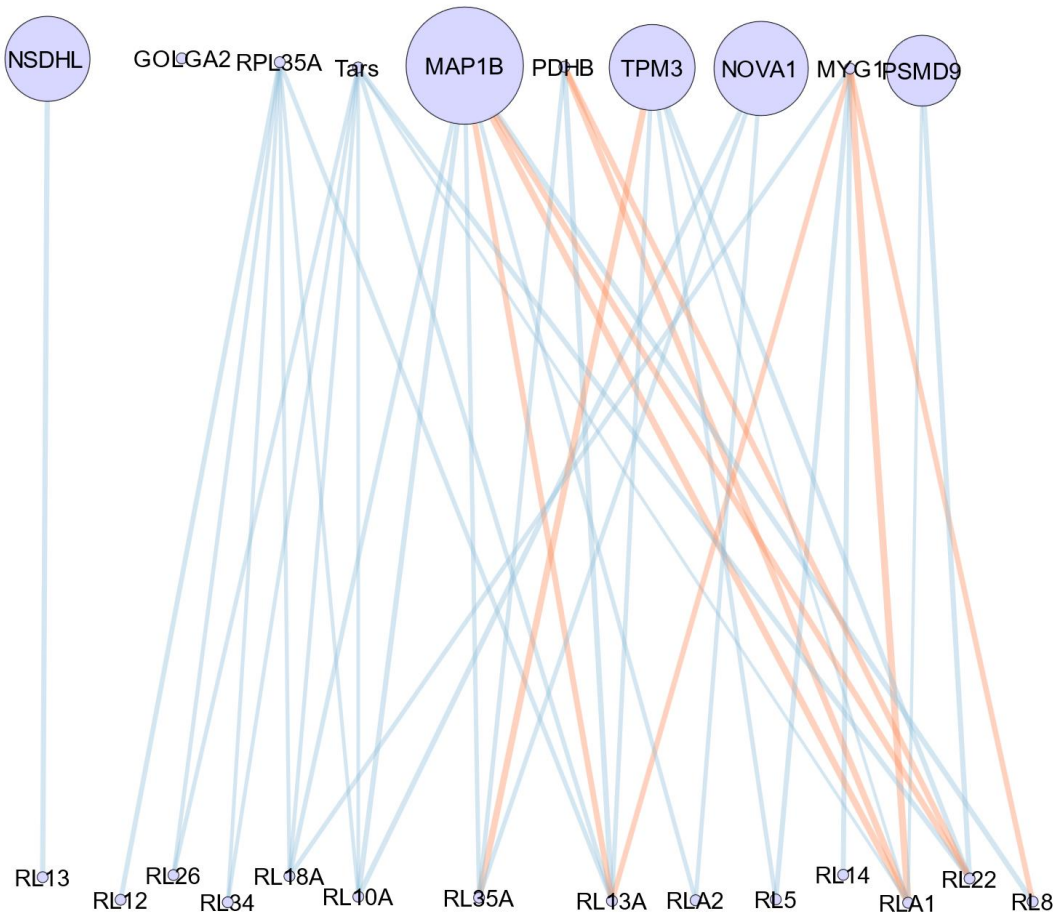


Figure 5.8: Ribosomal sub-networks of the top 10 betweenness centrality proteins. The top 10 proteins have a predominantly negative influence on the ribosomal proteins. The significant interactions attained from the ANNI were mapped using Cytoscape. Nodes = proteins, lines/edges = interactions. Edge colour indicates the directionality of the interaction, red = positive, blue = negative. Node size indicates the betweenness centrality, blue = low betweenness centrality, red = high betweenness centrality.

Within the 35,000 initial data points, the 100 highest values were used to generate figure 5.9; the strongest interactions between proteins. The strongest interactions are all inhibitory and are almost exclusively focused on negatively decreasing the expression of SNP25, DPYL2 and RTN4, which display an increased expression. The overlapping interactions between proteins regulating both DPYL2 and RTN4 suggests a similarity of function between the pathways that the two are involved in whereas SNP25 appears to be regulated by a diverse array of proteins with little overlap in regards to the interactions. These data suggest that as a result of

treatment (culture of neurons on the PLLA nanofibres), SNP25, Dpysl2 and Rtn4 are up-regulated whilst the negative influencers of these 3 proteins are up-regulated as a way of returning the system to equilibrium.

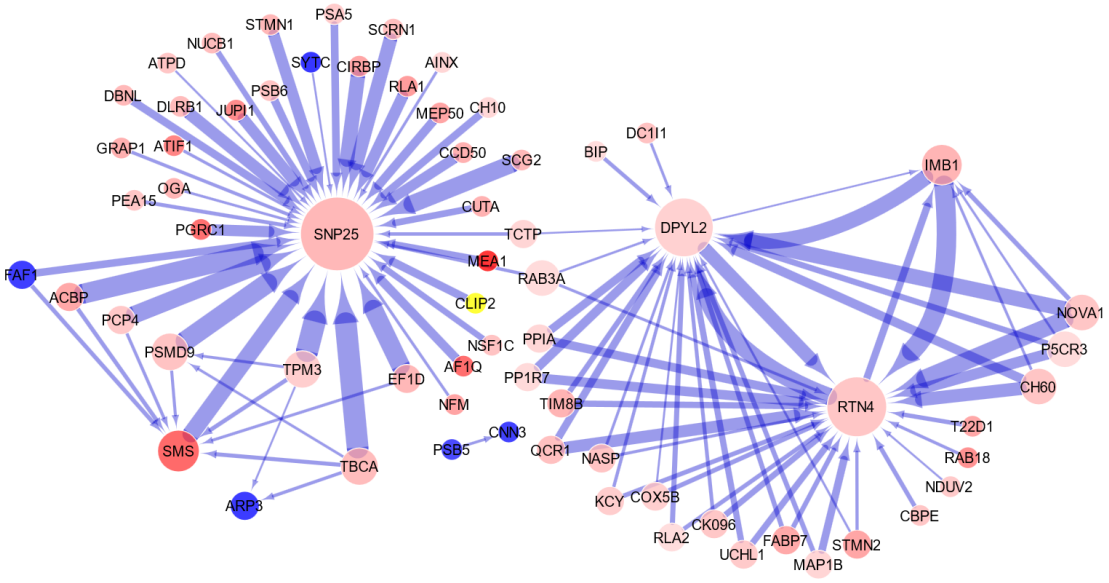


Figure 5.9: Artificial Neural Network Inference (ANNI) of protein interactions. The strongest influencers that are up-/down-regulated by culture of primary cortical neurons on aligned PLLA nanofibers are displayed. The size of the node is relative to the number of interactions within the system. The colour of the node is dependent on the expression, red = increased expression, blue = decreased expression whilst the intensity is relative to the fold-change. The arrows indicate the directionality of the influence. The colour of the arrows indicate the type of influence (red = positive influence, blue = negative influence) whilst the width of the arrow indicates the strength of the influence.

Plotting of the interaction values for each protein that targets SNP25, Dpysl2 and Rtn4 against the protein with the median interaction values (Cisy) (figure 5.10) illustrates that whilst these proteins exhibit a small number of interactions that are positive, the majority of proteins have strong negative influences; at both ends of the curve, non-linear distribution is observed for the key proteins that is absent for the median protein, Cisy.

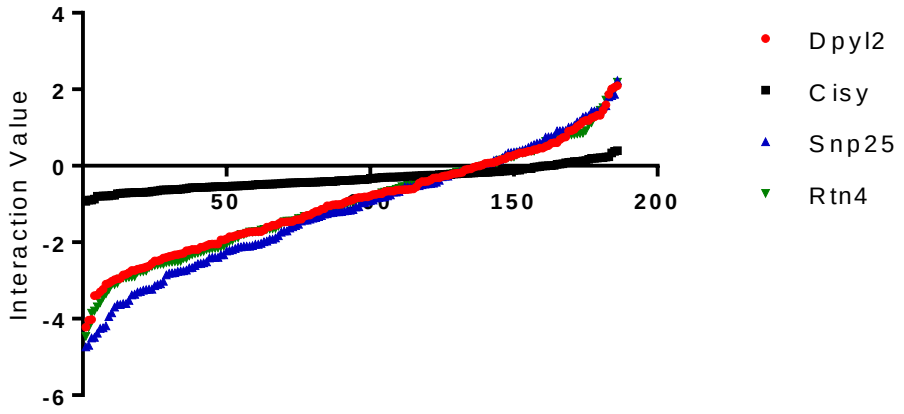


Figure 5.10: Frequency distribution of the strength of protein-protein interactions generated by the ANN inference.

The interactome of the strongest influencers (figure 5.9) revealed SNP25, Dpysl2 and Rtn4 as key targets that were up-regulated as a result of culture of neurons on PLLA nanofibres.

| | Targets: | | | Targeted by: | | |
|---|---|---|---|---|---|---|
| | Snap-25 | Rtn4 | Dpysl2 | Snap-25 | Rtn4 | Dpysl2 |
| Positive influence | Tpm3, Dpysl2, Map1b, Dbi | Cnn3, Tpm3, Dbnl | Tpm3, Tubb2b, Dbnl | Tubb3, Ncan | Pafah1b2, Tubb2b, Cnn3, Arl3, Dcx, Tubb3, Prdx4, Pkm, Stxbp1, Dbi, Ncan, Tpm3 | Pkm, Tubb2b, Prdx4, Tubb3, Arl3, Dcx, Dbi, Stxbp1, Ncan |
| Negative influence | Cntn1, Arl3, Atp5pf, Aldh2, Acat1, Hmgb1 | Dpysl2, Map1b, Uchl1, Fabp7, Rab18, Nasp, Vim, Acat1, Atp5pf | Uchl1, Mapb1b, Fapb7, Nasp, Vim, Rab18, Acat1 | Tpm3, Dbnl, Pafah1b2, Pkm, Cntn1 | Dpysl2, Rab18, Cntn1, Uchl1 | Rab18, Cntn1, Uchl1, Dbnl |

Table 5.4: Distinguishing between increased developed due to increased regulation of Snap-25, Rtn4 and Dpysl2 and active induction of developmental mechanisms by these 3 proteins. All proteins displayed were detected in the developmental gene ontology in Metacore. For all of the 3 key proteins, developmental proteins that target them are predominantly negative influencers; the system is attempting to restore equilibrium to Snap25, Rtn4 and Dpysl2 via down-regulation. Interestingly, Dpysl2 and Rtn4 are predominantly positive influencers of developmental proteins while Snap25 is again, predominantly a negative influencer of developmental proteins.

The downstream targets of these proteins were investigated and interactions that were greater than 1 standard deviation from the global average were collated and filtered using the

"Development" gene ontology (table 5.4). Downstream developmental targets of Rtn4 and Dpysl2 were predominantly positively influenced whilst the downstream developmental targets of SNP25 were predominantly negatively influenced by SNP25. These results suggest that whilst all 3 key proteins drive expression of developmental proteins indirectly through a regulatory feedback as the system tries to reduce expression (figure 5.9 and table 5.4), both Rtn4 and Dpysl2 can also drive developmental protein expression through direct positive interactions at downstream targets. These results were not exclusive to the developmental proteins. Figure 5.15 shows the results of investigation into the strongest interactions up and downstream of the key nodes. Referring to the downstream networks, proteins that were influenced by the key nodes exhibited significant differences between the key nodes and the median protein CISY for only 2 generations (figure 5.11D and 5.11E). In contrast, upstream proteins exhibited significantly stronger interactions on proteins within the network across a minimum of 3 generations (Figure 5.11A and 5.11B). Similarly, the convergence of proteins-protein interactions on specific targets was evident earlier in protein interactions upstream of the key nodes rather than the downstream proteins (figure 5.11C and 5.11F).

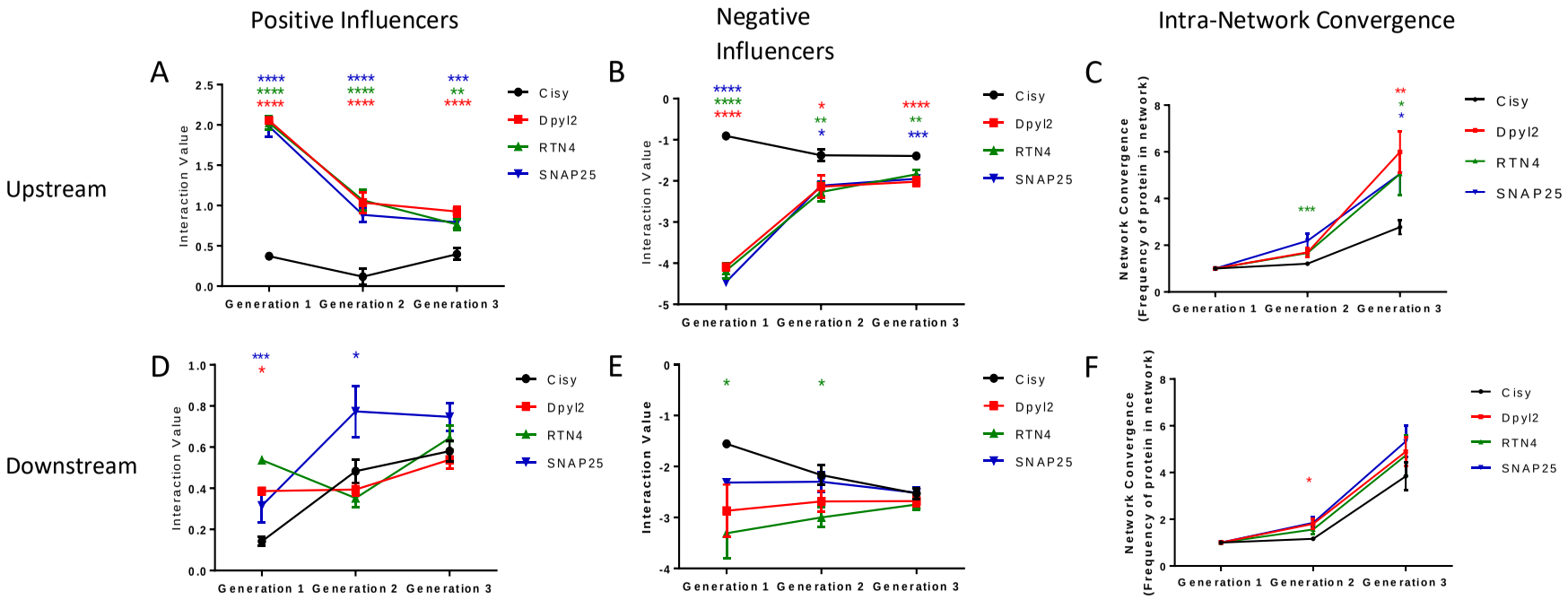


Figure 5.11: Analysing protein-protein interactions up and downstream of key nodes, Dpyl2, Rtn4 and SNAP-25, (A-C) Proteins upstream of the key nodes (D-F) Proteins downstream of the key nodes (A and D) Proteins upstream that have a positive influence within the network (B and E) Proteins that have a negative influence within the network (C and F) Average protein-protein interactions that converge on a single target.

Statistical analysis was performed using one way ANOVA at each generation. Tukey's multiple comparison test was used as a post hoc test (A) Generation 1: $F(3,8) = 114.9$, $p = <0.0001$; generation 2: $F(4,85) = 74.57$, $p = <0.0001$; generation 3: $F(3,284) = 9.903$, $p = <0.0001$ (B) Generation 1: $F(3,8) = 114.9$, $p = <0.0001$; generation 2: $F(4,85) = 4.056$, $p = 0.0103$ ; generation 3: $F(3,284) = 8.484$, $p = <0.0001$ (C) Generation 2: $F(3,82) = 5.195$, $p = 0.0025$; generation 3: $F(3,168) = 5.445$, $p = 0.0013$ (D) Generation 1: $F(3,8) = 13.72$, $p = 0.0016$; generation 2: $F(4,85) = 6.629$, $p = 0.0005$; generation 3: $F(3,284) = 1.103$, $p = 0.3483$ (E) Generation 1: $F(3,8) = 4.431$, $p = 0.0410$; generation 2: $F(4,85) = 3.725$, $p = 0.0153$; generation 3: $F(3,284) = 1.103$, $p = 0.3483$ (F) Generation 2: $F(3,89) = 3.846$, $p = 0.0122$; generation 3: $F(3,113) = 0.8185$, $p = 0.4862$

### 5.3.3 The ARX transcription factor and *in silico* protein network generation

Metacore highlighted the ARX protein as a transcription factor of interest due to the number of proteins that were upregulated that ARX acts as a transcription factor for. A network was modelled for proteins that were upregulated by ARX, including proteins that were downstream of them (figure 5.12). Within this network, several developmental/differentiation proteins were identified that were not detected by the mass spectrometry that are upregulated as a result of increased ARX expression (SH3TC2, TAL1, SHC, SALL4, NMDAR, IL-1β, NuRD complex, cyclin D and ENPP2). Proteins involved with epithelial-mesenchymal transition (EMT) were also evident within this network (SMAD1, SMAD4 and Snai1).

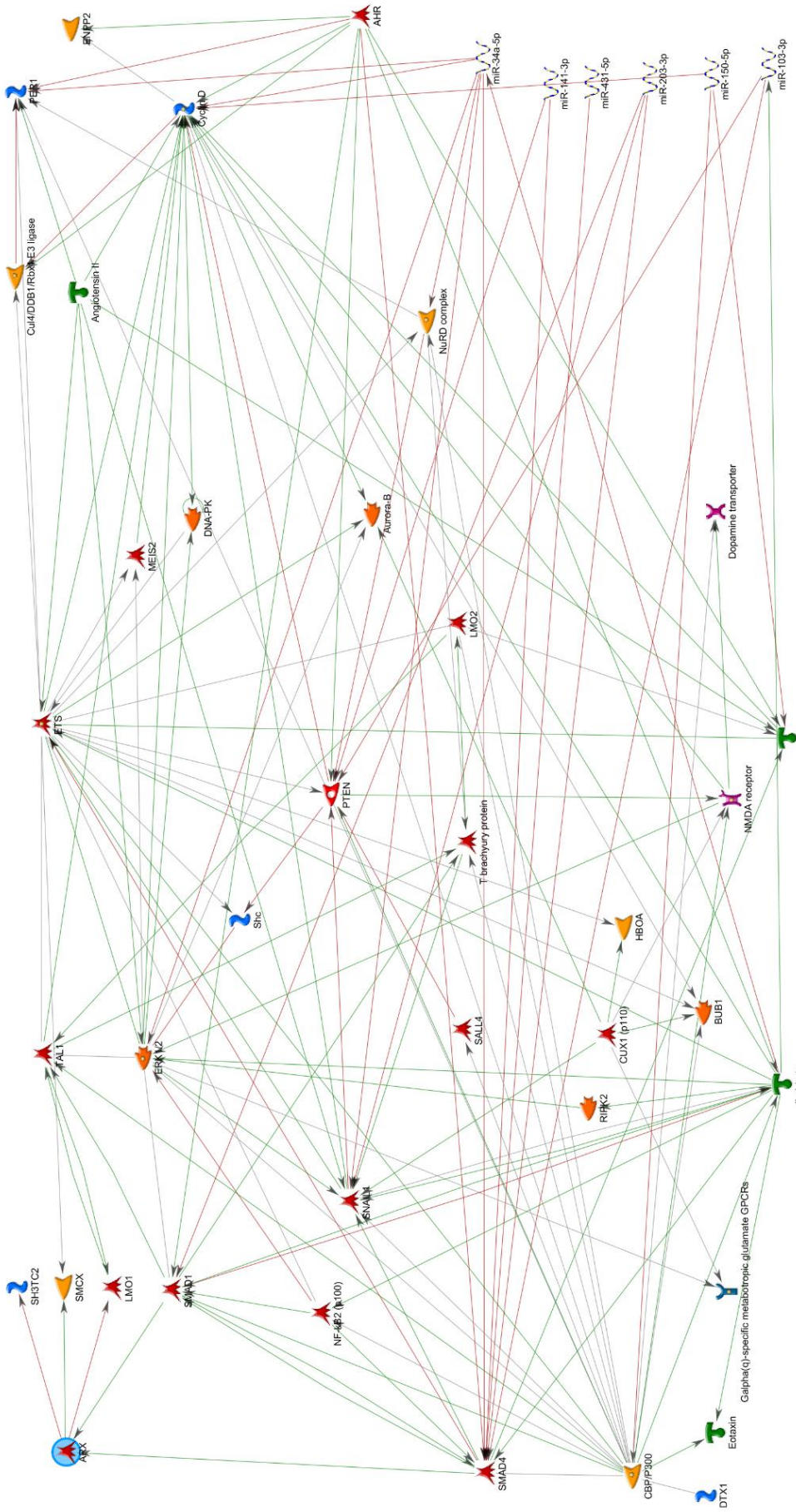


Figure 5.12: Network analysis of the ARX transcription factor, generated using Metacore. The network of the ARX transcription factor includes several markers of differentiation and development (highlighted in red), identified with Metacore. SMAD4, SNAI1 and SMAD1 are also markers for EMT (highlighted in blue).

## 5.3.4 Characterisation of the organoid and the mechanism of formation

To investigate the mechanism of formation of the organoid, 3 gene ontologies were used: synaptic, developmental and adhesion. For each of these gene ontologies, clear differences between control and the experimental condition (neuronal culture on aligned PLLA nanofibres) were observed in the fold change of protein expression (figure 5.13). Adhesion proteins display a clear decrease in expression (figure 5.13A) whereas developmental proteins exhibit a predominant shift towards increased expression of developmental markers for cortical neurons grown on the aligned PLLA nanofibres (figure 5.17C). Ribosomal proteins are a notable exception. Synaptic proteins exhibit approximately equal increase and decrease in expression as a result of culture of cortical neurons on the aligned PLLA nanofibres (figure 5.13B).

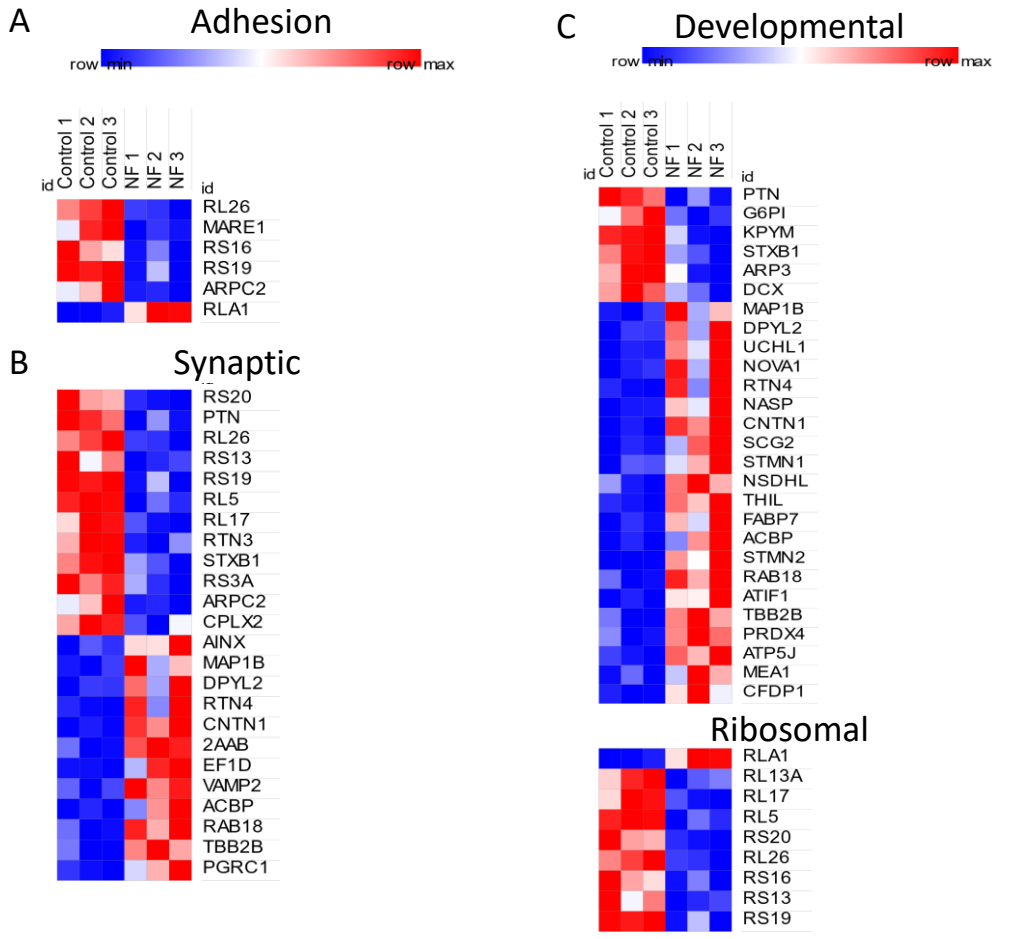


Figure 5.13: Fold changes for proteins that were deregulated for neurons grown on PLLA nanofibers relative to the control (NF = cortical neurons cultured on aligned PLLA nanofibres. Red = increased expression, blue = decreased expression). Proteins were sorted in to 3 gene ontology terms: adhesion (A), synaptic (B) and developmental (C)

Numerous proteins were observed in multiple gene ontologies, suggesting that some proteins were involved in an array of signalling processes (figure 5.14). A low degree of overlap was observed between adhesion and other gene ontologies, suggesting that alterations to adhesion is a distinct process within the formation of the organoids. A high degree of overlap is observed between the neuron projection, synaptic and developmental ontologies with most exhibiting greater than 50% overlap, indicating a complex process.

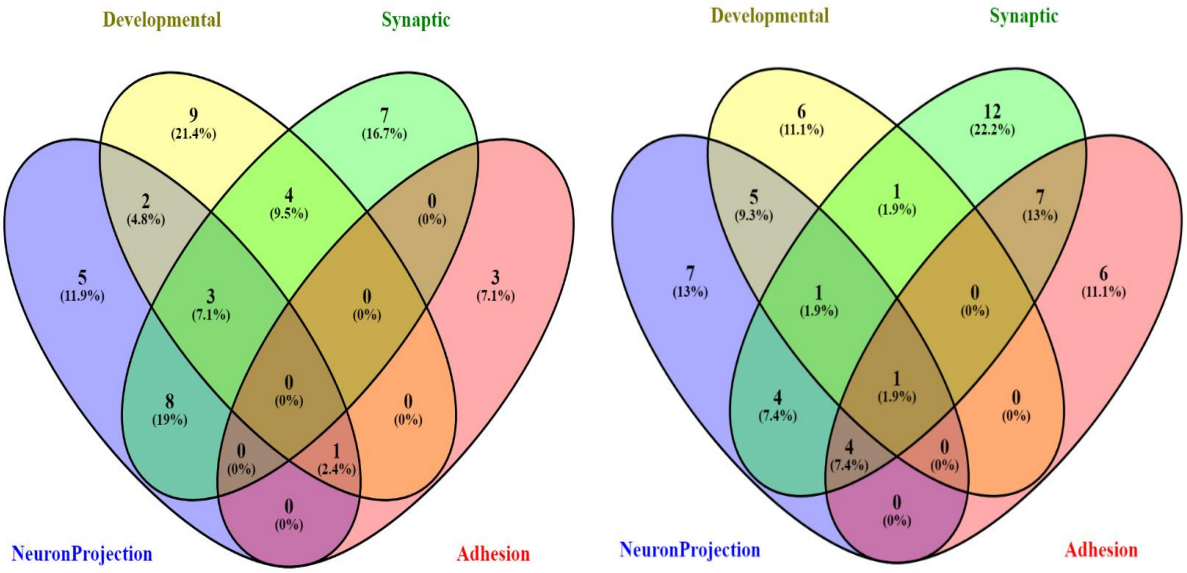


Up-regulated proteins Down-regulated proteins

Figure 5.14: Multi- and uni-functional proteins that were differentially expressed as a result of culturing primary cortical neurons on aligned PLLA nanofibers. For both up-regulated (A) and down-regulated (B) proteins, a large degree of multi-functionality is observed, notably for the synaptic proteins.

Comparison of the list of the strongest protein interactions against the Venn diagram of gene ontologies reveals that the strongest influencers are all up-regulated proteins (table 5.5). Of the strongest influencers, 37.1% were synaptic, 37.1% were neuron projection, 22.8% were developmental and only 2.9% were adhesion proteins.

| Category | Up-regulated | Down-regulated |
|---|---|---|
| Exclusively Developmental | Acat1; **Fabp7**; Phgdh; Atp5pf; Prdx4; Tubb3; **Nasp**; CNTN1; MAP1B | Impdh2; Pafah1b2; Phb2; Pkm; Atpif1; Dcx |
| Exclusively Adhesion | Cat; **Rplp1**; Arl3 | Ppp2ca; Snx3; Prdx2; Mapre1; Rps16; Rpl23 |
| Exclusively Synaptic | **Eef1d**; Ppp2r1b; **Ina**; **Psma5**; Tuba1a; Rplp2; Cntn1 | Ptn; Elavl1; Rab1b; Rps13; Rpl17; Rps3a; Rps20; Rpl18a; Map1lc3a; Fabp5; Rpl14; Rtn3 |
| Exclusively Neuron projection | **Clip2**; Khsrp; **Stmn1**; Dynlrb1; **Stmn2** | Hsp90ab1; Dcx; Dync1li1; Hsp90aa1; Ckb; Map1lc3b; Basp1 |
| Exclusively Neuron Projection and Developmental | **Tpm3**; **Uchl1** | Hmgb1; Cnn3; Arl3; Rps6; Gpi |
| Exclusively Neuron Projection and Adhesion | N/A | N/A |
| Exclusively Neuron Projection and Synaptic | **Nefm**; Vamp2; **Map1b**; **Cpe**; **Rtn4**; **Pgrmc1**; Sncb; **Snap25** | Apba1; Phb2; Got1; Cplx2 |
| Exclusively Developmental and Synaptic | Ncan; **Rab18**; Tubb2b; **Dbi** | Aldh2 |
| Exclusively Developmental and Adhesion | N/A | N/A |
| Exclusively Synaptic and Adhesion | N/A | Rps19; Rpl12; Rpl22; Rps18; Rps14; Rpl5; Rpl10a |
| Exclusively Neuron Projection, Synaptic and Adhesion | N/A | Rps3; Rpl26; Arpc2; St13 |
| Exclusively Neuron Projection, Synaptic and Developmental | **Dpysl2**; Vgf; **Dbnl** | Stxbp1 |
| Exclusively Neuron projection, Adhesion and Development | Vim | N/A |
| Exclusively Adhesion, Development and Synaptic | N/A | N/A |
| Common to all | N/A | Marcks |

Table 5.5: Summary of protein function and strength of interactions. Of the strongest interactions detailed in figure 2, 64 were unique proteins. 35 of the 64 unique influencers were detected within the assigned categories of “Developmental”, “Synaptic”, “Adhesion” or “Neuron Projection”. These strongest influencers are highlighted in bold. All of the strongest influencers were up-regulated. Of the 35 unique strongest influencers, 8 (22.8 %) were involved in developmental processes, 13 (37.1 %) were involved in synaptic processes, 1 protein (2.9 %) was involved in adhesion and 13 (37.1 %) were involved in neuron projections.

## 5.3.5 Metabolic changes induced by PLLA nanofibres

Deregulation of mitochondrial proteins was induced by culture of the nanofibres (figure 5.15A). The majority of proteins involved within the oxidative phosphorylation pathway were upregulated. Within differentiating neurons, substantial changes to metabolism occur; data suggest that mitochondrial changes in protein expression mimic what is observed during *in vivo* differentiation (figure 5.15B).

A

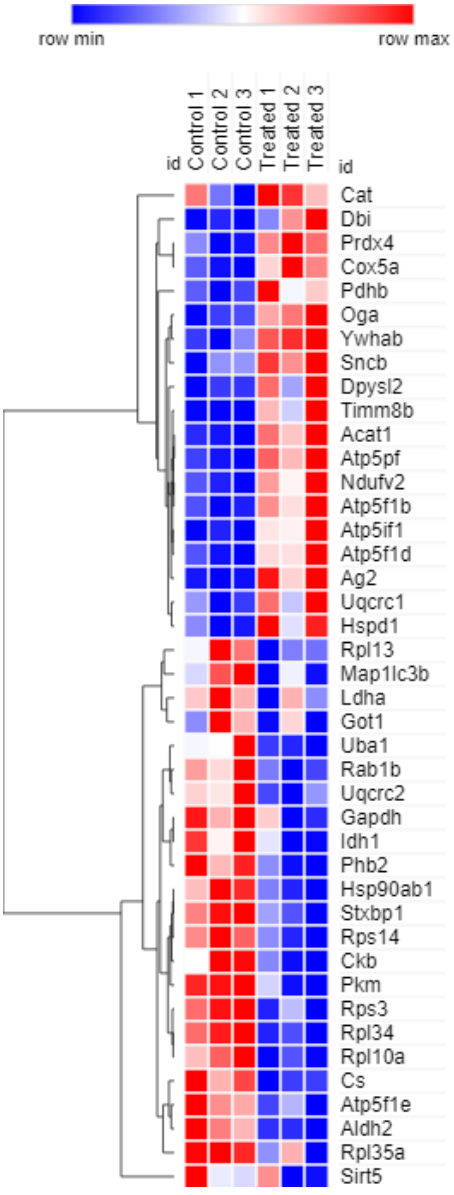


B

| Protein | Direction of fold change during differentiation | Direction of fold change in MS dataset |
|---|---|---|
| Ndufv2 (complex I) | Increase | Increase |
| Ndufs6 (complex I) | Increase | Increase |
| Ndufa10 (complex I) | Increase | Increase |
| SDHB (complex II) | Decrease | Decrease |
| Uqcrc1 (complex III) | Increase | Increase |
| Uqcrc2 (complex III) | Decrease | Decrease |
| Cox5a (complex IV) | Increase | Increase |
| Cox5b (complex IV) | Increase | Increase |
| Atp5f1b | Increase | Increase |
| Atp5f1c | Decrease | Decrease |
| Atp5f1d | Increase | Increase |
| Atp5f1e | Decrease | Increase |
| Atp5pf | Increase | Increase |

Figure 5.15: (A) Deregulation of metabolic enzymes as a result of culture of primary cortical neurons on aligned PLLA nanofibres (B) Deregulated proteins with a role in oxidative phosphorylation. 92% of proteins identified with mass spectrometry exhibit a fold change that is observed during differentiation of neurons, suggesting a more developed proteomic profile

## 5.3.6 Comparisons with the epithelial-mesenchymal transition (EMT)

Comparison with an EMT dataset (provided by Dr. Sarah Wagner) revealed similarities between directionality of protein/gene fold change (figure 5.16A) with approximately 55% of targets altering their expression in a similar direction whilst 39% were not in accordance. Whilst a significant positive correlation was observed between the expression of gene/proteins in the nanofibre and EMT datasets ($p = 0.0144$), the correlation was weak ($R^2 = 0.04146$) (figure 5.16B). Downregulation of adherens junctions is also a vital stage to EMT and thus, the deregulation of proteins belonging to the "adherens junction" gene ontology was investigated; the majority of proteins were downregulated (figure 5.16C).

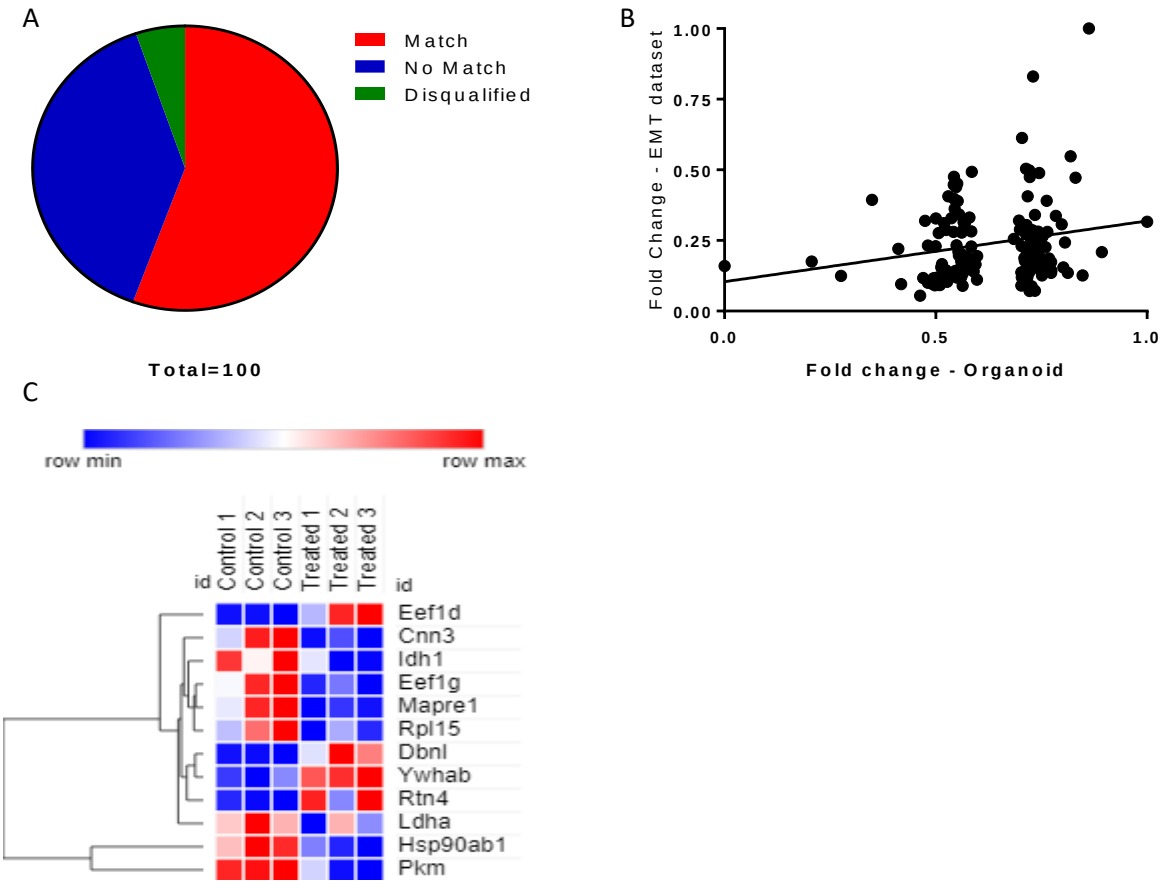


Figure 5.16: Similarities to the epithelial-mesenchymal transition (EMT) (A) Approximately 55% of proteins showed similar directionality of fold change between proteins of the organoid and EMT dataset whilst ≈39% showed an opposing directionality of fold change. Approximately 5% of values were discounted as the proteins were not detected in one or more of the EMT samples. (B) Linear regression for the two datasets: whilst a significant

correlation was observed (p = 0.0144), the $R^2$ remained low (0.04146) (C) Metacore analysis revealed deregulation of adherens junction; a process that occurs in EMT. The majority of proteins related to adherens junctions were observed to decrease in expression.

### 5.3.7 Markers of cerebral cortical lamination

Markers of cerebral cortical lamination were detected in both conditions and were significantly deregulated. Of the fourteen markers of cortical lamination that were deregulated on the nanofibres, 9 were up-regulated whilst 4 were down-regulated (table 5.5). An additional 4 markers of lamination were detected exclusively within the nanofibre treated lysates (table 5.6). Whilst the number of gene ontologies that each lamination marker appeared in was not significantly different (unpaired t-test, $t(9) = 2.002$, $p = 0.0763$), results were bordering significance.

| Protein | Multifunctional | Change of expression |
|---|---|---|
| Tuba1a | Synaptic | Increased expression |
| Tubb2b | Developmental, synaptic | Increased expression |
| Dpysl2 | Developmental, synaptic | Increased expression |
| Rtn4 | Synaptic | Increased expression |
| Rab5a | In data but not selected gene ontologies | Increased expression |
| Stmn2 | Neuron projection | Increased expression |
| Rab18 | Synaptic | Increased expression |
| Ncan | Synaptic, developmental | Increased expression |
| Dbnl | Synaptic, developmental | Increased expression |
| Marcks | Adhesion, synaptic, developmental, neuron projection | Decreased expression |
| Dcx | Developmental | Decreased expression |
| Stxbp1 | Neuron projection, developmental, synaptic | Decreased expression |
| Pak3 | In data but not selected gene ontologies | Decreased expression |

Table 5.5: Markers of lamination and gene ontologies. Markers of lamination were filtered by the pre-selected gene ontologies. The average number of gene ontologies that up-regulated proteins appeared in was 1.5 whereas for down-regulated proteins, the average was 2.66.

| Protein | Function | Up or down regulated | References |
|---|---|---|---|
| Tuba1a | Disruption results in abnormal cortical lamination | Increased expression | Evsyukova et al, 2013; Hanson et al, 2013 |
| Tubb2b | Regulate neuronal migration during corticogenesis | Increased expression | Evsyukova et al, 2013 |
| Dpysl2 | Regulate neuronal migration during corticogenesis | Increased expression | Evsyukova et al, 2013 |
| Rtn4 | Role in tangential migration | Increased expression | Evsyukova et al, 2013 |
| Rab5a | Role in radial migration | Increased expression | Evsyukova et al, 2013 |
| Stmn2 | Role in radial migration | Increased expression | Evsyukova et al, 2013 |
| Rab18 | Role in radial migration | Increased expression | Wu et al, 2016 |
| Ncan | Influences cortical folding | Increased expression | Schultz et al, 2014 |
| DBNL | Unclear mechanism but absence induces lissencephaly | Increased expression | Inoue et al, 2018 |
| Dcx | Role in tangential migration | Decreased expression | Evsyukova et al, 2013 |
| Pak3 | Role in tangential migration | Decreased expression | Evsyukova et al, 2013 |
| Stxbp1 | Disruption results in abnormal cortical lamination | Decreased expression | Hamada et al, 2017 |
| Marcks | Role in radial migration | Decreased expression | Weimer et al, 2009 |
| ApoE | Implicated in cortical lamination. *Reelin* knockout mouse fails to generate lamination; the ApoE receptor is a key component in this failure to laminate | Uniquely expressed on PLLA nanofibres | Hammond et al, 2009 |
| Tuba8 | Disruption results in abnormal cortical lamination | Uniquely expressed on PLLA nanofibres | Evsyukova et al, 2013; Abdollahi et al, 2009 |
| Napb | Role in interneuron migration | Uniquely expressed on PLLA nanofibres | Friocourt and Parnavelas, 2011 |
| Eml1 | Role in determining cleavage plane in early cortical progenitors | Uniquely expressed on PLLA nanofibres | Lyman and Chetkovich, 2015 |

Table 5.6: Deregulation of expression of proteins associated with cortical lamination as a result of culture on PLLA nanofibres. 9 proteins were upregulated whilst 4 were downregulated. 4 proteins associated with cortical lamination were detected in the nanofibre condition that were absent in the control.

## 5.3.8 Unique proteins

The total list of proteins that were identified for each condition (control and experimental) was sorted into a Venn diagram (figure 5.17A) and 24 proteins that were unique to the nanofibres treated condition were identified and analysed further (figure 5.17B). These proteins were mostly involved in metabolism, organelle localisation and neuronal development. Relatively limited formation of networks were observed with the majority of proteins exhibiting no connections with other unique proteins.

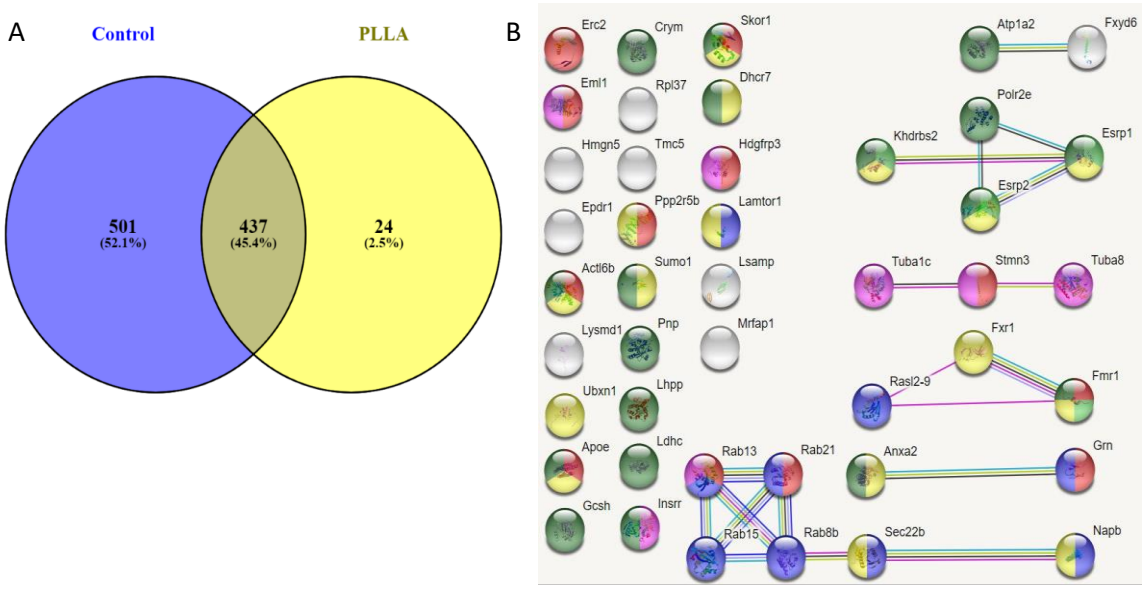


Figure 5.17: Proteins that were uniquely detected in the lysates of primary cortical neurons cultured upon aligned PLLA nanofibres. (A) Venn diagram representation; 24 unique proteins were detected (B) Network representation and functions of proteins uniquely detected for primary cortical neurons cultured on PLLA nanofibres. Red = Nervous system development, blue = establishment of localisation in the cell, light green = regulation of RNA splicing, yellow = regulation of metabolic process, pink = cytoskeletal organisation, dark green = organic substance metabolic process

## 5.4 Discussion

### 5.4.1 Overview and comparison to previous literature

*In vitro* three-dimensional culture of cells induces altered properties of those cells relative to their 2D counterparts. Cells cultured in 3D exhibit a greater susceptibility to pathologies and toxins, a greater degree of polarisation and altered $Ca^{2+}$ dynamics, proliferation and differentiation (Irons et al, 2008). Whilst nanofibres induce relatively two dimensional growth of cells relative to growth of cells in a hydrogel, relative to traditional cell culture on tissue culture plastic, cell growth still occurs within three dimensions and the porosity of the nanofibres allows basolateral diffusion that is absent in the tissue culture plastic counterpart. As a result, the morphology, alignment and clustering behaviours of cells is altered upon culture on aligned hydrophobic nanofibres (Chapter 3 and 4) and thus, significant alterations to the proteome are expected and observed (figure 5.1).

Previously, little work has been done on how nanofibres affect the proteome of neurons. A single study was identified as having a comparable dataset. Marote et al (2016) utilised a clonal neuroblastoma cell line (SH-SY5Y) cultured on both coated (laminin - 10µg/mL) and uncoated aligned PLLA nanofibres. However, Marote et al (2016) only identified 45 proteins that were differentially expressed in the control and experimental samples whereas our mass spectrometry yielded 186 proteins that were deregulated as a result of culture on PLLA nanofibres. The difference in numbers of proteins identified is likely due to the sample preparation; Marote et al (2016) performed mass spectrometry on several bands after performing gel electrophoresis rather than mass spectrometry of total lysates. Similar to Marote et al (2016), an increase in expression of markers associated with cell-cell adhesion was observed whilst the proteins involved in metabolism and protein synthesis were both observed to be deregulated, with a trend of down-regulation. The increased expression of

proteins involved in cell-cell adhesion and the decreased expression of cell-substrate adhesion is likely due to the hydrophobicity of the PLLA nanofibres. The adhesion of a cell to a cell or substrate are inversely proportional (Limongi et al, 2013; McCain et al, 2012) and this is reflected in both the proteome and the behaviour of the cells as they migrate across the surface to form the organoids. An interesting contrast between the dataset of Marote et al (2016) and ours is the up-regulation of heat shock proteins observed by Marote et al (2016), the inverse of what was observed in our study. This may be due to the mitotic nature of the SH-SY5Y cell line and the role of the heat shock proteins in proliferation, in addition to the attenuation of heat shock protein expression that occurs during the differentiation of primary neurons (Marote et al, 2016; Yang et al, 2008).

### 5.4.2 Characterisation of the cerebral cortical organoid

Organoids represent a more physiological model of the organ of origin than conventional 2D culture (Fatehullah et al, 2016). The data generated by mass spectrometry and artificial neural network inference suggest that the neurons cultured upon the nanofibres are more developed than their counterparts cultured in 2D. Proteins involved in neuronal development are significantly over-represented in the interactome (figure 5.4 and table 5.1). Proteins that are identified as important within the interactome using the betweenness centrality almost unanimously play a role in enhancing development and plasticity (table 5.2) and proteins that were identified as developmental proteins are deregulated with a directionality indicating increasing development as a result of culture on the nanofibres (figure 5.13C). Proteins that promote proliferation/inhibit differentiation, induce neurogenesis in immature neurons and initiate neurite formation/arborisation were down-regulated (Pekovic et al, 2009; Moreb, 2008; Fang et al, 2012; Dhaliwal et al, 2016; Broeke et al 2010; Leondaritis et al, 2015; Hamada et al, 2017; Brudvig et al, 2018), suggesting a more mature, differentiated neuronal culture

upon the nanofibres. The downregulation of ribosomal proteins and proteins involved in protein synthesis, also observed by the previously mentioned Marote et al (2016), is a further indication of the more advanced nature of the organoids; ribosomal proteins are downregulated throughout forebrain development (Chau et al, 2018). Conversely, up-regulated proteins had notable roles in radial migration/lamination of the cortex, fasciculation, guidance and growth of axons and neuronal polarisation (Jaglin et al, 2009; Wu et al, 2016; Ip et al, 2014; Inatani et al, 2001; Inoue et al, 2018; Haenisch et al, 2005; Latremoliere et al, 2018), indicative of development of physiological cytoarchitecture although immunohistochemistry is required to support this.

| **Up-regulated proteins** | | | **Down-regulated proteins** | | |
|---|---|---|---|---|---|
| **Function** | **Protein(s)** | **References** | **Function** | **Protein(s)** | **References** |
| Radial migration/cortical lamination | Rab18, Dpysl2, Tubb2B, Ncan, DBNL, NOVA1, NSDHL | Jaglin et al, 2009; Wu et al, 2016; Ip et al, 2014; Inatani et al, 2001; Inoue et al, 2018 ; Störchel et al, 2015; Xin et al, 2017 ; Hu et al, 2018 ; Cunningham et al, 2009 | Promote proliferation/inhibit differentiation | Phb2, IMPDH2, Aldh2 | Kowno et al, 2014; Pekovic et al, 2009; Moreb, 2008 |
| Axon fasciculation, guidance and growth | CNTN1, Ncan, Tubb3 | Haenisch et al, 2005; Inatani et al, 2001; Latremoliere et al, 2018 | Induce neurogenesis in immature neurons | Dcx, HMGB1 | Fang et al, 2012; Dhaliwal et al, 2016 |
| Neuronal polarisation | DBNL, Dpysl2 | Inoue et al, 2018; Ip et al, 2014 | Initiate neurite outgrowths and promote arborisation | Marcks, Stxbp1 | Broeke et al 2010; Leondaritis et al, 2015; Hamada et al, 2017; Brudvig et al, 2018 |

Table 5.7: Developmental proteins and their ascribed functions

### 5.4.3 Elucidation of the mechanism that promotes organoid formation

The regression analysis of Chapter 4 (figure 4.6) suggests a relationship between the clustering behaviours and neurite outgrowth/fasciculation whilst proteomics thus far has heavily emphasised the highly developed nature of the organoid. Four gene ontologies were chosen to investigate whether the clustering of cells, bundling of neurites and neurite outgrowth influences the development of the organoids. “Adhesion” was chosen as a proxy for cell clustering as loss of cell-substrate adhesion/gain of cell-cell adhesion promotes the clustering of neurons (Limongi et al, 2013). “Neuron projection” was chosen to represent the neurite extension and fasciculation, “synaptic” was chosen due to the key role of SNP-25 in the interactome (figure 5.9) whilst “developmental” was selected due to the previous proteomic analysis.

Neurons cultured upon the nanofibres exhibited reduced expression of cell-substrate adhesion proteins (Marcks, Arpc2) (Estrada-Bernal et al, 2009; Rotty et al, 2017) and an increase in expression of proteins that inhibit adhesion (catalase) (Yata et al, 2009). In contrast, changes to the proteome associated with dynamic adhesion and cell-cell interactions were observed (Prdx2, vimentin) (Park et al, 2011; Ivaska et al, 2007). The alterations to the proteome reflect the observed clustering behaviours of the cells described in Chapter 3 and 4; the loss of cell-substrate adhesion is counter-balanced by increased cell-cell adhesion (Limongi et al, 2013; McCain et al, 2012), facilitating the increased migration and soma clustering behaviours (Segev et al, 2003).

Upon clustering, the previous assumption of Chapter 4 was that the clustering stimulated the extensive neurite outgrowth through ligand-receptor interactions of cell surface ligands of the neurites. Figure 5.9, table 5.4 and figure 5.14 contradict this and suggest that synapse development is key to the observed behaviours of the neurons grown on the nanofibres. The majority of the strongest interactions of the interactome are all inhibitory and target SNP25, a

synaptic protein (figure 5.9). Additionally, synaptic proteins and neuron projection exhibited the highest degree of overlap with other gene ontologies (figure 5.14) and had the highest percentage of strongest influencers relative to other gene ontologies (table 5.5).

Peter's rule states that connectivity of neurons (via synapses) can be predicted based on the coincident availability of axons and dendrites (Peters et al, 1979; Braitenburg and Schüz, 1998); proximity generates synapses. For decades, the rule was quantitatively untested but recent validation of the rule demonstrated ≈ 85% accuracy in the entorhinal cortex and ≈ 100% accuracy in the hippocampus (Rees et al, 2017). Thus, the mechanism of generating the organoids is proposed to be induction of soma clustering due to limited adhesion of cells to the surface and promotion of cell-cell adhesion, subsequent fasciculation of neurites and generation of a number of synapses significantly higher than a conventional dispersed 2D culture due to the proximity and overlap of the neurite arbors. The subsequent proteomic changes to synaptic and neuron projection proteins are then able to drive the developmental changes that are observed due to the multi-functionality of the proteins (figure 5.14). The changes to morphology observed in Chapter 4, figure 4.4 corroborate this; all morphological features appear to follow a linear trend until day 7, at which point, neurite length, neurite bundle diameter and cell cluster diameter all exhibit a robust increase in the rate of growth. At approximately 7 DIV, synapses are mature and neurons become electrically active.

### 5.4.4 Network analysis

Global analysis of the network using Cytoscape validated the hypothesis that the organoid formation may be inducing a more developed profile within the cortical neurons; gene ontologies associated with development were significantly overrepresented (figure 5.4 and table 5.1). Betweenness centrality (BC) was used to explore the network further. Betweenness

centrality measures the degree to which a protein acts as a “hub” or bridge within the network. It is measured by calculating the shortest path length between each protein pair in a network and calculating what proportion of them pass through a third protein. The greater the betweenness centrality, the greater the protein's ability to act as a hub (Melak and Gakkhar, 2015). This analysis serves to identify widely influential although potentially weak influencers within the system that are inducing the observed developmental changes. Within the results of the betweenness centrality analysis, the 10 proteins that were detected were all involved in processes such as development, polarity and synaptic plasticity and showed upregulation (table 5.2). Sub-networks were generated to determine the influence of the well-connected proteins on developmental proteins. Ribosomal proteins are known to decrease throughout forebrain development (Chau et al, 2018); the majority of the proteins with high BC exhibit strong influence on the ribosomal proteins, predominantly negative influence (figure 5.8). In contrast, the influence of high BC proteins on the developmental proteins is mixed (figure 5.7). Tars and RPL35a exert wide ranging negative influence, although their role in reducing protein synthesis may be key to explaining this negative influence of protein expression (Chau et al, 2018; Uniprot). NOVA1, MAP1B, MYG1 and PDHB exert strong positive influence on developmental proteins and thus may represent targets that are crucial to the generation of the developed organoid proteome (figure 5.7). These proteins could be exploited to modulate the development of the organoid; to enhance or reduce development, in order to target specific developmental stages for research. In contrast, NSDHL, GOLGA2 and PSMD9 exhibit relatively negligible connectivity with the identified proteins, developmental or ribosomal (figure 5.7 and 5.8). NSDHL itself was identified as a developmental protein (figure 5.13) whereas GOLGA2 and PSMD9 have roles in asymmetric cell division and positive regulation of transcription respectively (Uniprot). Whilst they are important nodes within the network, they are not involved directly in development.

Analysis of the strongest influencers of the interactome demonstrated that SNAP-25, Dpyl2 and RTN4 were key signalling nodes within the system; all of the strongest interactions were centred on downregulating these proteins, implying that the regulation of these proteins facilitates the greater changes that are observed. This was explored further by generating targeted interactomes, focused on these 3 nodes. Interactions up and downstream of these proteins were investigated. Referring to figures 5.11A and 5.11B, significant difference between interactions was maintained to a much greater degree for proteins that were upstream of the key nodes than they were for the average protein CISY, suggesting that it is the regulation of the proteins rather than the proteins themselves that are vital to the formation of the organoid. Further, within the expanded interactome network for each protein, a greater degree of convergence was observed with significantly fewer unique proteins appearing in the interactome networks upstream of the key nodes (figure 5.11C). Convergence within protein-protein interaction networks is indicative of a non-random network, a point of the signalling network that is important to the overall mechanism (Weßling et al, 2014) and thus, the expanded interactome identifies potential influencers for individual proteins that may not possess the strength of interaction to be considered a key node in the initial global network analysis but play a role for the individual nodes. These secondary nodes include MAP1B, a marker for synaptic plasticity (Tortosa et al, 2011), Myg1, a protein that is putatively associated with neuronal differentiation (Phillips et al, 2009), and FAF1, a protein associated with neurodevelopmental apoptosis (De Zio et al, 2008).

### 5.4.5 The epithelial-mesenchymal transition (EMT), developmental process and integration into the endogenous circuitry of the host

The epithelial-mesenchymal transition (EMT) is a process typically associated with cancer but plays other important physiological roles. Three types of EMT have been documented to date;

embryonic development (type 1), inflammatory, regenerative and in chronic cases, fibrotic processes (type 2) and cancer progression (type 3) (Kalluri and Weinberg, 2009). The three types of EMT are involved in distinct processes and whilst some variation is observed between the biochemical processes, a large number of signalling molecules are shared between them (Zeisberg and Neilson, 2009).

Within the cerebral cortex, type 1 EMT occurs during the lamination of the cortex. The early neuroepithelium is comprised of columnar cells which generates the radial glial cells. During the development of the cortex, radial glial cells undergo indirect neurogenesis, with one progeny exhibiting ciliary components while the other becomes multipolar and exhibits EMT properties (Singh and Solecki, 2015). E-cadherin and adherens junctions that apically anchor neuronal progenitors to the ventricular zone are down-regulated and radial and tangential migration of the progenitors occurs (Singh and Solecki, 2015; Lamouille et al, 2014). Upon migration towards the cortical plate, polarised morphology is re-established as cell-cell contacts are re-established with the glial scaffolds that guide the migration of the progenitors (Famulski and Solecki, 2013). Maturation of the neurons then occurs as the soma translocates to the cortical plate and mature through interactions between the maturing neurons and the extracellular matrix, secreted molecules of neighbouring cells and cell-cell contacts with cortical plate neurons (Famulski and Solecki, 2013). The organoid that forms as a result of culture upon PLLA nanofibres demonstrated a 55.55% overlap with a neuroblastoma EMT model when investigating the directionality of the fold changes (figure 5.16). Linear regression was performed to quantify the relationship between the magnitude of the fold changes in the two datasets. A significant correlation was found between the two datasets although the correlation was weak ($R^2$ = 0.048). This likely due to the use of protein data for the organoid and RNA data for the EMT dataset. One meta-study revealed that the average $R^2$ value from

plots of mRNA and protein concentration for the same cells was 0.4 (Vogel and Marcotte, 2012); quantitative comparison between the organoid data (primary neurons) to an EMT model (prostate cancer) would yield even lower correlation of global data. Thus, whilst the results are significant, the correlation is poor as the magnitudes of the fold change do not necessarily translate between mRNA and protein. Due to this, the semi-quantitative directionality of fold change is suggested to give a greater representation of cellular behaviours than the quantitative comparison.

Key markers for EMT such as CADH and FINC were not detected within the mass spectrometry. Further validation would be needed to determine the degree to which the organoid formation captures the EMT-like process that occurs during corticogenesis. Targeted metacore analysis revealed deregulation of adherens junctions; the majority of the proteins associated with adherens junctions were downregulated as a result of neuronal culture on aligned PLLA nanofibres (figure 5.16C). A more targeted approach is needed to further determine the similarity of the mechanism to EMT-like corticogenesis.

The epithelial-mesenchymal transition may also be indicative of the ability of the cells within the implant to integrate into host circuitry. Due to the role of EMT in the wound healing process, it has been suggested as a means of characterising wound healing in transplantation studies, however, elevated levels of EMT markers are associated with rejection and fibrosis (Fintha et al, 2019). This is proposed to be due to two factors; overactive EMT increases the proliferation of myofibroblasts that contribute to inflammation and partial EMT, resulting in de-differentation of cells without subsequent re-differentiation (Fintha et al, 2019). A partial EMT phenotype is observed for cells of the organoid; both mesenchymal markers (vimentin) and epithelial markers (multiple keratins) are expressed. A partial EMT phenotype has been

observed for cells migrating in clusters (Aiello et al, 2018). Previous chapters discuss the formation of organoids as being dependent on basin collapse and the migration of clusters towards each other. The partial EMT phenotype that is present within the organoid may be necessary to facilitate the assembly, yet that same partial EMT phenotype is suggestive of elevated capacity for fibrosis and rejection upon implantation. Within the CNS, glial scarring is the fibrosis associated with injury and chronic inflammation and is an inducer of localised neurodegeneration (McConell et al, 2009). However, transplantation studies that investigate the partial EMT phenotype typically use adult kidneys and lungs as a tissue source (Fintha et al, 2009), tissues which vary significantly from embryonic neurons. Limited transplantation studies have been done with neurons and data is scarce; it is unclear whether these trends will be reflected in neurons as well as kidneys and lungs.

### 5.4.6 Metabolic changes

Extensive changes to the mitochondrial proteome were also observed for neurons cultured upon the PLLA nanofibres. The observed changes to the metabolism of the cell are likely due to the abundance of lactate that occurs upon degradation of poly-L-lactic acid nanofibres (Santoro et al, 2016) in addition to the altered differentiation state induced by the fibres.

Lactic acid has previously been discussed as a bioactive molecule with beneficial properties to the implanted cells, including promotion of angiogenesis, wound healing, neuroprotection and suppression of inflammation (Sun et al, 2017). Lactic acid is also buffered to lactate which can be used as an energy substrate by neurons to perform oxidative phosphorylation and generate ATP in the absence of glucose, likely the cause of the metabolic changes observed in figure 5.15A (Mason et al, 2017).

Neurons cultured on the nanofibres appear to exhibit a shift away from aerobic glycolysis as a source of ATP in favour of alternative mechanisms. Acat1, FABP7 and Dbi are involved in the conversion of ketones to acetyl Co-A and storage of acetyl Co-A respectively (Bouyakdan et al, 2015; Pfieger and Ungerer, 2011) and were up-regulated, circumventing glucose-dependent production of acetyl Co-A to a degree. Conversely, LDHa increases glucose uptake (Zhang et al, 2017), Rap1b is expressed as a defence against hyperglycaemia (Sun et al, 2008) and GAPDH is involved in gluconeogenesis and these aerobic glycolytic proteins were all down-regulated. In contrast to the proteins of aerobic glycolysis, the majority of detected proteins involved in oxidative phosphorylation were upregulated (figure 5.15B). Proteins involved in oxidative phosphorylation typically increase during differentiation of the cerebral cortex (Agostini et al, 2016), although there are some exceptions (Zheng et al, 2016). Approximately 92% of proteins appear to exhibit deregulation in the direction that would be expected of increasing differentiation (figure 5.15B), further supporting the hypothesis that the organoids are more differentiated than their 2D counterparts.

The decrease in aerobic glycolytic proteins may be explained by the differentiation and development of the neurons. Both predicted and measured aerobic glycolysis increases in the early developing brain and decreases to a steady baseline in adult life (figure 5.15B; Goyal et al, 2014). These results suggest that the decrease in aerobic glycolytic proteins appears to indicate that the cortical neurons are more developed than the neurons grown in 2D, appearing to further support the developmental hypothesis. However, whilst this trend is true for the whole brain, neotenous regions of the brain, including the cerebral cortex, are noted for being exceptions to the rule of decreasing glycolysis during maturation; within the cerebral cortex, aerobic glycolysis increases during development and plateaus due to the high plasticity of the region (Goyal et al, 2014). The study notes that decreasing glycolysis in the cerebral

cortex is associated with reduced plasticity and growth of spines but is correlated with maintenance and stability of spines. It is possible that culture on the nanofibres may decrease the plasticity of the neurons contained within the system. Whilst this is not necessarily an issue if the organoid were to be used for a high throughput *in vitro* cell culture for toxicology, pharmacology, etc, it represents a hurdle for the use of the organoid for implantation as the organoid would form a closed-circuit and would poorly integrate in to the existing host circuitry. Further research is required to determine the exact cause of the decrease expression of glycolytic enzymes and whether this relates to the plasticity of the neurons within the organoid. Additionally, the shift towards oxidative phosphorylation suggests a greater dependence on oxygen. Upon implantation, one of the greatest causes of death for exogenous cells is the lack of vascularisation and subsequent ischaemia that results (Sortwell et al, 2000). Whilst lowering the glycolytic capacity and increasing the oxidative phosphorylation capacity may indicate well for the differentiation aspect of the neurons, it is a poor indicator for the survival of neurons within the implant.

### 5.4.7 Evidence for lamination within the organoid

Discussed previously in Chapter 1, the lamination of the cortex has been theorised to play a role in maximising spatial efficiency and temporal synchronisation of action potentials through control of the length of the neurons utilised by a neuronal ensemble during activity. Whilst mass spectrometry does not yield any spatial information of protein expression or tell us about the cytoarchitecture, the proteomic profiles warrant further investigation in regards to lamination. In the nanofibre sample, 9 proteins associated with lamination of the cortex were upregulated whilst 4 were down-regulated. Four additional proteins associated with lamination were expressed by the neurons of the nanofibre sample (table 5.6). Of note, down-regulated proteins were involved in more gene ontologies than up-regulated proteins (table

5.5). Whilst the sample size is limited, the relevance of this is illustrated by the decreased expression of Marcks. Marcks is a multi-functional protein with roles in a diverse array of cell signalling pathways. The expression of Marcks, a marker of cortical lamination, is decreased, Marcks also plays a role in adhesion (figure 5.13A) and may have been down-regulated as a result of the reduced adhesion on hydrophobic nanofibres. Whilst the expression of cortical lamination markers is inconsistent, a trend is observed that is suggestive of cortical lamination on the nanofibres that is limited in the control. The absence of consistency indicates that whilst the nanofibres promote a near physiological developmental mechanism, it is not entirely accurate. Additional immunostaining to determine the cytoarchitecture of the neurons within the neurons will be required to further quantify the architecture and investigate the spatial expression of lamination markers further. Alternately, mass spectrometry imaging would be a powerful molecular technique to probe the expression of proteins in a spatial manner.

### 5.4.8 Unique proteins

Twenty-four proteins were detected that were uniquely expressed in the lysates gathered from the nanofibres that were not detected for the control whilst for the control, 501 proteins were detected that were not detected in the nanofibre lysates (figure 5.17A). Enrichment using bioinformatics tools revealed similarities to the pattern of increasing development that was revealed with the quantitative mass spectrometry data (figure 5.17B); 27% of unique proteins have a role in nervous system development whilst 15% play a role in cytoskeletal organisation. In addition to the observed changes to nervous system development and cytoskeletal organisation, metabolism again appears as a systemic process that is altered by culture of primary cortical neurons on the nanofibres.

### 5.4.9 Limitations to characterisation using proteomic analysis

Significant alterations to the proteome were observed due to culture on the nanofibre substrate. These were attributed to the increased cell clustering and an intrinsic synaptic-driven developmental program. However, numerous factors have changed due to the use of nanofibres and attributing the proteomic changes to any one factor would be reductionist. As previously mentioned, the PLLA nanofibres degrade to lactic acid, a bioactive molecule (Sun et al, 2017). Nanofibres have different mechanical properties (conductivity, porosity, Young's modulus, etc) to tissue culture plastic (Hosseinkhani et al, 2014); alterations to mechanical properties have demonstrated a wide range of effects on cellular behaviours (Saha et al, 2008; Chao et al, 2009; Yang et al, 2005). Three-dimensional culture is yet another factor that is able to contribute towards alterations in cell behaviours and protein expression (Irons et al, 2008). Thus, untangling the exact causative mechanism behind the development of the organoids is difficult and defining to what degree each factor contributes towards the final proteome would require a significant degree of further study and analysis.

### 5.4.10 Future directions

Mass spectrometry served to elucidate the mechanism of organoid formation and characterise the organoid but it also highlighted other avenues of research that require pursuing further; most notably the alterations to the metabolism of the cortical neurons and the lamination of the organoid.

Neurons cultured upon the nanofibres exhibited an increase in proteins within the electron transport chain and an apparent shift away from glycolysis and towards fatty acid/lactate based metabolism. An increase in the expression of electron transport chain proteins may be a result of an increased number of mitochondria or an increase in expression of these proteins. Labelling of the mitochondria with a specific dye such as Mitotracker would allow for

quantification of mitochondrial number and mitochondrial fission/fusion as a means of assessing normal mitochondrial function (Waterham et al, 2007). The apparent shift from glycolytic to free fatty acid/lactate metabolism is an additional avenue that warrants further characterisation. Post-implantation into a host, exogenous neurons undergo apoptosis due to a range of factors including an energy deficit due to poor vascularisation (Sortwell et al, 2000). An organoid that can utilise lactate as an energy source, implanted on a scaffold that degrades to lactate, would be highly beneficial as a greater number of neurons may survive implantation as a result of the metabolic shift. Further research is required on the metabolic capabilities of the organoid.

Lamination has been touched upon previously; upregulation of markers of lamination is evident. Whilst the individual neurons may be expressing a molecular profile that is increasingly laminar, the laminar structure of the brain is comprised of many neurons, complexed into a tissue-wide architecture. Further work is needed to determine whether the increased expression of laminar markers induces a more representative profile at a single-cell level or induces the formation of a laminar tissue.

## 5.5 Conclusion

Proteomic analysis of the organoids aided in the characterisation of the organoid and elucidation of the mechanism of organoid formation but raised as many questions as were answered. Significant efforts must be made to explore the organoid further to determine the precise degree of similarity of the organoid to the *in vivo* developing cerebral cortex. In an effort to characterise their own cerebral cortical organoid, Camp et al (2015) employed single cell RNA-seq and advanced bioinformatics to characterise their organoid against human fetal cerebral cortex. Similarly, multiple time points would be necessary to monitor the development over time as proteins may not exhibit linear trends.

Similarity between exogenous and endogenous neurons for the purposes of integration into existing synaptic circuitry has been discussed previously (Chapter 1). Proteomic analysis has demonstrated a shift towards a more developed, increasingly plastic culture of neurons by culturing cortical neurons on aligned PLLA nanofibres, suggesting a benefit of 3D culture to developing an implant to facilitate cortical rewiring.

# Chapter 6: Characterisation of the Organoid using Nanostring nCounter Analysis

## 6.1 Introduction

Further molecular characterization of the organoid was performed using the Nanostring platform. The Nanostring platform quantifies hundreds of target mRNA molecules using reporter probes. Each reporter probe has 35-50 bases that are specific to the target gene and a fluorescent barcode specific to the target. Reporter probes are allowed to hybridise with mRNA of the sample and then immobilized and using an electrical current, aligned within the nCounter cartridge. To quantify the expression level of a specific gene, the number of barcodes specific to the target gene is counted within the cartridge and tabulated (Kulkarni, 2011). Due to the specificity of RNA/probe binding, Nanostring quantification was employed to enhance the specificity of the characterization of the organoids relative to the shotgun approach of mass spectrometry.

## 6.2 Methods

### 6.2.1 RNA isolation

RNA was isolated from primary cortical neurons on day 11 of growth on a control surface (poly-l-lysine and laminin, described Chapter 2) or aligned PLLA nanofibres (described Chapter 2).

RNA was extracted using a Zymo RNA miniprep kit. Briefly, cells were lysed using RNA lysis buffer which was subsequently diluted with an equal volume of ethanol (99%) and vortexed. The mixture was transferred to the Zymo spin columns and centrifuged, flow through was discarded. RNA Prep Buffer (400uL) was added to the column and centrifuged, discarding the flow through. RNA Wash Buffer (700uL) was added to the spin column which was centrifuged and the flowthrough discarded. In column DNase treatment was performed. DNase I (40µl) was added to each of the columns, incubated at room temperature for 15 minutes before proceeding to

the next washing step. RNA Wash Buffer (400uL) was added to the columns and centrifuged for 2 minutes to ensure that the wash buffer was removed. The column was then transferred to an RNase free tube and 50uL of RNase free water was added to the column and used to elute the RNA upon centrifugation. All centrifugation was performed at 12,000g for 30 seconds at room temperature unless stated otherwise. RNA was stored at -80$^{o}$C until use.

## 6.2.2 RNA concentration and purification

Zymo RNA Clean and Concentrator kit was used to purify the RNA and concentrate the samples for use with the Nanostring. Briefly, dilute RNA samples were diluted in RNA Binding Buffer at a 2:1 ratio and mixed. An equal volume of ethanol (99%) was added and mixed. The sample was then transferred to a Zymo spin column and centrifuged for 30 seconds, discarding the flow through. RNA Prep Buffer (400uL) was added to the column and centrifuged, discarding the flowthrough. RNA wash buffer (700uL) was added to the column and centrifuged, discarding the flowthrough. RNA Wash Buffer (400uL) was added to the column which was centrifuged for 2 minutes to ensure total removal of the buffer. The spin column was then transferred to an RNase free collection tube and RNA was eluted by addition of 6uL of RNase free water and centrifugation. All centrifugation was performed at room temperature at 12,000g for 30 seconds unless stated otherwise.

## 6.2.3 RNA Quantification

RNA quantification was performed using a Nanodrop 8000 for both the purity and the concentration. A 260/280 ratio between 1.8 and 2.1 and a 260/230 ratio of between 1.8 and 2.1 was within the range for use on the Nanostring. RNA concentration was required to be greater than 25ng/µl. Samples were stored at -80°C until usage.

### 6.2.4 Nanostring nCounter XT Gene Expression Assay for Gene Expression Profiling

For the Nanostring nCounter assay, 8 samples were extracted with the purity required. The murine Neuropathology profiling panel was used, consisting of 760 genes that were functionally annotated by Nanostring. Samples (150ng total RNA) were hybridized for 20 hours at 65°C with 8µL of reporter probe and 2µL of capture probe. After hybridization, excess probe was removed from the samples using an nCounter Prepstation and magnetic beads. Samples were then immobilized on a streptavidin-coated cartridge. The cartridge was then scanned using an nCounter digital analyser to gather raw data which was then processed using Nanostring's nCounter Advanced Analysis Software (v.4.0). Normalisation was performed using housekeeper genes selected from the dataset that exhibited the lowest degree of variation. Quality control checks were performed within the software; no samples were flagged as needing to be removed from analysis. Differential Expression, Cell Type Profiling and Pathway analysis were all performed using the nSolver Advanced Analysis module (V.2.0.115) once normalization had been performed. Significant deregulation of genes was confirmed if a Benjamini-Yekutieli *p* value was less than 0.05.

### 6.2.5 Orthogonal Validation

Several genes overlapped between the mass spectrometry and the Nanostring panel. Regression analysis was used to determine the degree of correlation between observed fold changes for the protein and RNA, as quantified by mass spectrometry and Nanostring nCounter assay respectively.

## 6.2.6 Artificial Neural Network Inference (ANNI)

Network inference was performed using the ANNI described in Chapter 5 using the previously described methodology. Data input into the ANNI consisted of 152 significantly deregulated genes. Data was then visualized in Cytoscape and the BiNGO plugin was used to determine enriched gene ontologies amongst the deregulated genes.

# 6.3 Results

Orthogonal validation was attempted for the Nanostring; overlapping proteins between the mass spectrometry dataset were compared to the Nanostring dataset to determine the degree of correlation. Poor correlation was observed (figure 6.1). Further validation of this dataset is needed.

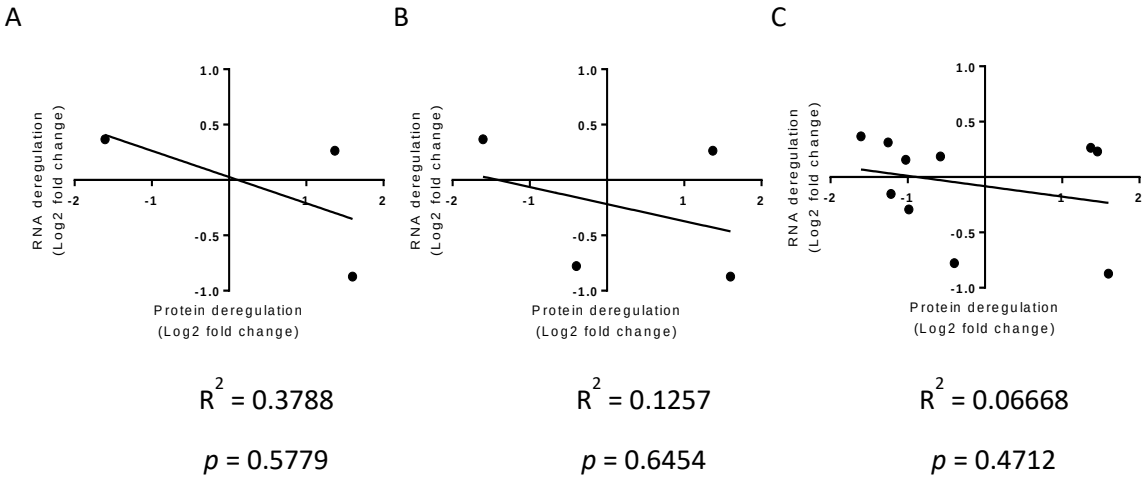


Figure 6.1: Orthogonal validation. No validation was possible using the mass spectrometry dataset for the Nanostring. All deregulated genes were compared to protein fold changes at varying stringency levels (A) Correlation between deregulated genes and proteins with >70% confidence value within the mass spectrometry dataset (B) Correlation between deregulated genes and proteins with >50% confidence value within the mass spectrometry dataset (C) Correlation between deregulated genes and any protein detected within the mass spectrometry dataset

The Nanostring nCounter analysis annotates its genes with processes associated with each of the genes including plasticity, development and ageing (figure 6.2A), neurotransmission (figure 6.2B), neuron-glia interaction (figure 6.2C), neuroinflammation (figure 6.2D), structure and compartmentalization (figure 6.2E) and metabolism (figure 6.2F). Of the described processes, all showed extensive down-regulation of genes.

Figure 6.2 illustrates the directionality of the fold change but does not illustrate how the genes are affecting the listed process. Global significance score was used as a metric to understand how processes were affected; if a gene with inhibitory activity within a process exhibits decreased expression, that process is stimulated. The distinction is not captured by heatmaps. Figure 6.3A visualizes the shift in various processes from the control to the organoid whilst figure 6.3B exhibits their global significance score. All processes other than "Neuronal Cytoskeleton" showed a negative fold change for the organoid relative to the control (figure 6.3A). However, referring to figure 6.3B, carbohydrate metabolism also displays an overall increase in activity.

For each of the processes, replicates are displayed in figure 6.4. Interestingly, data from the organoids appears more homogenous than the controls for all of the tested processes.

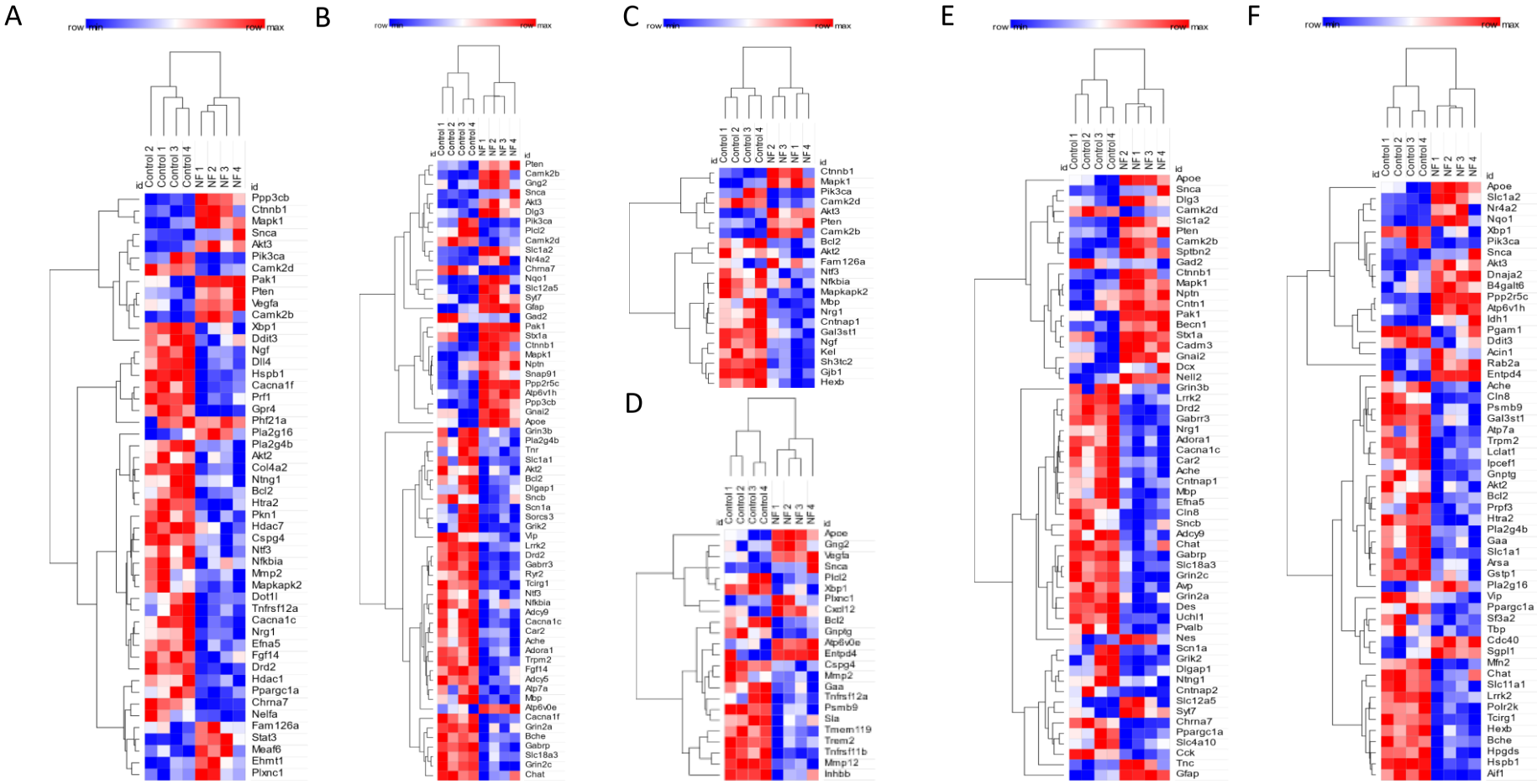


Figure 6.2: Gene themes, annotated by Nanostring and heatmaps representing fold change of significantly deregulated genes. Values are normalised across rows; blue indicates low expression relative to other samples, red indicates elevated expression relative to other samples. (A) Plasticity, Development and Aging (B) Neurotransmission (C) Neuron-glia interaction (D) Neuroinflammation (E) Structure and compartmentalisation (F) Metabolism

A

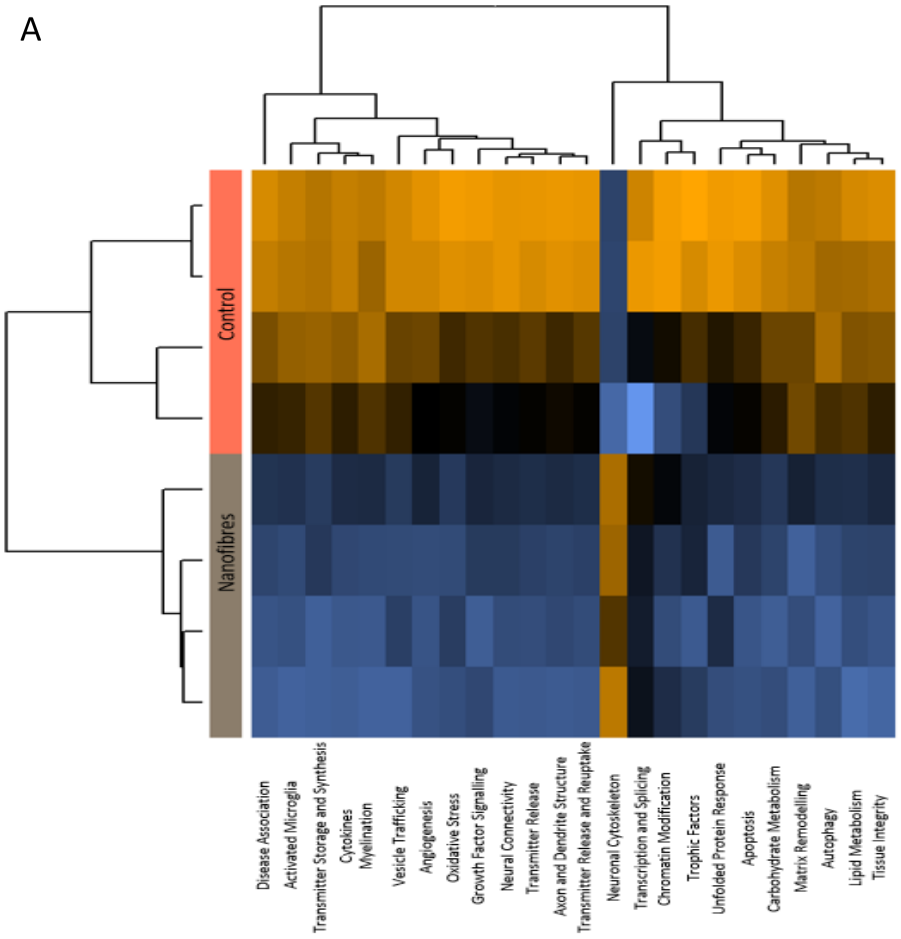


B

| Pathway Annotation | Global Significance Score |
|---|---|
| Activated Microglia | -2.096 |
| Angiogenesis | -2.157 |
| Apoptosis | -1.35 |
| Autophagy | -2.259 |
| Axon and Dendrite Structure | -0.858 |
| Carbohydrate Metabolism | 2.628 |
| Chromatin Modification | -1.46 |
| Cytokines | -1.38 |
| Disease Association | -1.726 |
| Growth Factor Signalling | -1.161 |
| Lipid Metabolism | -2.146 |
| Matrix Remodelling | -4.063 |
| Myelination | -2.34 |
| Neural Connectivity | -1.98 |
| Neuronal Cytoskeleton | 1.311 |
| Oxidative Stress | -1.984 |
| Tissue Integrity | -0.422 |
| Transcription and Splicing | -0.946 |
| Transmitter Release | -1.121 |
| Transmitter Response and Reuptake | -1.606 |
| Transmitter Synthesis and Storage | -1.753 |
| Trophic Factors | -1.287 |
| Unfolded Protein Response | -2.007 |
| Vesicle Trafficking | -1.136 |

Figure 6.3: Gene annotations, annotated by Nanostring. Values are normalised across rows; orange indicates increased expression relative to other samples, blue indicates decreased expression relative to other samples. (A) Heatmap visualisation of fold changes in various processes (B) Global significance scores for each of the processes

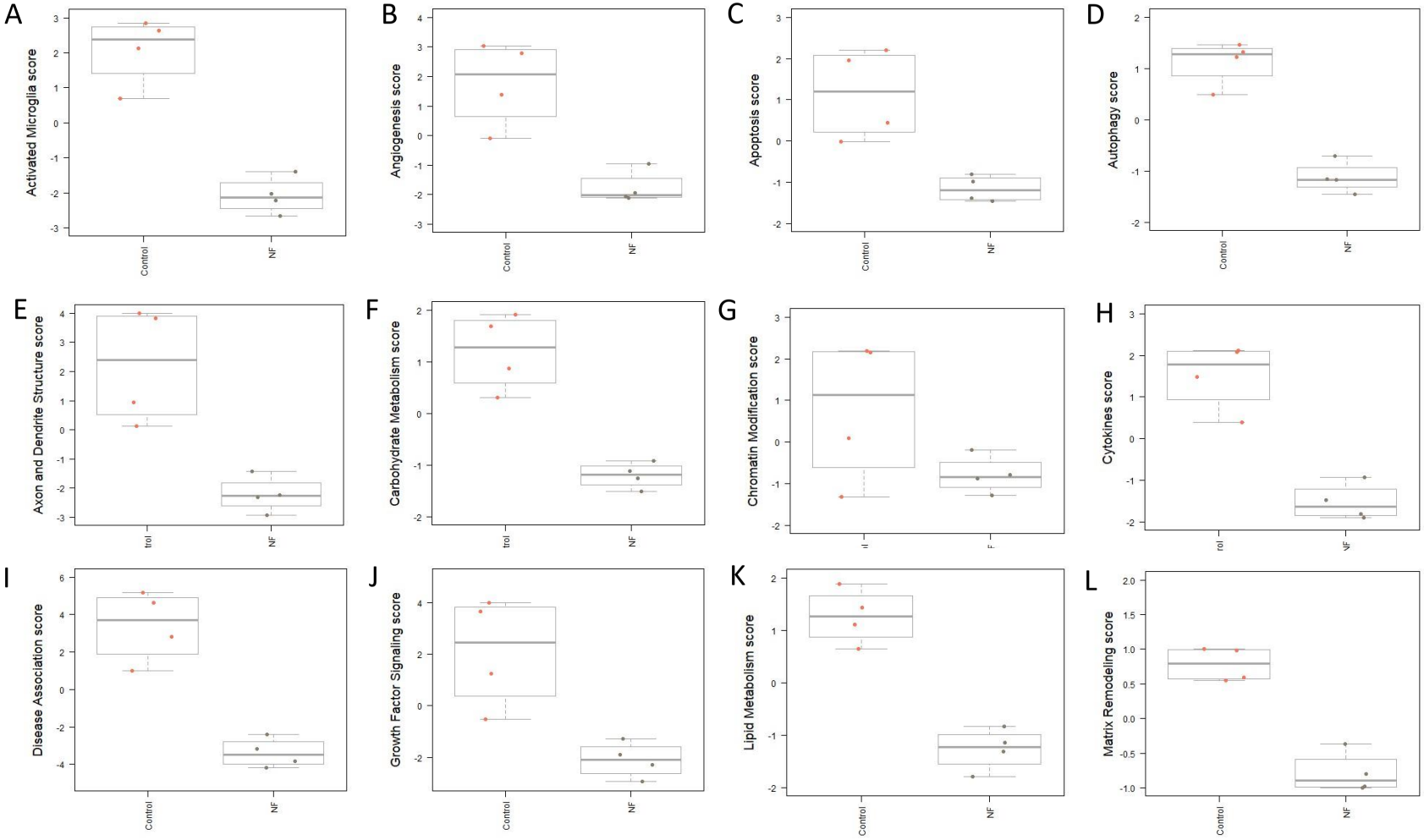


Figure 6.4: Individual gene annotations, annotated by Nanostring, visualised as box plots. (A) Activated Microglia (B) Angiogenesis (C) Apoptosis (D) Autophagy (E) Axon and Dendrite Structure (F) Carbohydrate Metabolism (G) Chromatin Modification (H) Cytokines (I) Disease Association (J) Growth Factor Signalling (K) Lipid Metabolism (L) Matrix Remodelling

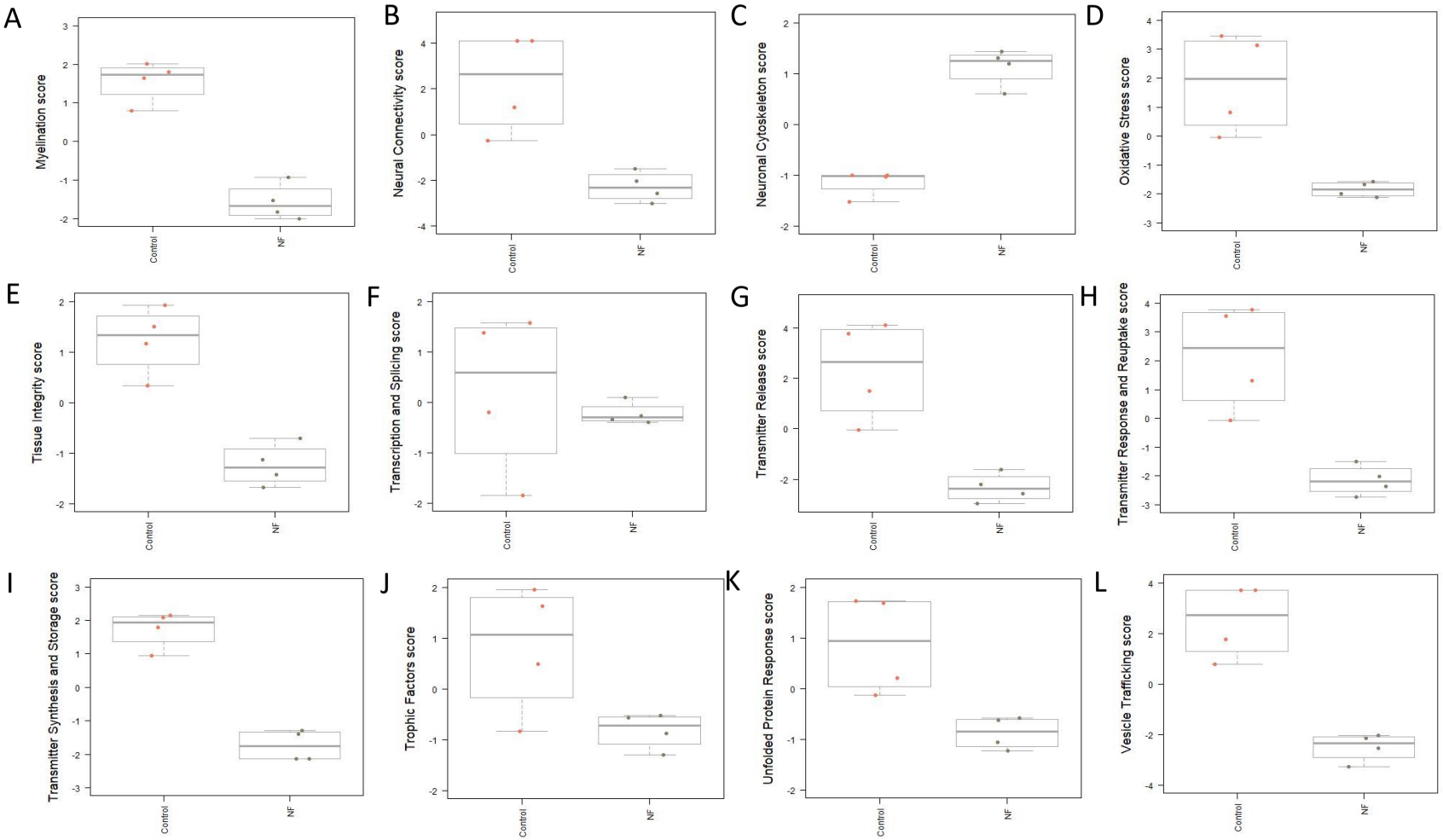


Figure 6.5: Individual gene annotations, annotated by Nanostring, visualised as box plots. (A) Myelination (B) Neural Connectivity (C) Neuronal Cytoskeleton (D) Oxidative Stress (E) Tissue Integrity (F) Transcription and Splicing (G) Transmitter Release (H) Transmitter Response and Reuptake (I) Transmitter Synthesis (J) Trophic Factors (K)

Significant alterations were observed for many of the neural cellular sub-populations. Whilst neurons did not exhibit a significant fold change (figure 6.6 and 6.7A; $t(6) = 1.09$, $p = 0.41872$), all other cell types did (Astrocytes, figure 6.7B; $t(6) = 2.578$, $p = 0.041872$. Oligodendrocytes, figure 6.7C; $t(6) = 7.314$, $p = 0.0003333$. Microglia, figure 6.7D; $t(6) = 7.718$, p = 0.000369. Endothelial cells, figure 6.7E; $t(6) = 5.893$, $p = 0.00106$).

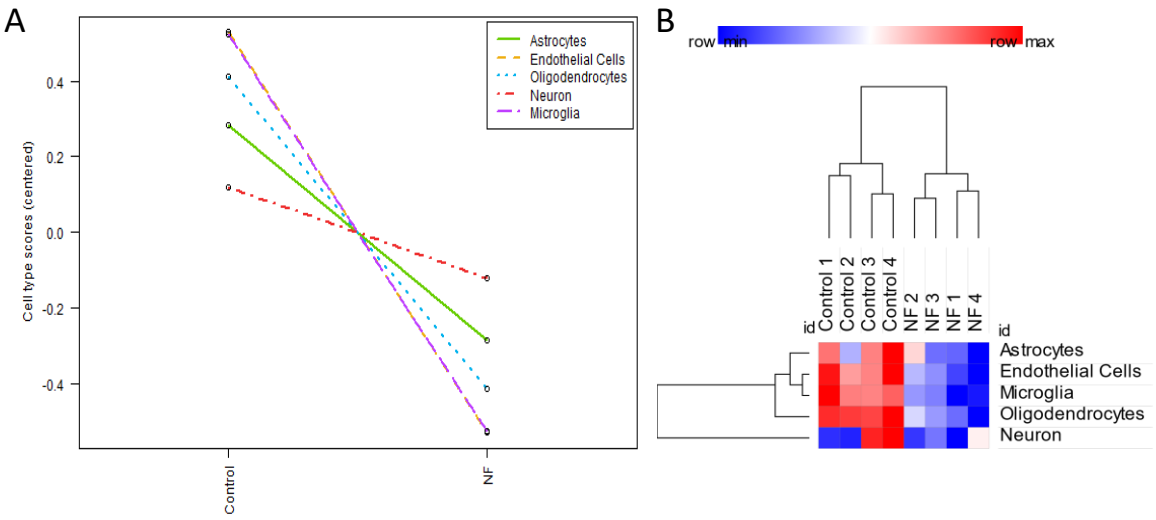


Figure 6.6: Molecular quantification of sub-population within the CNS. (A) Line graph representation of the fold changes of the cellular sub-populations (B) Heatmap visualisation for each of the replicates for each of the cellular sub-populations.

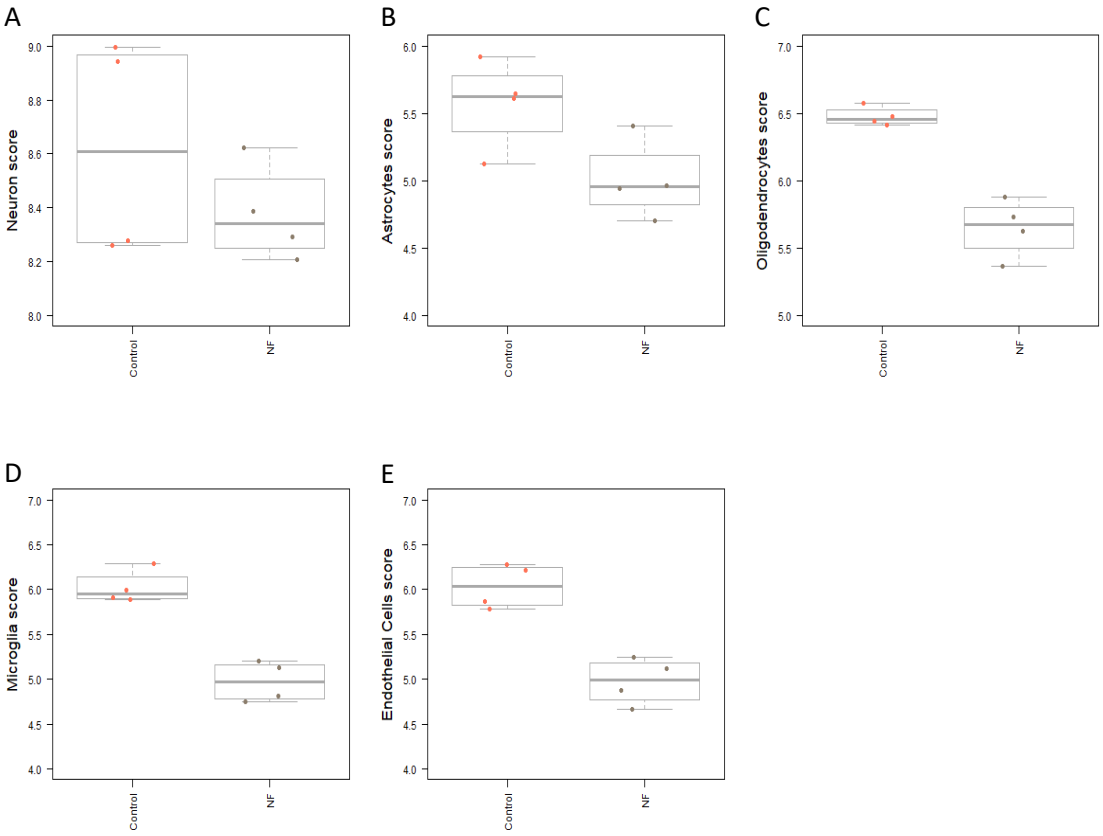


Figure 6.7: Box plots for each of the cell populations. Unpaired t-tests were used to test for significance (A) Neurons exhibited no significant difference between cell counts for the control and the aligned PLLA nanofibres ($t(6) = 1.09$, $p = 0.41872$) (B) A significant decrease in astrocytes was observed due to culture of the neuron on PLLA nanofibres ($t(6) = 2.578$, $p = 0.041872$) (C) A significant decrease in oligodendrocyte count was observed for cells cultured on aligned PLLA nanofibres ($t(6) = 7.314$, $p = 0.0003333$) (D) A significant decrease in microglia was observed due to culture of the neuron on PLLA nanofibres ($t(6) = 7.718$, $p = 0.000369$) (E) A significant decrease in endothelial cell count was observed due to culture of the neuron on PLLA nanofibres ($t(6) = 5.893$, $p = 0.00106$)

Network analysis was performed for the Nanostring data using the same method that was used for the mass spectrometry data. The interactome of the 50 strongest influencers were visualised using Cytoscape (figure 6.8A). Within this network Aif1, Des and Ipcef1 were identified as key signalling hubs due to the extent of their signalling to other genes. Within this network, significantly overrepresented gene ontologies were identified using the BiNGO plugin of Cytoscape (figure 6.8B). The majority of processes appear to play a role in electrochemical activity; via synapses or ionic homeostasis.

A

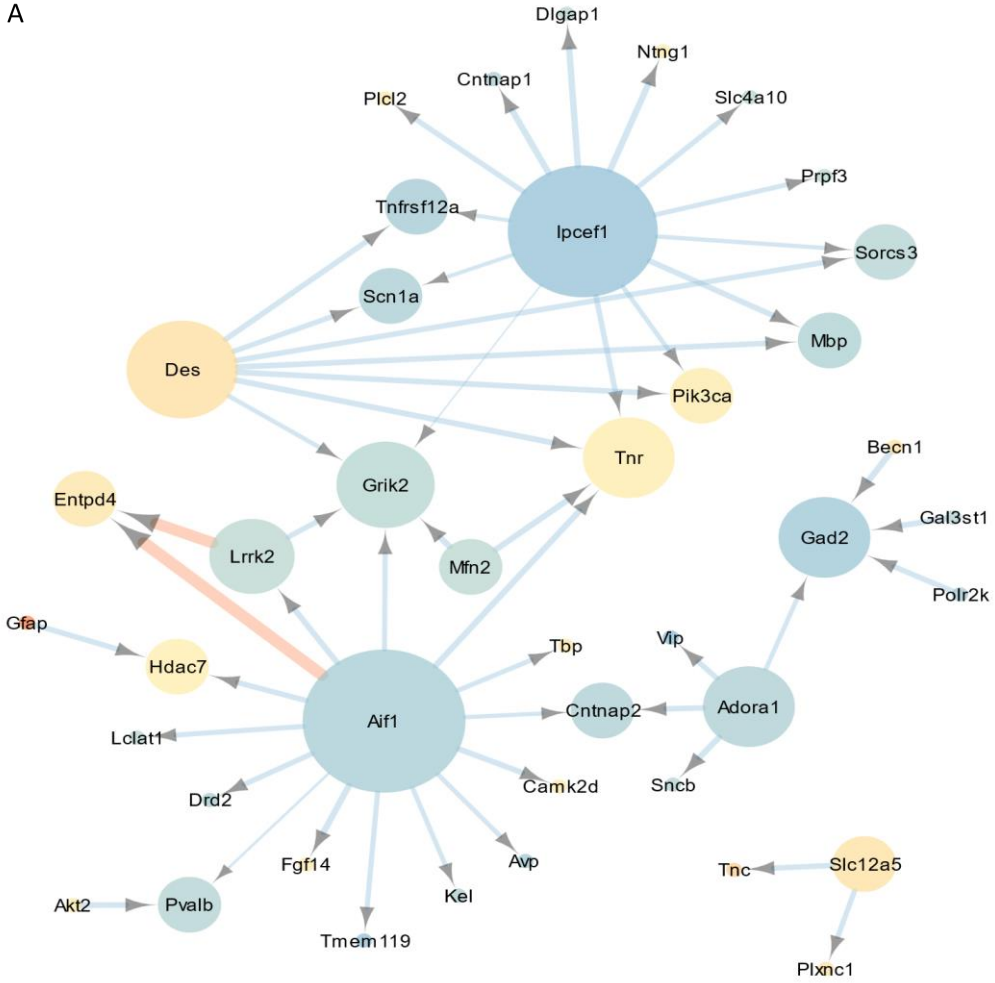


B

| Gene Ontology | Corrected *p* Values |
|---|---|
| Ion Homeostasis | 0.00002007 |
| Cell Communication | 0.00002007 |
| Cellular Ion Homeostasis | 0.00004706 |
| Transmission of Nerve Impulse | 0.00004706 |
| Cellular Chemical Homeostasis | 0.00004706 |
| Chemical Homeostasis | 0.00004706 |
| Negative Regulation of Glutamatergic Synaptic Transmission | 0.0001011 |
| Negative Regulation of Transmission of Nerve Impulse | 0.0001011 |
| Cellular Homeostasis | 0.0001359 |
| Negative Regulation of Neurological System Process | 0.0001359 |

Figure 6.8: Output of ANNI using the significantly deregulated genes identified by the Nanostring, visualised using Cytoscape (A) ANNI analysis of the most influenced and influential genes within the transcriptome. Node size is proportional to edge count, node colour is proportional to RNA expression fold change (blue = decreased, red = increase), arrow size is proportional to the strength of influence and the colour is proportional to the direction of influence (red = positive, blue = negative) (B) The 10 most significantly overrepresented

The nodes that were identified as signalling hubs (Aif1, Des and Ipcef1) were investigated to elucidate possible functions that they use to exert their influence (Table 6.1). Aif1, Des and Ipcef1 were identified as hubs that are involved in regulating neuroinflammation and oxidative stress.

| Key Node | Function/Localisation | Genes | Direction of Deregulation | Reference |
|---|---|---|---|---|
| Aif1 (Activated Microglia Marker) | Highly expressed in activated inflammatory microglia | Grik2, Lrrk2 | Decreased | Yamada et al, 2006; Russo, 2019; Thei et al, 2018 |
| | Expressed in specific subtypes of microglia | Tmem119, Fgf14 | Decreased and increased respectively | Satoh et al, 2017; Baalman et al, 2015 |
| | Potentiates inflammation | Avp | Decreased | Szmydynger-Chodobska et al, 2010 |
| | Neuroprotective via microglia modulation | Hdac7, Tnr, Camkiid | Increased | Genade and Lang, 2014; Kannan et al, 2013; Ye et al, 2019 |
| Des (Pericyte Marker) | Highly expressed in activated inflammatory microglia | Grik2, Scn1a | Decreased | Yamada et al, 2006; Russo, 2019 |
| | Induced by inflammation | Tnfrsf12a, Pik3ca, Tnr | Decreased, Increased, Increased | Gomez et al, 2016; Rustenhoven et al, 2017; Hedberg et al, 2019 |
| | Myelination | Mbp | Decreased | French et al, 2009 |
| Ipcef1 (Oxidative Stress Marker) | Highly expressed in activated inflammatory microglia | Grik2, Scn1a | Decreased | Yamada et al, 2006; Russo, 2019 |
| | Induced by inflammation | Tnfrsf12a, Pik3ca, Tnr | Decreased, Increased, Increased | Gomez et al, 2016; Rustenhoven et al, 2017; Hedberg et al, 2019 |
| | Myelination | Mbp | Decreased | French et al, 2009 |

Table 6.1: Summary of the sub-networks of important nodes identified in figure 6.8

## 6.4 Discussion

### 6.4.1 Correlation

Orthogonal validation was used to validate the Nanostring analysis; mRNA expression compared against protein. The correlation between mRNA and protein was notably poor although is comparable to values observed for postnatal neuronal development (Breen et al, 2018); weak correlation is typically observed for dynamic systems in development. A weak negative

correlation was observed for the 3 stringencies of correlation (figure 6.1) and no significance was observed between RNA expression and protein expression. Interestingly, the ANNI data from the previous chapter (Chapter 5, figure 5.12) demonstrated that all of the strongest influences within the detected proteome were negative influences, forecasting downregulation of proteins. The mRNA profiles of the organoid at a comparative time point are in agreement; the majority of mRNAs are downregulated and a negative correlation is observed although no significance was detected. Quantitative PCR or gene arrays would be required to validate the dataset.

## 6.4.2 Mechanism of formation of the organoid

Chapter 5 details the evidence for the hypothesised mechanism of formation of the organoid; close proximity induces synapse formation which drives development. In contrast to this, the Nanostring data exhibits a decrease in markers associated with plasticity and development (figure 6.2A), neural connectivity (figure 6.3B, 6.4N), axon and dendrite structure (figure 6.3B, 6.4E), neurotransmitter release (figure 6.3, 4S), synthesis and storage (figure 6.3B, 6.4U) and vesicle trafficking (figure 6.3B, 6.4X). Whilst the two datasets appear contradictory, the temporal dynamics of gene expression and the ANN data aid in elucidating the mechanism. Whilst the proteome represents the present behaviours of the cell, the transcriptome represents what the cell will do; the future of the cell. The poor correlation between the two is frequently observed for dynamic and developing systems (figure 6.1A-C) (Breen et al, 2018). The mass spectrometry data in Chapter 5 exhibits upregulation of the synaptic protein SNP-25 as a key regulator of the observed effects. In figure 5.9 of Chapter 5, the interactome exhibits mass negative influence on SNP-25; the interactome appears to be to pruning the synapses and reduce the total synaptic count. Within the Nanostring data, the mRNA displays an overall decrease in neural connectivity and synaptic behaviours (figure 6.2A, 6.5B, 6.5G, 6.5I, 6.5J, 6.5L),

validating the predictions of the ANNI. Similarly, within the mass spectrometry an up-regulation of RTN-4 was observed; a protein that plays a role in reducing axon branching and facilitating axon fasciculation (Uniprot). Within the Nanostring data, axon and dendrite structure were observed to decrease on the global significance scores (figure 6.3B), indicative of a reduction in growth and pruning of the axon. The expression of proteins detected by the mass spectrometer and interactions within the system predicted by the ANNI are observed to have a knock-on effect on to the transcribed mRNA that were detected by the Nanostring.

The overgrowth of synapses and axons and subsequent pruning of the neural circuitry is a developmental process. The reason for this is yet unknown but allows for activity-dependent refinement of circuitry; regression is key to correct functionality (Riccomagno and Kolodkin, 2015). Evidence overwhelming indicates that synaptic pruning is occurring within the organoids at the time that the mRNA was extracted from the organoid. Synaptic mRNAs and neural connectivity genes were unanimously downregulated (figure 6.2A, 6.5B, 6.5G, 6.5I, 6.5J, 6.5L). Pathway analysis demonstrates downregulation of genes associated with glutamatergic, cholinergic, dopaminergic synapses (Appendix; table 7). Furthermore, many of these pathways overlap with and regulate the PI3K pathway, which was also detected independently of its involvement with other pathways. PI3K was shown to be negatively regulated in addition to being downregulated (Appendix; table 7); reduction in PI3K/Akt signalling has been documented to play a crucial role in both synaptic pruning and axonal pruning (Riccomagno and Kolodkin, 2015). The processes of axonal and synaptic pruning are closely related, GSA analysis reveals a loss of “Axon and Dendrite Structure” (figure 6.3B). Proximity of neurites induces synapse formation (Peters et al, 1979; Braitenburg and Schüz, 1998). By reducing the axon and dendrite complexity and proximity, synaptic count is theoretically decreased.

Future work should aim to determine whether the synaptic pruning that is evident on the nanofibres is present in the control. Whilst it is possible that the nanofibres and the organoid recapitulate the developmental process of synaptic pruning, only one time point has been studied thus far. It is also possible that the neurons of the control underwent pruning earlier or later than the neurons of the organoid. Whilst the increase in synaptic protein expression, developed profile and greater proximity of the organoid suggests that they have generated more synapses and are thus more likely to undergo regressive synaptic pruning, it currently remains an unknown.

### 6.4.3 Cellular sub-populations

In Chapter 1, the various sub-cellular populations of the CNS were discussed. In brief, whilst neurons comprise the computational component of the CNS that leads to the overall functionality, oligodendrocytes and astrocytes are crucial supporting cells, providing metabolic and trophic support (Kandel, 2000). Endothelial cells also represent a key cellular sub-population within the CNS that were not discussed previously, comprising the blood brain barrier, regulating the entry of immune cells, metabolites, drugs and ions in to the CNS (Johnson et al, 2018). Microglia resident macrophages within the CNS, and play a role in eliminating microbes, protein aggregates and synapses within the healthy and diseased brain (Colonna and Butovsky, 2017). Previous studies have demonstrated that the greater the similarity between exogenous and endogenous cells, the greater the degree of integration, thus by more closely mimicking the cellular populations, it is hypothesized that a greater degree of synaptic integration should be observed between endogenous circuitry and exogenous neurons.

The Nanostring nCounter assay uses the abundance of several cell-specific genes to quantify the abundance of the cells themselves. By culturing dissociated cortex on the aligned PLLA

nanofibres, all cell populations were decreased in abundance (figure 6.6A) although this was not significant for neurons (figure 6.7A). Interestingly, this suggests that the significant increase in LDH that was observed previously (Chapter 4, figure 4.4) may be derived from the loss of non-neuronal populations although further research is required as the nanofibres may have limited the proliferation rate of non-neuronal cells rather than increasing the cell death. Astrocytes, oligodendrocytes, microglia and endothelial cells were all significantly decreased (figure 6.7B-E). Whilst the mass spectrometry described in the previous chapter demonstrated an increase in developmental profile of neurons cultured on the nanofibres, the decrease in cellular heterogeneity of the culture may be a significant hindrance for the development of the implant. Use of astrocyte/oligodendrocyte/microglia/endothelial cell conditioned medium or a microfluidic system containing other cellular populations may be able to generate even more advanced physiological models for use as a high throughput *in vitro* model of the cerebral cortex.

For an implant, the homogeneity of the neuronal culture is a double-edged sword. Astrocytes have demonstrated beneficial properties for exogenous and endogenous neurons upon implantation. One study found that co-culturing neurons with astrocytes prior to implantation aided in their differentiation and engraftment upon implantation (Roy et al, 2006). However, within a month of implantation, de-differentiation was observed, suggesting that exposure to soluble factors within the media *in vitro* were insufficient to maintain differentiation *in vivo* (Roy et al, 2006). In contrast, direct implantation of astrocytes in to a host with the endogenous neurons enhanced long term potentiation and propagated Ca2+ signals 3-fold faster than the control group (Han et al, 2013). A live cell population of astrocytes with positive feedback loops aids in the maintenance of some of the high level functions of the differentiated neurons but in the absence of these cell types, soluble factors appear to be able to partially replicate their effects. Wang et al (2016) provide a potential solution to the limited number of astrocytes

present on the nanofibres; the group attached glial derived neurotrophic factor (GDNF) to the surface of the nanofibres and observed increased engraftment of the attached neurons. Similarly, Low et al (2015) encapsulated retinoic acid and BDNF in to their nanofibres and attained sustained release of their molecules for up to 14 days. By doping GDNF or other neurotrophic factors in to the nanofibres, degradation of the fibres would lead to the release of the soluble factors that could serve to replace the missing astrocytes from the culture, potentially enhancing engraftment, differentiation and growth that has been limited by the homogenous culture.

Oligodendrocyte count was observed to decrease (figure 6.6 and 6.7C) whilst genes associated with remyelination were also significantly reduced (figure 6.3B). White matter dysfunction is associated with numerous pathologies, affecting the temporal dynamics of neural networks (Nasrabady et al, 2018; Foong et al, 2000; Hattori et al, 2011), thus, due to their role in myelination and establishing neural dynamics through salutatory conduction, oligodendrocytes are a desirable feature of a cellular implant. Previous studies have shown oligodendrocytes aid in remyelination and functional repair (Faulkner and Keirstead, 2005), a desirable property for re-wiring studies. However, myelin is inherently inhibitory to neurite outgrowth and restricts neuronal plasticity (Silver et al, 2019). Thus, whilst remyelination is desirable, ideally, the process should occur after neurite growth and synaptic integration to prevent inhibition of the two processes. Within the cellular implant, low levels of oligodendrocytes during the initial implantation would be desirable with the potential second cellular delivery or stimulation of endogenous myelination to facilitate successful physiological re-wiring. Thus the decrease in oligodendrocyte count on the implant prior to implantation may be a desirable quality. The proposed mechanism for the loss of oligodendrocytes is discussed later in this chapter.

Microglia are effectors of both neurodegeneration and neuroprotection within the CNS during injury and regenerative processes. These distinctions appear to be due to distinct subclasses of microglia that are involved in early (M2 microglia) and late stages (M1 microglia); M1 microglia release inflammatory cytokines that can inhibit regeneration whilst M2 microglia secrete trophic factors and phagocytose toxic debris (Jin and Yamashita, 2016). Whilst activated microglia have been observed to decrease (figure 6.3B), no information on the subclass of microglia is available and based on cell count data alone, little can be inferred from this data about benefits or detriment to the implant. Further research is required however, as nanofibres have demonstrated the ability to polarise microglia to the anti-inflammatory phenotype (Pires et al, 2014) and the ANNI data suggests that the microglia represent a crucial effector in the observed changes to the organoid relative to the control (figure 6.8; Aif1).

The observed decrease in endothelial cells is intriguing. Endothelial cell proliferation and differentiation is dependent on VEGF signaling (Mackenzie and Ruhrberg, 2012); an increase in VEGF should induce an increase in endothelial cell count, mass spectrometry showed an increase in VEGF (Chapter 5, figure 5.13). The absence of this increase in cell count is suggestive of cellular selection by the material itself; hydrophobic surfaces have previously been documented to inhibit endothelial growth (Ruardy et al, 1997). Upon implantation, rapid vascularization is desirable to limit hypoxia, ROS and ultimately, cell death (Sortwell et al, 2000). The global decrease in angiogenic markers (figure 6.3B) in addition to the decreased cellular profile of endothelial cells is a limitation to the implant although it should be noted that endothelial cells are rarely considered upon implantation of cells in to the CNS.

## 6.4.4 Network inference

Within the interactome generated by ANNI and Cytoscape, 3 nodes are evident as crucial influencers; Aif1, Ipcef1 and Des. These 3 influencers are markers for microglia, ROS and pericytes respectively (Postler et al, 2000; Basu et al, 2012; Stapor et al, 2014).

Aif1 is a marker for activated microglia and is downregulated, exerting negative influence on almost all genes that are connected with it. This hub appears to be associated with anti-inflammatory effects, synaptic pruning and neuroprotection. Grik2 and Lrrk2 are both highly expressed by microglia (Yamada et al, 2006; Russo, 2019); the negative influence that Aif1 has on these two markers is likely just due to the loss of total microglia that is observed in figure 6.6 and 6.7D. Similarly, Tmem119 and Fgf14 are markers for specific sub-types of microglia; macrophage derived microglia (Satoh et al, 2017) and satellite microglia respectively (Baalman et al, 2015). Whilst the loss of total microglia likely explains the negative influence that microglial marker Aif1 has on Tmem119, Fgf14 shows increased expression while strong negative influence is exerted on it (figure 6.8). Satellite microglia reside at the axon-initial segment of neurons and are theorised to play a role in synaptic pruning (Baalman et al, 2015), suggesting a possible increase in synaptic pruning. However, microglia are vital to the synaptic pruning of inhibitory synapses on Pvalb expressing GABAergic neurons (Chen et al, 2014; Nakayama et al, 2018); loss of microglia (figure 6.6 and 6.7D) does exert a negative influence on Pvalb in figure 6.8, suggesting a loss of inhibitory synaptic pruning. Microglia-dependent synaptic pruning is poorly characterised currently but Baalman et al (2015) suggest that microglia are heterogenous and many sub-populations may exist. The data appear to suggest that microglia are mediating pruning in different compartments for different sub-populations of neurons although extensive further characterisation is needed. Avp potentiates inflammatory markers (Szmydynger-Chodobska et al, 2010); loss of activated microglia, as indicated by figures 6.3B and 6.4A, supports the negative influence that is exerted on Avp. Hdac7, Tnr and CamkiiD are all genes

that are expressed in response to inflammation; decreased activated microglia is indicative of decreased inflammation should exert negative influence on them, which is observed from Aif1 (figure 6.7). However, their overall expression is still increased despite the negative influence, suggesting other influencers on their expression. Interestingly, 2 of the genes are neuroprotective via modulation of microglia activity (Tnr and HDAC7) (Genade and Lang, 2014; Kannan et al, 2013) whilst the literature only suggests that the third gene (Camkiid) is neuroprotective with little characterisation for the mechanism (Ye et al, 2019). Whilst a mechanism has not been determined experimentally, Camkiid has been observed to modulate expression of NF-κB (Shih et al, 2015) which is a known activator of microglia (Popiolek-Barczyk and Mika, 2016); the ANNI may have predicted a possible mechanism for Camkiid neuroprotection that has not yet been tested experimentally.

Des is a marker of pericytes; pericytes control blood flow and are vital in the vascularization process (Stapor et al, 2014). Des is a secondary hub associated with anti-inflammatory effects. Under pathological conditions, pericytes can differentiate towards an inflammatory microglial fate (Sakuma et al, 2016). Increased expression of Des results in negative influence on Grik2 and Scn1a, which are both highly expressed in activated microglia (Yamada et al, 2006; Thei et al, 2018), limiting inflammation. Additionally, Tnfrsf12a (a TNF receptor), PI3K and Tnr expression are all induced by inflammation (Gomez et al, 2016; Rustenhoven et al, 2017; Hedberg et al, 2019); increased Des exerts negative influence on these 3 nodes, further supporting the role of pericytes in the organoid as an anti-inflammatory cell.

Des also negatively influences Mbp (myelin basic protein) (figure 6.7). Physiologically, pericytes are capable of inducing differentiation of stem cells to an oligodendrocytic fate and supporting re-myelination of damaged white matter (Nowicki et al, 2018). This result is contradictory from

a physiological perspective. However, this is theorised to be due to the surface selecting for pericytes, at the cost of oligodendrocytes. Previously discussed is the property of PLLA to degrade to lactic acid which is then buffered to lactate. Lactate is capable of stimulating HIF-1α (Hée et al, 2015) which is capable of induces proliferation of pericytes (Geranmayeh et al, 2019). In contrast, lactic acid can also induce ROS (Riemann et al, 2011) which oligodendrocytes are particularly vulnerable to during maturation (French et al, 2009), thus PLLA can cause increased pericyte number and decreased oligodendrocytes.

The third and final key node within the triad is Ipcef1; a marker that is upregulated during oxidative stress. The network of Ipcef1 overlaps with that of Des by a great degree which is unsurprising, given the physiological role of pericytes in reducing hypoxia/oxidative stress (Stapor et al, 2014). Similar to Des, Ipcef targets inflammatory markers, exerting a negative influence on them (Grik2, Scn1a, Tnr, Tnfrsf12a, Scn1a, Pik3ca). Thus, this node is another anti-inflammatory node, however, the Ipcef1 node predominantly focuses on inflammation relating to ROS. Other effects of the influential Ipcef1 node include regulation of neuron morphology and connectivity. Ipcef1 negatively influences Dlgap1, a synaptic scaffold protein (Uniprot). Oxidative stress is known to induce an increase in synaptic count (Oswald et al, 2018), thus loss of oxidative stress should negatively affect synapses, supporting the theory that the organoids are undergoing synaptic pruning. Neuronal morphology is also influenced by Ipcef1; Ntng1 is negatively influenced by Ipcef1 and plays a role in neurite extension and axon guidance (Yaguchi et al, 2014). Ntng1 receives strong negative influence from Ipcef1 but still remains overexpressed, this may be due to the influence of nanofibre topography on axon guidance and extension (Yang et al, 2005).

Table 6.1 summarises the array of influences exerted by the 3 most influential genes. Figure 6.8 shows the genes that are most influential in the generation of the organoids. The three crucial nodes appear to indicate a global shift towards and anti-inflammatory, anti-oxidant phenotype within the organoid.

### 6.4.5 Processes relating to implantation

Implantation remains the final goal for primary cortical neurons grown on the nanofibres. The Nanostring characterized various cellular processes that will aid or inhibit the survival of cells upon implantation. Upon implantation, the majority of cells die through loss of ECM and subsequent anoikis, withdrawal of trophic factors, hypoxia and ROS generation (Sortwell et al, 2000). Plasticity is the most relevant aspect of the Nanostring quantification; in the absence of plasticity and synaptic integration of exogenous neurons in to endogenous neuronal circuitry, rewiring will not occur, although bystander effects (described in Chapter 1) may still benefit the host. Plasticity appears to decrease for neurons within the organoid (figure 6.2A), however, a reduction in oxidative stress is associated with reduced synapse formation (Kiffin et al, 2006). Mass spectrometry reveals extensive upregulation of anti-oxidant proteins (Appendix, table 6) whilst the Nanostring shows a decrease in oxidative stress (figure 6.3B; figure 6.5D), indicative of reduced synapse formation. Whilst the *in vitro* data suggests a loss of plasticity due to a loss of oxidative stress, this may be reverted *in vivo* as the implanted cells will be under extensive oxidative stress (Sortwell et al, 2000). Additionally, the up-regulation of antioxidant defences in conjunction with the decreased expression of markers of neuroinflammation (figure 6.2D) may aid the survival of neurons upon implantation.

However, decreased expression of markers associated with angiogenesis (figure 6.4B), cytokines (figure 6.4H) and growth factors (figure 6.4J) are potential detriments to the survival and

integration of implanted neurons. After oxidative stress, Sortwell et al (2000) describe withdrawal of cytokines and growth factors as the second greatest detriment to the survival of endogenous neurons. In contrast, whilst promotion of angiogenesis by the implanted neurons would be ideal in order to limit hypoxia upon implantation, the suggested increase in pericyte number (the increase in Des expression, figure 6.8) may yield benefits due to their role as anti-inflammatory mediators in addition to their involvement in vascularization and stabilization of the vascular structures (Stapor et al, 2014). Further quantification is required however, as the presence of pericytes is supported by the expression of Des, which whilst it is a pericyte marker (Stapor et al, 2014), is only a single indicator. Further validation is needed.

### 6.4.6 Summary

In the previous chapter, ANNI was used to hypothesise a mechanism by which the organoid develops a more developed profile relative to the 2D control. Within this chapter, RNA was quantified rather than proteins, shedding light on the processes that the cells are attempting to undertake. Synaptic pruning appears to be in progress, as demonstrated by the loss of plasticity (figure 6.2A), decrease in connectivity and synaptic marker expression (figure 6.2B, 6.5B, 6.5G, 6.5I, 6.5J, 6.5L), decrease in oxidative stress (figure 6.3B) and increased expression of synaptic pruning markers such as caspase 3 and PI3K (Appendix; table 7). This is yet another developmental process that is poorly understood and lacks a model that is capable of representing it well. The breadth of the characterization afforded by the Nanostring has identified this yet further work and validation of the model is needed to confirm that synaptic pruning occurs at this time point. A time course of immunohistochemistry, western blotting or mass spec would be ideal; any of the three techniques performed at multiple time points would confirm the downregulation of synaptic markers that begins at 11 DIV would be confirmation of synaptic pruning.

The work presented within this chapter illustrates the importance of oxidative stress in plasticity and due to the extensive oxidative stress that the organoid will be under during implantation, this may serve to benefit the synaptic integration of the implant by increasing the plasticity of the organoid. Whilst the organoid appears to have shifted towards decreased angiogenesis relative to the control, neuroinflammation and oxidative stress have both decreased which will aid the survival of neurons upon implantation.

# Chapter 7: Optimisation of Transfection of Primary Cortical Neurons

## 7.1 Introduction

Thus far, experiments detail a method of generating a structure that is capable of re-wiring the cortex and the characterisation of the cellular structure. Upon implantation, a method of quantifying the ability of the implant to perform *in vivo* is needed. Implantation of neurons in to the CNS is rarely accompanied by integration of the exogenous cells into existing circuitry; the key feature of re-wiring the cortex. Whilst electrophysiological measurements are the gold standard for determining the degree of innervation of endogenous neural circuitry by exogenous cells, methods such as morphological analysis of implanted neurons, reversal of behavioural deficits caused by ablation and quantification of graft volume/density have all been employed (Wang et al, 2016; Tornero et al, 2013; Falkner et al, 2016). However, all of these methods have their own limitations. Morphological analysis of implanted cells requires the use of cells from different species of animals to allow for immunofluorescent differentiation between host and exogenous neurons, necessitating use of immunocompromised animals or immunosuppressants to prevent rejection (Brevig et al, 2000) which may influence the behaviours of implanted cells. Additionally, whilst morphological analysis typically includes staining for synaptic markers to indicate integration into circuitry, it does not confirm mature electrophysiological behaviours. Similar to morphological analysis, quantification of graft volume/density requires immunocompromised or immunosuppressed animals and cannot confirm mature electrophysiological behaviours. Reversal of behavioural deficits is the ultimate goal of the ability to re-wire neural circuitry within the CNS, however, the precise mechanism that facilitates the reversal of behavioural deficits is not established by using this as a means of quantifying integration of neurons into existing circuitry. Implanted cells are capable of secreting factors that can promote

endogenous neurogenesis, modulate the immune system and provide trophic support, aiding in the behavioural recovery in the absence of synaptic re-wiring (Ma et al, 2015), thus the method can be used but requires validation and characterisation of the mechanism.

To counter the limitations present in other methods, optogenetic control was opted for as the method of quantifying integration in to endogenous circuitry. A secondary method such as morphological analysis will be employed as a validation method, post-*in vivo* experiment. Optogenetics is a tool utilised to exert control over cellular activity using light to activate a transfected protein (Guru et al, 2015). The choice of protein that is transfected determines the cellular activity that is affected (depolarisation, hyperpolarisation or even modulation of biochemical signalling (Tischer and Weiner, 2015)) whilst the method of transfection determines the degree of expression and the sub-populations that are transfected (Guru et al, 2015). The dependence on light allows for a high degree of temporal resolution whilst spatial resolution can be controlled by focus of the application of light and the location of the transfected cells. *In vitro*, spatial control is very high as individual dendritic spines can be targeted by laser (Packer et al, 2012) and their activity modulated but *in vivo*, limitations are more evident. Transfection of neurons *in vivo* is typically performed by administration of viral particles in to the desired region and diffusion of the viral particles decreases the accuracy of the transfection (Serruya et al, 2017).

The goal of the implant is to create a non-physiological axonal path between two points that were not connected previously; such as visual and auditory cortex. In this example, any activation of the auditory cortex as a response to visual stimulus must have been transmitted via the implant due to the presence of the non-physiological neuronal path. However, the

property of nanofibres to induce alignment and neurite outgrowth may facilitate endogenous neuronal outgrowth along the nanofibres and thus, detection of visually-stimulated action potentials in auditory cortex may not be due to integration of exogenous neurons but instead, due to regrowth of endogenous neurons. By introducing a selective method of depolarising the exogenous neurons, integration of exogenous neurons can be confirmed. Detection of visually stimulated action potentials within the auditory cortex, in addition to the detection of light-evoked action potentials in the auditory cortex, indicates successful re-wiring of the cortex via the exogenous neurons. If a significant difference is detected between the visual stimulus-evoked response and the optogenetically-induced response, endogenous regrowth and subsequent integration has also occurred. Whilst the ability to generate a pathway that facilitates endogenous regrowth would bode well for brain repair, it is not the aim.

An adeno associated virus (AAV) was chosen as the vector for the optogenetic transgenes. AAVs are replication incompetent in the absence of co-infection with other viruses (typically AAVs) and do not integrate into the genome, instead persisting as episomes within the nucleus, limiting the oncogenic potential of the virus (Naso et al, 2017).These two factors that make them ideal for gene therapy and *in vivo* uses. Relative to non-viral methods of transfection such as electroporation or lipofection, AAVs have low toxicity, high efficiency and can induce stable, long term transfection (Royo et al, 2008). Compared to other viral methods, AAV benefits from lower potential for oncogenesis. Lentiviral transfection has a comparable efficiency to AAV but due to the possibility of lentiviral integration in to the genome, it is associated with a non-zero chance of oncogenic transformation (though tumours do not typically occur without transfecting a transgene that targets tumour suppressor pathways) (White et al, 2017).

Upon delivery in to the cell, transgene expression is controlled by two key factors; AAV serotype and choice of the promoter. Multiple serotypes of AAV have been confirmed for AAVs each with a range of tissue tropisms and kinetics of expression (Zincarelli et al, 2008). Serotype AAV2 was selected to transfect the primary rodent cortical neurons. AAV2 has demonstrated minimal cytotoxicity in rodent cortical neurons (Howard et al, 2008) and additionally, at least one study has demonstrated that AAV2 can induce cell death in the absence of transduction with the transgene (Duverger et al, 2002); a factor that has the potential to select only the positively transfected cells. Promoter choice limits the ability of the AAV to depolarise non-neuronal cells. hSyn is a highly specific neuronal promoter that allows long term expression of the transgene in the adult rodent brain (Gompf et al, 2015; Jgamadze et al, 2012) and cultured embryonic neurons (Kügler et al, 2003). *In vivo* use of hSyn as a promoter in the cortex has demonstrated a preference towards transfection of inhibitory neurons rather than excitatory neurons at low viral titers (Nathanson et al, 2009) although the multiplicity of infection (MOI) is difficult to quantify *in vivo* due to the diffuse nature of the transduction. In addition, low numbers of total transduced cells were present in the low titre conditions; high percentage of transfected cells indicates that both inhibitory and excitatory neurons had been transfected. At higher MOI, exposure of primary neurons to AAV2 with the hSyn promoter resulted in transfection which was representative of the neuronal sup-populations of the cortex; 80% of transfected neurons were excitatory whilst 20% were inhibitory neurons (Nathanson et al, 2009).

The transgene of choice to induce light-sensitivity in the primary cortical neurons is channelrhodopsin-2 (Chr2). Chr2 is a light-gated cation-selective ion channel naturally found

in *Chlamydomonas reinhardtii* that depolarise in response to 450nm light (Nagel et al, 2003). H134R is a gain of function mutation that produces larger photocurrents but slows down the kinetics of the channel. Chr2 has been used to optogenetically depolarise rodent cortical neurons *in vivo* (Fan et al, 2015; Kwon et al, 2015); use of Chr2 in conjunction with electrodes implanted downstream of the implant should allow the separation of the effects of endogenous re-growth and integration of exogenous neurons as discussed previously. Chr2 has also demonstrated excellent biocompatibility; primate studies transfecting Chr2 have observed widespread expression of Chr2 with no histological abnormalities in neurons or glia and no cellular or antibody based immune reactions over several months (Han et al, 2009).

## 7.2 Methods

### 7.2.1 Co-localisation of the transfected fluorescent marker and DAPI within primary cortical neurons

Primary cortical neurons were dissociated and cultured on PLL and laminin coated tissue culture plastic or uncoated PLLA nanofibres using protocols described previously (Chapter 2; section 2.2.2, 2.2.3, 2.2.6). Cells were plated at a density of 25,000 cells/cm$^2$. For each material, cells were transfected with AAV-hSyn-hChr2(H134R)-mCherry at a range of multiplicity of infections (MOI) to determine the ideal concentration of viral particles. The MOI selected were $10^1$, $10^2$,$10^3$, $10^4$ whilst the control received only a media change with a volume equivalent to the volume used to deliver the viral particles. Cells were exposed to AAV overnight prior to a media change to virus-free media. Transfections were performed on 1 or 7 days in vitro (DIV). After 11 DIV, cells were fixed using 4% PFA for 20 minutes and nuclear stained with DAPI prior to fluorescent visualisation to determine the percentage of the cellular population that had been successfully transfected by the AAV. Cells were manually counted and were considered

to be successfully transfected if DAPI and mCherry co-localised. Results were validated with the Leica co-localisation software.

3-factor ANOVA was used to determine the influence of MOI, the day of transfection and the substrate the cells are transfected upon on the efficiency of the transfection.

### 7.2.2 Intracellular localisation of the channelrhodopsin-2 protein

Primary cortical neurons were dissociated and cultured on poly-L-lysine and laminin coated plates as described previously (Chapter 2, section 2.2.2, 2.2.3, 2.2.4). Cells were plated at a density of 25,000 cells/cm$^2$ and transfected at an MOI of $10^2$. After 11 DIV, cells were fixed in 4% PFA for 20 minutes and permeabilised with 0.1% Triton X-100 for 20 minutes. Cells were incubated in blocking buffer (3% BSA) for 1 hour at room temperature prior to incubation in primary antibody (anti-Chr2; 1:50 dilution in 3% BSA) overnight at 4°C. Cells were then incubated in secondary antibody (FITC-labelled anti-mouse IgG, 1:50) at room temperature for 2 hours before nuclear staining with DAPI and subsequent visualisation. Three five minute washes of PBS were applied between each incubation period.

### 7.2.3 Confirming functional expression of Chr2 in AAV-hSyn-hChr2(H134R)-mCherry transfected primary cortical neurons

Primary cortical neurons were dissociated and cultured on uncoated PLLA nanofibres using protocols described previously (Chapter 2, section 2.2.2, 2.2.3, 2.2.4). Briefly, cells were plated at a density of 25,000 cells/cm$^2$. 24 hours after seeding, cells were transfected with AAV-hSyn-hChr2(H134R)-mCherry at an MOI of 0, $10^1$, $10^2$,$10^3$, $10^4$. Cells were maintained at 37$^o$C in a humidified incubator at 5% $CO_2$ for 10 days. At 10 DIV cells were loaded with Fura red-AM. Fura red-AM was added to the media to a final concentration of 5µM and incubated for 30 minutes at 37$^o$C. Cells were then washed with PBS prior to the addition of Kreb's solution that the recordings were performed in. Recordings were performed on a BMG LABTECH Clariostar microplate reader. Measurements were taken every 0.21 seconds for 90 seconds. Baseline was

defined as the average of the first 5 values of the recording, baseline was removed by dividing each value by the baseline. Results were then expressed as a percentage of the control. Inter-$Ca^{2+}$ influx intervals and average change in amplitude of oscillations were quantified using a custom MATLAB script.

## 7.2.4 Confirming the presence of nanoparticulates and quantification of nanoparticle size

Untreated PLLA nanofibres and laser cut polyester sheets were incubated for 24 or 72 hours in 500µL PBS at pH 7.4 in 24 well plates whilst the negative control was incubation of PBS alone. The supernatant was removed from the nanofibres and was subsequently loaded into a Zetaview Nanoparticle Tracking Analyzer. Nanoparticle sizes were tested for significance using an unpaired t-test.

Nanoparticles were also visualised using the JSM-7100F SEM to visualise them. 5µL of supernatant was placed onto a carbon tape-coated SEM stub which was then sputter coated in a vacuum to remove the supernatant and coat the nanoparticles in 5nm of gold.

## 7.2.5 Alterations to pH due to nanofibre degradation

Untreated PLLA nanofibres were incubated for 0, 1, 3, 5, 7 or 14 days in 500µL PBS at pH 7.4 in 24 well plates whilst the negative control was incubation of PBS alone. No pH change was observed for the PBS alone. The supernatant was removed from the nanofibres at each time point and the pH was tested using a pH meter.

## 7.2.6 Morphological changes induced by transfection of primary cortical neurons with AAV-hSyn-hChr2(H134R)-mCherry

Primary cerebral cortical neurons were isolated as described in Chapter 2, section 2.2.2 and seeded to poly-L-lysine and laminin (5µg/ml) coated tissue culture plastic at a cell density of

25,000 cells/cm$^2$ in NbActiv1 medium and maintained at 37$^o$C in a humidified incubator. 24 hours after seeding, cells were transfected with AAV-hSyn-hChr2(H134R)-mCherry at an MOI of $10^2$. Control cells and transfected cells were placed in the Incucyte S3 Live-Cell analysis system for 5 days. During these 5 days, neurite length, branch points, neurite bundle diameter and cell cluster diameter were measured. Images were taken every hour with 4 replicates and 9 fields of vision per replicate. The neurite length, branch points and clustering behaviour of every cell within the field of vision were quantified by the Incucyte. Neurite bundle diameters were measured using ImageJ. Every 3 hours, the diameters of 10 neurite bundles were measured for 3 fields of vision as a single replicate; 3 replicates were used per time point. The alignment of neurites was quantified using the Directionality plugin of ImageJ. Every three hours, dispersion of neurites was measured for 3 fields of view as a single replicate; 3 replicates were used. Rate of neurite growth, rate of branching and cell clustering behaviours were then calculated from the data generated by the Incucyte and a t-test was used to check for significant differences between the control and transfected neuron cellular behaviours.

### 7.2.7 mCherry as a method of tracking cell survival of cells *in vivo*

Primary cortical neurons were seeded to aligned PLLA nanofibre scaffolds, fabricated as described in Chapter 2, section 2.2.6. Cells were seeded at a density of 25,000 cells/cm$^2$. Neurons were transfected with AAV-hSyn-hChr2(H134R)-mCherry at an MOI of $10^2$ at 3 DIV. At 7 DIV, fluorescent intensity was quantified using a BMG LABTECH Clariostar. Recordings were taken with an excitation wavelength of 570±15nm and an emission wavelength of 620±20nm. For each cell density, 3 replicates of 3 neuronal cultures transfected at an MOI of $10^2$ were employed. An average fluorescence intensity was calculated for each cell density where then plotted to a scatterplot and a regression value was calculated to determine the correlation between fluorescence and cell count.

Fluorescence intensity of an area was calculated using images taken of cells transfected in the same manner that were then fixed for 20 minutes in 4% paraformaldehyde and nuclear stained with DAPI. Using ImageJ, fluorescence intensities were gathered for the background and 10 clusters of cells per field of vision. For each replicate, 3 fields of vision were employed and 3 replicates were used. Equation 5 was used to calculate background corrected total fluorescence (BCTF) which was then plotted against area.

$$\boldsymbol{BCTF} = \boldsymbol{Integrated\ Density} - (\boldsymbol{Area\ of\ selected\ cell\ X\ Mean\ fluorescence\ of\ background\ readings})$$

Equation 5: Calculating background corrected total fluorescence

## 7.3 Results

Cells were transfected with various MOIs of AAV-hSyn-hChr2(H134R)-mCherry, fixed and stained with DAPI. Manual quantification of the transfection efficiency revealed high levels of transfection for all conditions; subsequent validation with automated co-localisation software revealed the same trend although with much lower values (results not shown). This is a result of the method of the automated co-localisation; mCherry was primarily cytosolic whilst the DAPI stain is a nuclear stain. As a result, a proportion of the mCherrry will not overlap with the nuclear stain, thus lowering the values detected for the automated quantification of co-localisation. From the multifactorial ANOVA, the substrate that neurons were cultured upon and the viral concentration had significant effects on the expression of mCherry ($p = <0.001$ for each, figure 7.1B and 7.C respectively) whilst the time of transfection was not significant (figure 7.1D). However, interactions between factors were observed. Time of transfection became significant when comparing the co-localisation values between the two different

substrates, tissue culture plastic and PLLA nanofibres (figure 7.2A). Alone, viral concentration and substrate both significantly affected the expression of mCherry but an additional interaction was observed between the two factors (figure 7.2B). No significant interaction was found between the viral concentration and the time of transfection (figure 7.2C), however, results were bordering significance ($p$ = 0.055).

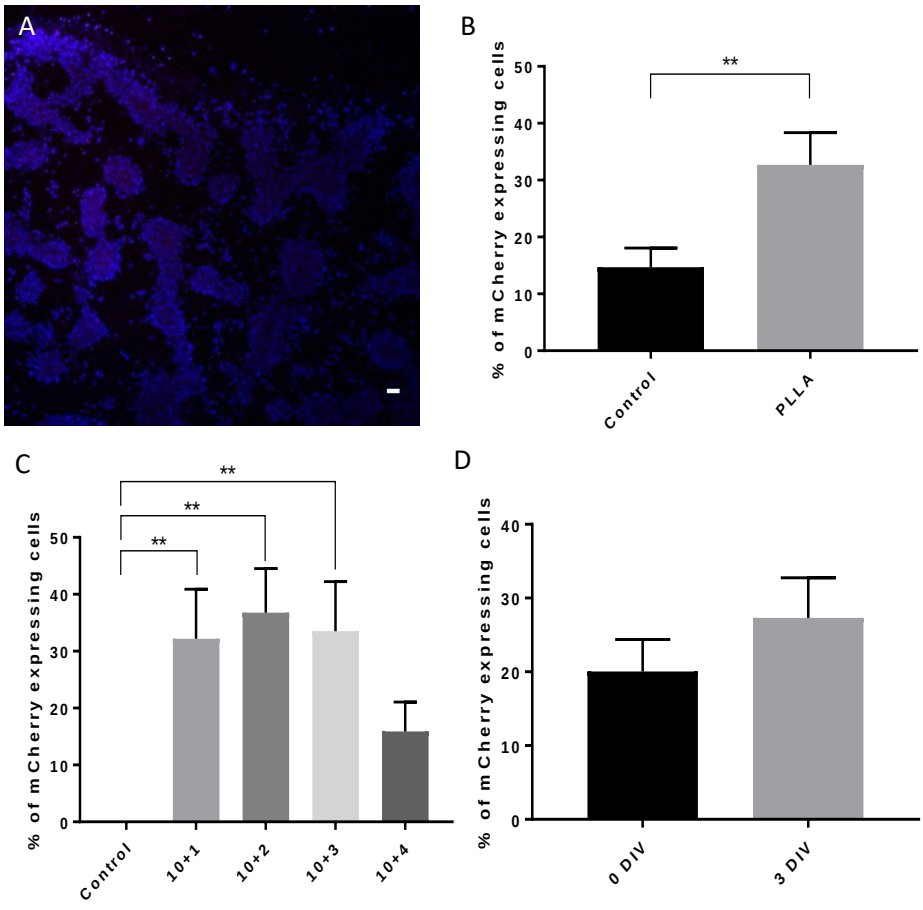


Figure 7.1: Optimisation of transfection of primary cortical neurons with AAV-hSyn-hChr2(H134R)-mCherry. (A) Transfected neurons grown on PLLA nanofibers, stained with DAPI, mCherry co-localises with the nuclear stain. (B) Significantly higher transfection of cells was observed for neurons cultured on aligned PLLA nanofibers (unpaired t-test: $t(58) = 2.721$, $p = 0.0086$) (C) Viral concentration significantly influences transfection efficiency (one-way ANOVA, $F = 5.043$, $p = 0.0016$. Dunnett's multiple comparison test. Control vs 10+1: $p = 0.0063$. Control vs 10+2: $p = 0.0015$. Control vs 10+3: $p = 0.0042$. Control vs 10+4: $p = 0.3067$) (D) Time of transfection did not significantly affect transfection efficiency (unpaired t-test: $t(58) = 1.046$, $p = 0.30$)

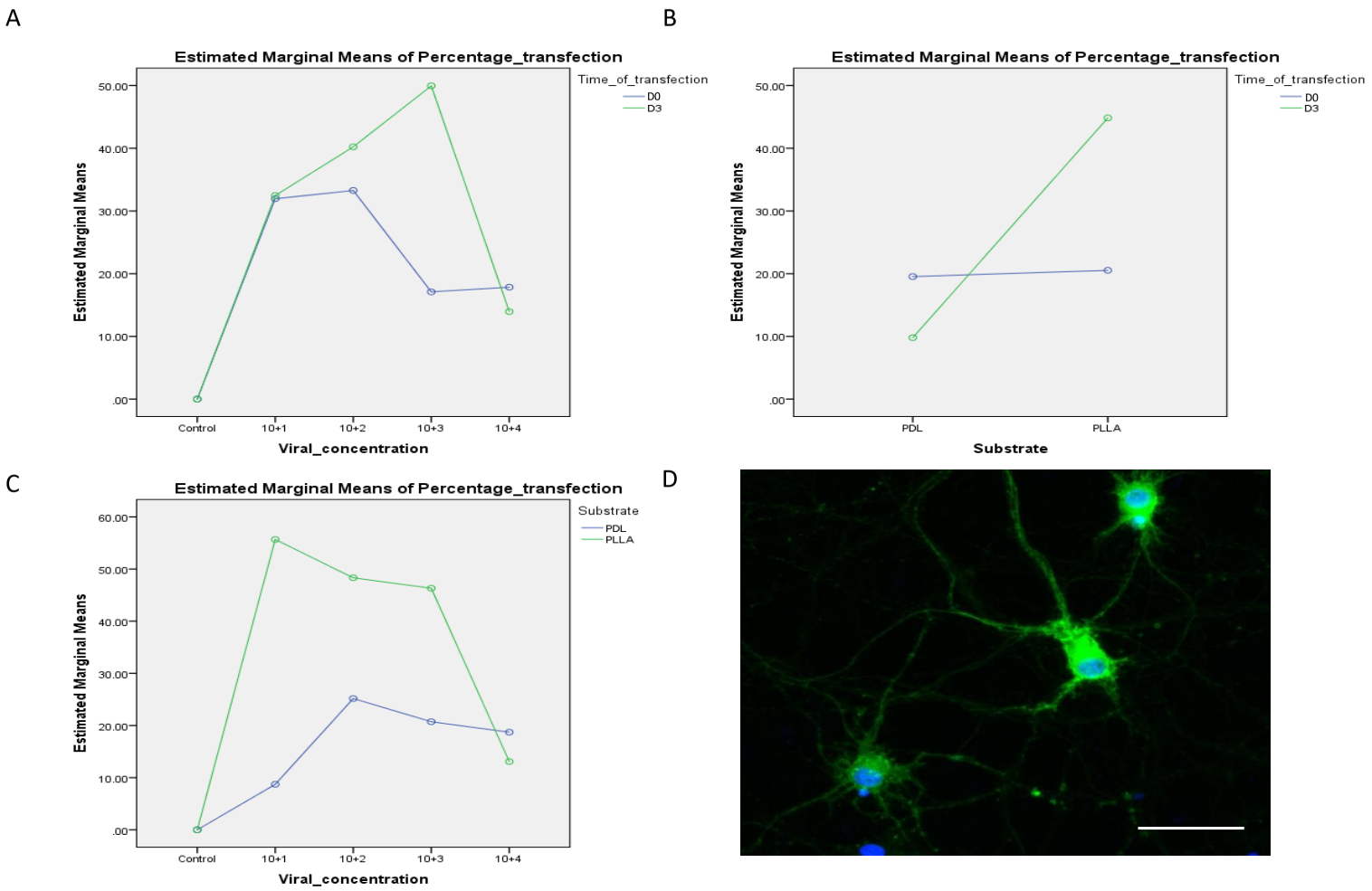


Figure 7.2: Interactions between factors that influence transfection efficiency and localisation of expression of Chr2 in primary cortical neurons (A) Viral concentration did not have a significant interaction with the time of transfection ($p$ = 0.085) (B) The substrate that neurons were cultured on had a significant interaction with the day that neurons were transfected on ($p$ = <0.001) (C) Viral concentration has a significant interaction with the substrate that the cells are cultured on ($p$ = 0.004) (D) Chr2 is ubiquitously expressed throughout the cell; the soma and neurites have strongly stained against the Chr2 antibody. Scale bar = 50 µm.

Nanoparticles were theorised to be the cause of increased transfection efficiency. Nanoparticulates were confirmed within the supernatant of nanofibres cultured in PBS which was then confirmed to originate from the laser cut polyester sheets (figure 7.3A and 7.3B), although it appears as though nanofibres can reduce the population size of the nanoparticles, potentially through binding the nanoparticles (figure 7.3B). No significant change was observed between the nanoparticulate populations between 0 and 3 DIV (figure 7.3C and 7.D). Incubation of PLLA nanofibres in an isotonic buffer is capable of inducing a significant decrease in pH within 24 hours that is maintained for up to 14 DIV (figure 7.3E).

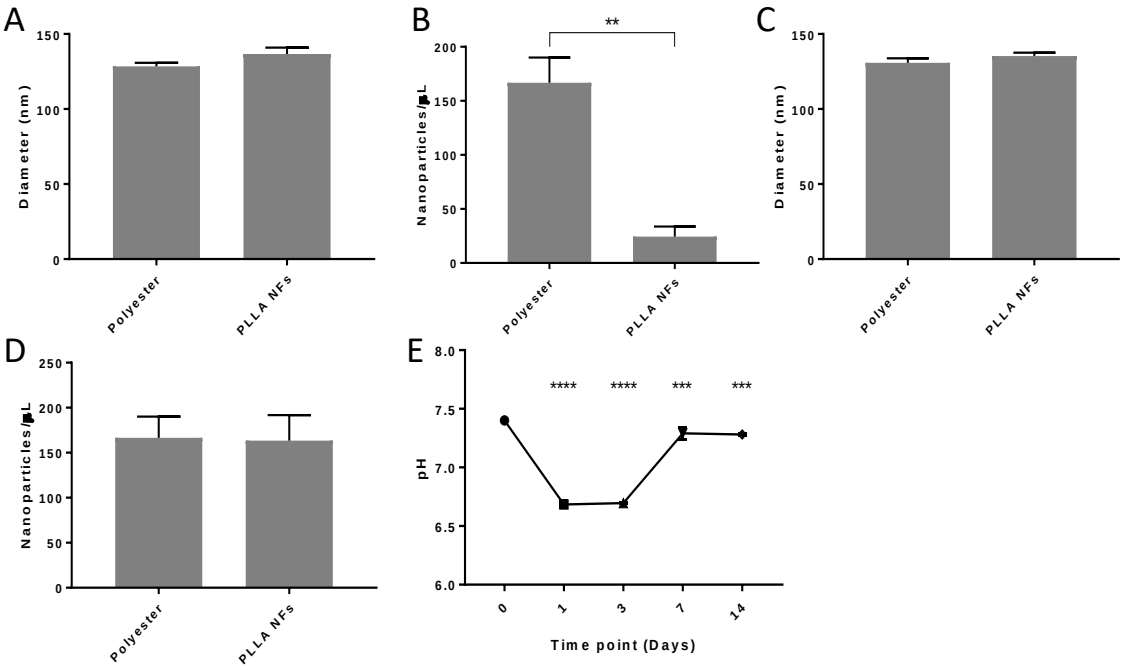


Figure 7.3: Possible mechanisms for the increased transfection efficiency observed for neurons grown on PLLA nanofibers. (A) No significant difference was detected between nanoparticulate diameter for nanoparticles isolated from polyester or PLLA NF supernatant (unpaired t-test: $t(598) = 1.672$, $p = 0.0951$) (B) A significantly larger number of nanoparticles were detected for the polyester alone condition (unpaired t-test: $t(4) = 5.664$, $p = 0.0048$) (C) No significant difference was observed between the nanoparticle diameters between day 1 and day 3 (unpaired t-test: $t(964) = 1.191$, $p = 0.2388$) (D) No significant difference was observed between the number of nanoparticles on day 1 and day 3 (unpaired t-test: $t(4) = 0.09054$, $p = 0.9322$) (E) Significant reduction in pH of the supernatant that nanofibres were cultured in occurred over a two week period (one-way ANOVA: $F = 664.5$, $p = <0.0001$. Dunnett's multiple comparison test. Day 0 vs Day 1: $p = <0.0001$. Day 0 vs Day 3: $p = <0.0001$. Day 0 vs Day 7: $p = 0.0007$. Day 0 vs Day 14: $p = 0.0003$)

An MOI of $10^2$ was selected as the optimal viral concentration. Initial immunostaining of cells transfected with an MOI of $10^2$ revealed ubiquitous expression of the Chr2 protein across the entirety of the cell with notably high expression within the soma (figure 7.2D). Optogenetic control of cells was initially demonstrated using a Clariostar plate reader. Fura red-AM was loaded in to cells and cells were excited at a wavelength of 470±15nm; a wavelength which excites both the calcium indicator and the channelrhodopsin. All transfected cells demonstrate a increase in $Ca^{2+}$ (indicated by an decrease in fluorescence) relative to the control. A dose dependent response was not observed for the MOI used to transfect the cells; cells transfected with $10^2$ viral particles/cell demonstrated the greatest influx of $Ca^{2+}$ in response to the depolarising wavelength of light whilst cells transfected with $10^1$, $10^3$ and $10^4$ viral particles/cell demonstrated similar responses to each other (figure 7.4A). Analysis of the fluorescent values using MATLAB software revealed two distinct changes to the $Ca^{2+}$ influxes. Average change in fluorescence exhibited a wide standard error margin and no significant difference between different MOIs (one-way ANOVA, $F(3) = 1.422$, $p = 0.2960$) but a trend toward negative average change to amplitude was observed for all transfected cells. Inter-oscillation intervals for the transfected neurons were significantly lower than those of the control cell (one-way ANOVA, $F(107) = 17.4$, $p = 0.0055$) and exhibited a viral dose-dependent response (figure 7.4C).

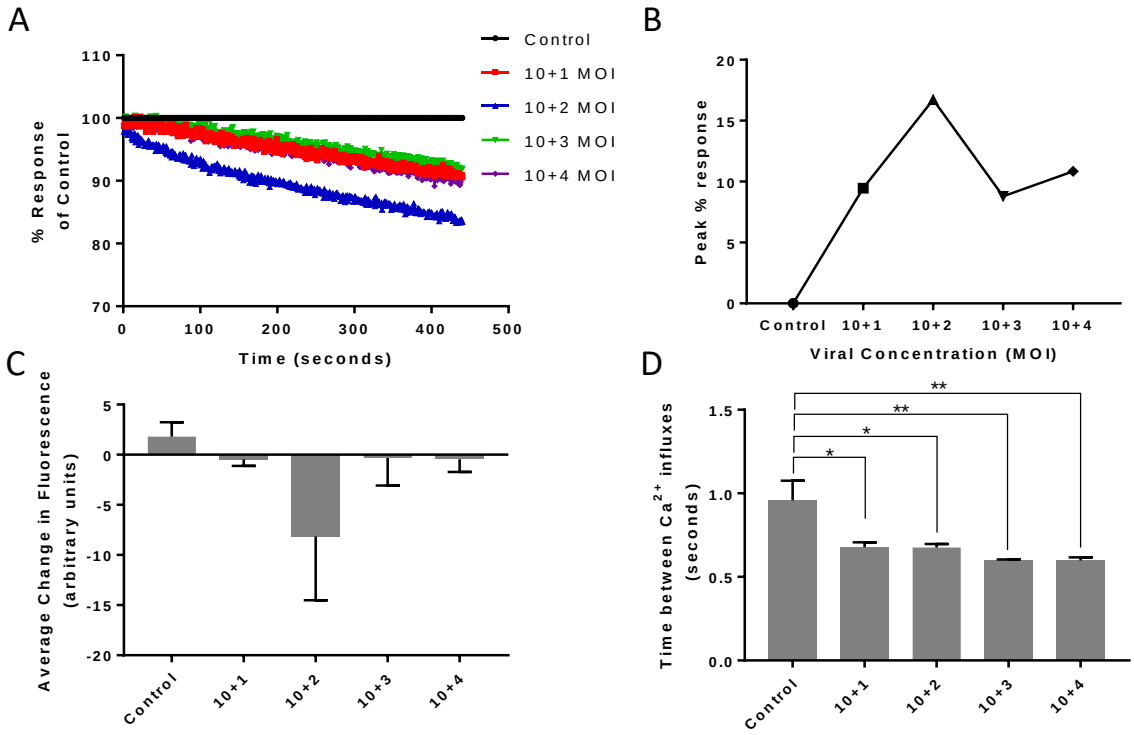


Figure 7.4: Optogenetic control of depolarisation of transfected primary cortical neurons (A) Control and transfected neurons were exposed to light at a wavelength of 473nm; all transfected cells demonstrated a subsequent decrease in fluorescence (increase in intracellular $Ca^{2+}$) (B) Maximal % response for transfected cells upon photostimulation (C) Transfected cells exhibit negative average change in fluorescence; all transfected cells trended towards increasing $Ca^{2+}$ (D) Transfected cells exhibit a significantly lower time between $Ca^{2+}$ influxes than the control cells (one-way ANOVA, $F = 7.162$, $p = 0.0055$. Dunnett's multiple comparison test. Control vs 10+1: $p = 0.0167$. Control vs 10+2: $p = 0.0156$. Control vs 10+3: $p = 0.0034$. Control vs 10+4: $p = 0.0034$.

Primary cortical neurons transfected with AAV-hSyn-hChr2(H134R)-mCherry demonstrated no change in morphology as a result of transfection. Real-time imaging was run for 4 days; hourly images of the cells were taken and subsequently analysed using the Incucyte software (figure 7.5).

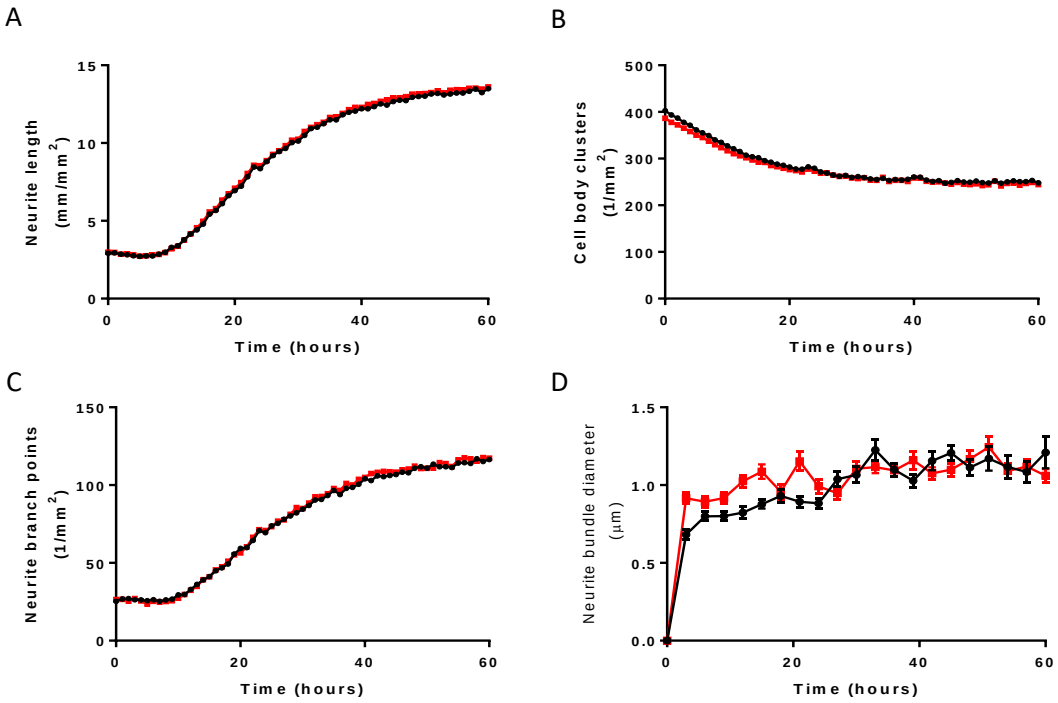


Figure 7.5: Real time tracking of morphological features of primary cortical neurons transfected by AAV using the Incucyte Live Cell Analysis system. Black = control, red = primary cortical neurons transfected by AAV (A) Neurite length (B) Cell clustering behaviour (C) Neurite branching (D) Neurite fasciculation

Over a period of 4 days, control and transfected neurons were visualised using the Incucyte system and analysed using the associated software. Neurite length, branch points and cell clustering behaviours were not affected by the transfection process (figure 7.5). Neuronal rates of growth, branching, cell clustering behaviours and neurite bundle diameter were quantified over the 4 day period and were not significantly affected by transfection (figure 7.6).

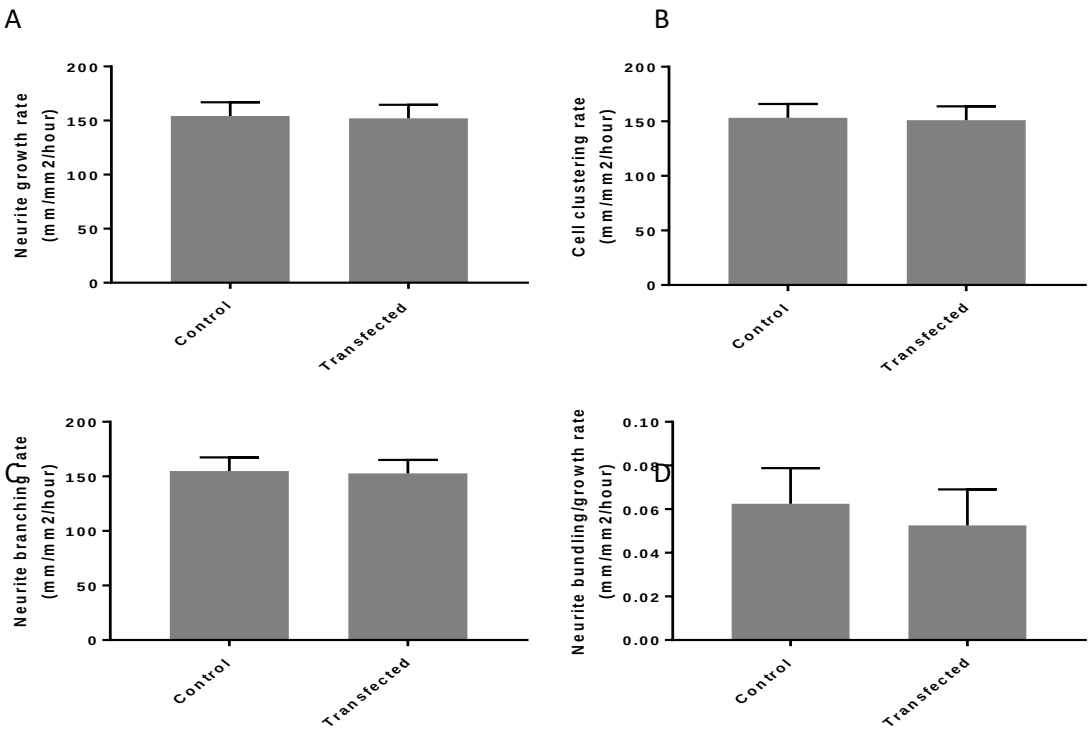


Figure 7.6: Quantification of rates of growth for primary cortical neurons transfected by AAV (A) Neurite growth rate is not significantly altered by transfection (unpaired t-test: $t(272) = 0.1266$, $p = 0.9025$) (B) Cell clustering rate is not significantly altered by transfection (unpaired t-test: $t(272) = 0.1152$, $p = 0.9083$) (C) Neurite branching rate is not significantly altered by transfection (unpaired t-test: $t(272) = 0.1266$, $p = 0.9025$) (D) Neurite fasciculation is not significantly altered by transfection (unpaired t-test: $t(40) = 0.6019$, $p = 0.5506$)

The linearity of cell number and fluorescence was calculated by seeding cells at different seeding densities, transfecting cells at an MOI of $10^2$ and measuring the fluorescent intensity at the excitation wavelength of mCherry. Results indicate a strong positive correlation between the number of cells present and the fluorescence intensity ($R^2 = 0.744$, $p = <0.0001$, figure 7.7A). Referring to the residuals however (figure 7.7B), non-Gaussian distribution of data is evident; the predictors are missing a variable. Cells that are clustered together in previous studies appeared to have a higher fluorescence intensity than those that are more dispersed. Plotting baseline corrected fluorescence intensity against area indicates a strong positive correlation ($R^2 = 0.8791$, $p = <0.0001$) (figure 7.7C) and the residual plots (figure 7.7D) show Gaussian distribution of the residuals; the area predicts the fluorescent intensity. Results indicate that

whilst fluorescence is proportional to fluorescent intensity, the degree of clustering has an additional influence; potentiating the fluorescent signal.

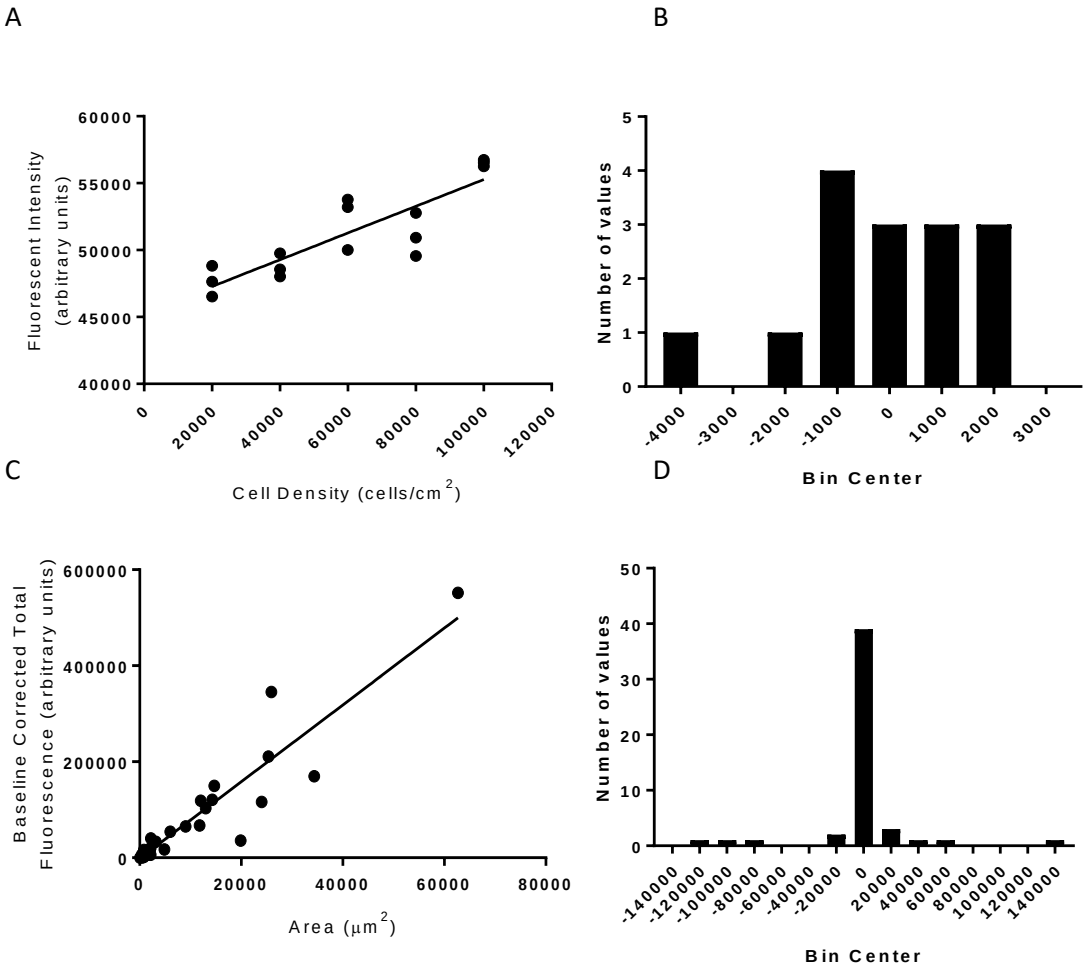


Figure 7.7: Fluorescence relative to cell count and cell density (A) Fluorescence positively correlates with cell number ($R^2$ = 0.744, $p$ = <0.0001) (B) Residual plots for A; non-Gaussian distribution is observed, a variable is not accounted for by this model (C) Fluorescent intensity positively correlates with area of cells ($R^2$ = 0.8791, $p$ = <0.0001) (D) Residual plots for C; Gaussian distribution is observed, accounting for the area that cells occupy corrects the previous model.

## 7.4 Discussion

### 7.4.1 Initial Optimisation

A commercially available AAV (AAV-hSyn-hChr2(H134R)-mCherry, VectorCore) was selected for the transfection of primary cortical neurons. As previously discussed, viral serotype and promoter can be used to influence the expression of the transgene in a specific tissue. Studies that have employed the same AAV serotype and promoter as the commercially available AAV have utilised a diverse range of models such as *in vivo* models, primary cortical neurons, primary hippocampal neurons and cell lines (Nathanson et al, 2009; Zhang et al 2012; Fan et al 2015; Kwon et al 2015; Michel et al, 2005; Duverger et al, 2002). Whilst these studies demonstrate successful transfection and expression of transgenes, transfection is performed using a range of MOIs from $10^3$ to $10^8$. Optimisation of transfection was needed. Transfection efficiency was quantified as the amount of DAPI stained cells that co-localised with mCherry. Multifactorial ANOVA was used to investigate how several factors can influence transfection. Relative to the control, the substrate that the neurons were grown on and the viral concentration had significant effects on the transfection efficiency (figure 7.1B and 7.1C).

### 7.4.2 Mechanism for nanofibre induced transfection efficiency potentiation

Neurons cultured on nanofibres displayed a significant increase in transfection efficiency and several factors may be the cause of this; porosity, acidification of the culture media, the creation of nanoparticulates or a combination of all three factors. Nanofibres are an inherently porous structure that facilitate diffusion of molecules (Loh et al, 2013). As the cells grow on the nanofibres and across the pores, a greater surface area of the cells is exposed to the virus-bearing media and may be the cause of the increase in transfection efficiency. Whilst it is possible that porosity may enable greater exposure to the viral particles, at least one study has demonstrated the negative effect of porosity on the transfection of cells grown in three

dimensions, in two different cell lines (Xie et al, 2001), although this study was in mitotic cell lines rather than post-mitotic primary neurons. The acidification of the media caused by the degrading nanofibres (figure 7.3E) may play a role in the increased transfection efficiency. AAV2 particles are typically endocytosed via clathrin coated pits and escape the endosome in a low-pH dependent manner before trafficking to the nucleus along microtubules (Xiao and Samulski, 2012). The mechanism behind the viral escape is not fully characterised but is thought to be due to maturation of the viral particles induced by the low pH. The low pH induces conformational change, activating phospholipase $A_2$, which subsequently lyses a pore in the endosome, facilitating escape in to the cytoplasm (Liu et al, 2012; Stahnke et al, 2011). The low pH of the extracellular media due to the degradation of the PLLA nanofibres may promote increased viral efficiency by allowing the virus to mature externally to the cell and bypassing the endosome entirely by entering the cell by lysing the cell membrane and entering the cytoplasm directly after maturation rather than escaping the endosome. Alternately, the low pH external to the cell may accelerate the acidification of the early endosome upon endocytosis, increasing the rate that viral particles mature and escape, thus escaping destruction by the lysosome/proteasome (Nonnenmacher and Weber, 2012). Both hypothetical mechanisms are dependent on entering the cytoplasm more rapidly than would normally be possible, minimising the chance of exposure to the lysosome and thus increasing the intracellular viral titre by reducing the degradation. Alternatively, nanoparticulates have previously been used as a means of delivering genes into cells for transfection, increasing the efficiency or altering the tropism of viral vectors (Panyam and Labhasetwar, 2003; Rajagopal et al, 2018; Mailander and Landfester, 2009). PLLA nanoparticles with a diameter of 80-210 nm have been previously confirmed to be able to penetrate HeLa cells, independent of the charge of the particle (Musyanovych et al, 2011). Using the Zetaview, the presence of nanoparticles was confirmed within the supernatant that PLLA nanofibres were cultured in, averaging approximately 130nm (figure 7.3A). It is possible that the presence of the nanofibres, and thus

nanoparticulates, may be the cause of the increased transfection efficiency. If this were the case, the virus may also have altered tropism and co-localisation studies may be needed to confirm that only neuronal cells are transfected and that the transfected neurons are approximately 80% glutamatergic and 20% GABAergic. However, no significant difference was observed in the nanoparticulate population (nanoparticle diameter or count) between D0 and D3, suggesting that the nanoparticles do not play a role in the significant increase in transfection. The presence of nanoparticulates is a possible concern for the purposes of implantation and nanoparticulates have demonstrated cyototixicty and genotoxicity, dependent on material and size (Yang et al, 2010). As they appear to originate from the polyester used to collect electrospun nanofibres (figure 7.3A), alterations to the electrospinning fabrication process may be required to reduce nanoparticle count.

Viral concentration significantly affected the transfection efficiency, however, a non-dose dependent effect was observed. Decreasing transfection efficiency was observed at the highest MOI of AAV tested; closer examination reveals that the significant decrease in transfection efficiency is only present for neurons transfected on PLLA nanofibres (figure 7.2C). For MOIs of $10^2$, $10^3$ and $10^4$, elevated transfection efficiency is observed on nanofibres whilst at an MOI of $10^4$, the transfection efficiency is approximately equal to the efficiency of transfection on the control surface. Further characterisation is required to determine the mechanism behind the non-dose dependent response. A possible mechanism for this would be steric hindrance. If the increase in viral transfection efficiency was due to the virus binding to the nanoparticles, then it is possible that an excessive number of viral particles sterically hindered the uptake of the viral particles in the cell, lowering the transfection efficiency. Steric hindrance of nanoparticulate-mediated transfection has been observed previously (Sung et al, 2003). Alternatively, the nanofibres and viral particles in conjunction may have increased the

expression of inflammatory markers; inflammatory markers have previously been observed to reduce expression of transgenes although this was performed in primary liver cells (Breous et al, 2011).

### 7.4.3 Light-Induced Depolarisation of Transfected Primary Cortical Neurons

Whilst the transfection efficiency exhibited a non-dose dependent response to viral concentration, the electrophysiological activity of transfected cells in response to light was dose-dependent. Referring to figure 7.4, quantification of the electrophysiological activities of the cells, increasing viral concentration increased the responsiveness of cells to light: the higher the viral concentration, the shorter the time between $Ca^{2+}$ influxes. This suggests that whilst a lower percentage of cells were transfected, those that were transfected exhibited a higher expression of the Chr2 transgene although protein quantification would be necessary to confirm this. This contradictory result is also observed by Howard et al (2008) for several of the tested AAV serotypes (although AAV2 was not amongst these).

Interactions between factors were also noted to influence the transfection efficiency. An interaction between the time of transfection and the material that cells were cultured upon observed. Transfecting neurons at 3 DIV rather than 1 DIV significantly increased the transfection efficiency for neurons grown on nanofibres but not the PDL/laminin control. This may be due to the mechanism that AAV use to traffic in to the perinuclear space. Microtubules are utilised by the AAV particles to travel to the nucleus, disruption of the microtubules can inhibit the transfection efficiency (Xiao and Samulski, 2012). Hydrophobic surfaces can delay cytoskeletal development (Marote et al, 2016) whereas hydrophobic nanoparticles can disrupt physiological microtubule dynamics (Kuang and Xu, 2013); thus, rather than neurons cultured

on PLLA nanofibres displaying an elevation in transfection efficiency at later time points, AAV transfection may be inhibited at earlier time points. An interaction between viral concentration and the cell culture surface was also detected. However, the proposed mechanism for the increase in potency and efficacy of AAV particles grown on PLLA nanofibres has already been described in the previous paragraph (increased porosity, acidification of media and formation of nanoparticulates).

Calcium influx was induced in transfected primary cortical neurons as a response to light, demonstrating photosensitivity and successful transfection of Chr2. To facilitate the recording of a large number of replicates, recordings were performed using a fluorescent plate reader. Whilst this facilitated high throughput collection of data, it prevented the use of multiple wavelengths of light for excitation and detection of emission due to the limitations of the plate reader. Due to this, a calcium indicator (Fura red-AM) that had an overlapping spectra with Chr2 was employed, allowing stimulation and recording simultaneously. All transfected cells exhibited a $Ca^{2+}$ influx as a response to 470nm of light, regardless of MOI. This photosensitivity was not observed for the control. The raw data (figure 4A) indicates a viral dose-independent response whilst the time between $Ca^{2+}$ influxes demonstrated a dose-dependent response (figure 7.4C). These seemingly contradictory results are likely a factor of cell survival. The Clariostar plate reader that was used to attain the fluorescent values measures a global fluorescence value of the well that cells are cultured in. Neurons transfected with a MOI of 1 $x10^2$ exhibited the greatest decrease in total fluorescence because survival was likely to be higher at lower MOI than higher MOI, thus more cells were present to contribute to the total global fluorescence values. AAV2 demonstrates no cytotoxicity at MOI of 2 x $10^2$ in cortical neurons yet at greater multiplicities of infection, significant increases in cytotoxicity are observed, despite being negligible relative to the cytotoxicity of other serotypes (Howard et al,

2008). In contrast, the quantification of the time between intervals exhibited a dose-dependent response because the neurons that did survive the transfection likely expressed a higher quantity of Chr2 and thus, were more capable of depolarising as a response to light.

### 7.4.4 Quantification of Morphological Alterations due to Chr2 Transfection

Although studies rarely note a morphological difference as a result of optogenetic transfection, at least one study has noted that Channelrhodopsin-2 transfection can alter the axonal morphology of rodent cortical neurons *in* vivo in an expression-dependent manner (Miyashita et al, 2013). Given that the formation of the organoids that were observed on aligned PLLA nanofibres were determined by neurite behaviours (Segev et al, 2003), it is key to confirm that the act of transfection with mCherry and Chr2 does not interfere with neurite behaviours or subsequent clustering. Primary cortical neurons on 2D tissue culture plastic were virally transfected with Chr2 and no morphological changes were observed. Unfortunately, due to the linear nature of the nanofibre networks, culture of neurons on nanofibres and visualisation using the Incucyte system resulted in false detection of neurites, thus the experiment was performed in conventional 2D culture to attain data in real-time. Whilst the mCherry expression could facilitate fluorescent tracking of the movement of cells on the nanofibres, expression was limited to the cell bodies and could not be detected by the Incucyte. However, the key difference between the selected 2D surface and the 3D nanofibre surface is the difference in wettability. The 2D tissue culture plastic is more hydrophilic and thus, cells are less likely to migrate and cluster on the surface (Ryans, 2008). However, migration across the surface to form cellular clusters was still observed on the hydrophilic 2D culture surface and thus, 2D culture was accepted as a model of transfected primary cortical neurons on nanofibres for initial testing.

### 7.4.5 Tracking of the exogenous neurons *in vivo*

The fluorescent tag, mCherry, was proposed to have a use in the *in vivo* application of the transfected cells. As the mCherry within transfected cells fluoresces, a fluorescent *in vivo* imaging system (Perkin Elmer, IVIS Spectrum) was proposed as a means of tracking both the survival of cells within the implant and the rate of neurite extension. Red wavelengths of light are known to penetrate tissue to a greater degree than other wavelengths of light (van Gemert and Welch,1989), thus supporting the role of mCherry as a means of tracking the progress of growth upon implantation. However, referring to figure 7.1A, the signal from mCherry is notably weak and localised to the cell body; using confocal microscopy, no neurites were detected using mCherry as a fluorescent marker. It is unlikely that the extending neurites will be able to be detected *in vitro.* However, referring to figure 7.7A and 7.7C, a linear relationship was found between the fluorescent intensity at the emission wavelength of mCherry and the number of cells, suggesting that mCherry has the potential to be used as a means of monitoring the survival of the cells *in vivo.* This remains conditional on the detection limits of the IVIS imager; if the *in vivo* imager is capable of detecting the light through the skull of the implant recipient, this method can be utilised to assess cell survival. However, a limitation to quantifying cell number through fluorescence was evident in the residuals histogram (figure 7B). The residual plots indicate non-Gaussian distribution when plotting fluorescence vs cell count; a factor other than cell number influences the fluorescence intensity. Quantification of fluorescence intensity using ImageJ demonstrated a robust correlation between the fluorescence intensity and the area of the cell cluster, despite correction of the fluorescence intensity based on area. The residual plots for this regression indicate Gaussian distribution (figure 7.7D), suggesting that the area is the missing predictor; the more densely packed the cells are, the greater the ability to detect the fluorescence intensity of the cells. Whilst this experiment was performed in 2D conventional culture, the clustered 3D nature of the cells to be implanted should aid in the *in vivo* detection of the cells.

### 7.4.6 Limitations to transfection of primary cortical neurons for the purpose of re-wiring the cortex

A limitation for transfected cells is that AAV transfected primary neurons exhibit an increase in mitochondrial membrane potential post-transfection (Duverger et al, 2002). Whilst this is not enough to be considered cytotoxic, it can predispose the cells towards apoptosis, as seen in the study of Duverger et al (2002). Upon implantation, anoikis, ischaemia and withdrawal of trophic factors are present and are pro-apoptotic factors (Sortwell et al, 2000); an increase in mitochondrial membrane potential may induce a greater percentage of cells to undergo apoptosis than would if cells were implanted in the absence of AAV-mediated transfection. Whilst implanting at earlier developmental stages appears to increase the likelihood of synaptic integration of exogenous cells, this would likely increase the rate of apoptosis of implanted cells. 72 hours after AAV mediated transfection, there is a significant reduction and subsequent plateau in mitochondrial membrane potential (Duverger et al, 2002), thus the implantation of AAV-transfected primary cortical neurons should occur a minimum of 72 hours after transfection.

## 7.5 Conclusion

Neurons grown on aligned PLLA nanofibres have demonstrated the ability to generate electrically active cerebral cortical organoids whilst the work described in this chapter describes the methodology employed to transfect them with a transgene capable of determining the degree of integration upon implantation in to the *in vivo* cerebral cortex.

# Chapter 8: Conclusions and future directions

## 8.1 Summary

In Chapter 3, several qualities were listed as desirable for exogenous neurons that were to be implanted into a host for the purposes of rewiring neural circuitry within the cerebral cortex. For the purposes of rewiring, neurons should: possess cortical areal identity, be embryonic, exhibit clustered cell bodies with aligned, fasciculated neurites and demonstrate electrical activity (Michelsen et al, 2015, Ideguchi et al, 2010; Gaspard et al, 2008; Espuny-Carmacho et al, 2013, Tang-Schomer et al, 2014, Dunnett and Bjorklund, 2017). Use of embryonic primary cortical neurons as a cellular model facilitates the electrical activity, cortical areal identity and early developmental stage. The research presented within this thesis indicates a method of generating the clustered cell bodies with aligned, fasciculated neurites. Proteomic analysis of these cellular architectures suggests that neurons within these structures are more developed and physiological than their 2D counterparts whilst the network inference and Nanostring aid in elucidating a mechanism. The electrical activity and responsiveness of the neurons to physiological agonists was also tested and confirmed, further reinforcing the capacity to use the primary cortical neurons cultured on aligned PLLA nanofibres as the basis for cellular implants for cortical rewiring.

## 8.2 Current Limitations to Cortical Re-Wiring using the Aligned PLLA Nanofibre Derived Methodology

Whilst the research presented describes a methodology to generate physiological cellular architectures using a material that is suitable for implantation and further *in vivo* studies, the next steps would be the engineering of a delivery system that is capable of injecting aligned nanofibres bearing cellular structures into the CNS in a way that is amenable to neuronal viability. Methods of delivery of nanofibres into the host typically do not preserve alignment

in a way that facilitates rewiring. Examples include placing of membranes on the surface of the brain (Tseng et al, 2013), insertion of bundled fibres in to cavities (Hwang et al, 2014; Jaiswal et al, 2013; Alvarez et al, 2014) and sectioning fibres and suspending them in a hydrogel (Rivet et al, 2015; Wang et al, 2016). The noteworthy exceptions include rolling the sheet in to a spiral and injecting this spiral (Nisbet et al, 2009) and placing the nanofibres in an external conduit for injection (Koh et al, 2010; Kim et al, 2008; Maclean, 2017). The two most viable options for delivery would be to draw them up into a needle for injection or to move the nanofibres into a protective conduit for implantation. Each presents limitations.

Assuming that the nanofibre membrane could be electrospun into a shape with desirable diameters, drawing the nanofibres into the needle would require the application of shear stress upon the neurons of the implant. The generalised effects of shear stress on cells are extensive. Shear stress has demonstrated the ability to induce DNA damage, inhibit protein synthesis, increase nitric oxide synthesis and induce $Ca^{2+}$ influx and if shear stress is high enough, inducing nitric oxide-dependent cell death (Triyoso and Good, 2004), thus mandating that shear stress be considered as an inhibitory factor for cellular delivery. No cell is predicted to be capable of surviving shear stress in excess of $10^5$ dynes (Triyoso and Good, 2004), whilst 200 dynes is capable of inducing instantaneous necrosis in a neuronal model (LaPlaca et al, 1997). Neuron-specific effects of shear stress are also significant. Neurite outgrowth and alignment are influenced by shear stresses that are significantly lower than the forces that are capable of killing cells. As little as 5 microdynes were capable of inducing significant alterations to neurite directionality and inducing further neurite outgrowth (Kim et al, 2006). Electrophysiologically, 140 dynes/$cm^2$ was capable of inducing significant alterations to the membrane permeability of primary cortical neurons, an effect which was observed to be rate dependent (LaPlaca et al, 2006). Permeable neurons within the culture were non-electrically

excitable whilst their non-permeable counterparts retained physiological spiking activity. Whilst high degrees of shear stress have negative consequences in regards to cellular viability, lower levels of shear stress will induce detachment from the surface and topographical reorganisation prior to this. Cellular adhesion to hydrophobic surfaces is notably poor (Valamehr et al, 2008) and the nanofibres of the implant exhibit hydrophobicity; shear stress may detach cells due to poor adherence. Segev et al (2003) state that neuronal cluster formation is due to neurites of cells contacting each other, exerting 150 microdynes of force on each other and if this 150 microdynes of force exceeds the adherent force the surface exerts on cells, cluster formation and migration occurs. Migration occurs on the nanofibres, thus from this it can be inferred that the force holding cells in place is below 150 microdynes, suggesting an upper limit for shear stress that can be applied to cells upon delivery. On the other hand, delivery of the organoid into the cortex within a conduit containing cellularised aligned nanofibres would shield the cells from the shear stress that is inherent to simply drawing up the nanofibres into a needle although testing would be required to determine the degree of shear stress generated by delivery in this way. The limitation to the conduit is the added dimensions of the implant. Smaller implants were associated with negative outcomes on the implant; increasing diameter positively correlates with decreasing neuronal staining and increased glial scarring (Spencer et al, 2017), indicative of greater glial scar formation which is a known neurodegenerative factor (McConell et al, 2009). These are the considerations for the next stage of development for an implant to rewire the cerebral cortex.

## 8.3 Future directions and implications on the transplantation and modelling of neurons

Within the thesis, the possibility that the organoid can be used as a high-throughput, developmentally advanced tissue model for use in the pharmaceutical industry has been discussed. *In vitro* cultures of neurons are inherently non-physiological whilst 3D cell culture

has yielded increasingly physiological responses in a number of aspects. Neuronal 3D cultures have an additional level of complexity relative to other tissues due to the complexity that is inherent to the function of the brain. Connections between neurons within the brain can occur at specific spatial nodes, specific temporal intervals or both (Köse-Dunn et al, 2017). In the absence of this level of connectivity, structure and thus function is fundamentally different between the *in vivo* and *in vitro* neurons, promoting the rise of differences in cellular behaviours. Generating representative 3D neural circuitry *in vitro* is difficult yet models that can do (henceforth referred to as Tissue Engineered Neural Networks – TENNs) so have numerous potential applications *in vitro.* The methods of generating organoids described within this thesis have the potential to be used in the following *in vitro* technologies as TENNs.

### 8.3.1 Cerebral Cortical Organoids as Cellular Models for High-Throughput Pharmacological/Toxicological Studies

Electrically active 2D cultures do not represent the natural electrophysiology of neurons *in vivo.* Typically, neurons are allowed to grow to form networks with random topologies prior to experimentation yet electrophysiological activity is altered by topology and neurons *in vivo* have a highly defined architecture *in vivo* (Kandel, 2012). Random topologies of neurons have reduced ability to recruit monosynaptic excitatory post synaptic currents (EPSCs) and exhibit earlier development of synchronised bursting activity than patterned topologies, suggesting network structure plays a key role in determining cellular electrical behaviours (Marconi et al, 2012). Whilst implementation of structure on 2D networks of dissociated neurons has a notable effect of the nature of the network that forms, implementing 3D topologies on dissociated neurons has a greater influence. Two dimensional cultures exhibit high levels of bursting and little random spike activity, in contrast to the low levels of bursting and high

random spiking that is observed in random networks that form in 3D. In addition, culture of random 3D networks results in desynchrony as multiple networks are formed and downstream signalling adds additional latency time in to network activity (Frega, 2016; Severino et al, 2016). Similar results have been observed when culturing neurons in 3D whilst controlling the topology of the neurites within the network. Dhobale et al (2018) used a hydrogel based cylindrical 3D structure with neuronal populations seeded to either end as a TENN. Calcium imaging revealed similar desynchronised regimes; highly synchronised activity locally with less synchronous long-range activity. The group also demonstrated anisotropic information flow through the 3D construct, similar to what is observed *in vivo*. Amongst other properties, 3D culture of neurons result in multiple networks that innervate each other rather than a single synchronous network, thus 3D neuronal cultures present a more biofidelic model of brain function than 2D cultures.

Tang-Schomer et al (2014) formulated a brain-like tissue of silk donut structures with pores filled with a collagen hydrogel. The model exhibited elevated viability relative to the 2D and collagen hydrogel controls, increased expression of proteins involved with neuronal adhesion, regenerative growth and synaptogenesis and an improvement in electrophysiological activities. However, whilst the neurites were segregated from the soma, the neurites still exhibited a random topology. Similarly, Jo et al (2016) generated midbrain-like organoids from pluripotent stem cells that exhibited functional midbrain dopaminergic neural networks, GABAergic innervation and transcriptomic profiles that resemble prenatal midbrain neurons. The dopaminergic neurons were also capable of producing neuromelanin, a controversial molecule that has been indicated as a potential cause of Parkinson's disease (Jo et al, 2016); a feat that has not been replicated in 2D culture. These results and many others demonstrate the utility

of 3D culture of neurons and the value of 3D cell culture for generating physiologically relevant tissues for study.

In contrast to the model of Tang-Schomer et al (2014), the TENN model described by Harris et al (2016) attempts to more closely mimic the 3D structure of the brain by generating aligned, fasciculated neurites, interconnecting 3D clusters of cell bodies (Tang-Schomer et al, 2014). The TENNs of Harris et al (2016) can theoretically be formulated as a bidirectional structure as both ends of the structure can be seeded, potentially with different neuronal subpopulations, and thus innervate each other. The bidirectional structure of the TENN serves two purposes; first, afferent and efferent connections are established and maintained, providing growth factors to cells within the TENN. Second, the bidirectional structure would also formulate a simple neural circuit. Due to the emergent functionality of neurons a neural circuit can be suggested to be the smallest unit of the central nervous system (CNS) (Yuste, 2015), and thus the TENN may be more representative of true CNS tissue than traditional cultures. The restriction of the direction of the neurite outgrowth may also result in improvement of the electrophysiological properties of the neurons as they extend neurites along the longitudinal axis of the TENN, thus some patterning is present. Patterned neurite outgrowth has been demonstrated to have some beneficial effects on electrophysiological activity (Marconi et al, 2012).

Whilst existing models of the brain such as organotypic cultures and 2D cultures are a functional model of the brain, 3D tissue engineered neural networks have demonstrated their role as a more biofidelic model of the brain electrophysiologically, transcriptomically and structurally. As a result, 3D neuronal cultures should increase the accuracy of cell models for traditional high-throughput applications such as those found in drug screening and toxicology.

Due to the ease of generation of the cerebral cortical organoids described within this thesis, they represent a promising method of generating the 3D architectures that are representative of the architectures found within the physiological neural circuitry. Further characterisation of the electrophysiological properties of the organoids is required before their use as biofidelic models of the brain for electrophysiological purposes. Frega et al (2016) developed a method of characterising 3D neuronal activity using a microelectrode array that may be suited to characterisation of the organoid to sufficient spatiotemporal resolution.

### 8.3.2 Cerebral Cortical Organoids as a Macro-Neuronal Circuit *In Vitro*

2D cultures have been generated that mirror specific networks such as the cortical-striatal pathway (Peyrin et al, 2011), cortical-thalamic (Kanagasabapathi et al, 2012) and the hippocampal-entorhinal pathway (Berdichevsky et al, 2011). Several studies have gone beyond patterning the neural network and have replicated specific physiological circuits, in addition to those that have generated the entire cortical regions with numerous complexed micro-circuits (Lancaster and Knoblich, 2013). These models demonstrate promotion of various advantageous properties such as elevated dendritic spine formation, synaptogenesis, arbor complexity and synchronisation of activity between cultures. However, the models only mimic the connection between two nodes within the CNS in a 2D manner. Other studies have generated circuits with numerous nodes in 3D. Choi et al (2013) generated a series of interconnected cortical neurospheres that expressed markers specific to the layers of the cortex. These connected neurospheres were utilised to test β-amyloid neurotoxicity. In contrast, Jeong et al (2015) differentiated cortical neural precursor cells in a series of channels and demonstrated interconnected neurospheres with mixed populations of cells, exhibiting electrical activity.

Whilst these structures have found use in developmental biology, toxicology and neuroscience, the idea of generating physiological neural structures can be taken further. The cortical organoids could be used to further the concept of generating *in vitro* circuitry by defining the network manually. With greater control over the seeding process, the organoids could be complexed similarly to the assembly of a circuit board, in order to generate advanced neural circuitry that is identical to the 3D structural architecture of the brain. As an example, Figure 8.1 illustrates the direct and indirect pathways of movement, the degradation of which is associated with Parkinson's disease. The architecture could roughly be approximated with a series of organoids seeded with glutamatergic, dopaminergic, GABAergic and cholinergic neurons. Studies for Parkinson's disease that make use of an *in vitro* model typically use single cell populations in 2D culture. Often cell lines are employed due to ease of culture as such cell lines are capable of synthesising, metabolising and transporting dopamine although primary cells are still employed (Sridharan et al, 2015; Wang et al, 2014; Xu et al, 2014). One of the features of Parkinson's disease is the disruption of global neural circuitry in addition to the loss of neurons of the substantia nigra (Kim et al, 2017) and as such, an *in vitro* model that simulated the full circuit would be of greater relevance than *in vitro* models that focus solely on loss of neurons. In addition, white matter alterations precede gray matter alterations and white matter damage correlates with cognitive impairment for Parkinson's disease (Hattori et al, 2011), a 3D *in vitro* model with a greater focus on the white matter pathways is a necessity. In addition, white matter abnormalities have also been demonstrated to be involved with multiple other neurological pathologies such as Alzheimer's disease (Lee et al, 2016; Rieckmann et al, 2016), autism (Ameis and Catani, 2015) and schizophrenia (Fujino et al, 2014). The involvement of white matter abnormalities in so many pathological states warrants an engineered tissue that allows for controlled growth of white matter pathways as an increasingly physiological model in order to better understand these conditions. The cerebral

cortical organoid described within this thesis compartmentalises the cells in to distinct grey and white matter regions and with further research in to methods of inducing myelination of the neurites, could represent a means of generating macro-neural circuitry.

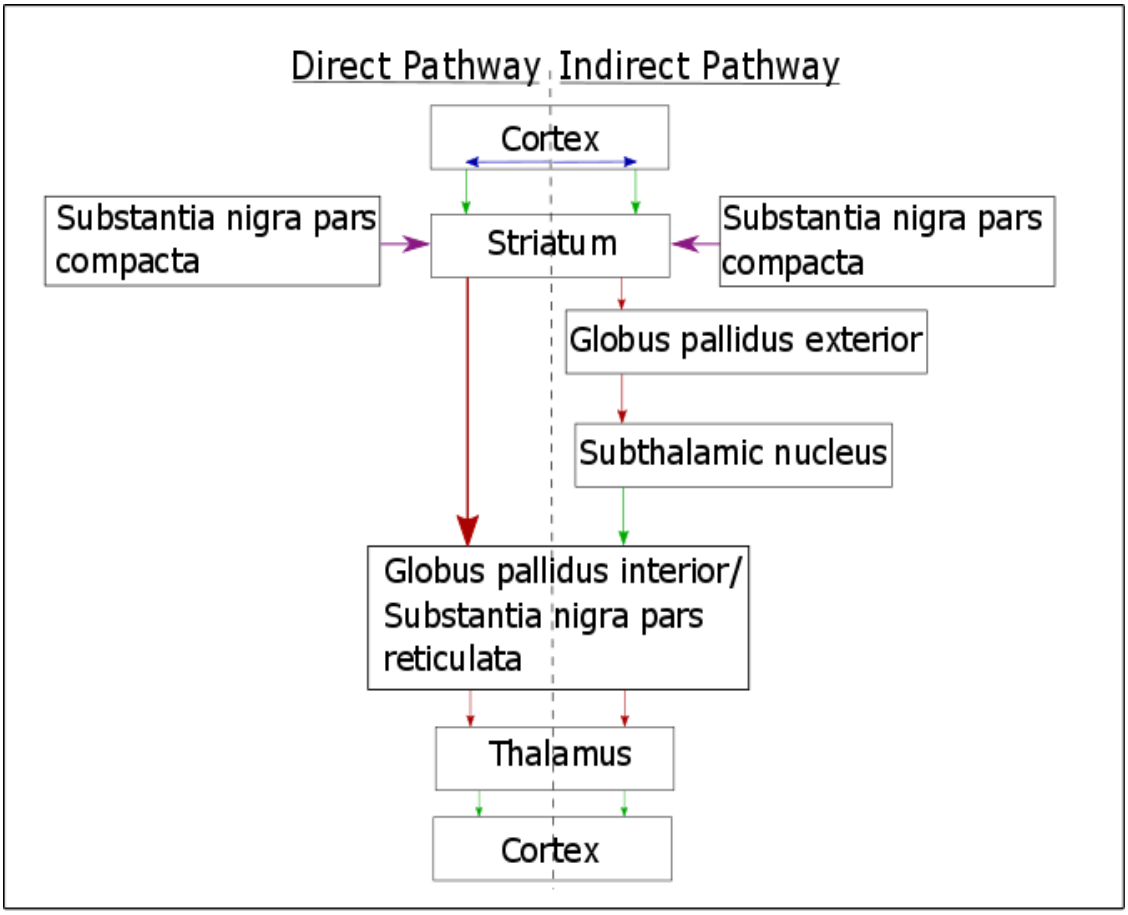


Figure 8.1: The direct and indirect motor pathways. The degeneration of these pathways is associated with Parkinson's disease. Green = glutamatergic, red = GABAergic, blue = acetylcholinergic, purple = dopaminergic. The motor pathway could be simulated with multiple TENNs complexed to form the macro-circuit.

### 8.3.3 Biomimetic Systems and Neurocontrollers

Artificial systems mimic biological neural networks due to the efficiency, adaptability and robustness of the biological neural network, yet 2D cultures are a reductionist system relative to the complexity of the *in vivo* neural networks. The *in vivo* brain represents a small world

network, a topology that is adaptive, efficient and dynamic (Bassett and Bullmore, 2006) whilst 2D conventional cultures are random networks. Small world networks have demonstrated the ability to reduce the learning time and error rate of artificial neural networks (Simard et al, 2005) and are optimal for information storage (Labiouse et al, 2002). 3D neuronal cultures can form small-world topologies (Severino et al, 2016; Dhobale et al, 2018), meriting their use in biohybrid systems over 2D cultures. The multiple synchrony regimes observed in 3D cultures (Severino et al, 2016; Dhobale et al, 2018; Frega et al, 2016) are indicative of multiple networks or complex dynamics, further supporting the idea that 3D cultures may be capable of performing computations that 2D cultures are too reductionist to perform. In addition, fasciculation of axons has been hypothesised to promote more reliable electrophysiological behaviours (Davis et al, 2017). With the 3D nature and fasciculated neurites, the cerebral cortical organoids may represent an opportunity to generate physiological neural networks that can be mimicked to improve the adaptability, robustness and efficiency of algorithms.

Additionally, due to the dynamic nature of biological systems, the field of robotics utilises hybrid systems of biological neural networks and artificial devices in order to overcome complex problems within the field (Vassanelli and Mahmud, 2016; Eiben et al, 2012). Multiple studies have demonstrated the ability to interface biological neurons with a synthetic body in order to study learning and plasticity and to develop algorithms that are tolerant to faults and are capable of self-repair (Webster-Wood et al, 2017). Dissociated neuronal cultures have been extensively used (DeMarse et al, 2001; Bakkum et al, 2004; Novellino et al, 2007; Warwick et al, 2010), however, the field would benefit from the use of more complex 3D neural structures. Neural architectures that mimic the *in vivo* architectures have been demonstrated to increase the effectiveness of these artificial devices (Webster-Wood et al, 2017). The studies listed thus far (DeMarse et al, 2001; Bakkum et al, 2004; Novellino et al, 2007; Warwick et al, 2010) utilise

dissociated neurons without imparting topologies upon them; random networks form from the dissociated neurons that are then restructured based on feedback loops and plasticity. Yet the problem remains that 2D randomly formed networks are less physiological than their organised 3D counterparts. At the time of writing, research utilising 3D neural architectures as neural controllers in artificial devices is limited. At least one group has utilised a neuromuscular circuit explant from *Aplysia californica* (Webster et al, 2017) whilst Frega et al (2016) developed a 3D neural network grown directly from dissociated neurons onto a microelectrode array and notes that it could be used as a biohybrid. Due to the nature of a tissue explant, the neuromuscular circuit explant from *Aplysia californica* suffers from the inherent organisation of the structure they are derived from; they are limited in size and structure is relatively determined with only plasticity to affect it (Webster et al, 2017). There is a need for self-assembling, adaptable and organised 3D neural structure that could be fulfilled by the cortical organoids to provide the patterned, robust neural circuitry that is required for biohybrid systems. Study of the electrophysiological properties of the organoids within this thesis were relatively shallow and further characterisation and spatial analysis of connectivity would be required, ideally with a microelectrode array.

### 8.3.4 Brain-machine interface

Brain-machine interfaces (BMI) are a developing aspect of neuroscience and can be utilised for repair (such as the cochlear implant for hearing loss or deep brain stimulation for movement disorders (Serruya et al, 2017)) or eventually, enhancement. BMIs require 3 components: a sensor capable of recording from a population of neurons; a decoder that can interpret the electrophysiological signals into commands; and actuators (Hochberg et al, 2006). TENNs represent one strategy for a stable, long term sensor capable of recording/stimulating activity with high resolution within the cortex. Intracortical electrodes are have several benefits over

extra-cranial systems; higher resolution of neuronal signal recordings and the ability to directly interface with the substrate that controlled activities prior to injury/disease (reducing the amount of time between input and output) (Hochberg and Donoghue, 2006). However, chronic implantation of invasive electrodes typically results in progressive loss of signal. Due to the mismatch between the elastic modulus of the brain and the electrode, chronic shear and differential motion occurs, resulting in microtraumas and chronic inflammation (Harris et al, 2011). Chronic inflammation occurs which is inherently neurodegenerative to the local neuronal population (McConnell et al, 2009). Methods of reducing the elastic modulus or reducing the shear stress/movement of the implant are being developed (Wu et al, 2015; Sohal et al, 2016; Sridharan et al, 2015) and a variety of methods of delivery that do not require needles, insertion shuttles or catheters are also being trialled (Harris et al, 2016; Vitale et al, 2017). Whilst these improvements to the existing methodologies are yielding promising results and increasing tolerance for the implants, there is an alternative.

Implanted intracortical electrodes attain their high resolution through their close contact to the neuron that originates the signal, in contrast to tools such as electroencephalography, which has low spatial resolution and poor source localisation due to the large distance between the origin and the point of signal recording (Hochberg and Donoghue, 2006). Due to the potential role for TENNs in re-wiring the brain as a long term implant, TENNs used to rewire must by necessity be non-inflammatory and possess a low elastic modulus to minimise glial scarring. As a result, TENNs could theoretically be used to reroute outputs to the surface of the brain, allowing for greater spatial resolution with a less invasive technique. The re-routing of connections could be achieved by inserting a unipolar TENN through the cortex, with the seeded end acting as a “biological electrode” and neurites extending within the niche of the TENN to the surface of the brain. Non-invasive, previously low resolution recording techniques

could then be used to detect neural signals from relatively deep regions of the cortex with a higher degree of resolution. Currently, only the Cullen research group (Harris et al, 2016; Adewole et al, 2017; Struzyna et al, 2018) have a TENN that possess the pre-requisites to perform the rewiring.

## 8.4 Conclusion

With the current stage of the research, aligned PLLA nanofibres can generate neurons with more accurate biochemical and morphological features than traditional 2D culture. In the immediate future, these biomaterial structures could be used within the pharmaceutical industry as models of neurons for drug discovery and toxicology. For all other applications, further validation studies are needed. For use in developmental neurobiology, time course data for the proteome and interactome would be needed to quantify the accuracy of the developmental programme of the neurons of the organoid relative to the developmental programme of the embryonic cerebral cortex. For regenerative medicine through rewiring, delivery remains a hurdle. Whilst the organoid can be self-assembled using the nanofibre membrane, it does not form in a controlled way, as discussed in Chapter 3. The laminar structure of the membrane is prohibitive to needle based insertion into the brain along ablated pathways and tailoring the structure towards a columnar structure would be necessary, possible with multiple sheets stacked to generate a 3D profile of the nanofibre sheets. Alternately, 3D columnar architectures of airgap electrospun nanofibres could be used to generate the desired implantable structures (Jha et al, 2011). Similar to the issues with regenerative medicine, assembly of macro-neuronal circuitry is dependent on the formation of the cellular structures in a controlled way. Further research using optical tweezers has been suggested as a means of combatting the random nature of seeding onto the membrane and controlling aggregation (Chapter 3).

In summary, the method of generating physiological architectures discussed within offers potential benefits to a wide range of industries and disciplines but for the purposes of rewiring of the cerebral cortex, a significant amount of additional work is required, most notably for the development of a delivery system.

# Appendix

## 9.1 Cells and Tissues

| **Item** | **Catalogue number** | **Company** |
|---|---|---|
| Sprague Dawley rat cortical neurons | CKit | Brainbits |
| Pregnant Sprague Dawley rats | - | Charles River |

Table 1: Cells and tissues used throughout the PhD

## 9.2 Reagents

| **Item** | **Catalogue number** | **Company** |
|---|---|---|
| Trypan blue | 1450021 | Biorad |
| NbActiv1 | NbActiv1500 | Brainbits |
| Hibernate-E without $Ca^{2+}$ | HECA | Brainbits |
| Protein inhibitor cocktail | 539197 | Calbiochem |
| Nanostring Murine Neuropathology Panel | N/A | Nanostring |
| RNeasy mini kit | 74104 | Qiagen |

| | | |
|---|---|---|
| T25 cell culture flasks | 83.391 | Sarstedt |
| T75 cell culture flasks | 83.3911 | Sarstedt |
| 6, 12, 24 well tissue culture plates | 83.3920, 83.3921, 83.3922 | Sarstedt |
| 15ml and 50ml red top tubes | 62.553.020, 62.559 | Sarstedt |
| Pipette filter tips; 10, 200 and 1000 µL | 70.1130, 70.760.102, 70.762.100 | Sarstedt |
| Microtubes (0.5, 1.5 and 2ml) | 72.699, 72.696, 72.708 | Sarstedt |
| Isopropanol | N/A | Sigma Aldrich |
| Dimethyl Sulfoxide | D2650 | Sigma-Aldrich |
| Penicillin-Streptomycin | P4333 | Sigma-Aldrich |
| Poly-L-lactic acid | 94829 | Sigma-Aldrich |
| Retinoic acid | R2625 | Sigma-Aldrich |
| Papain | P4762 | Sigma-Aldrich |
| Gentamicin | G1397 | Sigma-Aldrich |
| Urea | U5378 | Sigma-Aldrich |
| Octyl-Beta-Glycopyranoside | O8001 | Sigma-Aldrich |
| Dithiothreitol | D9779 | Sigma-Aldrich |
| Triton X-100 | X100 | Sigma-Aldrich |
| Paraformaldehyde | 158127 | Sigma-Aldrich |
| Glycine | G8898 | Sigma-Aldrich |

| | | |
|---|---|---|
| Tris | 10708976001 | Sigma-Aldrich |
| SDS | 74255 | Sigma-Aldrich |
| Acrylamide | A4058 | Sigma-Aldrich |
| HBSS (10x) without $Ca^{2+}$, $Mg^{2+}$ or phenol red | 14185045 | Thermo Fisher Scientific |
| StemPro Accutase | A1110501 | Thermo Fisher Scientific |
| DMEM/F12, glutamax supplement | 31331028 | Thermo Fisher Scientific |
| Fetal bovine serum | 10270106 | Thermo Fisher Scientific |
| Phosphate buffered saline, pH 7.4 | 10010023 | Thermo Fisher Scientific |
| Collagen type I, rat tail | A1048301 | Thermo Fisher Scientific |
| Media 199, 10x | 11825015 | Thermo Fisher Scientific |
| Phosphate buffered saline, 10x pH 7.4 | 70011044 | Thermo Fisher Scientific |
| Neurobasal | 21103049 | Thermo Fisher Scientific |
| B27 | 17504044 | Thermo Fisher Scientific |
| Glutamax | 35050061 | Thermo Fisher Scientific |
| Lowry assay kit | 23240 | Thermo Fisher Scientific |
| Hibernate-E with $Ca^{2+}$ | A1247601 | Thermo Fisher Scientific |
| Pierce LDH cytotoxicity assay kit | 1354269 | Thermo Fisher Scientific |
| Fluovolt | F10488 | Thermo Fisher Scientific |

| | | |
|---|---|---|
| Fura Red AM | F3021 | Thermo Fisher Scientific |
| AAV-hSyn-hChr2(H134R)-mCherry | N/A | Vectorcore |
| RNA Clean and Concentrator-5 | R1013 | Zymo |

Table 2: Reagents used throughout the course of the PhD

## 9.3 Antibodies

| **Item** | **Use** | **Catalogue number** | **Host species** | **Application (dilution)** | **Species reactivity** | **Company** |
|---|---|---|---|---|---|---|
| Anti-beta III Tubulin antibody [2G10] (Alexa Fluor® 488) | Primary | ab195879 | Mouse | 1:50 (IF), 1:1000 (WB) | Rat, human | Abcam |
| Anti-VDAC1 | Primary | D73D12 | Rabbit | 1:1000 (WB) | Mouse, rat, human | Cell Signalling Technology |
| Anti-mouse IgG, HRP linked | Secondary | 7076S | Horse | 1:1000 (WB) | - | Cell Signalling Technology |
| Anti-rabbit IgG, HRP linked | Secondary | 7074S | Goat | 1:1000 (WB) | - | Cell Signalling Technology |
| Anti-Chr2 [15E2] | Primary | 651180 | Mouse | 1:100 (IF) | - | Progen |
| Anti-Nestin (Rat-401) | Primary | Sc-33677 | Mouse | 1:50 (IF) | Mouse, rat, human | Santa-Cruz |

| | | | | | | |
|---|---|---|---|---|---|---|
| Anti-βIII tubulin | Primary | Sc-51670 | Mouse | 1:100 (IF) | Mouse, rat, human | Santa-Cruz |
| Anti-GFAP | Primary | Sc-65343 | Mouse | 1:100 (IF) | Rat, mouse, porcine, human | Santa-Cruz |
| Anti-mouse IgG-TRITC | Secondary | T5393-.5ml | Goat | 1:300 (IF) | All mouse IgG subclasses, IgA and IgM | Sigma Aldrich |
| Fluorescein anti-mouse IgG antibody | Secondary | FI-2000 | Horse | 1:300 (IF) | Mouse IgM, Rat IgG | Vector Laboratories |

Table 3: Antibody concentration, specificity and uses

## 9.4 Equipment

| **Equipment** | **Company** |
|---|---|
| TC20 Cell Counter | Biorad |
| Western Blotting Tank | Biorad |
| Clariostar Fluorescent Plate Reader | BMG Labtech |
| ImageQuant LAS 4000 | Fujifilm |
| JBA5 Water Bath | Grant instruments |

| | |
|---|---|
| Scanning Electron Microscope (JSM-7100F) | Jeol |
| Drop Shape Analyzer 10MK2 | Kruss |
| SP5 Confocal Microscope | Leica |
| Custom Electrospinning Rig | N/A |
| nCounter Analysis System | Nanostring |
| NE-1000 Syringe Pump | New Era Pump Systems |
| MCO-18AC- PE $CO_2$ Incubator | Panasonic |
| TripleTOF 6600 Mass Spectrometer | Sciex |
| Stuart Sb162 Heated Magnetic Stirrer | Sigma-Aldrich |
| Heraeus Multifuge X3 | Thermo Fisher Scientific |
| CO2 Laser Cutter, SP series | Trotec |

Table 4: Equipment and Suppliers of the equipment used throughout the PhD

## 9.5 Software

| **Software** | **Company** |
|---|---|
| Morpheus Heatmaps | Broad Institute |
| Metacore | Clarivate Analytics |
| Advanced Imaging Data Analyzer (AIDA) v 3.44 | Elysia-Raytest |
| Graphpad Prism v7.0 | Graphpad Software Inc |

| | |
|---|---|
| Statistical Package for the Social Sciences (SPSS) statistics 26 | IBM |
| Cytoscape | Institute of Systems Biology |
| ANNI algorithm | John Van Geest Cancer Centre, Nottingham Trent University |
| FIJI; ImageJ | Open Source Software |

Table 5: Software used over the course of the PhD

## 9.6 Mass Spectrometry raw data

| Protein Name | Protein | Fold Change (Control vs Nanofibres) | log 2 Fold Change (Control vs Nanofibres) | Confidence Value |
|---|---|---|---|---|
| PRDX4 | Peroxiredoxin-4 | 9.25 | 3.21 | 97.18% |
| TBB2B | Tubulin beta-2B chain | 11.75 | 3.56 | 95.24% |
| 2AAB | Serine/threonine-protein phosphatase 2A 65 kDa regulatory subunit A beta isoform | 2.95 | 1.56 | 93.04% |
| CFDP1 | Craniofacial development protein 1 | 13.24 | 3.73 | 92.91% |
| CUTA | Protein CutA | 2.60 | 1.38 | 89.75% |
| CK096 | Uncharacterized protein C11orf96 homolog | 2.26 | 1.18 | 89.52% |
| COX2 | Cytochrome c oxidase subunit 2 | 3.79 | 1.92 | 89.01% |
| HS90A | Heat shock protein HSP 90-alpha | -5.17 | -2.37 | 87.53% |
| JUPI1 | Hematological and neurological expressed 1 protein | 4.64 | 2.21 | 87.33% |
| DPYL2 | Dihydropyrimidinase-related protein 2 | 2.14 | 1.10 | 86.67% |
| PTMS | Parathymosin | 2.54 | 1.35 | 86.53% |
| INS1 | Insulin-1 | -6.53 | -2.71 | 86.45% |
| U2AF4 | Splicing factor U2AF 26 kDa subunit | 4.79 | 2.26 | 85.45% |
| FABP7 | Fatty acid-binding protein, brain | 3.28 | 1.71 | 85.21% |
| K2C1 | Keratin, type II cytoskeletal 1 | 7.46 | 2.90 | 85.12% |
| STMN2 | Stathmin-2 | 3.83 | 1.94 | 84.55% |
| AF1Q | Protein AF1q | 8.10 | 3.02 | 84.23% |
| RS20 | 40S ribosomal protein S20 | -4.87 | -2.28 | 84.09% |
| CPLX2 | Complexin-2 | -1.61 | -0.69 | 84.05% |
| RLA1 | 60S acidic ribosomal protein P1 | 4.77 | 2.25 | 83.56% |
| PGRC1 | Membrane-associated progesterone receptor component 1 | 6.49 | 2.70 | 83.00% |

| | | | | |
|---|---|---|---|---|
| MLP3B | Microtubule-associated proteins 1A/1B light chain 3B | -11.05 | -3.47 | 82.44% |
| SRSF6 | Serine/arginine-rich splicing factor 6 | 2.99 | 1.58 | 82.17% |
| EF1D | Elongation factor 1-delta | 2.59 | 1.38 | 82.08% |
| STMN1 | Stathmin | 3.43 | 1.78 | 82.03% |
| MCRI1 | Mapk-regulated corepressor-interacting protein 1 | 3.85 | 1.95 | 82.02% |
| COX5A | Cytochrome c oxidase subunit 5A, mitochondrial | 3.97 | 1.99 | 81.83% |
| T22D1 | TSC22 domain family protein 1 | 4.21 | 2.07 | 81.56% |
| RAB18 | Ras-related protein Rab-18 | 6.93 | 2.79 | 80.51% |
| RTN3 | Reticulon-3 | -2.27 | -1.18 | 80.26% |
| KCRB | Creatine kinase B-type | -2.82 | -1.50 | 79.88% |
| BASP1 | Brain acid soluble protein 1 | -4.04 | -2.01 | 79.36% |
| NOVA1 | RNA-binding protein Nova-1 | 2.54 | 1.34 | 79.28% |
| G6PI | Glucose-6-phosphate isomerase | -6.11 | -2.61 | 79.09% |
| SCRN1 | Secernin-1 | 3.32 | 1.73 | 79.01% |
| RL13A | 60S ribosomal protein L13a | -3.24 | -1.70 | 78.59% |
| K2C73 | Keratin, type II cytoskeletal 73 | 4.47 | 2.16 | 78.30% |
| 1433G | 14-3-3 protein gamma | 2.65 | 1.40 | 78.14% |
| SCG2 | Secretogranin-2 | 2.70 | 1.44 | 77.61% |
| TERA | Transitional endoplasmic reticulum ATPase | -5.31 | -2.41 | 77.53% |
| MARE1 | Microtubule-associated protein RP/EB family member 1 | -3.85 | -1.94 | 77.53% |
| RL17 | 60S ribosomal protein L17 | -3.42 | -1.77 | 77.13% |
| CNTN1 | Contactin-1 | 2.58 | 1.37 | 76.98% |
| ENOA | Alpha-enolase | 2.20 | 1.14 | 76.56% |
| NASP | Nuclear autoantigenic sperm protein | 3.11 | 1.64 | 76.55% |
| K2C5 | Keratin, type II cytoskeletal 5 | 5.22 | 2.38 | 76.45% |
| KPYM | Pyruvate kinase PKM | -3.02 | -1.59 | 76.34% |
| PTN | Pleiotrophin | -8.84 | -3.14 | 76.28% |
| RRAS | Ras-related protein R-Ras | 2.14 | 1.10 | 76.19% |
| TBCA | Tubulin-specific chaperone A | 2.48 | 1.31 | 76.16% |
| ATPB | ATP synthase subunit beta, mitochondrial | 4.41 | 2.14 | 76.04% |
| ACBP | Acyl-CoA-binding protein | 6.00 | 2.59 | 76.00% |
| HS90B | Heat shock protein HSP 90-beta | -1.77 | -0.82 | 75.97% |
| NSDHL | Sterol-4-alpha-carboxylate 3-dehydrogenase, decarboxylating | 2.71 | 1.44 | 75.88% |
| H14 | Histone H1.4 | 2.28 | 1.19 | 75.84% |
| FUBP2 | Far upstream element-binding protein 2 | 2.62 | 1.39 | 75.67% |
| MATR3 | Matrin-3 | -3.75 | -1.91 | 75.58% |
| ATIF1 | ATPase inhibitor, mitochondrial | 5.45 | 2.45 | 75.51% |
| RMXRL | RNA-binding motif protein, X chromosome retrogene-like | -3.05 | -1.61 | 75.51% |
| CIRBP | Cold-inducible RNA-binding protein | 5.85 | 2.55 | 75.31% |
| QCR1 | Cytochrome b-c1 complex subunit 1, mitochondrial | 4.73 | 2.24 | 75.15% |

| | | | | |
|---|---|---|---|---|
| CCD50 | Coiled-coil domain-containing protein 50 | 3.71 | 1.89 | 75.07% |
| BIP | 78 kDa glucose-regulated protein | 2.11 | 1.08 | 74.84% |
| SC22B | Vesicle-trafficking protein SEC22b | 3.04 | 1.60 | 74.74% |
| THIL | Acetyl-CoA acetyltransferase, mitochondrial | 3.62 | 1.86 | 74.62% |
| RL26 | 60S ribosomal protein L26 | -3.13 | -1.65 | 74.57% |
| H2AZ | Histone H2A.Z | -6.12 | -2.61 | 74.54% |
| RL5 | 60S ribosomal protein L5 | -3.60 | -1.85 | 74.49% |
| FABPH | Fatty acid-binding protein, heart | -5.15 | -2.37 | 74.40% |
| AINX | Alpha-internexin | 2.22 | 1.15 | 74.29% |
| VAMP2 | Vesicle-associated membrane protein 2 | 4.26 | 2.09 | 74.21% |
| K22E | Keratin, type II cytoskeletal 2 epidermal | 6.57 | 2.72 | 74.01% |
| ARP3 | Actin-related protein 3 | -2.92 | -1.54 | 73.96% |
| EIF3B | Eukaryotic translation initiation factor 3 subunit B | -2.87 | -1.52 | 73.67% |
| THIO | Thioredoxin | -4.72 | -2.24 | 73.51% |
| COX5B | Cytochrome c oxidase subunit 5B, mitochondrial | 3.02 | 1.59 | 73.50% |
| TYB10 | Thymosin beta-10 | 4.34 | 2.12 | 73.44% |
| DC1L1 | Cytoplasmic dynein 1 light intermediate chain 1 | -4.70 | -2.23 | 73.43% |
| FSCN1 | Fascin | -2.55 | -1.35 | 73.39% |
| PSMD9 | 26S proteasome non-ATPase regulatory subunit 9 | 2.98 | 1.57 | 73.35% |
| DEST | Destrin | -3.21 | -1.68 | 73.07% |
| PPIA | Peptidyl-prolyl cis-trans isomerase A | 2.14 | 1.10 | 73.03% |
| UCHL1 | Ubiquitin carboxyl-terminal hydrolase isozyme L1 | 3.03 | 1.60 | 73.00% |
| STXB1 | Syntaxin-binding protein 1 | -3.17 | -1.67 | 72.58% |
| RS13 | 40S ribosomal protein S13 | -3.56 | -1.83 | 72.53% |
| K1C10 | Keratin, type I cytoskeletal 10 | 6.10 | 2.61 | 72.53% |
| RTN4 | Reticulon-4 | 2.84 | 1.51 | 72.48% |
| G3P | Glyceraldehyde-3-phosphate dehydrogenase | -5.36 | -2.42 | 72.41% |
| ARPC2 | Actin-related protein 2/3 complex subunit 2 | -2.44 | -1.29 | 72.39% |
| RS19 | 40S ribosomal protein S19 | -8.47 | -3.08 | 72.30% |
| TCPD | T-complex protein 1 subunit delta | -3.67 | -1.88 | 72.20% |
| 1433Z | 14-3-3 protein zeta/delta | 3.24 | 1.70 | 72.10% |
| ARC1A | Actin-related protein 2/3 complex subunit 1A | -4.03 | -2.01 | 72.04% |
| RAN | GTP-binding nuclear protein Ran | -2.62 | -1.39 | 71.90% |
| DCX | Neuronal migration protein doublecortin | -3.04 | -1.61 | 71.74% |
| SF3B4 | Splicing factor 3B subunit 4 | 3.94 | 1.98 | 71.46% |
| ATP5J | ATP synthase-coupling factor 6, mitochondrial | 12.22 | 3.61 | 71.43% |
| RS12 | 40S ribosomal protein S12 | 2.47 | 1.30 | 71.33% |
| MEA1 | Male-enhanced antigen 1 | 7.55 | 2.92 | 71.31% |

| | | | | |
|---|---|---|---|---|
| FAF1 | FAS-associated factor 1 | -3.16 | -1.66 | 71.28% |
| MAP1B | Microtubule-associated protein 1B | 2.20 | 1.14 | 71.16% |
| ALBU | Serum albumin | 5.71 | 2.51 | 70.88% |
| RS16 | 40S ribosomal protein S16 | -5.73 | -2.52 | 70.80% |
| HGS | Hepatocyte growth factor-regulated tyrosine kinase substrate | 2.07 | 1.05 | 70.70% |
| KCY | UMP-CMP kinase | 4.38 | 2.13 | 70.42% |
| DPYL3 | Dihydropyrimidinase-related protein 3 | 2.25 | 1.17 | 70.40% |
| RSSA | 40S ribosomal protein SA | -3.27 | -1.71 | 70.33% |
| UFD1 | Ubiquitin fusion degradation protein 1 homolog | -4.76 | -2.25 | 70.28% |
| CH10 | 10 kDa heat shock protein, mitochondrial | 2.74 | 1.45 | 70.20% |
| THIC | Acetyl-CoA acetyltransferase, cytosolic | 3.71 | 1.89 | 69.90% |
| KAD1 | Adenylate kinase isoenzyme 1 | 2.81 | 1.49 | 69.69% |
| CH60 | 60 kDa heat shock protein, mitochondrial | 2.72 | 1.45 | 69.52% |
| 1433T | 14-3-3 protein theta | -3.64 | -1.86 | 69.51% |
| PSB6 | Proteasome subunit beta type-6 | 2.84 | 1.50 | 69.45% |
| STIP1 | Stress-induced-phosphoprotein 1 | -2.34 | -1.23 | 69.38% |
| ODPB | Pyruvate dehydrogenase E1 component subunit beta, mitochondrial | 4.57 | 2.19 | 69.25% |
| VIME | Vimentin | 3.33 | 1.74 | 69.25% |
| RS14 | 40S ribosomal protein S14 | -3.40 | -1.76 | 69.17% |
| MYG1 | UPF0160 protein MYG1, mitochondrial | 4.19 | 2.07 | 69.10% |
| TTC5 | Tetratricopeptide repeat protein 5 | -16.38 | -4.03 | 68.84% |
| CLIP2 | CAP-Gly domain-containing linker protein 2 | 2.87 | 1.52 | 68.83% |
| PFD2 | Prefoldin subunit 2 | 2.04 | 1.03 | 68.83% |
| RL35A | 60S ribosomal protein L35a | -24.08 | -4.59 | 68.73% |
| RL12 | 60S ribosomal protein L12 | -5.43 | -2.44 | 68.69% |
| RL22 | 60S ribosomal protein L22 | -1.84 | -0.88 | 68.65% |
| IDHC | Isocitrate dehydrogenase [NADP] cytoplasmic | -2.27 | -1.18 | 68.62% |
| DC1I1 | Cytoplasmic dynein 1 intermediate chain 1 | 3.17 | 1.67 | 68.52% |
| NDUV2 | NADH dehydrogenase [ubiquinone] flavoprotein 2, mitochondrial | 2.57 | 1.36 | 68.42% |
| PHB2 | Prohibitin-2 | -5.63 | -2.49 | 68.31% |
| TBB3 | Tubulin beta-3 chain | -3.38 | -1.76 | 68.15% |
| RL10 | 60S ribosomal protein L10 | -8.24 | -3.04 | 68.02% |
| NOLC1 | Nucleolar and coiled-body phosphoprotein 1 | -4.76 | -2.25 | 67.72% |
| RS23 | 40S ribosomal protein S23 | -4.07 | -2.02 | 67.65% |
| FABP5 | Fatty acid-binding protein, epidermal | -4.31 | -2.11 | 67.50% |
| F10A1 | Hsc70-interacting protein | -3.00 | -1.59 | 67.43% |
| COF1 | Cofilin-1 | -2.64 | -1.40 | 67.40% |
| RL15 | 60S ribosomal protein L15 | -1.91 | -0.93 | 67.37% |

| | | | | |
|---|---|---|---|---|
| NUCB1 | Nucleobindin-1 | 4.76 | 2.25 | 67.22% |
| TCTP | Translationally-controlled tumor protein | 1.94 | 0.95 | 67.05% |
| PEA15 | Astrocytic phosphoprotein PEA-15 | 2.55 | 1.35 | 66.77% |
| CALX | Calnexin | 3.43 | 1.78 | 66.75% |
| K1C19 | Keratin, type I cytoskeletal 19 | 7.30 | 2.87 | 66.70% |
| TYB4 | Thymosin beta-4 | -7.41 | -2.89 | 66.60% |
| NTF2 | Nuclear transport factor 2 | 2.41 | 1.27 | 66.60% |
| CSN2 | COP9 signalosome complex subunit 2 | -2.83 | -1.50 | 66.52% |
| RS3 | 40S ribosomal protein S3 | -3.60 | -1.85 | 66.42% |
| ATPD | ATP synthase subunit delta, mitochondrial | 3.57 | 1.84 | 66.41% |
| NDUS6 | NADH dehydrogenase [ubiquinone] iron-sulfur protein 6, mitochondrial | 2.99 | 1.58 | 66.28% |
| RL27 | 60S ribosomal protein L27 | -11.94 | -3.58 | 66.13% |
| PP14B | Protein phosphatase 1 regulatory subunit 14B | -3.96 | -1.99 | 66.00% |
| GRAP1 | GRIP1-associated protein 1 | 3.09 | 1.63 | 65.63% |
| AP2B1 | AP-2 complex subunit beta | -5.44 | -2.44 | 65.60% |
| MEP50 | Methylosome protein 50 | 4.12 | 2.04 | 65.56% |
| PPP6 | Serine/threonine-protein phosphatase 6 catalytic subunit | 5.65 | 2.50 | 65.55% |
| NDUAA | NADH dehydrogenase [ubiquinone] 1 alpha subcomplex subunit 10, mitochondrial | 5.33 | 2.42 | 65.44% |
| MARE2 | Microtubule-associated protein RP/EB family member 2 | 3.39 | 1.76 | 65.34% |
| NEUM | Neuromodulin | -3.10 | -1.63 | 65.27% |
| RS28 | 40S ribosomal protein S28 | 7.67 | 2.94 | 64.95% |
| RAB1B | Ras-related protein Rab-1B | -2.08 | -1.06 | 64.63% |
| TRY3 | Cationic trypsin-3 | -6.37 | -2.67 | 64.51% |
| ROA3 | Heterogeneous nuclear ribonucleoprotein A3 | -3.05 | -1.61 | 64.47% |
| CISY | Citrate synthase, mitochondrial | -4.53 | -2.18 | 64.21% |
| AK1A1 | Alcohol dehydrogenase [NADP(+)] | -3.70 | -1.89 | 64.16% |
| ELAV1 | ELAV-like protein 1 | -3.07 | -1.62 | 63.99% |
| QCR2 | Cytochrome b-c1 complex subunit 2, mitochondrial | -3.31 | -1.73 | 63.86% |
| ROA1 | Heterogeneous nuclear ribonucleoprotein A1 | -2.98 | -1.57 | 63.75% |
| SMS | Somatostatin | 7.61 | 2.93 | 63.74% |
| MOFA1 | MORF4 family-associated protein 1 | 3.76 | 1.91 | 63.65% |
| PDIA4 | Protein disulfide-isomerase A4 | -5.41 | -2.44 | 63.52% |
| 40057 | Septin-9 | -3.99 | -2.00 | 63.48% |
| SFR1 | Swi5-dependent recombination DNA repair protein 1 homolog | 2.17 | 1.12 | 63.16% |
| GOGA2 | Golgin subfamily A member 2 | 3.63 | 1.86 | 63.11% |
| CSRP2 | Cysteine and glycine-rich protein 2 | -4.13 | -2.05 | 63.03% |
| PSB5 | Proteasome subunit beta type-5 | -4.68 | -2.23 | 62.76% |
| NUP62 | Nuclear pore glycoprotein p62 | -2.18 | -1.12 | 62.75% |

| | | | | |
|---|---|---|---|---|
| 1433F | 14-3-3 protein eta | 6.15 | 2.62 | 62.75% |
| PPID | Peptidyl-prolyl cis-trans isomerase D | -8.56 | -3.10 | 62.72% |
| ARP2 | Actin-related protein 2 | -2.44 | -1.29 | 62.65% |
| TRY1 | Anionic trypsin-1 | -1.90 | -0.92 | 62.58% |
| CDC37 | Hsp90 co-chaperone Cdc37 | 1.33 | 0.41 | 62.57% |
| DLRB1 | Dynein light chain roadblock-type 1 | 2.18 | 1.12 | 62.43% |
| PTMA | Prothymosin alpha | 2.02 | 1.01 | 62.32% |
| INS2 | Insulin-2 | 2.06 | 1.04 | 62.09% |
| EF1A2 | Elongation factor 1-alpha 2 | -4.96 | -2.31 | 62.04% |
| TXD12 | Thioredoxin domain-containing protein 12 | 3.36 | 1.75 | 61.80% |
| RS18 | 40S ribosomal protein S18 | -5.49 | -2.46 | 61.50% |
| HBB1 | Hemoglobin subunit beta-1 | 4.10 | 2.04 | 61.42% |
| VGF | Neurosecretory protein VGF | 3.34 | 1.74 | 61.29% |
| CATA | Catalase | 2.44 | 1.29 | 61.26% |
| RL14 | 60S ribosomal protein L14 | -3.14 | -1.65 | 60.86% |
| SYUB | Beta-synuclein | 3.19 | 1.67 | 60.65% |
| HNRPM | Heterogeneous nuclear ribonucleoprotein M | -3.01 | -1.59 | 60.53% |
| DDX4 | Probable ATP-dependent RNA helicase DDX4 | -2.54 | -1.34 | 60.13% |
| RS3A | 40S ribosomal protein S3a | -4.20 | -2.07 | 60.08% |
| IF4A2 | Eukaryotic initiation factor 4A-II | -1.45 | -0.54 | 60.06% |
| K2C1B | Keratin, type II cytoskeletal 1b | 6.39 | 2.68 | 60.03% |
| TBB4B | Tubulin beta-4B chain | 1.82 | 0.86 | 59.87% |
| RLA2 | 60S acidic ribosomal protein P2 | 3.05 | 1.61 | 59.86% |
| DNJA2 | DnaJ homolog subfamily A member 2 | -4.70 | -2.23 | 59.60% |
| IMB1 | Importin subunit beta-1 | 4.44 | 2.15 | 59.55% |
| ALDH2 | Aldehyde dehydrogenase, mitochondrial | -8.73 | -3.13 | 59.35% |
| COR1B | Coronin-1B | -5.05 | -2.34 | 59.29% |
| NUCKS | Nuclear ubiquitous casein and cyclin-dependent kinase substrate 1 | -1.97 | -0.98 | 59.16% |
| ALDR | Aldose reductase | 1.96 | 0.97 | 59.02% |
| EF1G | Elongation factor 1-gamma | -1.79 | -0.84 | 58.93% |
| SUMO2 | Small ubiquitin-related modifier 2 | 1.47 | 0.56 | 58.77% |
| DCTN2 | Dynactin subunit 2 | 2.33 | 1.22 | 58.43% |
| IF4A3 | Eukaryotic initiation factor 4A-III | -1.64 | -0.71 | 58.40% |
| TBB5 | Tubulin beta-5 chain | -2.82 | -1.49 | 58.37% |
| GNAO | Guanine nucleotide-binding protein G(o) subunit alpha | 1.88 | 0.91 | 58.19% |
| MARCS | Myristoylated alanine-rich C-kinase substrate | -3.35 | -1.75 | 57.99% |
| TIM8B | Mitochondrial import inner membrane translocase subunit Tim8 B | 6.24 | 2.64 | 57.77% |
| ALDOA | Fructose-bisphosphate aldolase A | -4.24 | -2.08 | 57.59% |
| H15 | Histone H1.5 | 3.03 | 1.60 | 57.40% |
| MVD1 | Diphosphomevalonate decarboxylase | -3.25 | -1.70 | 57.35% |

| | | | | |
|---|---|---|---|---|
| PP2AB | Serine/threonine-protein phosphatase 2A catalytic subunit beta isoform | 1.93 | 0.95 | 57.34% |
| VIGLN | Vigilin | -2.97 | -1.57 | 57.34% |
| HSP7C | Heat shock cognate 71 kDa protein | 1.82 | 0.86 | 57.27% |
| RS29 | 40S ribosomal protein S29 | -4.82 | -2.27 | 57.07% |
| MLP3A | Microtubule-associated proteins 1A/1B light chain 3A | -3.63 | -1.86 | 57.05% |
| NCAN | Neurocan core protein | 3.81 | 1.93 | 56.99% |
| AP2S1 | AP-2 complex subunit sigma | -13.79 | -3.79 | 56.90% |
| SERA | D-3-phosphoglycerate dehydrogenase | 4.88 | 2.29 | 56.87% |
| ATPG | ATP synthase subunit gamma, mitochondrial | -9.70 | -3.28 | 56.86% |
| SYTC | Threonine--tRNA ligase, cytoplasmic | -6.36 | -2.67 | 56.71% |
| AATC | Aspartate aminotransferase, cytoplasmic | -6.54 | -2.71 | 56.58% |
| PSMD1 | 26S proteasome non-ATPase regulatory subunit 1 | -5.33 | -2.41 | 56.56% |
| PSA3 | Proteasome subunit alpha type-3 | -2.39 | -1.26 | 56.45% |
| APBA1 | Amyloid beta A4 precursor protein-binding family A member 1 | -3.84 | -1.94 | 56.42% |
| HSBP1 | Heat shock factor-binding protein 1 | 2.74 | 1.45 | 56.37% |
| ML12B | Myosin regulatory light chain 12B | -6.87 | -2.78 | 56.26% |
| VDAC2 | Voltage-dependent anion-selective channel protein 2 | 2.28 | 1.19 | 56.26% |
| SNP25 | Synaptosomal-associated protein 25 | 5.19 | 2.38 | 56.16% |
| MARE3 | Microtubule-associated protein RP/EB family member 3 | -2.75 | -1.46 | 56.02% |
| 1433E | 14-3-3 protein epsilon | -3.80 | -1.92 | 55.98% |
| PA1B3 | Platelet-activating factor acetylhydrolase IB subunit gamma | -4.78 | -2.26 | 55.91% |
| RL10A | 60S ribosomal protein L10a | -4.28 | -2.10 | 55.73% |
| NFM | Neurofilament medium polypeptide | 3.71 | 1.89 | 55.69% |
| SUCA | Succinate--CoA ligase [ADP/GDP-forming] subunit alpha, mitochondrial | -3.14 | -1.65 | 55.46% |
| PCP4 | Purkinje cell protein 4 | 2.99 | 1.58 | 55.29% |
| TPM3 | Tropomyosin alpha-3 chain | 4.02 | 2.01 | 55.26% |
| LDHA | L-lactate dehydrogenase A chain | -4.52 | -2.18 | 55.24% |
| RL8 | 60S ribosomal protein L8 | -2.77 | -1.47 | 55.12% |
| GNAI3 | Guanine nucleotide-binding protein G(k) subunit alpha | -3.38 | -1.76 | 54.99% |
| RS5 | 40S ribosomal protein S5 | -6.94 | -2.80 | 54.98% |
| PAK3 | Serine/threonine-protein kinase PAK 3 | -2.69 | -1.43 | 54.86% |
| GDIA | Rab GDP dissociation inhibitor alpha | -3.14 | -1.65 | 54.63% |
| GBRL2 | Gamma-aminobutyric acid receptor-associated protein-like 2 | -1.95 | -0.96 | 54.63% |
| NSF1C | NSFL1 cofactor p47 | 2.40 | 1.26 | 54.60% |
| RAB3A | Ras-related protein Rab-3A | 1.55 | 0.63 | 54.51% |
| ATAT | Alpha-tubulin N-acetyltransferase 1 | -9.09 | -3.18 | 54.49% |
| RS15A | 40S ribosomal protein S15a | -5.77 | -2.53 | 54.43% |

| | | | | |
|---|---|---|---|---|
| GSTP1 | Glutathione S-transferase P | -1.32 | -0.40 | 54.41% |
| IF5A1 | Eukaryotic translation initiation factor 5A-1 | -2.68 | -1.42 | 54.35% |
| HNRPD | Heterogeneous nuclear ribonucleoprotein D0 | -2.45 | -1.29 | 54.32% |
| K1C42 | Keratin, type I cytoskeletal 42 | 5.17 | 2.37 | 54.31% |
| PA1B2 | Platelet-activating factor acetylhydrolase IB subunit beta | -3.79 | -1.92 | 54.28% |
| SDHB | Succinate dehydrogenase [ubiquinone] iron-sulfur subunit, mitochondrial | -6.98 | -2.80 | 54.20% |
| KAPCB | cAMP-dependent protein kinase catalytic subunit beta | -2.21 | -1.14 | 54.19% |
| ROA2 | Heterogeneous nuclear ribonucleoproteins A2/B1 | 3.13 | 1.65 | 54.17% |
| PSA4 | Proteasome subunit alpha type-4 | -3.45 | -1.79 | 54.16% |
| OGA | Protein O-GlcNAcase | 4.50 | 2.17 | 54.06% |
| DBNL | Drebrin-like protein | 3.41 | 1.77 | 53.98% |
| STML2 | Stomatin-like protein 2, mitochondrial | -5.85 | -2.55 | 53.95% |
| ATOX1 | Copper transport protein ATOX1 | 2.28 | 1.19 | 53.92% |
| TBA1A | Tubulin alpha-1A chain | -2.25 | -1.17 | 53.88% |
| H4 | Histone H4 | -6.80 | -2.77 | 53.81% |
| PRDX2 | Peroxiredoxin-2 | 1.83 | 0.87 | 53.76% |
| IMDH2 | Inosine-5'-monophosphate dehydrogenase 2 | -3.67 | -1.87 | 53.73% |
| CNN3 | Calponin-3 | -3.52 | -1.82 | 53.68% |
| COPG1 | Coatomer subunit gamma-1 | 2.63 | 1.40 | 53.61% |
| RAB5A | Ras-related protein Rab-5A | 7.10 | 2.83 | 53.51% |
| RL34 | 60S ribosomal protein L34 | -2.97 | -1.57 | 53.38% |
| CYTB | Cystatin-B | -4.42 | -2.14 | 53.33% |
| SIR5 | NAD-dependent protein deacylase sirtuin-5, mitochondrial | -2.29 | -1.20 | 52.94% |
| NPL4 | Nuclear protein localization protein 4 homolog | -8.13 | -3.02 | 52.93% |
| PHOCN | MOB-like protein phocein | 2.68 | 1.42 | 52.92% |
| CAN2 | Calpain-2 catalytic subunit | 1.95 | 0.97 | 52.77% |
| NH2L1 | NHP2-like protein 1 | 2.13 | 1.09 | 52.68% |
| RS25 | 40S ribosomal protein S25 | -3.61 | -1.85 | 52.63% |
| REEP5 | Receptor expression-enhancing protein 5 | -9.07 | -3.18 | 52.62% |
| KAPCA | cAMP-dependent protein kinase catalytic subunit alpha | -7.31 | -2.87 | 52.62% |
| RL23 | 60S ribosomal protein L23 | -2.06 | -1.04 | 52.61% |
| 6PGD | 6-phosphogluconate dehydrogenase, decarboxylating | -3.80 | -1.93 | 52.60% |
| PSB4 | Proteasome subunit beta type-4 | -4.93 | -2.30 | 52.37% |
| SNX3 | Sorting nexin-3 | 1.87 | 0.90 | 52.21% |
| EMC2 | ER membrane protein complex subunit 2 | -4.35 | -2.12 | 52.19% |
| RL13 | 60S ribosomal protein L13 | -3.05 | -1.61 | 52.16% |
| PLD3 | Phospholipase D3 | -6.04 | -2.59 | 52.15% |

| | | | | |
|---|---|---|---|---|
| PCNA | Proliferating cell nuclear antigen | -6.23 | -2.64 | 52.12% |
| ARL3 | ADP-ribosylation factor-like protein 3 | -3.82 | -1.93 | 52.12% |
| PROF1 | Profilin-1 | -6.31 | -2.66 | 52.07% |
| 1433B | 14-3-3 protein beta/alpha | 2.00 | 1.00 | 52.05% |
| CPSM | Carbamoyl-phosphate synthase [ammonia], mitochondrial | 2.08 | 1.05 | 51.96% |
| SRSF2 | Serine/arginine-rich splicing factor 2 | 5.19 | 2.38 | 51.88% |
| NDKB | Nucleoside diphosphate kinase B | -4.31 | -2.11 | 51.86% |
| GDIB | Rab GDP dissociation inhibitor beta | -3.17 | -1.67 | 51.83% |
| ODPA | Pyruvate dehydrogenase E1 component subunit alpha, somatic form, mitochondrial | -4.07 | -2.02 | 51.82% |
| RD23B | UV excision repair protein RAD23 homolog B | -4.80 | -2.26 | 51.82% |
| UBE2N | Ubiquitin-conjugating enzyme E2 N | -2.88 | -1.53 | 51.69% |
| SAP | Prosaposin | 3.56 | 1.83 | 51.61% |
| RS6 | 40S ribosomal protein S6 | -4.88 | -2.29 | 51.57% |
| RSMN | Small nuclear ribonucleoprotein-associated protein N | -3.38 | -1.76 | 51.51% |
| SYVC | Valine--tRNA ligase | -3.37 | -1.75 | 51.44% |
| H2A2A | Histone H2A type 2-A | -5.24 | -2.39 | 51.39% |
| COTL1 | Coactosin-like protein | -3.61 | -1.85 | 51.37% |
| ERF1 | Eukaryotic peptide chain release factor subunit 1 | -3.23 | -1.69 | 51.28% |
| GSTM1 | Glutathione S-transferase Mu 1 | -2.07 | -1.05 | 51.26% |
| CNBP | Cellular nucleic acid-binding protein | -2.22 | -1.15 | 51.12% |
| PSA7 | Proteasome subunit alpha type-7 | -2.97 | -1.57 | 51.07% |
| KPRP | Keratinocyte proline-rich protein | 3.27 | 1.71 | 51.03% |
| P5CR3 | Pyrroline-5-carboxylate reductase 3 | 1.87 | 0.90 | 51.01% |
| PP1R7 | Protein phosphatase 1 regulatory subunit 7 | 13.70 | 3.78 | 51.01% |
| CAPR1 | Caprin-1 | 2.72 | 1.44 | 50.77% |
| AMRP | Alpha-2-macroglobulin receptor-associated protein | 2.74 | 1.46 | 50.75% |
| HMGB1 | High mobility group protein B1 | -3.48 | -1.80 | 50.62% |
| PSB2 | Proteasome subunit beta type-2 | -8.46 | -3.08 | 50.50% |
| NONO | Non-POU domain-containing octamer-binding protein | 3.42 | 1.78 | 50.44% |
| PSA5 | Proteasome subunit alpha type-5 | 2.15 | 1.11 | 50.42% |
| 4F2 | 4F2 cell-surface antigen heavy chain | 2.46 | 1.30 | 50.42% |
| AMPH | Amphiphysin | -3.15 | -1.66 | 50.39% |
| RL18A | 60S ribosomal protein L18a | -5.06 | -2.34 | 50.35% |
| ATP5E | ATP synthase subunit epsilon, mitochondrial | -8.04 | -3.01 | 50.24% |
| TBB2A | Tubulin beta-2A chain | -5.55 | -2.47 | 50.14% |
| PROF2 | Profilin-2 | 3.37 | 1.75 | 50.01% |
| PP2AA | Serine/threonine-protein phosphatase 2A catalytic subunit alpha isoform | -7.10 | -2.83 | 50.00% |
| UBA1 | Ubiquitin-like modifier-activating enzyme 1 | -2.37 | -1.24 | 49.95% |

| | | | | |
|---|---|---|---|---|
| RS11 | 40S ribosomal protein S11 | -4.49 | -2.17 | 49.95% |
| CBPE | Carboxypeptidase E | 2.89 | 1.53 | 49.86% |
| ADRM1 | Proteasomal ubiquitin receptor ADRM1 | 2.67 | 1.42 | 49.75% |
| ELOC | Elongin-C | -4.75 | -2.25 | 49.45% |
| ENOG | Gamma-enolase | 1.93 | 0.95 | 49.39% |
| PRDX3 | Thioredoxin-dependent peroxide reductase, mitochondrial | -2.64 | -1.40 | 49.27% |
| RBM8A | RNA-binding protein 8A | 2.72 | 1.45 | 49.21% |
| AN32A | Acidic leucine-rich nuclear phosphoprotein 32 family member A | -2.14 | -1.10 | 49.15% |
| PPAC | Low molecular weight phosphotyrosine protein phosphatase | 2.10 | 1.07 | 49.10% |
| CAP1 | Adenylyl cyclase-associated protein 1 | -3.86 | -1.95 | 49.04% |
| DC1L2 | Cytoplasmic dynein 1 light intermediate chain 2 | -4.94 | -2.30 | 48.85% |
| NDRG3 | Protein NDRG3 | -2.31 | -1.21 | 48.77% |
| PTBP2 | Polypyrimidine tract-binding protein 2 | -4.87 | -2.28 | 48.73% |
| DDX1 | ATP-dependent RNA helicase DDX1 | -3.47 | -1.80 | 48.70% |
| SMCA4 | Transcription activator BRG1 | -3.16 | -1.66 | 48.59% |
| TOLIP | Toll-interacting protein | 3.54 | 1.83 | 48.55% |
| PICAL | Phosphatidylinositol-binding clathrin assembly protein | -3.17 | -1.66 | 48.51% |
| GSTM5 | Glutathione S-transferase Mu 5 | 6.62 | 2.73 | 48.49% |
| MDHM | Malate dehydrogenase, mitochondrial | -2.71 | -1.44 | 48.48% |
| PDCD6 | Programmed cell death protein 6 | -6.26 | -2.65 | 48.43% |
| GPM6A | Neuronal membrane glycoprotein M6-a | -3.28 | -1.71 | 48.40% |
| CATB | Cathepsin B | 2.93 | 1.55 | 48.12% |
| RL4 | 60S ribosomal protein L4 | -1.82 | -0.87 | 48.12% |
| PCNP | PEST proteolytic signal-containing nuclear protein | 3.67 | 1.87 | 48.09% |
| PIMT | Protein-L-isoaspartate(D-aspartate) O-methyltransferase | 5.20 | 2.38 | 48.04% |
| EF1A1 | Elongation factor 1-alpha 1 | -3.68 | -1.88 | 48.00% |
| ATPO | ATP synthase subunit O, mitochondrial | -3.47 | -1.80 | 47.98% |
| TAU | Microtubule-associated protein tau | 1.96 | 0.97 | 47.94% |
| PCYOX | Prenylcysteine oxidase | -5.32 | -2.41 | 47.76% |
| RL30 | 60S ribosomal protein L30 | -2.37 | -1.25 | 47.65% |
| DREB | Drebrin | -2.02 | -1.01 | 47.56% |
| COPD | Coatomer subunit delta | -3.43 | -1.78 | 47.53% |
| SERB | Phosphoserine phosphatase | -2.34 | -1.23 | 47.53% |
| PABP1 | Polyadenylate-binding protein 1 | -2.62 | -1.39 | 47.49% |
| SOSB1 | SOSS complex subunit B1 | -3.15 | -1.66 | 47.49% |
| SYT1 | Synaptotagmin-1 | -3.69 | -1.88 | 47.45% |
| CALR | Calreticulin | -1.65 | -0.72 | 47.44% |
| PSB1 | Proteasome subunit beta type-1 | -2.35 | -1.23 | 47.40% |

| | | | | |
|---|---|---|---|---|
| CYC | Cytochrome c, somatic | -3.56 | -1.83 | 47.28% |
| TIM8A | Mitochondrial import inner membrane translocase subunit Tim8 A | 2.83 | 1.50 | 47.25% |
| FETUA | Alpha-2-HS-glycoprotein | -5.79 | -2.53 | 47.18% |
| CD47 | Leukocyte surface antigen CD47 | 2.96 | 1.56 | 46.91% |
| CSK21 | Casein kinase II subunit alpha | -3.12 | -1.64 | 46.90% |
| PP1B | Serine/threonine-protein phosphatase PP1-beta catalytic subunit | -3.49 | -1.80 | 46.82% |
| RL28 | 60S ribosomal protein L28 | -9.78 | -3.29 | 46.74% |
| RL11 | 60S ribosomal protein L11 | -5.86 | -2.55 | 46.71% |
| FBRL | rRNA 2'-O-methyltransferase fibrillarin | -5.91 | -2.56 | 46.68% |
| EIF3G | Eukaryotic translation initiation factor 3 subunit G | -7.17 | -2.84 | 46.67% |
| CBR1 | Carbonyl reductase [NADPH] 1 | -4.44 | -2.15 | 46.51% |
| HXK1 | Hexokinase-1 | -6.15 | -2.62 | 46.43% |
| TPIS | Triosephosphate isomerase | -1.94 | -0.96 | 46.07% |
| TXNL1 | Thioredoxin-like protein 1 | 3.86 | 1.95 | 46.05% |
| CALM3 | Calmodulin-3 | -4.78 | -2.26 | 46.03% |
| C1QBP | Complement component 1 Q subcomponent-binding protein, mitochondrial | -5.64 | -2.49 | 46.01% |
| IPKA | cAMP-dependent protein kinase inhibitor alpha | 3.24 | 1.70 | 46.00% |
| PEPD | Xaa-Pro dipeptidase | -3.72 | -1.89 | 45.90% |
| TPD54 | Tumor protein D54 | 4.76 | 2.25 | 45.78% |
| RACK1 | Receptor of activated protein C kinase 1 | -3.81 | -1.93 | 45.72% |
| SHLB1 | Endophilin-B1 | -4.68 | -2.23 | 45.72% |
| NP1L1 | Nucleosome assembly protein 1-like 1 | -2.95 | -1.56 | 45.70% |
| AN32B | Acidic leucine-rich nuclear phosphoprotein 32 family member B | 11.08 | 3.47 | 45.69% |
| MINK1 | Misshapen-like kinase 1 | -4.78 | -2.26 | 45.66% |
| TIM9 | Mitochondrial import inner membrane translocase subunit Tim9 | -4.65 | -2.22 | 45.66% |
| MYL6 | Myosin light polypeptide 6 | 2.25 | 1.17 | 45.64% |
| KHDR3 | KH domain-containing, RNA-binding, signal transduction-associated protein 3 | -5.02 | -2.33 | 45.59% |
| NCALD | Neurocalcin-delta | -3.32 | -1.73 | 45.58% |
| PEBP1 | Phosphatidylethanolamine-binding protein 1 | -1.87 | -0.90 | 45.57% |
| RLA0 | 60S acidic ribosomal protein P0 | -3.01 | -1.59 | 45.57% |
| FXR1 | Fragile X mental retardation syndrome-related protein 1 | 1.93 | 0.95 | 45.57% |
| ENPL | Endoplasmin | -3.65 | -1.87 | 45.53% |
| MIF | Macrophage migration inhibitory factor | 2.40 | 1.26 | 45.52% |
| FUBP1 | Far upstream element-binding protein 1 | 2.84 | 1.51 | 45.52% |
| ADT1 | ADP/ATP translocase 1 | -4.25 | -2.09 | 45.51% |

| | | | | |
|---|---|---|---|---|
| TIM13 | Mitochondrial import inner membrane translocase subunit Tim13 | 2.96 | 1.57 | 45.36% |
| SPTN2 | Spectrin beta chain, non-erythrocytic 2 | -4.96 | -2.31 | 45.34% |
| VAPA | Vesicle-associated membrane protein-associated protein A | -1.56 | -0.64 | 45.32% |
| K1C14 | Keratin, type I cytoskeletal 14 | 5.22 | 2.38 | 45.31% |
| BZW1 | Basic leucine zipper and W2 domain-containing protein 1 | -1.83 | -0.87 | 45.28% |
| RL3 | 60S ribosomal protein L3 | -3.18 | -1.67 | 45.26% |
| TIM10 | Mitochondrial import inner membrane translocase subunit Tim10 | 3.02 | 1.59 | 45.24% |
| KIF5C | Kinesin heavy chain isoform 5C | 5.63 | 2.49 | 45.24% |
| RL35 | 60S ribosomal protein L35 | -9.54 | -3.25 | 45.22% |
| MDHC | Malate dehydrogenase, cytoplasmic | -6.18 | -2.63 | 45.19% |
| OGT1 | UDP-N-acetylglucosamine--peptide N-acetylglucosaminyltransferase 110 kDa subunit | -2.26 | -1.18 | 45.07% |
| IF4H | Eukaryotic translation initiation factor 4H | -2.99 | -1.58 | 45.05% |
| MAT2B | Methionine adenosyltransferase 2 subunit beta | -6.11 | -2.61 | 44.89% |
| VDAC3 | Voltage-dependent anion-selective channel protein 3 | 6.22 | 2.64 | 44.88% |
| CUL3 | Cullin-3 | 2.81 | 1.49 | 44.82% |
| ABI1 | Abl interactor 1 | -3.86 | -1.95 | 44.75% |
| MK08 | Mitogen-activated protein kinase 8 | -3.63 | -1.86 | 44.63% |
| GDIR1 | Rho GDP-dissociation inhibitor 1 | 1.90 | 0.92 | 44.62% |
| SAHH | Adenosylhomocysteinase | -3.41 | -1.77 | 44.58% |
| RBM3 | RNA-binding protein 3 | 11.01 | 3.46 | 44.57% |
| CRKL | Crk-like protein | 2.77 | 1.47 | 44.52% |
| COPB2 | Coatomer subunit beta' | -4.96 | -2.31 | 44.45% |
| HNRPK | Heterogeneous nuclear ribonucleoprotein K | -3.11 | -1.64 | 44.38% |
| DYL1 | Dynein light chain 1, cytoplasmic | -2.26 | -1.18 | 44.21% |
| TCPA | T-complex protein 1 subunit alpha | -2.10 | -1.07 | 44.18% |
| SLIT1 | Slit homolog 1 protein | -5.85 | -2.55 | 44.13% |
| PSA2 | Proteasome subunit alpha type-2 | -3.52 | -1.81 | 44.12% |
| RABE1 | Rab GTPase-binding effector protein 1 | 6.35 | 2.67 | 44.10% |
| PPM1G | Protein phosphatase 1G | 2.35 | 1.23 | 44.00% |
| SET | Protein SET | -3.24 | -1.70 | 43.85% |
| HNRH1 | Heterogeneous nuclear ribonucleoprotein H | 1.90 | 0.93 | 43.81% |
| PRDX5 | Peroxiredoxin-5, mitochondrial | -2.11 | -1.08 | 43.76% |
| GCSH | Glycine cleavage system H protein, mitochondrial | 3.56 | 1.83 | 43.74% |
| TEBP | Prostaglandin E synthase 3 | -2.99 | -1.58 | 43.73% |
| SYYC | Tyrosine--tRNA ligase, cytoplasmic | -7.77 | -2.96 | 43.67% |
| VATB2 | V-type proton ATPase subunit B, brain isoform | 2.01 | 1.00 | 43.64% |

| | | | | |
|---|---|---|---|---|
| IF2A | Eukaryotic translation initiation factor 2 subunit 1 | -2.62 | -1.39 | 43.62% |
| SYSC | Serine--tRNA ligase, cytoplasmic | -5.51 | -2.46 | 43.61% |
| AP2M1 | AP-2 complex subunit mu | -3.56 | -1.83 | 43.50% |
| AATM | Aspartate aminotransferase, mitochondrial | -7.35 | -2.88 | 43.47% |
| RTN1 | Reticulon-1 | 8.26 | 3.05 | 43.46% |
| PRS6A | 26S protease regulatory subunit 6A | 3.08 | 1.62 | 43.39% |
| RB6I2 | ELKS/Rab6-interacting/CAST family member 1 | 2.81 | 1.49 | 43.33% |
| NUDC | Nuclear migration protein nudC | 1.65 | 0.72 | 43.32% |
| PDIA6 | Protein disulfide-isomerase A6 | -2.57 | -1.36 | 43.30% |
| MT3 | Metallothionein-3 | 3.83 | 1.94 | 43.27% |
| MTPN | Myotrophin | 2.76 | 1.46 | 43.26% |
| SDHA | Succinate dehydrogenase [ubiquinone] flavoprotein subunit, mitochondrial | 2.54 | 1.35 | 43.25% |
| HNRDL | Heterogeneous nuclear ribonucleoprotein D-like | -2.25 | -1.17 | 43.20% |
| CXAR | Coxsackievirus and adenovirus receptor homolog | 2.72 | 1.44 | 43.08% |
| RS27A | Ubiquitin-40S ribosomal protein S27a | 2.69 | 1.43 | 43.06% |
| GARS | Glycine--tRNA ligase | -4.27 | -2.10 | 43.03% |
| AT1B1 | Sodium/potassium-transporting ATPase subunit beta-1 | 1.58 | 0.66 | 42.98% |
| STX1B | Syntaxin-1B | -3.16 | -1.66 | 42.98% |
| ASNS | Asparagine synthetase [glutamine-hydrolyzing] | -4.51 | -2.17 | 42.94% |
| PRS6B | 26S protease regulatory subunit 6B | 3.25 | 1.70 | 42.91% |
| LSAMP | Limbic system-associated membrane protein | 2.23 | 1.16 | 42.90% |
| ES1 | ES1 protein homolog, mitochondrial | 4.98 | 2.32 | 42.89% |
| PSB3 | Proteasome subunit beta type-3 | -5.93 | -2.57 | 42.85% |
| EIF3I | Eukaryotic translation initiation factor 3 subunit I | 2.74 | 1.45 | 42.79% |
| KHDR1 | KH domain-containing, RNA-binding, signal transduction-associated protein 1 | -5.63 | -2.49 | 42.79% |
| CAZA2 | F-actin-capping protein subunit alpha-2 | -1.85 | -0.89 | 42.78% |
| PPIB | Peptidyl-prolyl cis-trans isomerase B | -2.56 | -1.35 | 42.76% |
| RS7 | 40S ribosomal protein S7 | -2.83 | -1.50 | 42.67% |
| PRDX1 | Peroxiredoxin-1 | -2.26 | -1.18 | 42.61% |
| PDIA3 | Protein disulfide-isomerase A3 | -2.55 | -1.35 | 42.49% |
| DX39B | Spliceosome RNA helicase Ddx39b | -10.09 | -3.33 | 42.40% |
| ATPA | ATP synthase subunit alpha, mitochondrial | -2.63 | -1.39 | 42.34% |
| RL29 | 60S ribosomal protein L29 | 2.16 | 1.11 | 42.33% |
| AGRIN | Agrin | 7.63 | 2.93 | 42.33% |
| HSP74 | Heat shock 70 kDa protein 4 | -2.89 | -1.53 | 42.28% |
| PSME1 | Proteasome activator complex subunit 1 | -4.22 | -2.08 | 42.25% |

| | | | | |
|---|---|---|---|---|
| LYPA1 | Acyl-protein thioesterase 1 | -6.16 | -2.62 | 42.19% |
| RAB35 | Ras-related protein Rab-35 | -4.14 | -2.05 | 42.04% |
| LASP1 | LIM and SH3 domain protein 1 | 2.06 | 1.04 | 42.02% |
| PIPNA | Phosphatidylinositol transfer protein alpha isoform | -2.82 | -1.49 | 42.01% |
| PAIRB | Plasminogen activator inhibitor 1 RNA-binding protein | 4.15 | 2.05 | 41.96% |
| SPTN1 | Spectrin alpha chain, non-erythrocytic 1 | -4.29 | -2.10 | 41.95% |
| MFGM | Lactadherin | -3.66 | -1.87 | 41.95% |
| CLH1 | Clathrin heavy chain 1 | -1.74 | -0.80 | 41.90% |
| AT1B3 | Sodium/potassium-transporting ATPase subunit beta-3 | 3.55 | 1.83 | 41.77% |
| RL7A | 60S ribosomal protein L7a | -3.48 | -1.80 | 41.72% |
| RS2 | 40S ribosomal protein S2 | -2.52 | -1.34 | 41.64% |
| GRP75 | Stress-70 protein, mitochondrial | 2.81 | 1.49 | 41.62% |
| ZWINT | ZW10 interactor | -4.20 | -2.07 | 41.55% |
| SYPH | Synaptophysin | 1.79 | 0.84 | 41.38% |
| HNRPU | Heterogeneous nuclear ribonucleoprotein U | -2.58 | -1.36 | 41.29% |
| CAPZB | F-actin-capping protein subunit beta | -5.49 | -2.46 | 41.27% |
| DDAH2 | N(G),N(G)-dimethylarginine dimethylaminohydrolase 2 | 2.14 | 1.10 | 41.18% |
| ATP5I | ATP synthase subunit e, mitochondrial | -2.06 | -1.04 | 41.17% |
| DPYL1 | Dihydropyrimidinase-related protein 1 | -1.98 | -0.99 | 41.15% |
| SYDC | Aspartate--tRNA ligase, cytoplasmic | -6.20 | -2.63 | 41.12% |
| KCC2A | Calcium/calmodulin-dependent protein kinase type II subunit alpha | 2.71 | 1.44 | 41.07% |
| DPYL4 | Dihydropyrimidinase-related protein 4 | 2.11 | 1.07 | 41.00% |
| RL19 | 60S ribosomal protein L19 | -2.48 | -1.31 | 40.90% |
| CDC42 | Cell division control protein 42 homolog | -4.77 | -2.25 | 40.88% |
| STRN3 | Striatin-3 | 2.49 | 1.32 | 40.84% |
| GBB2 | Guanine nucleotide-binding protein G(I)/G(S)/G(T) subunit beta-2 | -2.36 | -1.24 | 40.83% |
| APT | Adenine phosphoribosyltransferase | -2.10 | -1.07 | 40.82% |
| ILF2 | Interleukin enhancer-binding factor 2 | -2.21 | -1.14 | 40.82% |
| STAM2 | Signal transducing adapter molecule 2 | -7.79 | -2.96 | 40.82% |
| LA | Lupus La protein homolog | -4.06 | -2.02 | 40.72% |
| AT2B2 | Plasma membrane calcium-transporting ATPase 2 | -7.85 | -2.97 | 40.66% |
| PP1G | Serine/threonine-protein phosphatase PP1-gamma catalytic subunit | -4.61 | -2.20 | 40.62% |
| ADDA | Alpha-adducin | -4.44 | -2.15 | 40.61% |
| RU1C | U1 small nuclear ribonucleoprotein C | -7.24 | -2.86 | 40.57% |
| LZIC | Protein LZIC | 8.31 | 3.06 | 40.40% |
| KPRB | Phosphoribosyl pyrophosphate synthase-associated protein 2 | -12.95 | -3.70 | 40.37% |

| | | | | |
|---|---|---|---|---|
| IF5 | Eukaryotic translation initiation factor 5 | -4.77 | -2.25 | 40.32% |
| PSA6 | Proteasome subunit alpha type-6 | 2.15 | 1.11 | 40.24% |
| F136A | Protein FAM136A | 2.28 | 1.19 | 40.11% |
| RS15 | 40S ribosomal protein S15 | -3.65 | -1.87 | 40.07% |
| OST48 | Dolichyl-diphosphooligosaccharide--protein glycosyltransferase 48 kDa subunit | 2.91 | 1.54 | 40.07% |
| FA98A | Protein FAM98A | 4.24 | 2.09 | 40.06% |
| NDUS4 | NADH dehydrogenase [ubiquinone] iron-sulfur protein 4, mitochondrial | -2.55 | -1.35 | 40.04% |
| MTAP2 | Microtubule-associated protein 2 | -3.71 | -1.89 | 40.04% |
| LDHB | L-lactate dehydrogenase B chain | -2.15 | -1.10 | 40.03% |
| HINT1 | Histidine triad nucleotide-binding protein 1 | -3.71 | -1.89 | 39.97% |
| ERP29 | Endoplasmic reticulum resident protein 29 | 1.83 | 0.88 | 39.96% |
| PDIA1 | Protein disulfide-isomerase | 2.38 | 1.25 | 39.96% |
| DCTN1 | Dynactin subunit 1 | -4.71 | -2.24 | 39.96% |
| CRK | Adapter molecule crk | 11.70 | 3.55 | 39.84% |
| AP1B1 | AP-1 complex subunit beta-1 | 1.47 | 0.55 | 39.80% |
| KIF2A | Kinesin-like protein KIF2A | -5.05 | -2.34 | 39.71% |
| ARL8B | ADP-ribosylation factor-like protein 8B | -2.38 | -1.25 | 39.64% |
| ESTD | S-formylglutathione hydrolase | 2.50 | 1.32 | 39.59% |
| PARK7 | Protein DJ-1 | 1.52 | 0.60 | 39.58% |
| BABA1 | BRISC and BRCA1-A complex member 1 | 5.29 | 2.40 | 39.47% |
| GSTM4 | Glutathione S-transferase Yb-3 | 5.09 | 2.35 | 39.45% |
| DYN1 | Dynamin-1 | -4.78 | -2.26 | 39.37% |
| DPYL5 | Dihydropyrimidinase-related protein 5 | -2.41 | -1.27 | 39.25% |
| CREB1 | Cyclic AMP-responsive element-binding protein 1 | 1.82 | 0.87 | 39.23% |
| EZRI | Ezrin | -1.96 | -0.97 | 39.20% |
| CTBP1 | C-terminal-binding protein 1 | -3.74 | -1.90 | 39.17% |
| NPTN | Neuroplastin | -1.49 | -0.58 | 39.17% |
| GSK3B | Glycogen synthase kinase-3 beta | -1.74 | -0.80 | 39.16% |
| GBB4 | Guanine nucleotide-binding protein subunit beta-4 | 2.75 | 1.46 | 39.16% |
| RB11B | Ras-related protein Rab-11B | 3.05 | 1.61 | 39.15% |
| GRB2 | Growth factor receptor-bound protein 2 | -2.91 | -1.54 | 39.14% |
| IF4E | Eukaryotic translation initiation factor 4E | -3.46 | -1.79 | 39.07% |
| LIS1 | Platelet-activating factor acetylhydrolase IB subunit alpha | -2.58 | -1.36 | 39.03% |
| ATP5H | ATP synthase subunit d, mitochondrial | 5.47 | 2.45 | 39.01% |
| SHOT1 | Shootin-1 | 2.41 | 1.27 | 38.92% |
| THIKA | 3-ketoacyl-CoA thiolase A, peroxisomal | 2.39 | 1.26 | 38.88% |
| ATG3 | Ubiquitin-like-conjugating enzyme ATG3 | -1.42 | -0.51 | 38.88% |

| | | | | |
|---|---|---|---|---|
| SCOC | Short coiled-coil protein | -2.17 | -1.12 | 38.88% |
| ENPP5 | Ectonucleotide pyrophosphatase/phosphodiesterase family member 5 | -4.87 | -2.28 | 38.88% |
| VATC1 | V-type proton ATPase subunit C 1 | -5.75 | -2.52 | 38.88% |
| ITPA | Inosine triphosphate pyrophosphatase | -9.51 | -3.25 | 38.88% |
| A4 | Amyloid beta A4 protein | 2.95 | 1.56 | 38.84% |
| DLG2 | Disks large homolog 2 | 4.49 | 2.17 | 38.83% |
| SODC | Superoxide dismutase [Cu-Zn] | 4.34 | 2.12 | 38.80% |
| PYGB | Glycogen phosphorylase, brain form | -2.86 | -1.52 | 38.79% |
| LGUL | Lactoylglutathione lyase | 3.18 | 1.67 | 38.77% |
| DOPD | D-dopachrome decarboxylase | 2.70 | 1.43 | 38.68% |
| HOME1 | Homer protein homolog 1 | -2.16 | -1.11 | 38.65% |
| IDI1 | Isopentenyl-diphosphate Delta-isomerase 1 | -2.50 | -1.32 | 38.63% |
| NCBP2 | Nuclear cap-binding protein subunit 2 | -4.28 | -2.10 | 38.62% |
| VPS29 | Vacuolar protein sorting-associated protein 29 | -3.08 | -1.62 | 38.55% |
| ANM1 | Protein arginine N-methyltransferase 1 | -4.22 | -2.08 | 38.54% |
| PUF60 | Poly(U)-binding-splicing factor PUF60 | -2.40 | -1.26 | 38.52% |
| 37500 | Septin-2 | 1.83 | 0.87 | 38.47% |
| AT1A3 | Sodium/potassium-transporting ATPase subunit alpha-3 | 2.21 | 1.14 | 38.45% |
| MIC25 | MICOS complex subunit Mic25 | -7.64 | -2.93 | 38.39% |
| RS21 | 40S ribosomal protein S21 | 1.44 | 0.52 | 38.36% |
| RINI | Ribonuclease inhibitor | 4.91 | 2.30 | 38.33% |
| PPIG | Peptidyl-prolyl cis-trans isomerase G | -2.96 | -1.57 | 38.30% |
| DJB11 | DnaJ homolog subfamily B member 11 | -2.76 | -1.46 | 38.24% |
| GLRX1 | Glutaredoxin-1 | 3.07 | 1.62 | 38.10% |
| RAB14 | Ras-related protein Rab-14 | -7.45 | -2.90 | 38.09% |
| HNRPL | Heterogeneous nuclear ribonucleoprotein L | -2.27 | -1.18 | 38.04% |
| AIP | AH receptor-interacting protein | 2.57 | 1.36 | 38.02% |
| BAX | Apoptosis regulator BAX | 1.78 | 0.83 | 37.94% |
| PLPR3 | Phospholipid phosphatase-related protein type 3 | 2.23 | 1.16 | 37.90% |
| VATE1 | V-type proton ATPase subunit E 1 | -5.36 | -2.42 | 37.89% |
| HPRT | Hypoxanthine-guanine phosphoribosyltransferase | -4.80 | -2.26 | 37.84% |
| GEPH | Gephyrin | -3.04 | -1.60 | 37.84% |
| PP1A | Serine/threonine-protein phosphatase PP1-alpha catalytic subunit | 2.26 | 1.18 | 37.82% |
| GBB1 | Guanine nucleotide-binding protein G(I)/G(S)/G(T) subunit beta-1 | -3.53 | -1.82 | 37.75% |
| 40787 | Septin-11 | -2.60 | -1.38 | 37.74% |
| HNRPQ | Heterogeneous nuclear ribonucleoprotein Q | -2.53 | -1.34 | 37.69% |
| HYOU1 | Hypoxia up-regulated protein 1 | -3.80 | -1.92 | 37.68% |

| | | | | |
|---|---|---|---|---|
| PSA1 | Proteasome subunit alpha type-1 | -3.20 | -1.68 | 37.67% |
| SGTA | Small glutamine-rich tetratricopeptide repeat-containing protein alpha | 2.47 | 1.30 | 37.61% |
| PPM1B | Protein phosphatase 1B | 1.97 | 0.98 | 37.59% |
| 37865 | Neuronal-specific septin-3 | -4.20 | -2.07 | 37.57% |
| RUVB1 | RuvB-like 1 | -3.43 | -1.78 | 37.54% |
| GMFB | Glia maturation factor beta | 3.49 | 1.80 | 37.46% |
| LRC59 | Leucine-rich repeat-containing protein 59 | -4.41 | -2.14 | 37.43% |
| TCPE | T-complex protein 1 subunit epsilon | -2.94 | -1.55 | 37.40% |
| BACH | Cytosolic acyl coenzyme A thioester hydrolase | 1.53 | 0.61 | 37.39% |
| CLCB | Clathrin light chain B | 1.69 | 0.75 | 37.38% |
| SCG3 | Secretogranin-3 | 2.35 | 1.24 | 37.35% |
| RL31 | 60S ribosomal protein L31 | -1.61 | -0.68 | 37.33% |
| TPP2 | Tripeptidyl-peptidase 2 | -3.98 | -1.99 | 37.33% |
| SKP1 | S-phase kinase-associated protein 1 | -7.04 | -2.82 | 37.28% |
| NLTP | Non-specific lipid-transfer protein | -1.33 | -0.41 | 37.28% |
| AT5F1 | ATP synthase F(0) complex subunit B1, mitochondrial | -4.76 | -2.25 | 37.24% |
| RAB7A | Ras-related protein Rab-7a | 2.35 | 1.23 | 37.17% |
| RAB1A | Ras-related protein Rab-1A | -3.04 | -1.61 | 37.12% |
| ECHM | Enoyl-CoA hydratase, mitochondrial | -2.05 | -1.03 | 37.11% |
| SF3A2 | Splicing factor 3A subunit 2 | -2.32 | -1.22 | 37.11% |
| NPM | Nucleophosmin | -2.63 | -1.40 | 37.07% |
| SEC13 | Protein SEC13 homolog | 1.82 | 0.87 | 36.96% |
| TCPG | T-complex protein 1 subunit gamma | -2.16 | -1.11 | 36.92% |
| RL27A | 60S ribosomal protein L27a | -3.12 | -1.64 | 36.90% |
| ACLY | ATP-citrate synthase | -2.35 | -1.23 | 36.84% |
| TKT | Transketolase | -2.42 | -1.28 | 36.72% |
| SV2A | Synaptic vesicle glycoprotein 2A | 2.66 | 1.41 | 36.71% |
| ICLN | Methylosome subunit pICln | 1.41 | 0.50 | 36.70% |
| TLE3 | Transducin-like enhancer protein 3 | 3.50 | 1.81 | 36.62% |
| AP1M1 | AP-1 complex subunit mu-1 | -5.87 | -2.55 | 36.62% |
| EF2 | Elongation factor 2 | -1.67 | -0.74 | 36.58% |
| RCN2 | Reticulocalbin-2 | 8.60 | 3.10 | 36.57% |
| RL6 | 60S ribosomal protein L6 | -1.38 | -0.46 | 36.57% |
| PLCB1 | 1-phosphatidylinositol 4,5-bisphosphate phosphodiesterase beta-1 | -1.60 | -0.67 | 36.56% |
| TMEDA | Transmembrane emp24 domain-containing protein 10 | -2.63 | -1.39 | 36.54% |
| KCRU | Creatine kinase U-type, mitochondrial | -2.93 | -1.55 | 36.53% |
| TCPB | T-complex protein 1 subunit beta | -2.24 | -1.16 | 36.45% |
| NCAM1 | Neural cell adhesion molecule 1 | 2.25 | 1.17 | 36.42% |
| RL24 | 60S ribosomal protein L24 | -4.16 | -2.06 | 36.39% |
| AOXA | Aldehyde oxidase 1 | -2.12 | -1.09 | 36.32% |

| | | | | |
|---|---|---|---|---|
| NEDD4 | E3 ubiquitin-protein ligase NEDD4 | -2.80 | -1.48 | 36.31% |
| ARLY | Argininosuccinate lyase | 3.54 | 1.83 | 36.30% |
| ARHG7 | Rho guanine nucleotide exchange factor 7 | -8.82 | -3.14 | 36.29% |
| MK01 | Mitogen-activated protein kinase 1 | 1.49 | 0.57 | 36.24% |
| DHE3 | Glutamate dehydrogenase 1, mitochondrial | -3.29 | -1.72 | 36.21% |
| ACTZ | Alpha-centractin | -3.18 | -1.67 | 36.14% |
| NEDD8 | NEDD8 | 4.58 | 2.20 | 36.12% |
| TRA2B | Transformer-2 protein homolog beta | -1.97 | -0.98 | 36.02% |
| MRP | MARCKS-related protein | -4.63 | -2.21 | 35.91% |
| NCKP1 | Nck-associated protein 1 | -1.74 | -0.80 | 35.90% |
| LIN7C | Protein lin-7 homolog C | -2.23 | -1.16 | 35.68% |
| WDR1 | WD repeat-containing protein 1 | 7.83 | 2.97 | 35.62% |
| PNPH | Purine nucleoside phosphorylase | 3.37 | 1.75 | 35.62% |
| KLC1 | Kinesin light chain 1 | 1.91 | 0.93 | 35.60% |
| RPN1 | Dolichyl-diphosphooligosaccharide--protein glycosyltransferase subunit 1 | 3.17 | 1.66 | 35.52% |
| SH3G2 | Endophilin-A1 | 2.05 | 1.04 | 35.34% |
| NDKA | Nucleoside diphosphate kinase A | -5.60 | -2.49 | 35.34% |
| CDV3 | Protein CDV3 homolog | 2.88 | 1.53 | 35.30% |
| FKBP4 | Peptidyl-prolyl cis-trans isomerase FKBP4 | 2.41 | 1.27 | 35.27% |
| AP180 | Clathrin coat assembly protein AP180 | -1.63 | -0.70 | 35.13% |
| ELAV2 | ELAV-like protein 2 | -4.34 | -2.12 | 35.04% |
| RS4X | 40S ribosomal protein S4, X isoform | -4.29 | -2.10 | 34.95% |
| CAND1 | Cullin-associated NEDD8-dissociated protein 1 | -4.11 | -2.04 | 34.89% |
| RAP2B | Ras-related protein Rap-2b | -1.45 | -0.54 | 34.87% |
| CD59 | CD59 glycoprotein | 2.06 | 1.04 | 34.74% |
| ALDOC | Fructose-bisphosphate aldolase C | 2.91 | 1.54 | 34.73% |
| RL21 | 60S ribosomal protein L21 | -3.75 | -1.91 | 34.71% |
| TMOD2 | Tropomodulin-2 | 3.63 | 1.86 | 34.70% |
| CAZA1 | F-actin-capping protein subunit alpha-1 | -4.76 | -2.25 | 34.68% |
| CSN8 | COP9 signalosome complex subunit 8 | 2.60 | 1.38 | 34.68% |
| MAP4 | Microtubule-associated protein 4 | 3.55 | 1.83 | 34.55% |
| HNRPC | Heterogeneous nuclear ribonucleoprotein C | -2.81 | -1.49 | 34.48% |
| PFKAL | ATP-dependent 6-phosphofructokinase, liver type | -5.16 | -2.37 | 34.41% |
| APEX1 | DNA-(apurinic or apyrimidinic site) lyase | 1.88 | 0.91 | 34.33% |
| OLA1 | Obg-like ATPase 1 | -5.38 | -2.43 | 34.23% |
| GLRX3 | Glutaredoxin-3 | 2.26 | 1.18 | 34.17% |
| OTUB1 | Ubiquitin thioesterase OTUB1 | -3.47 | -1.80 | 34.17% |
| PSB7 | Proteasome subunit beta type-7 | -2.54 | -1.34 | 34.08% |
| LMNB1 | Lamin-B1 | 3.03 | 1.60 | 34.04% |

| | | | | |
|---|---|---|---|---|
| PFKAM | ATP-dependent 6-phosphofructokinase, muscle type | -4.60 | -2.20 | 34.01% |
| LIPA3 | Liprin-alpha-3 | -3.96 | -1.98 | 33.96% |
| HMCS1 | Hydroxymethylglutaryl-CoA synthase, cytoplasmic | -3.53 | -1.82 | 33.96% |
| DDAH1 | N(G),N(G)-dimethylarginine dimethylaminohydrolase 1 | -4.38 | -2.13 | 33.96% |
| GNAS2 | Guanine nucleotide-binding protein G(s) subunit alpha isoforms short | 5.38 | 2.43 | 33.91% |
| DX39A | ATP-dependent RNA helicase DDX39A | 2.46 | 1.30 | 33.89% |
| NP1L4 | Nucleosome assembly protein 1-like 4 | 2.78 | 1.47 | 33.88% |
| PRPS1 | Ribose-phosphate pyrophosphokinase 1 | -4.32 | -2.11 | 33.88% |
| NSF | Vesicle-fusing ATPase | -3.36 | -1.75 | 33.82% |
| PDXK | Pyridoxal kinase | 2.90 | 1.53 | 33.76% |
| IDH3A | Isocitrate dehydrogenase [NAD] subunit alpha, mitochondrial | -8.27 | -3.05 | 33.75% |
| NUCB2 | Nucleobindin-2 | -3.83 | -1.94 | 33.70% |
| PHIPL | Phytanoyl-CoA hydroxylase-interacting protein-like | -2.74 | -1.45 | 33.68% |
| VAT1 | Synaptic vesicle membrane protein VAT-1 homolog | -2.09 | -1.07 | 33.64% |
| TBA4A | Tubulin alpha-4A chain | -4.59 | -2.20 | 33.63% |
| CSK2B | Casein kinase II subunit beta | 2.13 | 1.09 | 33.53% |
| HAP28 | 28 kDa heat- and acid-stable phosphoprotein | -6.50 | -2.70 | 33.53% |
| DHB4 | Peroxisomal multifunctional enzyme type 2 | -4.01 | -2.00 | 33.50% |
| GLNA | Glutamine synthetase | -4.43 | -2.15 | 33.50% |
| TPM1 | Tropomyosin alpha-1 chain | 4.37 | 2.13 | 33.45% |
| CTTB2 | Cortactin-binding protein 2 | 3.33 | 1.74 | 33.35% |
| SYRC | Arginine--tRNA ligase, cytoplasmic | -4.03 | -2.01 | 33.34% |
| DNJA1 | DnaJ homolog subfamily A member 1 | -6.60 | -2.72 | 33.34% |
| THOP1 | Thimet oligopeptidase | -3.67 | -1.88 | 33.32% |
| SH3G1 | Endophilin-A2 | 6.61 | 2.72 | 33.21% |
| YBOX1 | Nuclease-sensitive element-binding protein 1 | -3.02 | -1.59 | 33.20% |
| SYAC | Alanine--tRNA ligase, cytoplasmic | -3.11 | -1.64 | 33.19% |
| GAS7 | Growth arrest-specific protein 7 | 6.32 | 2.66 | 33.13% |
| STX7 | Syntaxin-7 | -6.57 | -2.72 | 33.02% |
| MYH9 | Myosin-9 | -3.79 | -1.92 | 32.90% |
| KCC2G | Calcium/calmodulin-dependent protein kinase type II subunit gamma | 3.02 | 1.59 | 32.85% |
| PHF5A | PHD finger-like domain-containing protein 5A | 10.53 | 3.40 | 32.73% |
| CAMKV | CaM kinase-like vesicle-associated protein | 2.01 | 1.01 | 32.66% |
| AGFG1 | Arf-GAP domain and FG repeat-containing protein 1 | -1.50 | -0.58 | 32.59% |
| KAP3 | cAMP-dependent protein kinase type II-beta regulatory subunit | 1.99 | 0.99 | 32.52% |
| CPSF5 | Cleavage and polyadenylation specificity factor subunit 5 | -4.10 | -2.03 | 32.35% |

| | | | | |
|---|---|---|---|---|
| IMPA1 | Inositol monophosphatase 1 | -2.35 | -1.23 | 32.27% |
| 6PGL | 6-phosphogluconolactonase | 2.71 | 1.44 | 32.23% |
| RS9 | 40S ribosomal protein S9 | -3.68 | -1.88 | 32.12% |
| RHOB | Rho-related GTP-binding protein RhoB | -1.70 | -0.77 | 32.12% |
| BAF | Barrier-to-autointegration factor | 2.37 | 1.24 | 32.11% |
| ACL6B | Actin-like protein 6B | -2.21 | -1.14 | 32.07% |
| TALDO | Transaldolase | -3.89 | -1.96 | 31.95% |
| PALM | Paralemmin-1 | 4.12 | 2.04 | 31.92% |
| UCHL3 | Ubiquitin carboxyl-terminal hydrolase isozyme L3 | 4.62 | 2.21 | 31.91% |
| 38596 | Septin-5 | -3.73 | -1.90 | 31.84% |
| H31 | Histone H3.1 | -2.54 | -1.35 | 31.76% |
| CSN1 | COP9 signalosome complex subunit 1 | -9.31 | -3.22 | 31.75% |
| SYN1 | Synapsin-1 | -1.95 | -0.97 | 31.73% |
| PACN1 | Protein kinase C and casein kinase substrate in neurons protein 1 | 2.03 | 1.02 | 31.73% |
| STX1A | Syntaxin-1A | -2.39 | -1.26 | 31.70% |
| TOM70 | Mitochondrial import receptor subunit TOM70 | -4.01 | -2.00 | 31.68% |
| VDAC1 | Voltage-dependent anion-selective channel protein 1 | -2.37 | -1.25 | 31.65% |
| TRFE | Serotransferrin | -3.50 | -1.81 | 31.61% |
| RALA | Ras-related protein Ral-A | -3.46 | -1.79 | 31.56% |
| TPM4 | Tropomyosin alpha-4 chain | -3.26 | -1.70 | 31.48% |
| PSMD2 | 26S proteasome non-ATPase regulatory subunit 2 | -3.95 | -1.98 | 31.48% |
| TFR1 | Transferrin receptor protein 1 | -2.52 | -1.33 | 31.43% |
| UCRI | Cytochrome b-c1 complex subunit Rieske, mitochondrial | -2.97 | -1.57 | 31.39% |
| PEF1 | Peflin | -2.47 | -1.30 | 31.29% |
| RS26 | 40S ribosomal protein S26 | -1.60 | -0.68 | 31.23% |
| CNRP1 | CB1 cannabinoid receptor-interacting protein 1 | 8.14 | 3.02 | 31.21% |
| GPC2 | Glypican-2 | 2.55 | 1.35 | 31.17% |
| ADHX | Alcohol dehydrogenase class-3 | 4.07 | 2.02 | 31.14% |
| CA2D1 | Voltage-dependent calcium channel subunit alpha-2/delta-1 | 2.69 | 1.43 | 31.04% |
| KI21B | Kinesin-like protein KIF21B | 3.29 | 1.72 | 31.03% |
| DYHC1 | Cytoplasmic dynein 1 heavy chain 1 | -3.20 | -1.68 | 30.89% |
| AP2A2 | AP-2 complex subunit alpha-2 | -3.05 | -1.61 | 30.87% |
| METK2 | S-adenosylmethionine synthase isoform type-2 | -4.01 | -2.00 | 30.86% |
| 2ABA | Serine/threonine-protein phosphatase 2A 55 kDa regulatory subunit B alpha isoform | -1.94 | -0.95 | 30.82% |
| PPCEL | Prolyl endopeptidase-like | 7.43 | 2.89 | 30.82% |
| BZW2 | Basic leucine zipper and W2 domain-containing protein 2 | -1.90 | -0.93 | 30.80% |
| PRS8 | 26S protease regulatory subunit 8 | -3.62 | -1.85 | 30.73% |

| | | | | |
|---|---|---|---|---|
| PSD11 | 26S proteasome non-ATPase regulatory subunit 11 | -2.25 | -1.17 | 30.60% |
| VISL1 | Visinin-like protein 1 | 2.10 | 1.07 | 30.59% |
| RFOX2 | RNA binding protein fox-1 homolog 2 | -2.60 | -1.38 | 30.49% |
| OAT | Ornithine aminotransferase, mitochondrial | -2.35 | -1.23 | 30.40% |
| SAFB1 | Scaffold attachment factor B1 | -4.37 | -2.13 | 30.27% |
| I2BPL | Interferon regulatory factor 2-binding protein-like | 1.38 | 0.46 | 30.19% |
| NDRG1 | Protein NDRG1 | -3.66 | -1.87 | 30.14% |
| MIC60 | MICOS complex subunit Mic60 | 3.78 | 1.92 | 30.11% |
| PPP5 | Serine/threonine-protein phosphatase 5 | 2.29 | 1.20 | 30.05% |
| OPA1 | Dynamin-like 120 kDa protein, mitochondrial | -4.49 | -2.17 | 30.04% |
| DPP3 | Dipeptidyl peptidase 3 | 2.61 | 1.38 | 30.01% |
| FAS | Fatty acid synthase | -2.46 | -1.30 | 29.99% |
| GNAQ | Guanine nucleotide-binding protein G(q) subunit alpha | -4.43 | -2.15 | 29.91% |
| DLDH | Dihydrolipoyl dehydrogenase, mitochondrial | -2.28 | -1.19 | 29.78% |
| HNRPF | Heterogeneous nuclear ribonucleoprotein F | 1.73 | 0.79 | 29.77% |
| PPCE | Prolyl endopeptidase | -2.74 | -1.46 | 29.77% |
| TOP2A | DNA topoisomerase 2-alpha | -4.50 | -2.17 | 29.64% |
| MYH10 | Myosin-10 | -1.96 | -0.97 | 29.50% |
| DCTN4 | Dynactin subunit 4 | -8.46 | -3.08 | 29.39% |
| RL18 | 60S ribosomal protein L18 | -2.35 | -1.23 | 29.07% |
| XPO1 | Exportin-1 | 2.52 | 1.33 | 29.06% |
| NUCL | Nucleolin | -3.08 | -1.62 | 29.01% |
| AL1A7 | Aldehyde dehydrogenase, cytosolic 1 | 2.36 | 1.24 | 28.88% |
| GPSM1 | G-protein-signaling modulator 1 | -2.68 | -1.42 | 28.76% |
| AT1A1 | Sodium/potassium-transporting ATPase subunit alpha-1 | 1.97 | 0.98 | 28.74% |
| OPCM | Opioid-binding protein/cell adhesion molecule | 1.71 | 0.78 | 28.71% |
| MCES | mRNA cap guanine-N7 methyltransferase | 2.92 | 1.55 | 28.68% |
| CSDE1 | Cold shock domain-containing protein E1 | 2.80 | 1.48 | 28.63% |
| AN32E | Acidic leucine-rich nuclear phosphoprotein 32 family member E | -2.90 | -1.54 | 28.55% |
| HS105 | Heat shock protein 105 kDa | -4.82 | -2.27 | 28.53% |
| NRDC | Nardilysin | -7.45 | -2.90 | 28.48% |
| TWF1 | Twinfilin-1 | -1.83 | -0.87 | 28.45% |
| PP2BB | Serine/threonine-protein phosphatase 2B catalytic subunit beta isoform | -6.36 | -2.67 | 28.45% |
| EIF3D | Eukaryotic translation initiation factor 3 subunit D | -8.24 | -3.04 | 28.43% |
| H2A3 | Histone H2A type 3 | -6.85 | -2.78 | 28.27% |
| VAC14 | Protein VAC14 homolog | 5.24 | 2.39 | 28.20% |
| ARF5 | ADP-ribosylation factor 5 | -2.83 | -1.50 | 28.18% |

| | | | | |
|---|---|---|---|---|
| SND1 | Staphylococcal nuclease domain-containing protein 1 | -5.54 | -2.47 | 28.13% |
| TIF1B | Transcription intermediary factor 1-beta | -3.03 | -1.60 | 28.13% |
| NEB2 | Neurabin-2 | 4.88 | 2.29 | 28.08% |
| RL32 | 60S ribosomal protein L32 | -2.93 | -1.55 | 28.00% |
| STX12 | Syntaxin-12 | -6.56 | -2.71 | 28.00% |
| SRC8 | Src substrate cortactin | 6.47 | 2.69 | 27.99% |
| RHOA | Transforming protein RhoA | -1.24 | -0.30 | 27.91% |
| RS8 | 40S ribosomal protein S8 | -2.44 | -1.29 | 27.81% |
| PURA | Transcriptional activator protein Pur-alpha | -4.05 | -2.02 | 27.79% |
| FPPS | Farnesyl pyrophosphate synthase | -3.71 | -1.89 | 27.77% |
| SYK | Lysine--tRNA ligase | -6.53 | -2.71 | 27.77% |
| PRUN1 | Protein prune homolog | -2.57 | -1.36 | 27.67% |
| RL7 | 60S ribosomal protein L7 | -2.50 | -1.32 | 27.56% |
| AL9A1 | 4-trimethylaminobutyraldehyde dehydrogenase | 3.56 | 1.83 | 27.55% |
| CSN3 | COP9 signalosome complex subunit 3 | -2.67 | -1.42 | 27.51% |
| CATD | Cathepsin D | 2.11 | 1.08 | 27.41% |
| RTCB | tRNA-splicing ligase RtcB homolog | -4.30 | -2.10 | 27.40% |
| KIF1B | Kinesin-like protein KIF1B | 2.10 | 1.07 | 27.38% |
| SYNJ1 | Synaptojanin-1 | -3.15 | -1.66 | 27.33% |
| VATF | V-type proton ATPase subunit F | 3.47 | 1.79 | 27.32% |
| DHPR | Dihydropteridine reductase | -3.91 | -1.97 | 27.22% |
| RUFY3 | Protein RUFY3 | -1.54 | -0.62 | 27.17% |
| KCC2D | Calcium/calmodulin-dependent protein kinase type II subunit delta | -1.85 | -0.89 | 27.14% |
| ACTN4 | Alpha-actinin-4 | -3.96 | -1.98 | 27.09% |
| ARF4 | ADP-ribosylation factor 4 | -5.15 | -2.36 | 27.01% |
| GRPE1 | GrpE protein homolog 1, mitochondrial | 2.26 | 1.18 | 26.97% |
| RS10 | 40S ribosomal protein S10 | -2.88 | -1.53 | 26.91% |
| KAP2 | cAMP-dependent protein kinase type II-alpha regulatory subunit | 2.19 | 1.13 | 26.57% |
| RAB6A | Ras-related protein Rab-6A | 3.50 | 1.81 | 26.54% |
| PRS7 | 26S protease regulatory subunit 7 | -2.37 | -1.25 | 26.35% |
| COR1A | Coronin-1A | 2.84 | 1.50 | 26.35% |
| QCR6 | Cytochrome b-c1 complex subunit 6, mitochondrial | 1.57 | 0.65 | 26.34% |
| CLCA | Clathrin light chain A | -2.18 | -1.13 | 26.30% |
| PRKRA | Interferon-inducible double-stranded RNA-dependent protein kinase activator A | 1.58 | 0.66 | 26.30% |
| GNAI1 | Guanine nucleotide-binding protein G(i) subunit alpha-1 | 3.29 | 1.72 | 26.21% |
| EFTU | Elongation factor Tu, mitochondrial | -3.06 | -1.62 | 26.05% |
| CHP1 | Calcineurin B homologous protein 1 | -2.71 | -1.44 | 25.96% |
| EIF3A | Eukaryotic translation initiation factor 3 subunit A | -4.60 | -2.20 | 25.87% |

| | | | | |
|---|---|---|---|---|
| RAB2A | Ras-related protein Rab-2A | -2.03 | -1.02 | 25.83% |
| PRDX6 | Peroxiredoxin-6 | 1.76 | 0.82 | 25.64% |
| ARPC5 | Actin-related protein 2/3 complex subunit 5 | -1.76 | -0.81 | 25.57% |
| ACTG | Actin, cytoplasmic 2 | 4.02 | 2.01 | 25.38% |
| EIF3C | Eukaryotic translation initiation factor 3 subunit C | 6.52 | 2.71 | 25.27% |
| BCAT1 | Branched-chain-amino-acid aminotransferase, cytosolic | -4.69 | -2.23 | 25.07% |
| DCLK1 | Serine/threonine-protein kinase DCLK1 | -3.85 | -1.95 | 24.98% |
| CYBP | Calcyclin-binding protein | -2.77 | -1.47 | 24.98% |
| UBQL1 | Ubiquilin-1 | 1.88 | 0.91 | 24.97% |
| NALCN | Sodium leak channel non-selective protein | -2.21 | -1.14 | 24.86% |
| 39326 | Septin-7 | -2.15 | -1.11 | 24.85% |
| TPR | Nucleoprotein TPR | 3.22 | 1.69 | 24.76% |
| FKB1A | Peptidyl-prolyl cis-trans isomerase FKBP1A | 1.64 | 0.71 | 24.74% |
| PPT1 | Palmitoyl-protein thioesterase 1 | -1.51 | -0.59 | 24.70% |
| GLOD4 | Glyoxalase domain-containing protein 4 | -1.86 | -0.90 | 24.56% |
| DDB1 | DNA damage-binding protein 1 | 1.72 | 0.79 | 24.42% |
| PSPC1 | Paraspeckle component 1 | 1.93 | 0.95 | 24.38% |
| HCD2 | 3-hydroxyacyl-CoA dehydrogenase type-2 | 1.94 | 0.95 | 24.20% |
| CLIP1 | CAP-Gly domain-containing linker protein 1 | 1.91 | 0.94 | 24.08% |
| DC1I2 | Cytoplasmic dynein 1 intermediate chain 2 | -2.25 | -1.17 | 23.97% |
| PHB | Prohibitin | -3.19 | -1.67 | 23.69% |
| CISD1 | CDGSH iron-sulfur domain-containing protein 1 | -3.29 | -1.72 | 23.67% |
| SSU72 | RNA polymerase II subunit A C-terminal domain phosphatase SSU72 | 2.12 | 1.08 | 23.66% |
| GSLG1 | Golgi apparatus protein 1 | -6.89 | -2.78 | 23.57% |
| LAT1 | Large neutral amino acids transporter small subunit 1 | 1.60 | 0.68 | 23.40% |
| RAC1 | Ras-related C3 botulinum toxin substrate 1 | -1.59 | -0.67 | 23.36% |
| E41L1 | Band 4.1-like protein 1 | 2.68 | 1.42 | 23.26% |
| RBBP7 | Histone-binding protein RBBP7 | 3.82 | 1.93 | 23.23% |
| MAP6 | Microtubule-associated protein 6 | 1.89 | 0.92 | 23.22% |
| TAGL3 | Transgelin-3 | -4.06 | -2.02 | 23.07% |
| SODM | Superoxide dismutase [Mn], mitochondrial | -3.25 | -1.70 | 23.02% |
| LMNA | Prelamin-A/C | 2.04 | 1.03 | 22.73% |
| ILF3 | Interleukin enhancer-binding factor 3 | -2.67 | -1.42 | 22.71% |
| SNAA | Alpha-soluble NSF attachment protein | 1.51 | 0.59 | 22.55% |
| CSN4 | COP9 signalosome complex subunit 4 | -2.85 | -1.51 | 22.43% |
| KCC2B | Calcium/calmodulin-dependent protein kinase type II subunit beta | -2.51 | -1.33 | 22.21% |

| | | | | |
|---|---|---|---|---|
| PGK1 | Phosphoglycerate kinase 1 | -2.50 | -1.32 | 22.16% |
| CELF2 | CUGBP Elav-like family member 2 | 2.28 | 1.19 | 21.94% |
| SCOT1 | Succinyl-CoA:3-ketoacid coenzyme A transferase 1, mitochondrial | 1.99 | 0.99 | 21.74% |
| HDGF | Hepatoma-derived growth factor | 2.97 | 1.57 | 21.59% |
| RASH | GTPase HRas | 1.23 | 0.30 | 21.51% |
| SARNP | SAP domain-containing ribonucleoprotein | 1.78 | 0.83 | 21.30% |
| VPP1 | V-type proton ATPase 116 kDa subunit a isoform 1 | 1.35 | 0.44 | 20.85% |
| STRAP | Serine-threonine kinase receptor-associated protein | -4.54 | -2.18 | 20.85% |
| RL23A | 60S ribosomal protein L23a | 2.22 | 1.15 | 20.81% |
| PA2G4 | Proliferation-associated protein 2G4 | -1.74 | -0.80 | 20.79% |
| ADDB | Beta-adducin | 5.38 | 2.43 | 20.64% |
| SRGP2 | SLIT-ROBO Rho GTPase-activating protein 2 | -4.23 | -2.08 | 20.58% |
| ACON | Aconitate hydratase, mitochondrial | -5.62 | -2.49 | 20.15% |
| NDUS1 | NADH-ubiquinone oxidoreductase 75 kDa subunit, mitochondrial | 2.64 | 1.40 | 19.92% |
| ERLN2 | Erlin-2 | 3.23 | 1.69 | 19.90% |
| EIF3H | Eukaryotic translation initiation factor 3 subunit H | -2.71 | -1.44 | 19.73% |
| PRP19 | Pre-mRNA-processing factor 19 | -1.94 | -0.96 | 19.61% |
| MYO5A | Unconventional myosin-Va | 15.13 | 3.92 | 19.42% |
| NCDN | Neurochondrin | -3.23 | -1.69 | 19.11% |
| RL36A | 60S ribosomal protein L36a | 1.63 | 0.71 | 18.58% |
| PSD13 | 26S proteasome non-ATPase regulatory subunit 13 | 2.53 | 1.34 | 18.38% |
| RAP1B | Ras-related protein Rap-1b | -3.13 | -1.65 | 18.24% |
| SYUA | Alpha-synuclein | -7.26 | -2.86 | 18.07% |
| CD81 | CD81 antigen | -1.78 | -0.83 | 17.91% |
| XPP1 | Xaa-Pro aminopeptidase 1 | -1.50 | -0.59 | 17.72% |
| PAK1 | Serine/threonine-protein kinase PAK 1 | 2.74 | 1.46 | 17.47% |
| RS27 | 40S ribosomal protein S27 | -1.20 | -0.26 | 17.20% |
| RPAB1 | DNA-directed RNA polymerases I, II, and III subunit RPABC1 | 4.14 | 2.05 | 17.13% |
| CTNB1 | Catenin beta-1 | 2.11 | 1.08 | 17.00% |
| PLPP | Pyridoxal phosphate phosphatase | -1.72 | -0.78 | 16.91% |
| PGAM1 | Phosphoglycerate mutase 1 | -1.98 | -0.99 | 16.75% |
| PYGL | Glycogen phosphorylase, liver form | -2.75 | -1.46 | 16.50% |
| KINH | Kinesin-1 heavy chain | -1.76 | -0.82 | 15.95% |
| UB2V2 | Ubiquitin-conjugating enzyme E2 variant 2 | -3.82 | -1.93 | 15.64% |
| YKT6 | Synaptobrevin homolog YKT6 | -3.97 | -1.99 | 15.06% |
| SDCB1 | Syntenin-1 | 8.07 | 3.01 | 15.01% |
| ODO2 | Dihydrolipoyllysine-residue succinyltransferase component of 2-oxoglutarate dehydrogenase complex, mitochondrial | 4.14 | 2.05 | 14.23% |

| | | | | |
|---|---|---|---|---|
| GCYB1 | Guanylate cyclase soluble subunit beta-1 | -1.50 | -0.59 | 14.11% |
| APLP2 | Amyloid-like protein 2 | 5.98 | 2.58 | 13.76% |
| RIPR2 | Protein FAM65B | 1.47 | 0.55 | 12.43% |
| RS24 | 40S ribosomal protein S24 | -2.24 | -1.16 | 12.25% |
| TIPRL | TIP41-like protein | 4.76 | 2.25 | 11.36% |
| CK5P2 | CDK5 regulatory subunit-associated protein 2 | -1.40 | -0.49 | 11.31% |
| DYLT1 | Dynein light chain Tctex-type 1 | 2.46 | 1.30 | 10.97% |
| PP2BA | Serine/threonine-protein phosphatase 2B catalytic subunit alpha isoform | -1.22 | -0.29 | 9.95% |
| AT2A2 | Sarcoplasmic/endoplasmic reticulum calcium ATPase 2 | 2.10 | 1.07 | 9.57% |
| GATM | Glycine amidinotransferase, mitochondrial | 1.91 | 0.94 | 5.86% |
| BAG6 | Large proline-rich protein BAG6 | -2.20 | -1.14 | 4.64% |
| OX2G | OX-2 membrane glycoprotein | 1.35 | 0.43 | 2.52% |
| KAD2 | Adenylate kinase 2, mitochondrial | -1.09 | -0.13 | 1.54% |
| SMCE1 | SWI/SNF-related matrix-associated actin-dependent regulator of chromatin subfamily E member 1 | 1.20 | 0.26 | 1.34% |
| RBMX | RNA-binding motif protein, X chromosome | 1.11 | 0.15 | 0.74% |

Appendix table 1: Raw data for the mass spectrometry described in Chapter 5

## 9.7 Nanostring raw data

| Probe Name | Accession # | NS Probe ID | NF | StDev of NF | Control | StDev of Control | NF vs. Control | P value of: NF vs. Control | t-statistic of: NF vs. Control |
|---|---|---|---|---|---|---|---|---|---|
| Gfap | NM_001131020.1 | NM_001131020.1:610 | 1276.32 | 507.93 | 187.89 | 95.83 | 6.79 | 0.00 | 7.63 |
| Apoe | NM_001305844.1 | NM_001305844.1:903 | 3632.65 | 2484.23 | 396.24 | 420.68 | 9.17 | 0.00 | 5.13 |
| Idh1 | NM_010497.2 | NM_010497.2:495 | 3076.70 | 705.51 | 1699.56 | 308.91 | 1.81 | 0.00 | 5.03 |
| Dcx | NM_010025.2 | NM_010025.2:8575 | 4329.49 | 975.29 | 2483.48 | 479.20 | 1.74 | 0.00 | 4.69 |
| Snca | NM_009221.2 | NM_009221.2:285 | 1093.84 | 230.34 | 625.48 | 93.86 | 1.75 | 0.00 | 5.01 |
| Akt3 | NM_011785.3 | NM_011785.3:2494 | 1015.61 | 263.62 | 577.23 | 113.82 | 1.76 | 0.00 | 4.36 |
| Cadm3 | NM_053199.3 | NM_053199.3:3295 | 2623.28 | 841.51 | 1373.75 | 355.89 | 1.91 | 0.00 | 4.19 |
| Pla2g16 | NM_139269.2 | NM_139269.2:568 | 230.61 | 74.48 | 104.23 | 26.45 | 2.21 | 0.00 | 4.38 |

| | | | | | | | | | |
|---|---|---|---|---|---|---|---|---|---|
| Nes | NM_016701.3 | NM_016701.3:2716 | 103.74 | 55.89 | 33.21 | 19.08 | 3.12 | 0.00 | 3.85 |
| Vegfa | NM_001025250.3 | NM_001025250.3:3015 | 1536.74 | 378.47 | 920.86 | 252.77 | 1.67 | 0.00 | 3.72 |
| Nqo1 | NM_008706.5 | NM_008706.5:430 | 833.20 | 376.70 | 286.82 | 40.48 | 2.90 | 0.00 | 5.24 |
| Syt4 | NM_009308.3 | NM_009308.3:1120 | 4789.17 | 944.53 | 3097.42 | 552.17 | 1.55 | 0.01 | 3.81 |
| Slc1a2 | NM_001077514.3 | NM_001077514.3:1675 | 819.02 | 299.65 | 414.73 | 71.86 | 1.97 | 0.01 | 4.35 |
| Gnai3 | NM_010306.2 | NM_010306.2:354 | 1360.48 | 262.07 | 923.31 | 189.63 | 1.47 | 0.01 | 3.49 |
| Becn1 | NM_019584.3 | NM_019584.3:1145 | 1872.60 | 518.80 | 1129.79 | 267.55 | 1.66 | 0.01 | 3.57 |
| Atp6v0e | NM_025272.2 | NM_025272.2:585 | 112.13 | 27.48 | 67.26 | 19.25 | 1.67 | 0.01 | 3.41 |
| Tnc | NM_011607.1 | NM_011607.1:5665 | 304.56 | 181.61 | 108.81 | 34.23 | 2.80 | 0.01 | 3.85 |
| Pcna | NM_011045.2 | NM_011045.2:590 | 954.25 | 154.71 | 693.74 | 101.70 | 1.38 | 0.01 | 3.51 |
| Casp3 | NM_009810.2 | NM_009810.2:630 | 645.84 | 103.15 | 466.20 | 79.67 | 1.39 | 0.01 | 3.27 |
| Aldh1l1 | NM_027406.1 | NM_027406.1:1340 | 63.29 | 39.13 | 20.15 | 0.40 | 3.14 | 0.01 | 4.59 |
| Cxcl12 | NM_021704.3 | NM_021704.3:259 | 419.65 | 193.06 | 200.24 | 76.10 | 2.10 | 0.01 | 3.24 |
| Rtn4 | NM_194053.3 | NM_194053.3:930 | 4843.22 | 1124.51 | 3202.29 | 650.94 | 1.51 | 0.01 | 3.37 |
| Pten | NM_008960.2 | NM_008960.2:5160 | 1426.79 | 347.63 | 959.00 | 167.71 | 1.49 | 0.01 | 3.38 |
| Ap3s1 | NM_009681.5 | NM_009681.5:610 | 2251.60 | 526.45 | 1505.08 | 321.16 | 1.50 | 0.01 | 3.20 |
| Ppp3ca | NM_008913.4 | NM_008913.4:1675 | 2020.69 | 444.74 | 1398.94 | 250.78 | 1.44 | 0.01 | 3.24 |
| Gnai2 | NM_008138.4 | NM_008138.4:971 | 5150.76 | 1879.68 | 2812.76 | 940.39 | 1.83 | 0.01 | 3.15 |
| Cdc40 | NM_027879.2 | NM_027879.2:1606 | 297.02 | 79.47 | 194.11 | 35.85 | 1.53 | 0.01 | 3.26 |
| Sptbn2 | NM_021287.1 | NM_021287.1:6145 | 1318.35 | 453.39 | 779.86 | 169.34 | 1.69 | 0.01 | 3.33 |
| Ipcef1 | NM_001033391.2 | NM_001033391.2:180 | 98.07 | 21.26 | 149.34 | 39.44 | -1.52 | 0.01 | -2.98 |
| Atp6v1d | NM_023721.2 | NM_023721.2:408 | 2268.15 | 564.03 | 1515.87 | 351.77 | 1.50 | 0.01 | 3.05 |
| Dnaja2 | NM_019794.4 | NM_019794.4:1045 | 956.98 | 263.56 | 626.85 | 126.39 | 1.53 | 0.02 | 3.16 |
| Atp6v1h | XM_006495434.2 | XM_006495434.2:1296 | 2842.42 | 859.05 | 1796.96 | 440.66 | 1.58 | 0.02 | 3.05 |

| | | | | | | | | | |
|---|---|---|---|---|---|---|---|---|---|
| Homer1 | NM_147176.2 | NM_147176.2:1165 | 1021.62 | 198.53 | 732.06 | 144.34 | 1.40 | 0.02 | 2.96 |
| Fxn | NM_008044.2 | NM_008044.2:218 | 675.30 | 167.17 | 435.34 | 128.60 | 1.55 | 0.02 | 2.90 |
| Map2 | NM_008632.2 | NM_008632.2:5243 | 4227.01 | 1222.27 | 2779.50 | 623.54 | 1.52 | 0.02 | 3.04 |
| Hif1a | NM_010431.2 | NM_010431.2:1294 | 1963.35 | 463.99 | 1359.10 | 287.85 | 1.44 | 0.02 | 2.97 |
| Rhoa | NM_016802.4 | NM_016802.4:1885 | 1495.84 | 279.63 | 1080.45 | 229.39 | 1.38 | 0.02 | 2.86 |
| Tbpl1 | NM_011603.5 | NM_011603.5:714 | 1064.84 | 238.37 | 754.94 | 146.74 | 1.41 | 0.02 | 2.95 |
| Bax | NM_007527.3 | NM_007527.3:735 | 348.27 | 80.64 | 221.12 | 85.59 | 1.58 | 0.02 | 2.79 |
| Mgmt | NM_008598.2 | NM_008598.2:350 | 111.91 | 33.24 | 69.06 | 14.78 | 1.62 | 0.02 | 3.04 |
| Mapk1 | NM_011949.3 | NM_011949.3:1210 | 2917.29 | 877.48 | 1923.31 | 384.58 | 1.52 | 0.02 | 3.02 |
| Ppp2r5c | NM_001135001.1 | NM_001135001.1:1400 | 2783.43 | 842.91 | 1808.66 | 398.51 | 1.54 | 0.02 | 2.97 |
| Trem2 | NM_031254.2 | NM_031254.2:646 | 41.02 | 19.25 | 71.86 | 15.75 | -1.75 | 0.02 | -3.10 |
| Ddc | NM_016672.4 | NM_016672.4:1358 | 34.78 | 7.90 | 50.61 | 15.84 | -1.46 | 0.02 | -2.75 |
| Gng2 | NM_010315.4 | NM_010315.4:1352 | 1366.42 | 555.76 | 762.75 | 229.65 | 1.79 | 0.02 | 2.93 |
| Pak1 | NM_011035.2 | NM_011035.2:1615 | 1894.65 | 550.61 | 1238.33 | 312.62 | 1.53 | 0.02 | 2.86 |
| Stat3 | NM_213659.2 | NM_213659.2:1360 | 393.78 | 130.82 | 245.77 | 52.53 | 1.60 | 0.02 | 3.03 |
| Nptn | NM_009145.2 | NM_009145.2:1110 | 2866.32 | 773.89 | 1983.32 | 355.01 | 1.45 | 0.02 | 2.91 |
| Dlg3 | NM_001177778.1 | NM_001177778.1:2586 | 1033.12 | 415.38 | 612.79 | 163.89 | 1.69 | 0.02 | 2.91 |
| Ctnnb1 | NM_007614.2 | NM_007614.2:2975 | 3151.72 | 1266.21 | 1831.82 | 390.64 | 1.72 | 0.02 | 3.03 |
| Cntn1 | NM_001159647.1 | NM_001159647.1:1070 | 3257.77 | 1027.73 | 2160.28 | 437.62 | 1.51 | 0.02 | 2.89 |
| Prkce | NM_011104.2 | NM_011104.2:1510 | 500.35 | 122.67 | 359.42 | 78.04 | 1.39 | 0.03 | 2.72 |
| Nell2 | NM_016743.2 | NM_016743.2:500 | 4353.92 | 1336.55 | 2877.68 | 543.10 | 1.51 | 0.03 | 2.87 |
| Adam10 | NM_007399.3 | NM_007399.3:2390 | 503.01 | 92.29 | 370.61 | 94.51 | 1.36 | 0.03 | 2.60 |
| Kcnj10 | NM_001039484.1 | NM_001039484.1:400 | 175.84 | 49.10 | 114.83 | 26.66 | 1.53 | 0.03 | 2.72 |
| Myh10 | NM_175260.2 | NM_175260.2:2540 | 2031.80 | 608.49 | 1340.68 | 378.94 | 1.52 | 0.03 | 2.63 |

| | | | | | | | | | |
|---|---|---|---|---|---|---|---|---|---|
| Sod1 | NM_011434.1 | NM_011434.1:406 | 4283.62 | 1016.94 | 3027.53 | 644.87 | 1.41 | 0.03 | 2.68 |
| Rras | NM_009101.2 | NM_009101.2:282 | 42.53 | 10.56 | 27.51 | 10.26 | 1.55 | 0.03 | 2.58 |
| Entpd4 | NM_026174.2 | NM_026174.2:845 | 120.41 | 34.63 | 82.11 | 19.13 | 1.47 | 0.03 | 2.66 |
| Inhbb | NM_008381.3 | NM_008381.3:1084 | 23.63 | 5.27 | 35.88 | 13.96 | -1.52 | 0.03 | -2.54 |
| Gucy1b3 | NM_017469.4 | NM_017469.4:372 | 732.64 | 243.84 | 461.27 | 125.37 | 1.59 | 0.03 | 2.61 |
| Pgk1 | NM_008828.2 | NM_008828.2:36 | 642.20 | 100.98 | 497.07 | 90.99 | 1.29 | 0.03 | 2.50 |
| Camk2b | NM_001174053.1 | NM_001174053.1:2825 | 1544.56 | 580.56 | 956.47 | 259.30 | 1.61 | 0.03 | 2.67 |
| Ppp3cb | NM_008914.1 | NM_008914.1:290 | 5090.79 | 1740.84 | 3342.43 | 723.91 | 1.52 | 0.03 | 2.71 |
| Snrpa | NM_001046637.1 | NM_001046637.1:880 | 377.25 | 81.33 | 274.22 | 67.25 | 1.38 | 0.03 | 2.49 |
| Clu | NM_013492.2 | NM_013492.2:354 | 2071.19 | 810.26 | 1161.02 | 305.72 | 1.78 | 0.03 | 2.72 |
| Stx1a | NM_016801.3 | NM_016801.3:72 | 2296.80 | 799.63 | 1472.05 | 446.67 | 1.56 | 0.03 | 2.54 |
| Arrb2 | NM_145429.4 | NM_145429.4:725 | 712.97 | 182.12 | 488.90 | 154.06 | 1.46 | 0.03 | 2.44 |
| Rab2a | NM_021518.3 | NM_021518.3:450 | 8320.94 | 2548.74 | 5774.24 | 1193.16 | 1.44 | 0.04 | 2.56 |
| Vcp | NM_009503.3 | NM_009503.3:510 | 5973.93 | 1657.04 | 4160.02 | 917.15 | 1.44 | 0.04 | 2.49 |
| Rit2 | NM_009065.2 | NM_009065.2:626 | 321.15 | 71.85 | 231.91 | 60.10 | 1.38 | 0.04 | 2.40 |
| Lrrc4 | NM_138682.2 | NM_138682.2:2790 | 401.75 | 102.69 | 288.43 | 62.77 | 1.39 | 0.04 | 2.48 |
| Lars | NM_134137.2 | NM_134137.2:945 | 1078.05 | 222.21 | 795.12 | 191.97 | 1.36 | 0.04 | 2.42 |
| Ppp3cc | NM_008915.2 | NM_008915.2:1020 | 781.21 | 238.30 | 547.17 | 107.98 | 1.43 | 0.04 | 2.55 |
| Syt7 | NM_018801.3 | NM_018801.3:990 | 352.20 | 134.67 | 221.22 | 64.76 | 1.59 | 0.04 | 2.50 |
| Plxnc1 | NM_018797.2 | NM_018797.2:2120 | 614.69 | 269.73 | 383.40 | 83.67 | 1.60 | 0.04 | 2.63 |
| Il13ra1 | NM_133990.4 | NM_133990.4:845 | 30.65 | 9.95 | 20.81 | 1.49 | 1.47 | 0.04 | 2.88 |
| Ppp2ca | NM_019411.4 | NM_019411.4:975 | 6863.10 | 2011.86 | 4802.16 | 1242.65 | 1.43 | 0.04 | 2.40 |
| Pik3r1 | NM_001024955.1 | NM_001024955.1:5664 | 464.81 | 120.76 | 340.73 | 65.90 | 1.36 | 0.04 | 2.43 |
| Dlg4 | NM_001109752.1 | NM_001109752.1:1866 | 2750.65 | 855.59 | 1840.33 | 520.04 | 1.49 | 0.04 | 2.37 |

| | | | | | | | | | |
|---|---|---|---|---|---|---|---|---|---|
| Tmem119 | NM_146162.2 | NM_146162.2:1550 | 35.35 | 13.81 | 53.95 | 10.94 | -1.53 | 0.04 | -2.56 |
| Bace1 | NM_011792.4 | NM_011792.4:3107 | 729.12 | 238.87 | 503.47 | 116.74 | 1.45 | 0.04 | 2.43 |
| Sox9 | NM_011448.4 | NM_011448.4:3540 | 54.32 | 21.88 | 28.61 | 10.16 | 1.90 | 0.05 | 2.45 |
| Atp6v0c | NM_009729.3 | NM_009729.3:569 | 15226.85 | 5027.39 | 9999.39 | 3541.53 | 1.52 | 0.05 | 2.31 |
| Atf4 | NM_009716.2 | NM_009716.2:812 | 10196.18 | 2418.57 | 7350.83 | 1903.19 | 1.39 | 0.05 | 2.31 |
| Eif2s1 | NM_026114.3 | NM_026114.3:665 | 1677.19 | 316.31 | 1294.87 | 236.73 | 1.30 | 0.05 | 2.32 |
| Arhgef10 | NM_001037736.1 | NM_001037736.1:1105 | 36.17 | 10.72 | 25.25 | 6.17 | 1.43 | 0.05 | 2.34 |
| Sgpl1 | NM_009163.3 | NM_009163.3:1200 | 344.62 | 126.63 | 231.60 | 42.03 | 1.49 | 0.05 | 2.49 |
| Gabrb3 | NM_008071.3 | NM_008071.3:4200 | 219.33 | 39.64 | 169.94 | 37.61 | 1.29 | 0.05 | 2.24 |
| Slu7 | NM_148673.3 | NM_148673.3:1034 | 671.82 | 107.64 | 520.99 | 132.35 | 1.29 | 0.05 | 2.22 |
| 3110043O21Rik | NM_001081343.1 | NM_001081343.1:1020 | 640.64 | 173.09 | 449.98 | 145.24 | 1.42 | 0.05 | 2.22 |
| Meaf6 | NM_027310.3 | NM_027310.3:178 | 414.44 | 162.33 | 271.02 | 65.82 | 1.53 | 0.05 | 2.39 |
| Gusb | NM_010368.1 | NM_010368.1:1735 | 50.71 | 22.39 | 29.64 | 8.71 | 1.71 | 0.05 | 2.36 |
| Insr | NM_010568.2 | NM_010568.2:7814 | 76.86 | 18.35 | 55.34 | 15.16 | 1.39 | 0.05 | 2.20 |
| Slc12a5 | NM_020333.2 | NM_020333.2:5618 | 483.89 | 240.31 | 290.33 | 94.94 | 1.67 | 0.05 | 2.33 |
| Pdgfrb | NM_008809.1 | NM_008809.1:1185 | 20.87 | 2.12 | 29.44 | 11.62 | -1.41 | 0.05 | -2.30 |
| Sec23a | NM_009147.2 | NM_009147.2:1445 | 1837.01 | 553.93 | 1314.82 | 266.83 | 1.40 | 0.06 | 2.31 |
| Atp6v0d1 | NM_013477.3 | NM_013477.3:640 | 948.58 | 295.03 | 652.78 | 208.95 | 1.45 | 0.06 | 2.19 |
| Mapt | NM_001038609.2 | NM_001038609.2:1202 | 3961.93 | 1149.36 | 2851.92 | 472.20 | 1.39 | 0.06 | 2.37 |
| Fam126a | XM_006535824.2 | XM_006535824.2:826 | 411.88 | 152.08 | 276.43 | 64.00 | 1.49 | 0.06 | 2.31 |
| Bad | NM_007522.3 | NM_007522.3:1146 | 943.23 | 217.53 | 675.98 | 217.00 | 1.40 | 0.06 | 2.15 |
| Ap2a2 | NM_007459.3 | NM_007459.3:2540 | 3849.78 | 1287.17 | 2628.15 | 718.66 | 1.46 | 0.06 | 2.22 |
| Acaa1a | NM_130864.3 | NM_130864.3:626 | 66.11 | 10.43 | 52.23 | 11.65 | 1.27 | 0.06 | 2.14 |
| Plcb3 | NM_008874.3 | NM_008874.3:1880 | 54.12 | 19.90 | 33.56 | 15.23 | 1.61 | 0.06 | 2.14 |

| | | | | | | | | | |
|---|---|---|---|---|---|---|---|---|---|
| Smn1 | NM_011420.2 | NM_011420.2:390 | 686.11 | 187.60 | 507.34 | 107.91 | 1.35 | 0.06 | 2.25 |
| Xab2 | NM_026156.2 | NM_026156.2:1616 | 695.68 | 184.87 | 495.71 | 160.05 | 1.40 | 0.06 | 2.13 |
| Des | NM_010043.1 | NM_010043.1:157 | 46.09 | 34.46 | 83.30 | 18.62 | -1.81 | 0.06 | -2.43 |
| Atp6v1a | NM_007508.5 | NM_007508.5:434 | 1977.96 | 503.43 | 1488.83 | 289.83 | 1.33 | 0.06 | 2.22 |
| Stx1b | NM_024414.2 | NM_024414.2:570 | 2678.09 | 838.75 | 1905.59 | 445.72 | 1.41 | 0.06 | 2.21 |
| Rad23b | NM_009011.4 | NM_009011.4:1585 | 4809.75 | 1381.75 | 3534.65 | 727.38 | 1.36 | 0.06 | 2.23 |
| Calb1 | NM_009788.4 | NM_009788.4:343 | 527.26 | 191.93 | 355.89 | 65.29 | 1.48 | 0.06 | 2.35 |
| Lypla1 | XM_006495472.2 | XM_006495472.2:648 | 854.08 | 262.71 | 612.55 | 129.28 | 1.39 | 0.06 | 2.25 |
| Ehmt1 | NM_001012518.2 | NM_001012518.2:2845 | 483.76 | 186.97 | 321.81 | 71.30 | 1.50 | 0.06 | 2.31 |
| Cab39 | NM_133781.4 | NM_133781.4:2830 | 1547.76 | 372.48 | 1187.00 | 232.85 | 1.30 | 0.06 | 2.17 |
| Mmp9 | NM_013599.2 | NM_013599.2:1570 | 30.88 | 9.80 | 44.43 | 10.50 | -1.44 | 0.06 | -2.20 |
| Cntnap1 | NM_016782.2 | NM_016782.2:1105 | 80.96 | 6.93 | 100.35 | 24.02 | -1.24 | 0.06 | -2.17 |
| Phf21a | NM_001109690.1 | NM_001109690.1:2324 | 47.37 | 15.78 | 30.68 | 12.45 | 1.54 | 0.06 | 2.11 |
| Polr2j | NM_011293.2 | NM_011293.2:70 | 844.57 | 200.10 | 638.82 | 123.37 | 1.32 | 0.06 | 2.18 |
| Prkcb | NM_008855.2 | NM_008855.2:8332 | 226.88 | 55.53 | 170.16 | 24.88 | 1.33 | 0.06 | 2.29 |
| F2 | NM_010168.2 | NM_010168.2:1010 | 31.41 | 13.61 | 48.34 | 9.93 | -1.54 | 0.06 | -2.29 |
| Akt1 | NM_001165894.1 | NM_001165894.1:898 | 2071.56 | 640.61 | 1396.34 | 507.17 | 1.48 | 0.06 | 2.10 |
| Rdx | NM_001104617.1 | NM_001104617.1:1384 | 996.13 | 262.85 | 746.87 | 156.42 | 1.33 | 0.06 | 2.17 |
| Pfn1 | NM_011072.4 | NM_011072.4:266 | 4229.86 | 923.07 | 3184.48 | 800.03 | 1.33 | 0.06 | 2.09 |
| Map2k1 | NM_008927.3 | NM_008927.3:1695 | 749.73 | 139.51 | 555.68 | 172.56 | 1.35 | 0.06 | 2.08 |
| Tor1a | NM_144884.1 | NM_144884.1:220 | 223.27 | 35.23 | 170.24 | 51.77 | 1.31 | 0.07 | 2.09 |
| Acin1 | NM_001085472.2 | NM_001085472.2:674 | 1586.99 | 551.14 | 1131.78 | 265.03 | 1.40 | 0.07 | 2.19 |
| Unc13a | NM_001029873.2 | NM_001029873.2:7755 | 1744.52 | 649.29 | 1219.82 | 229.19 | 1.43 | 0.07 | 2.25 |

| | | | | | | | | | |
|---|---|---|---|---|---|---|---|---|---|
| Gnptg | NM_172529.3 | NM_172529.3:95 | 177.39 | 27.99 | 214.60 | 30.22 | -1.21 | 0.07 | -2.13 |
| Mmp14 | NM_008608.3 | NM_008608.3:554 | 318.07 | 152.38 | 187.35 | 34.54 | 1.70 | 0.07 | 2.36 |
| Cd68 | NM_009853.1 | NM_009853.1:636 | 23.30 | 3.09 | 20.08 | 0.21 | 1.16 | 0.07 | 2.50 |
| Epha4 | NM_007936.3 | NM_007936.3:2796 | 145.70 | 49.54 | 104.24 | 26.71 | 1.40 | 0.07 | 2.09 |
| Gnptab | NM_001004164.2 | NM_001004164.2:1214 | 423.95 | 155.20 | 302.59 | 52.23 | 1.40 | 0.07 | 2.24 |
| Dnm1l | NM_001025947.1 | NM_001025947.1:2075 | 1362.31 | 284.66 | 1064.31 | 202.87 | 1.28 | 0.07 | 2.11 |
| Cp | NM_001042611.1 | NM_001042611.1:1750 | 103.53 | 60.23 | 208.89 | 158.71 | -2.02 | 0.07 | -2.05 |
| App | NM_007471.2 | NM_007471.2:511 | 7383.33 | 1707.13 | 5719.20 | 1126.17 | 1.29 | 0.07 | 2.13 |
| Gjb1 | NM_008124.2 | NM_008124.2:113 | 47.82 | 20.30 | 70.17 | 10.25 | -1.47 | 0.07 | -2.32 |
| B4galt6 | NM_019737.2 | NM_019737.2:1465 | 903.47 | 325.45 | 627.41 | 106.09 | 1.44 | 0.07 | 2.28 |
| Hras | NM_001130443.1 | NM_001130443.1:240 | 3124.08 | 888.20 | 2225.80 | 731.77 | 1.40 | 0.07 | 2.04 |
| Ugcg | NM_011673.3 | NM_011673.3:610 | 1318.71 | 533.46 | 903.95 | 204.71 | 1.46 | 0.07 | 2.18 |
| Jam3 | NM_023277.4 | NM_023277.4:145 | 292.97 | 90.51 | 214.36 | 42.91 | 1.37 | 0.07 | 2.13 |
| Opa1 | NM_001199177.1 | NM_001199177.1:2845 | 714.45 | 179.76 | 544.09 | 116.59 | 1.31 | 0.07 | 2.08 |
| Jun | NM_010591.2 | NM_010591.2:2212 | 596.27 | 179.27 | 408.87 | 163.31 | 1.46 | 0.07 | 2.01 |
| Npas4 | NM_153553.4 | NM_153553.4:580 | 965.15 | 449.26 | 545.12 | 367.07 | 1.77 | 0.07 | 2.01 |
| Prkaca | NM_008854.3 | NM_008854.3:699 | 3241.38 | 1069.68 | 2245.60 | 773.23 | 1.44 | 0.07 | 2.02 |
| Mapk9 | NM_207692.1 | NM_207692.1:260 | 874.48 | 250.41 | 651.17 | 163.77 | 1.34 | 0.08 | 2.04 |
| Gtf2b | NM_145546.1 | NM_145546.1:346 | 596.15 | 113.42 | 468.27 | 116.32 | 1.27 | 0.08 | 1.98 |
| Cul1 | NM_012042.3 | NM_012042.3:919 | 1370.93 | 290.84 | 1075.21 | 266.66 | 1.28 | 0.08 | 1.97 |
| Gsk3b | NM_019827.3 | NM_019827.3:2215 | 2316.06 | 702.80 | 1715.00 | 421.44 | 1.35 | 0.08 | 2.02 |
| Fus | NM_139149.2 | NM_139149.2:15 | 1877.60 | 433.86 | 1486.62 | 187.51 | 1.26 | 0.08 | 2.12 |
| Csnk2a2 | NM_009974.3 | NM_009974.3:1066 | 1162.44 | 374.14 | 852.10 | 189.61 | 1.36 | 0.08 | 2.02 |
| Adra2a | NM_007417.4 | NM_007417.4:3594 | 186.37 | 33.59 | 151.82 | 28.45 | 1.23 | 0.08 | 1.98 |

| | | | | | | | | | |
|---|---|---|---|---|---|---|---|---|---|
| Mapk10 | NM_001081567.1 | NM_001081567.1:1496 | 1421.68 | 452.49 | 1057.97 | 200.22 | 1.34 | 0.08 | 2.06 |
| Vip | NM_011702.2 | NM_011702.2:395 | 212.42 | 99.60 | 344.88 | 172.28 | -1.62 | 0.08 | -1.94 |
| Mta1 | NM_054081.2 | NM_054081.2:955 | 1167.10 | 396.60 | 827.16 | 226.07 | 1.41 | 0.08 | 1.97 |
| Ube3a | NM_173010.3 | NM_173010.3:2025 | 1027.82 | 245.70 | 803.00 | 188.61 | 1.28 | 0.09 | 1.93 |
| Gpr37 | NM_010338.2 | NM_010338.2:1828 | 117.52 | 37.19 | 84.18 | 23.36 | 1.40 | 0.09 | 1.95 |
| Sncaip | NM_001199151.1 | NM_001199151.1:1385 | 230.45 | 78.51 | 164.61 | 32.70 | 1.40 | 0.09 | 2.04 |
| Gtf2h1 | NM_008186.4 | NM_008186.4:830 | 408.50 | 92.79 | 323.27 | 65.60 | 1.26 | 0.09 | 1.93 |
| Pqbp1 | NM_001252528.1 | NM_001252528.1:212 | 427.25 | 82.64 | 340.41 | 69.85 | 1.26 | 0.09 | 1.91 |
| C1qa | NM_007572.2 | NM_007572.2:566 | 26.77 | 13.34 | 40.70 | 11.44 | -1.52 | 0.09 | -1.95 |
| Crebbp | NM_001025432.1 | NM_001025432.1:3770 | 849.54 | 299.11 | 621.96 | 129.51 | 1.37 | 0.09 | 1.99 |
| Taf10 | NM_020024.3 | NM_020024.3:357 | 1952.77 | 576.41 | 1347.92 | 597.93 | 1.45 | 0.09 | 1.89 |
| Synj1 | NM_001045515.1 | NM_001045515.1:4090 | 624.77 | 157.86 | 493.06 | 101.96 | 1.27 | 0.09 | 1.94 |
| Gsr | NM_010344.4 | NM_010344.4:1507 | 334.93 | 117.11 | 237.50 | 66.77 | 1.41 | 0.09 | 1.96 |
| Fasl | NM_010177.3 | NM_010177.3:645 | 40.98 | 16.57 | 58.18 | 9.27 | -1.42 | 0.09 | -2.09 |
| Gnao1 | NM_010308.3 | NM_010308.3:754 | 4346.68 | 1453.32 | 3190.67 | 642.83 | 1.36 | 0.09 | 2.01 |
| Snap91 | NM_001277986.1 | NM_001277986.1:3170 | 2855.65 | 1008.11 | 2087.37 | 449.38 | 1.37 | 0.09 | 1.99 |
| Glrb | NM_010298.5 | NM_010298.5:704 | 777.47 | 164.25 | 623.59 | 131.97 | 1.25 | 0.09 | 1.88 |
| Prkcg | NM_011102.3 | NM_011102.3:1580 | 210.42 | 78.16 | 151.52 | 17.12 | 1.39 | 0.09 | 2.10 |
| Cast | NM_009817.1 | NM_009817.1:1820 | 21.22 | 3.08 | 31.43 | 21.09 | -1.48 | 0.10 | -1.92 |
| Rapgef2 | NM_001099624.2 | NM_001099624.2:5580 | 856.77 | 266.14 | 657.90 | 118.78 | 1.30 | 0.10 | 1.95 |
| Scamp2 | NM_022813.3 | NM_022813.3:526 | 156.63 | 75.40 | 105.66 | 21.49 | 1.48 | 0.10 | 2.01 |
| Pla2g6 | NM_001199023.1 | NM_001199023.1:768 | 270.83 | 114.34 | 176.82 | 69.54 | 1.53 | 0.10 | 1.88 |
| Srsf4 | NM_020587.2 | NM_020587.2:524 | 496.82 | 187.89 | 354.00 | 103.22 | 1.40 | 0.10 | 1.88 |

| | | | | | | | | | |
|---|---|---|---|---|---|---|---|---|---|
| Ncf1 | NM_001286037.1 | NM_001286037.1:970 | 42.78 | 19.97 | 62.92 | 15.92 | -1.47 | 0.10 | -1.95 |
| Tada2b | NM_001170454.1 | NM_001170454.1:3224 | 402.48 | 129.38 | 303.15 | 54.60 | 1.33 | 0.10 | 1.93 |
| Trim28 | NM_011588.3 | NM_011588.3:1615 | 2437.70 | 758.52 | 1800.85 | 520.88 | 1.35 | 0.10 | 1.83 |
| Tpm1 | NM_024427.4 | NM_024427.4:426 | 894.62 | 225.67 | 706.96 | 144.54 | 1.27 | 0.10 | 1.86 |
| Fos | NM_010234.2 | NM_010234.2:1330 | 2624.02 | 1302.62 | 1477.77 | 1260.18 | 1.78 | 0.10 | 1.81 |
| Usp21 | NM_013919.4 | NM_013919.4:1590 | 173.30 | 54.81 | 128.92 | 35.42 | 1.34 | 0.10 | 1.84 |
| Drd4 | NM_007878.2 | NM_007878.2:962 | 29.21 | 23.21 | 50.14 | 21.00 | -1.72 | 0.10 | -1.84 |
| Ptdss2 | NM_013782.4 | NM_013782.4:844 | 413.93 | 134.66 | 304.49 | 86.98 | 1.36 | 0.10 | 1.82 |
| Bcl2l1 | NM_009743.4 | NM_009743.4:200 | 744.99 | 261.54 | 551.48 | 140.29 | 1.35 | 0.11 | 1.85 |
| Slc11a1 | NM_013612.2 | NM_013612.2:945 | 38.57 | 15.13 | 55.76 | 17.98 | -1.45 | 0.11 | -1.86 |
| Ptdss1 | NM_008959.3 | NM_008959.3:1830 | 860.31 | 234.14 | 669.26 | 127.75 | 1.29 | 0.11 | 1.85 |
| Gsn | NM_146120.3 | NM_146120.3:624 | 154.74 | 61.63 | 108.59 | 23.68 | 1.43 | 0.11 | 1.92 |
| Ache | NM_009599.3 | NM_009599.3:1073 | 78.23 | 31.96 | 115.06 | 32.52 | -1.47 | 0.11 | -1.83 |
| Xiap | NM_009688.2 | NM_009688.2:1654 | 346.61 | 96.41 | 271.65 | 53.87 | 1.28 | 0.11 | 1.83 |
| Gria1 | NM_001252403.1 | NM_001252403.1:2476 | 740.06 | 221.11 | 570.73 | 100.75 | 1.30 | 0.11 | 1.86 |
| Gtf2h3 | NM_181410.3 | NM_181410.3:38 | 220.46 | 75.55 | 163.55 | 30.30 | 1.35 | 0.11 | 1.87 |
| Abl1 | NM_009594.4 | NM_009594.4:1378 | 193.44 | 51.78 | 153.99 | 18.35 | 1.26 | 0.11 | 1.90 |
| Park7 | NM_020569.3 | NM_020569.3:334 | 1470.88 | 448.69 | 1090.09 | 369.74 | 1.35 | 0.11 | 1.74 |
| Sirt1 | NM_019812.2 | NM_019812.2:843 | 140.42 | 25.28 | 117.44 | 21.81 | 1.20 | 0.11 | 1.74 |
| Atp6v1e1 | NM_007510.2 | NM_007510.2:1025 | 40.76 | 22.44 | 64.48 | 16.40 | -1.58 | 0.12 | -1.84 |
| Cyp4x1 | NM_001003947.1 | NM_001003947.1:564 | 234.35 | 61.25 | 184.71 | 41.95 | 1.27 | 0.12 | 1.73 |
| Hap1 | NM_010404.3 | NM_010404.3:2552 | 192.59 | 80.29 | 128.62 | 59.63 | 1.50 | 0.12 | 1.72 |
| Cck | NM_031161.2 | NM_031161.2:351 | 296.83 | 45.10 | 374.56 | 114.95 | -1.26 | 0.12 | -1.72 |
| Ccnd1 | NM_007631.1 | NM_007631.1:2000 | 37.27 | 12.07 | 26.83 | 9.39 | 1.39 | 0.12 | 1.72 |

| | | | | | | | | | |
|---|---|---|---|---|---|---|---|---|---|
| Atxn2 | NM_009125.2 | NM_009125.2:3036 | 1116.86 | 338.96 | 875.98 | 162.64 | 1.27 | 0.12 | 1.77 |
| Hnrnpm | NM_001109913.1 | NM_001109913.1:606 | 963.74 | 194.79 | 778.02 | 187.46 | 1.24 | 0.12 | 1.69 |
| Ggt1 | NM_008116.2 | NM_008116.2:1025 | 42.40 | 15.62 | 62.76 | 18.63 | -1.48 | 0.12 | -1.77 |
| Sh3tc2 | NM_172628.2 | NM_172628.2:2150 | 58.67 | 39.00 | 91.90 | 17.65 | -1.57 | 0.12 | -1.87 |
| Cul2 | NM_029402.3 | NM_029402.3:2528 | 1077.69 | 231.78 | 885.15 | 163.52 | 1.22 | 0.13 | 1.71 |
| Cnksr2 | NM_177751.2 | NM_177751.2:628 | 1779.09 | 384.03 | 1385.23 | 456.47 | 1.28 | 0.13 | 1.67 |
| Ryr1 | NM_009109.1 | NM_009109.1:11830 | 62.44 | 25.58 | 87.62 | 24.56 | -1.40 | 0.13 | -1.72 |
| Raf1 | NM_029780.3 | NM_029780.3:550 | 1383.16 | 427.73 | 1069.72 | 254.44 | 1.29 | 0.13 | 1.71 |
| Prkcsh | NM_008925.1 | NM_008925.1:1295 | 2378.84 | 756.42 | 1811.43 | 475.72 | 1.31 | 0.13 | 1.70 |
| Tradd | NM_001033161.2 | NM_001033161.2:562 | 49.14 | 26.19 | 71.81 | 16.36 | -1.46 | 0.13 | -1.75 |
| Ube2k | NM_016786.3 | NM_016786.3:1212 | 84.24 | 18.09 | 66.23 | 17.18 | 1.27 | 0.13 | 1.64 |
| Nsf | NM_008740.2 | NM_008740.2:395 | 3585.86 | 1122.68 | 2799.76 | 585.04 | 1.28 | 0.13 | 1.71 |
| Sri | NM_001080974.2 | NM_001080974.2:470 | 454.11 | 91.92 | 379.75 | 54.29 | 1.20 | 0.13 | 1.70 |
| Egr1 | NM_007913.5 | NM_007913.5:515 | 945.68 | 717.74 | 468.81 | 601.70 | 2.02 | 0.13 | 1.64 |
| Atp13a2 | NM_029097.2 | NM_029097.2:1360 | 989.27 | 294.64 | 763.38 | 204.27 | 1.30 | 0.13 | 1.66 |
| Tardbp | NM_001003899.2 | NM_001003899.2:3060 | 355.33 | 73.36 | 287.32 | 67.89 | 1.24 | 0.14 | 1.63 |
| Fgf12 | NM_001276419.1 | NM_001276419.1:632 | 1740.26 | 405.65 | 1406.29 | 263.03 | 1.24 | 0.14 | 1.67 |
| Nr4a2 | NM_001139509.1 | NM_001139509.1:1626 | 710.11 | 368.55 | 473.21 | 97.87 | 1.50 | 0.14 | 1.76 |
| Avp | NM_009732.2 | NM_009732.2:52 | 45.36 | 20.24 | 62.61 | 12.86 | -1.38 | 0.14 | -1.72 |
| Slc18a3 | NM_021712.2 | NM_021712.2:845 | 40.48 | 13.70 | 52.46 | 12.63 | -1.30 | 0.14 | -1.65 |
| Cdk5 | NM_007668.3 | NM_007668.3:77 | 545.41 | 193.72 | 409.16 | 119.39 | 1.33 | 0.14 | 1.63 |
| Gpr4 | NM_175668.4 | NM_175668.4:212 | 27.96 | 9.54 | 38.66 | 15.17 | -1.38 | 0.14 | -1.59 |
| Lsm7 | NM_025349.2 | NM_025349.2:37 | 478.00 | 123.91 | 383.71 | 86.25 | 1.25 | 0.14 | 1.61 |

| | | | | | | | | | |
|---|---|---|---|---|---|---|---|---|---|
| Phf2 | NM_011078.2 | NM_011078.2:3590 | 462.39 | 119.93 | 377.39 | 65.14 | 1.23 | 0.15 | 1.64 |
| Magee1 | NM_053201.3 | NM_053201.3:2362 | 470.25 | 194.98 | 343.61 | 92.74 | 1.37 | 0.15 | 1.63 |
| Plcb1 | NM_019677.1 | NM_019677.1:495 | 484.22 | 152.24 | 379.79 | 72.98 | 1.27 | 0.15 | 1.64 |
| Ccnh | NM_023243.2 | NM_023243.2:960 | 240.43 | 63.39 | 173.13 | 67.88 | 1.39 | 0.15 | 1.54 |
| Ring1 | NM_009066.3 | NM_009066.3:243 | 312.21 | 86.19 | 246.87 | 62.08 | 1.26 | 0.16 | 1.56 |
| Psen2 | NM_001128605.1 | NM_001128605.1:560 | 265.37 | 59.60 | 220.58 | 44.89 | 1.20 | 0.16 | 1.57 |
| Sf3a2 | NM_013651.4 | NM_013651.4:494 | 395.25 | 99.91 | 324.57 | 58.44 | 1.22 | 0.16 | 1.58 |
| Dlat | NM_145614.4 | NM_145614.4:2046 | 1120.35 | 336.35 | 886.70 | 230.97 | 1.26 | 0.16 | 1.54 |
| Cacna1f | NM_019582.2 | NM_019582.2:4215 | 27.50 | 8.46 | 35.84 | 11.23 | -1.30 | 0.16 | -1.51 |
| Mag | NM_010758.2 | NM_010758.2:1670 | 26.16 | 5.88 | 33.49 | 11.81 | -1.28 | 0.16 | -1.51 |
| Mbp | NM_010777.3 | NM_010777.3:761 | 94.97 | 18.27 | 113.71 | 27.81 | -1.20 | 0.16 | -1.50 |
| Fmr1 | NM_008031.2 | NM_008031.2:765 | 726.34 | 123.54 | 610.06 | 145.59 | 1.19 | 0.17 | 1.50 |
| Aars | NM_146217.4 | NM_146217.4:716 | 2667.20 | 868.36 | 2092.83 | 421.43 | 1.27 | 0.17 | 1.56 |
| Nrxn1 | NM_001346960.1 | NM_001346960.1:2013 | 1295.34 | 277.41 | 1029.69 | 344.53 | 1.26 | 0.17 | 1.49 |
| Erbb3 | NM_010153.1 | NM_010153.1:1290 | 54.03 | 29.86 | 78.83 | 15.56 | -1.46 | 0.17 | -1.62 |
| Dagla | NM_198114.2 | NM_198114.2:685 | 170.92 | 72.78 | 129.11 | 24.97 | 1.32 | 0.17 | 1.57 |
| Itga5 | NM_001314041.1 | NM_001314041.1:2622 | 57.62 | 33.60 | 84.33 | 28.99 | -1.46 | 0.17 | -1.52 |
| Negr1 | NM_001039094.2 | NM_001039094.2:770 | 1445.69 | 536.18 | 1112.83 | 219.84 | 1.30 | 0.17 | 1.56 |
| Stat1 | NM_009283.3 | NM_009283.3:1590 | 125.94 | 43.99 | 95.66 | 20.02 | 1.32 | 0.17 | 1.55 |
| Cln3 | NM_001146311.1 | NM_001146311.1:378 | 32.45 | 7.72 | 40.91 | 13.78 | -1.26 | 0.18 | -1.45 |
| Nfe2l2 | NR_132727.1 | NR_132727.1:193 | 146.59 | 41.41 | 118.83 | 21.74 | 1.23 | 0.18 | 1.50 |
| Mtor | NM_020009.2 | NM_020009.2:2432 | 486.04 | 238.80 | 349.61 | 82.23 | 1.39 | 0.18 | 1.54 |
| Fgf2 | NM_008006.2 | NM_008006.2:509 | 68.46 | 20.99 | 54.09 | 9.21 | 1.27 | 0.18 | 1.52 |
| Grm5 | NM_001143834.1 | NM_001143834.1:4242 | 620.44 | 143.97 | 516.00 | 119.41 | 1.20 | 0.18 | 1.45 |

| | | | | | | | | | |
|---|---|---|---|---|---|---|---|---|---|
| Pdpk1 | NM_001080773.2 | NM_001080773.2:856 | 758.62 | 269.76 | 599.25 | 119.40 | 1.27 | 0.19 | 1.49 |
| Trp53 | NM_011640.1 | NM_011640.1:1835 | 20.30 | 0.42 | 20.00 | 0.00 | 1.01 | 0.19 | 1.60 |
| Lsm2 | NM_001110101.2 | NM_001110101.2:641 | 20.00 | 0.00 | 21.27 | 2.49 | -1.06 | 0.19 | -1.49 |
| Mal | NM_001171187.1 | NM_001171187.1:685 | 37.16 | 26.81 | 54.77 | 12.02 | -1.47 | 0.19 | -1.53 |
| Tcerg1 | NM_001039474.1 | NM_001039474.1:468 | 881.95 | 257.95 | 718.31 | 165.65 | 1.23 | 0.19 | 1.43 |
| Arhgap44 | NM_001099288.1 | NM_001099288.1:904 | 328.68 | 147.15 | 240.94 | 79.43 | 1.36 | 0.19 | 1.45 |
| Axin2 | NM_015732.4 | NM_015732.4:1120 | 45.20 | 17.72 | 33.83 | 11.68 | 1.34 | 0.19 | 1.40 |
| Palm | NM_023128.4 | NM_023128.4:548 | 1738.50 | 579.40 | 1375.29 | 322.31 | 1.26 | 0.20 | 1.43 |
| Tgfb1 | NM_011577.1 | NM_011577.1:1470 | 22.98 | 4.57 | 20.15 | 0.40 | 1.14 | 0.20 | 1.54 |
| Trim37 | NM_197987.2 | NM_197987.2:972 | 520.36 | 185.77 | 412.07 | 83.39 | 1.26 | 0.20 | 1.43 |
| Ins2 | NM_008387.3 | NM_008387.3:266 | 58.14 | 37.13 | 82.46 | 21.34 | -1.42 | 0.20 | -1.45 |
| Pik3cb | NM_029094.3 | NM_029094.3:1970 | 491.96 | 140.77 | 401.15 | 91.54 | 1.23 | 0.20 | 1.39 |
| Ncam1 | NM_001113204.1 | NM_001113204.1:740 | 4127.51 | 1364.68 | 3232.16 | 1120.70 | 1.28 | 0.20 | 1.37 |
| Sirt2 | NM_022432.4 | NM_022432.4:435 | 863.79 | 244.09 | 697.25 | 185.30 | 1.24 | 0.20 | 1.38 |
| Slc6a3 | NM_010020.3 | NM_010020.3:1082 | 54.11 | 40.72 | 82.71 | 19.11 | -1.53 | 0.20 | -1.46 |
| Nfkbib | NM_010908.4 | NM_010908.4:382 | 20.12 | 0.28 | 21.73 | 3.29 | -1.08 | 0.20 | -1.42 |
| Mto1 | NM_026658.2 | NM_026658.2:1058 | 20.00 | 0.00 | 22.58 | 6.05 | -1.13 | 0.21 | -1.42 |
| Cers6 | NM_172856.3 | NM_172856.3:678 | 497.85 | 99.89 | 427.22 | 83.59 | 1.17 | 0.21 | 1.36 |
| Adcyap1 | NM_001315503.1 | NM_001315503.1:2625 | 462.13 | 116.46 | 372.27 | 90.01 | 1.24 | 0.21 | 1.38 |
| Gdnf | NM_010275.2 | NM_010275.2:460 | 68.71 | 30.29 | 92.54 | 28.86 | -1.35 | 0.21 | -1.37 |
| Pla2g4b | XM_925095.2 | XM_925095.2:310 | 153.85 | 49.99 | 194.65 | 43.94 | -1.27 | 0.21 | -1.38 |
| Adora1 | NM_001008533.3 | NM_001008533.3:1603 | 89.44 | 27.29 | 110.77 | 21.52 | -1.24 | 0.21 | -1.39 |
| Grin2a | NM_008170.2 | NM_008170.2:1788 | 53.64 | 22.73 | 67.24 | 3.55 | -1.25 | 0.21 | -1.47 |

| | | | | | | | | | |
|---|---|---|---|---|---|---|---|---|---|
| Polr2h | NM_145632.2 | NM_145632.2:100 | 534.39 | 146.33 | 439.11 | 100.73 | 1.22 | 0.22 | 1.34 |
| Mmp12 | NM_008605.3 | NM_008605.3:592 | 67.68 | 61.05 | 102.74 | 22.96 | -1.52 | 0.22 | -1.43 |
| Aif1 | NM_019467.2 | NM_019467.2:55 | 48.91 | 21.49 | 63.44 | 14.44 | -1.30 | 0.22 | -1.37 |
| Rela | NM_009045.4 | NM_009045.4:645 | 53.15 | 19.70 | 39.85 | 16.24 | 1.33 | 0.22 | 1.30 |
| Gabrp | NM_146017.3 | NM_146017.3:484 | 40.78 | 37.16 | 60.88 | 15.05 | -1.49 | 0.23 | -1.39 |
| Tcirg1 | NM_001136091.1 | NM_001136091.1:1345 | 69.38 | 36.31 | 92.14 | 18.08 | -1.33 | 0.23 | -1.37 |
| Gata2 | NM_008090.4 | NM_008090.4:2960 | 38.08 | 18.06 | 51.51 | 13.34 | -1.35 | 0.23 | -1.35 |
| Trpm2 | NM_138301.2 | NM_138301.2:2106 | 103.84 | 30.31 | 125.96 | 23.49 | -1.21 | 0.23 | -1.32 |
| Cldn5 | NM_013805.4 | NM_013805.4:975 | 55.75 | 44.63 | 81.77 | 23.59 | -1.47 | 0.23 | -1.35 |
| Sucla2 | NM_011506.1 | NM_011506.1:955 | 1322.58 | 235.66 | 1136.20 | 264.83 | 1.16 | 0.23 | 1.27 |
| Mutyh | NM_001159581.1 | NM_001159581.1:709 | 70.07 | 26.56 | 89.59 | 24.32 | -1.28 | 0.23 | -1.30 |
| Cxxc1 | NM_028868.3 | NM_028868.3:1749 | 292.92 | 89.82 | 241.10 | 61.70 | 1.21 | 0.24 | 1.28 |
| Hdac6 | NM_010413.3 | NM_010413.3:2195 | 371.25 | 148.15 | 290.44 | 79.49 | 1.28 | 0.24 | 1.28 |
| Mapk8 | NM_016700.3 | NM_016700.3:970 | 507.56 | 162.60 | 384.00 | 160.03 | 1.32 | 0.24 | 1.25 |
| Tnfrsf12a | NM_001161746.1 | NM_001161746.1:517 | 109.59 | 46.04 | 146.03 | 55.68 | -1.33 | 0.24 | -1.26 |
| Il6ra | NM_010559.2 | NM_010559.2:2825 | 32.67 | 18.31 | 44.77 | 19.19 | -1.37 | 0.24 | -1.25 |
| Taf4 | NM_001081092.1 | NM_001081092.1:3016 | 214.25 | 57.86 | 177.60 | 42.80 | 1.21 | 0.24 | 1.26 |
| Dll4 | NM_019454.2 | NM_019454.2:542 | 47.70 | 27.45 | 64.39 | 22.06 | -1.35 | 0.24 | -1.27 |
| Myc | NM_010849.4 | NM_010849.4:630 | 667.08 | 197.01 | 540.07 | 175.61 | 1.24 | 0.25 | 1.23 |
| Chrna7 | NM_007390.3 | NM_007390.3:335 | 377.68 | 144.99 | 484.98 | 116.97 | -1.28 | 0.25 | -1.27 |
| Gad2 | NM_008078.2 | NM_008078.2:769 | 1717.84 | 940.71 | 2421.78 | 1241.88 | -1.41 | 0.25 | -1.23 |
| Tnf | NM_013693.2 | NM_013693.2:514 | 39.45 | 23.07 | 53.56 | 14.29 | -1.36 | 0.25 | -1.28 |
| Erlec1 | NM_025745.3 | NM_025745.3:940 | 645.80 | 117.76 | 567.16 | 97.51 | 1.14 | 0.25 | 1.23 |
| Ddx23 | NM_001080981.1 | NM_001080981.1:2175 | 381.90 | 96.44 | 325.07 | 68.66 | 1.17 | 0.26 | 1.22 |

| | | | | | | | | | |
|---|---|---|---|---|---|---|---|---|---|
| Cplx1 | NM_007756.3 | NM_007756.3:327 | 285.46 | 92.49 | 225.81 | 100.73 | 1.26 | 0.26 | 1.20 |
| Hspb1 | NM_013560.2 | NM_013560.2:630 | 50.70 | 22.33 | 63.58 | 14.59 | -1.25 | 0.26 | -1.25 |
| Hdac2 | NM_008229.2 | NM_008229.2:1010 | 48.68 | 31.49 | 69.74 | 20.53 | -1.43 | 0.26 | -1.25 |
| Crtc2 | NM_028881.2 | NM_028881.2:1477 | 46.89 | 20.34 | 35.47 | 14.36 | 1.32 | 0.27 | 1.18 |
| Polr2k | NM_001039368.1 | NM_001039368.1:323 | 63.19 | 37.03 | 82.77 | 18.71 | -1.31 | 0.27 | -1.22 |
| Grn | NM_008175.3 | NM_008175.3:2010 | 158.62 | 40.91 | 133.20 | 27.08 | 1.19 | 0.27 | 1.19 |
| Prkcq | NM_008859.2 | NM_008859.2:1210 | 38.96 | 11.22 | 30.73 | 16.33 | 1.27 | 0.28 | 1.15 |
| Adrb2 | NM_007420.2 | NM_007420.2:680 | 31.07 | 26.68 | 43.70 | 13.65 | -1.41 | 0.28 | -1.18 |
| Lmna | NM_001002011.2 | NM_001002011.2:1611 | 713.55 | 143.11 | 613.86 | 144.75 | 1.16 | 0.28 | 1.15 |
| Cacna1c | NM_001159535.1 | NM_001159535.1:1000 | 89.53 | 31.99 | 108.69 | 19.72 | -1.21 | 0.28 | -1.19 |
| Ddit3 | NM_007837.3 | NM_007837.3:255 | 1536.57 | 428.75 | 1856.92 | 412.96 | -1.21 | 0.28 | -1.18 |
| Grin3b | NM_130455.2 | NM_130455.2:2030 | 23.34 | 6.79 | 28.44 | 10.44 | -1.22 | 0.28 | -1.14 |
| Il10ra | NM_008348.2 | NM_008348.2:2522 | 67.83 | 41.43 | 91.32 | 15.11 | -1.35 | 0.28 | -1.22 |
| Tbr1 | NM_009322.3 | NM_009322.3:2354 | 231.25 | 35.67 | 202.66 | 52.08 | 1.14 | 0.29 | 1.13 |
| Tnfrsf11b | NM_008764.3 | NM_008764.3:684 | 71.05 | 41.24 | 91.19 | 16.04 | -1.28 | 0.29 | -1.20 |
| Ccs | XM_006531645.1 | XM_006531645.1:185 | 266.34 | 67.33 | 229.62 | 43.49 | 1.16 | 0.29 | 1.15 |
| Itpr2 | NM_010586.1 | NM_010586.1:4365 | 28.03 | 5.14 | 23.84 | 8.42 | 1.18 | 0.29 | 1.12 |
| Atrn | NM_009730.2 | NM_009730.2:1375 | 640.70 | 127.78 | 568.68 | 101.16 | 1.13 | 0.29 | 1.14 |
| Taf9 | NM_027139.5 | NM_027139.5:324 | 508.78 | 75.42 | 421.02 | 159.33 | 1.21 | 0.29 | 1.13 |
| Sorl1 | NM_011436.3 | NM_011436.3:2720 | 160.23 | 39.31 | 135.22 | 40.84 | 1.18 | 0.29 | 1.11 |
| Efnb3 | NM_007911.5 | NM_007911.5:2880 | 46.13 | 27.45 | 60.78 | 20.76 | -1.32 | 0.29 | -1.13 |
| Drd2 | NM_010077.2 | NM_010077.2:630 | 77.17 | 38.53 | 96.61 | 16.12 | -1.25 | 0.29 | -1.17 |
| Cnot10 | NM_153585.5 | NM_153585.5:714 | 213.75 | 63.10 | 182.29 | 38.32 | 1.17 | 0.30 | 1.13 |
| Chrm5 | NM_205783.2 | NM_205783.2:1170 | 54.45 | 25.18 | 69.38 | 21.62 | -1.27 | 0.30 | -1.13 |

| | | | | | | | | | |
|---|---|---|---|---|---|---|---|---|---|
| Entpd2 | NM_009849.2 | NM_009849.2:1016 | 93.46 | 34.14 | 73.13 | 21.83 | 1.28 | 0.30 | 1.13 |
| Cdk2 | NM_016756.4 | NM_016756.4:831 | 179.05 | 64.95 | 143.38 | 29.80 | 1.25 | 0.30 | 1.13 |
| Ldhc | NM_013580.4 | NM_013580.4:470 | 51.66 | 42.12 | 71.40 | 22.17 | -1.38 | 0.30 | -1.13 |
| Gtf2ird1 | NM_001081464.1 | NM_001081464.1:1430 | 464.41 | 146.43 | 393.57 | 75.84 | 1.18 | 0.30 | 1.12 |
| Optn | NM_181848.4 | NM_181848.4:1018 | 175.52 | 43.43 | 138.70 | 68.06 | 1.27 | 0.30 | 1.08 |
| Gnai1 | NM_010305.1 | NM_010305.1:470 | 1916.49 | 365.65 | 1649.16 | 460.32 | 1.16 | 0.31 | 1.08 |
| P2ry12 | NM_027571.3 | NM_027571.3:439 | 41.67 | 23.48 | 54.73 | 14.74 | -1.31 | 0.31 | -1.12 |
| Islr2 | NM_001161538.1 | NM_001161538.1:1782 | 1753.33 | 660.01 | 1433.39 | 425.71 | 1.22 | 0.31 | 1.09 |
| Sirt7 | NM_153056.2 | NM_153056.2:575 | 83.02 | 15.15 | 74.65 | 10.23 | 1.11 | 0.32 | 1.08 |
| Tenm2 | NM_011856.3 | NM_011856.3:1452 | 537.54 | 189.04 | 454.63 | 81.07 | 1.18 | 0.32 | 1.08 |
| Camk2g | NM_001039138.1 | NM_001039138.1:2525 | 33.77 | 5.07 | 40.39 | 18.04 | -1.20 | 0.33 | -1.04 |
| Dnm2 | NM_001039520.1 | NM_001039520.1:1148 | 40.62 | 27.92 | 54.41 | 20.23 | -1.34 | 0.33 | -1.07 |
| Grm2 | NM_001160353.1 | NM_001160353.1:2770 | 273.00 | 62.51 | 239.66 | 53.42 | 1.14 | 0.33 | 1.04 |
| Gga1 | NM_145929.2 | NM_145929.2:1896 | 40.80 | 17.74 | 50.70 | 11.88 | -1.24 | 0.33 | -1.07 |
| Scn1a | NM_018733.2 | NM_018733.2:1030 | 259.08 | 87.63 | 325.60 | 131.55 | -1.26 | 0.33 | -1.03 |
| Cdk5r1 | NM_009871.2 | NM_009871.2:3280 | 22.88 | 5.79 | 20.49 | 1.40 | 1.12 | 0.33 | 1.09 |
| Flt1 | NM_010228.3 | NM_010228.3:1550 | 48.38 | 33.27 | 64.47 | 16.96 | -1.33 | 0.33 | -1.07 |
| Grin2d | NM_008172.2 | NM_008172.2:1201 | 70.44 | 21.71 | 84.21 | 20.93 | -1.20 | 0.33 | -1.04 |
| Mnat1 | NM_008612.2 | NM_008612.2:914 | 298.73 | 59.90 | 262.41 | 58.98 | 1.14 | 0.33 | 1.02 |
| Drd1 | NM_010076.3 | NM_010076.3:1785 | 42.18 | 28.26 | 56.98 | 20.14 | -1.35 | 0.33 | -1.04 |
| Epha5 | NM_007937.3 | NM_007937.3:2005 | 1116.30 | 280.29 | 965.65 | 270.51 | 1.16 | 0.34 | 1.02 |
| Mmp19 | NM_021412.2 | NM_021412.2:1140 | 47.42 | 23.41 | 59.33 | 12.72 | -1.25 | 0.34 | -1.04 |
| Naglu | NM_013792.2 | NM_013792.2:2334 | 20.64 | 1.52 | 22.43 | 5.14 | -1.09 | 0.34 | -1.01 |
| Gpr84 | NM_030720.1 | NM_030720.1:315 | 40.32 | 21.31 | 49.91 | 9.80 | -1.24 | 0.35 | -1.03 |

| | | | | | | | | | |
|---|---|---|---|---|---|---|---|---|---|
| Tgfbr2 | NM_009371.2 | NM_009371.2:475 | 46.48 | 22.48 | 58.36 | 16.17 | -1.26 | 0.35 | -1.02 |
| Rab3a | NM_009001.6 | NM_009001.6:1272 | 3165.37 | 1343.46 | 2547.63 | 850.83 | 1.24 | 0.35 | 1.00 |
| Cacnb2 | NM_023116.3 | NM_023116.3:735 | 134.28 | 39.63 | 114.31 | 34.42 | 1.17 | 0.35 | 0.99 |
| Chl1 | NM_007697.2 | NM_007697.2:2010 | 1034.35 | 294.49 | 883.81 | 275.44 | 1.17 | 0.35 | 0.97 |
| Dld | NM_007861.4 | NM_007861.4:252 | 1270.90 | 247.65 | 1119.06 | 290.93 | 1.14 | 0.36 | 0.97 |
| Aqp4 | NM_009700.2 | NM_009700.2:130 | 20.00 | 0.00 | 20.08 | 0.21 | -1.00 | 0.36 | -1.00 |
| C4a | NM_011413.2 | NM_011413.2:4186 | 20.00 | 0.00 | 20.21 | 0.56 | -1.01 | 0.36 | -1.00 |
| Egf | NM_010113.3 | NM_010113.3:1886 | 20.00 | 0.00 | 21.79 | 6.24 | -1.09 | 0.36 | -1.00 |
| Esam | NM_027102.3 | NM_027102.3:495 | 20.00 | 0.00 | 20.95 | 2.90 | -1.05 | 0.36 | -1.00 |
| Grin2b | NM_008171.3 | NM_008171.3:6340 | 20.00 | 0.00 | 20.47 | 1.33 | -1.02 | 0.36 | -1.00 |
| Lama2 | NM_008481.2 | NM_008481.2:208 | 20.00 | 0.00 | 20.65 | 1.90 | -1.03 | 0.36 | -1.00 |
| Mmrn2 | NM_153127.3 | NM_153127.3:2622 | 20.00 | 0.00 | 20.99 | 3.04 | -1.05 | 0.36 | -1.00 |
| Nol3 | NM_030152.4 | NM_030152.4:916 | 20.00 | 0.00 | 22.03 | 7.35 | -1.10 | 0.36 | -1.00 |
| Ntrk1 | NM_001033124.1 | NM_001033124.1:1481 | 20.00 | 0.00 | 20.21 | 0.56 | -1.01 | 0.36 | -1.00 |
| Ube2n | NM_080560.3 | NM_080560.3:2376 | 20.00 | 0.00 | 20.23 | 0.62 | -1.01 | 0.36 | -1.00 |
| Supt7l | NM_028150.1 | NM_028150.1:180 | 20.00 | 0.00 | 20.06 | 0.15 | -1.00 | 0.36 | -1.00 |
| Adcy8 | NM_009623.2 | NM_009623.2:2655 | 271.35 | 51.53 | 240.67 | 61.65 | 1.13 | 0.36 | 0.97 |
| Myct1 | NM_026793.2 | NM_026793.2:180 | 56.48 | 40.80 | 72.46 | 17.14 | -1.28 | 0.36 | -1.01 |
| Oxr1 | NM_001130163.1 | NM_001130163.1:2976 | 915.06 | 197.87 | 801.06 | 191.98 | 1.14 | 0.36 | 0.97 |
| Pde1b | NM_008800.1 | NM_008800.1:595 | 99.01 | 30.20 | 86.97 | 14.31 | 1.14 | 0.36 | 0.99 |
| Cul3 | NM_016716.4 | NM_016716.4:1662 | 776.36 | 172.74 | 680.89 | 168.23 | 1.14 | 0.36 | 0.96 |
| Gaa | NM_008064.3 | NM_008064.3:1390 | 129.13 | 50.70 | 154.28 | 31.93 | -1.19 | 0.36 | -0.99 |
| Pgam1 | NM_023418.2 | NM_023418.2:466 | 3639.50 | 754.91 | 3253.06 | 602.55 | 1.12 | 0.37 | 0.96 |
| Itga7 | NM_008398.2 | NM_008398.2:2435 | 21.46 | 2.02 | 23.23 | 4.70 | -1.08 | 0.37 | -0.95 |
| Prkca | NM_011101.3 | NM_011101.3:6965 | 109.23 | 25.61 | 96.95 | 16.28 | 1.13 | 0.37 | 0.96 |

| | | | | | | | | | |
|---|---|---|---|---|---|---|---|---|---|
| L1cam | NM_008478.3 | NM_008478.3:3560 | 904.72 | 256.24 | 788.58 | 201.17 | 1.15 | 0.37 | 0.95 |
| Mapk3 | NM_011952.2 | NM_011952.2:825 | 487.97 | 72.04 | 449.84 | 59.61 | 1.08 | 0.37 | 0.95 |
| Uchl1 | NM_011670.2 | NM_011670.2:54 | 56.96 | 31.03 | 70.56 | 13.04 | -1.24 | 0.37 | -0.98 |
| Cxcr4 | NM_009911.3 | NM_009911.3:704 | 49.10 | 28.74 | 61.55 | 17.07 | -1.25 | 0.37 | -0.96 |
| Atf6 | NM_001081304.1 | NM_001081304.1:4765 | 20.08 | 0.17 | 20.00 | 0.00 | 1.00 | 0.37 | 1.00 |
| Dlx2 | NM_010054.2 | NM_010054.2:1891 | 20.87 | 2.12 | 20.00 | 0.00 | 1.04 | 0.37 | 1.00 |
| Ninj2 | NM_016718.2 | NM_016718.2:244 | 20.08 | 0.17 | 20.00 | 0.00 | 1.00 | 0.37 | 1.00 |
| Plxnb3 | NM_019587.2 | NM_019587.2:2862 | 20.01 | 0.02 | 20.00 | 0.00 | 1.00 | 0.37 | 1.00 |
| Ppt1 | NM_008917.3 | NM_008917.3:1714 | 20.08 | 0.17 | 20.00 | 0.00 | 1.00 | 0.37 | 1.00 |
| Prpf31 | NM_001159714.1 | NM_001159714.1:1765 | 21.79 | 4.82 | 20.00 | 0.00 | 1.09 | 0.37 | 1.00 |
| Ptprn2 | NM_011215.2 | NM_011215.2:4158 | 20.92 | 2.25 | 20.00 | 0.00 | 1.05 | 0.37 | 1.00 |
| Tlr2 | NM_011905.2 | NM_011905.2:255 | 20.08 | 0.17 | 20.00 | 0.00 | 1.00 | 0.37 | 1.00 |
| Brms1l | NM_001037756.2 | NM_001037756.2:1770 | 206.67 | 60.01 | 175.68 | 52.07 | 1.18 | 0.38 | 0.93 |
| C6 | NM_016704.2 | NM_016704.2:170 | 78.29 | 69.93 | 104.45 | 20.78 | -1.33 | 0.38 | -0.97 |
| Nkx6-2 | NM_183248.3 | NM_183248.3:265 | 23.04 | 6.13 | 26.52 | 8.61 | -1.15 | 0.38 | -0.92 |
| Notch1 | NM_008714.2 | NM_008714.2:1425 | 270.77 | 116.50 | 225.86 | 35.39 | 1.20 | 0.38 | 0.96 |
| Polr2b | NM_153798.2 | NM_153798.2:1090 | 305.96 | 103.72 | 252.95 | 85.65 | 1.21 | 0.38 | 0.91 |
| Nelfa | NM_011914.2 | NM_011914.2:930 | 431.90 | 109.19 | 384.36 | 84.02 | 1.12 | 0.39 | 0.92 |
| Slc17a6 | NM_080853.3 | NM_080853.3:2825 | 825.69 | 215.84 | 694.01 | 275.11 | 1.19 | 0.39 | 0.91 |
| Shh | NM_009170.3 | NM_009170.3:2055 | 76.48 | 44.52 | 97.23 | 33.04 | -1.27 | 0.39 | -0.92 |
| Akt2 | NM_001110208.1 | NM_001110208.1:2504 | 213.75 | 42.14 | 193.01 | 34.17 | 1.11 | 0.39 | 0.91 |
| Bche | NM_009738.3 | NM_009738.3:300 | 54.56 | 39.10 | 68.43 | 17.25 | -1.25 | 0.39 | -0.93 |
| Nmb | NM_026523.2 | NM_026523.2:500 | 70.38 | 30.67 | 84.49 | 20.38 | -1.20 | 0.40 | -0.91 |
| Atp8a2 | NM_015803.2 | NM_015803.2:185 | 575.59 | 208.23 | 495.63 | 126.48 | 1.16 | 0.40 | 0.89 |

| | | | | | | | | | |
|---|---|---|---|---|---|---|---|---|---|
| Sf3b2 | NM_030109.2 | NM_030109.2:2654 | 29.29 | 14.53 | 36.30 | 13.78 | -1.24 | 0.40 | -0.88 |
| Chmp2b | NM_026879.2 | NM_026879.2:920 | 21.22 | 3.08 | 20.08 | 0.21 | 1.06 | 0.40 | 0.93 |
| Pla2g4f | NM_001024145.2 | NM_001024145.2:2002 | 36.11 | 21.03 | 45.72 | 17.15 | -1.27 | 0.41 | -0.88 |
| Myd88 | NM_010851.2 | NM_010851.2:1595 | 46.29 | 32.79 | 59.87 | 22.23 | -1.29 | 0.41 | -0.87 |
| Nova1 | NM_021361.1 | NM_021361.1:370 | 524.57 | 183.95 | 451.58 | 101.06 | 1.16 | 0.41 | 0.88 |
| Grm1 | NM_001114333.2 | NM_001114333.2:2125 | 47.56 | 19.24 | 55.48 | 10.87 | -1.17 | 0.42 | -0.88 |
| Atg5 | NM_053069.5 | NM_053069.5:774 | 20.26 | 0.59 | 22.18 | 8.10 | -1.10 | 0.42 | -0.87 |
| Grin1 | NM_008169.2 | NM_008169.2:492 | 192.06 | 71.74 | 165.13 | 39.28 | 1.16 | 0.42 | 0.86 |
| Xbp1 | NM_013842.2 | NM_013842.2:825 | 1023.81 | 303.94 | 903.54 | 192.49 | 1.13 | 0.42 | 0.85 |
| Gss | NM_008180.1 | NM_008180.1:728 | 215.78 | 76.86 | 185.18 | 52.44 | 1.17 | 0.43 | 0.82 |
| Shank2 | NM_001081370.2 | NM_001081370.2:4930 | 93.51 | 32.49 | 79.84 | 23.74 | 1.17 | 0.43 | 0.82 |
| Cadps | NM_001042617.1 | NM_001042617.1:3524 | 2794.64 | 942.92 | 2452.18 | 591.94 | 1.14 | 0.43 | 0.83 |
| Plekho2 | NM_153119.2 | NM_153119.2:406 | 71.25 | 12.84 | 64.79 | 14.50 | 1.10 | 0.44 | 0.81 |
| Trf | NM_133977.2 | NM_133977.2:1940 | 28.91 | 14.82 | 34.72 | 11.31 | -1.20 | 0.44 | -0.81 |
| Lamb2 | NM_008483.3 | NM_008483.3:712 | 81.81 | 30.50 | 68.22 | 22.39 | 1.20 | 0.44 | 0.81 |
| Il6 | NM_031168.1 | NM_031168.1:200 | 106.72 | 27.42 | 94.54 | 23.98 | 1.13 | 0.44 | 0.81 |
| Psmb8 | NM_010724.2 | NM_010724.2:362 | 42.75 | 20.17 | 50.94 | 12.34 | -1.19 | 0.44 | -0.82 |
| Slc9a6 | NM_172780.3 | NM_172780.3:1479 | 26.25 | 8.02 | 30.93 | 14.38 | -1.18 | 0.45 | -0.79 |
| Sncb | NM_033610.2 | NM_033610.2:676 | 149.32 | 32.61 | 167.88 | 44.06 | -1.12 | 0.45 | -0.79 |
| Cpt1b | NM_009948.2 | NM_009948.2:924 | 43.75 | 14.43 | 50.04 | 11.77 | -1.14 | 0.45 | -0.80 |
| Efna5 | NM_207654.2 | NM_207654.2:1130 | 103.36 | 28.27 | 113.75 | 15.22 | -1.10 | 0.46 | -0.79 |
| Tbp | NM_013684.3 | NM_013684.3:70 | 295.90 | 86.13 | 263.31 | 59.41 | 1.12 | 0.47 | 0.76 |
| Ep300 | NM_177821.6 | NM_177821.6:4305 | 468.11 | 123.16 | 413.77 | 138.78 | 1.13 | 0.47 | 0.75 |
| Gdpd2 | NM_023608.3 | NM_023608.3:1438 | 31.79 | 8.37 | 27.85 | 12.40 | 1.14 | 0.47 | 0.74 |

| | | | | | | | | | |
|---|---|---|---|---|---|---|---|---|---|
| Tie1 | NM_011587.2 | NM_011587.2:2715 | 23.95 | 7.15 | 21.77 | 2.80 | 1.10 | 0.47 | 0.77 |
| Sorcs3 | NM_025696.3 | NM_025696.3:1868 | 237.62 | 63.81 | 266.32 | 70.84 | -1.12 | 0.48 | -0.74 |
| Gstp1 | NM_013541.1 | NM_013541.1:421 | 159.25 | 77.61 | 188.00 | 38.78 | -1.18 | 0.48 | -0.77 |
| Frmpd4 | NM_001033330.2 | NM_001033330.2:4690 | 187.45 | 51.21 | 165.58 | 51.92 | 1.13 | 0.48 | 0.74 |
| Plcl2 | NM_013880.3 | NM_013880.3:475 | 969.22 | 212.67 | 885.23 | 195.28 | 1.09 | 0.48 | 0.73 |
| Pmp22 | NM_008885.2 | NM_008885.2:395 | 127.09 | 43.80 | 110.96 | 28.87 | 1.15 | 0.49 | 0.74 |
| Cdk5rap3 | NM_030248.1 | NM_030248.1:248 | 205.98 | 74.28 | 181.60 | 50.32 | 1.13 | 0.49 | 0.72 |
| Pvalb | NM_013645.3 | NM_013645.3:60 | 30.23 | 15.43 | 35.19 | 10.77 | -1.16 | 0.50 | -0.71 |
| Ngf | NM_001112698.1 | NM_001112698.1:630 | 41.34 | 23.99 | 49.80 | 19.67 | -1.20 | 0.50 | -0.71 |
| Src | NM_001025395.2 | NM_001025395.2:968 | 386.79 | 166.58 | 333.99 | 85.53 | 1.16 | 0.50 | 0.71 |
| Arsa | NM_009713.4 | NM_009713.4:2802 | 160.90 | 46.73 | 143.43 | 32.88 | 1.12 | 0.50 | 0.70 |
| Fgf14 | NM_207667.3 | NM_207667.3:692 | 95.67 | 23.99 | 87.04 | 19.76 | 1.10 | 0.51 | 0.69 |
| Chat | NM_009891.2 | NM_009891.2:584 | 45.10 | 22.41 | 51.79 | 11.53 | -1.15 | 0.51 | -0.71 |
| Npy | NM_023456.2 | NM_023456.2:230 | 670.53 | 199.40 | 600.65 | 157.49 | 1.12 | 0.51 | 0.68 |
| Epha6 | NM_007938.2 | NM_007938.2:3730 | 56.54 | 51.33 | 70.86 | 27.52 | -1.25 | 0.52 | -0.69 |
| U2af2 | NM_133671.3 | NM_133671.3:131 | 125.69 | 51.60 | 109.75 | 27.15 | 1.15 | 0.53 | 0.66 |
| Napsa | NM_008437.1 | NM_008437.1:1144 | 21.22 | 3.08 | 20.35 | 0.98 | 1.04 | 0.53 | 0.68 |
| Epo | NM_007942.2 | NM_007942.2:216 | 23.05 | 7.42 | 25.80 | 9.67 | -1.12 | 0.53 | -0.65 |
| Prl | NM_011164.1 | NM_011164.1:115 | 47.81 | 39.29 | 58.38 | 12.14 | -1.22 | 0.53 | -0.68 |
| Ryr2 | NM_023868.1 | NM_023868.1:3720 | 78.89 | 31.03 | 87.89 | 15.15 | -1.11 | 0.54 | -0.66 |
| Cd44 | NM_009851.2 | NM_009851.2:3075 | 72.50 | 39.34 | 83.81 | 20.08 | -1.16 | 0.54 | -0.66 |
| Gal3st1 | NM_001177691.1 | NM_001177691.1:1197 | 84.83 | 36.79 | 97.25 | 24.91 | -1.15 | 0.54 | -0.66 |
| Gad1 | NM_008077.4 | NM_008077.4:746 | 810.96 | 511.61 | 1005.92 | 638.94 | -1.24 | 0.54 | -0.64 |
| Casp6 | NM_009811.3 | NM_009811.3:360 | 75.56 | 35.89 | 88.16 | 22.86 | -1.17 | 0.54 | -0.65 |

| | | | | | | | | | |
|---|---|---|---|---|---|---|---|---|---|
| Kel | NM_032540.3 | NM_032540.3:1020 | 40.94 | 24.45 | 48.52 | 19.69 | -1.19 | 0.54 | -0.63 |
| Plcb4 | NM_013829.2 | NM_013829.2:242 | 86.04 | 6.41 | 95.16 | 38.40 | -1.11 | 0.55 | -0.63 |
| Grm8 | NM_008174.2 | NM_008174.2:1770 | 72.48 | 43.79 | 85.15 | 17.63 | -1.17 | 0.55 | -0.65 |
| Pik3ca | NM_008839.1 | NM_008839.1:1255 | 863.57 | 207.84 | 794.32 | 184.80 | 1.09 | 0.55 | 0.62 |
| Nefl | NM_010910.1 | NM_010910.1:1303 | 385.85 | 118.55 | 424.26 | 58.35 | -1.10 | 0.55 | -0.64 |
| Park2 | NM_016694.3 | NM_016694.3:648 | 142.30 | 54.47 | 128.24 | 20.37 | 1.11 | 0.55 | 0.63 |
| Nrg1 | NM_178591.2 | NM_178591.2:1116 | 97.77 | 47.08 | 110.86 | 23.19 | -1.13 | 0.56 | -0.62 |
| Ide | NM_031156.2 | NM_031156.2:500 | 631.09 | 182.94 | 576.88 | 144.36 | 1.09 | 0.56 | 0.60 |
| Grin2c | NM_010350.2 | NM_010350.2:2408 | 40.88 | 16.94 | 47.01 | 19.60 | -1.15 | 0.56 | -0.60 |
| Pkn1 | NM_001199593.1 | NM_001199593.1:1380 | 140.81 | 45.47 | 129.25 | 21.42 | 1.09 | 0.57 | 0.60 |
| Psmb9 | NM_013585.2 | NM_013585.2:540 | 91.33 | 34.32 | 101.93 | 26.51 | -1.12 | 0.57 | -0.59 |
| Dgkb | NM_178681.4 | NM_178681.4:1798 | 115.43 | 23.85 | 107.15 | 26.58 | 1.08 | 0.57 | 0.58 |
| Nefh | NM_010904.3 | NM_010904.3:3384 | 43.81 | 14.82 | 50.17 | 19.24 | -1.15 | 0.58 | -0.58 |
| Stx2 | NM_007941.2 | NM_007941.2:225 | 153.77 | 56.91 | 139.14 | 29.05 | 1.11 | 0.58 | 0.59 |
| Gabrr3 | NM_001081190.1 | NM_001081190.1:635 | 81.92 | 71.92 | 96.21 | 24.53 | -1.17 | 0.58 | -0.59 |
| Dlgap1 | NM_027712.3 | NM_027712.3:1654 | 204.65 | 34.06 | 218.61 | 51.20 | -1.07 | 0.58 | -0.57 |
| Cers4 | NM_026058.4 | NM_026058.4:1458 | 34.15 | 11.82 | 30.10 | 13.23 | 1.13 | 0.59 | 0.56 |
| Mmp16 | NM_019724.3 | NM_019724.3:3075 | 598.10 | 133.85 | 559.05 | 112.73 | 1.07 | 0.59 | 0.57 |
| Ret | NM_001080780.1 | NM_001080780.1:5175 | 88.43 | 28.60 | 97.37 | 24.56 | -1.10 | 0.59 | -0.56 |
| Ang | NM_007447.2 | NM_007447.2:425 | 20.84 | 2.05 | 20.33 | 0.92 | 1.03 | 0.60 | 0.56 |
| Fn1 | NM_010233.1 | NM_010233.1:2627 | 96.89 | 33.50 | 112.47 | 65.26 | -1.16 | 0.60 | -0.55 |
| Lclat1 | NM_001177967.1 | NM_001177967.1:2646 | 121.29 | 32.70 | 129.91 | 21.07 | -1.07 | 0.60 | -0.55 |
| Gfpt1 | NM_013528.3 | NM_013528.3:718 | 1061.19 | 305.14 | 982.36 | 200.58 | 1.08 | 0.60 | 0.55 |
| Ppargc1a | NM_008904.2 | NM_008904.2:690 | 325.14 | 75.76 | 349.86 | 87.20 | -1.08 | 0.60 | -0.55 |

| | | | | | | | | | |
|---|---|---|---|---|---|---|---|---|---|
| Bcl2 | NM_009741.3 | NM_009741.3:1844 | 194.75 | 36.60 | 207.40 | 42.63 | -1.06 | 0.60 | -0.54 |
| Angpt2 | NM_007426.3 | NM_007426.3:2020 | 32.75 | 17.19 | 28.93 | 12.28 | 1.13 | 0.60 | 0.54 |
| Smpd4 | NM_001164610.1 | NM_001164610.1:1136 | 63.36 | 27.15 | 70.55 | 12.81 | -1.11 | 0.60 | -0.55 |
| Nfkbia | NM_010907.2 | NM_010907.2:646 | 122.88 | 22.48 | 116.69 | 16.00 | 1.05 | 0.61 | 0.54 |
| Cntn4 | NM_001109751.1 | NM_001109751.1:590 | 147.18 | 54.86 | 162.63 | 52.33 | -1.11 | 0.61 | -0.53 |
| Kif3a | NM_008443.3 | NM_008443.3:2474 | 27.85 | 11.18 | 25.23 | 7.84 | 1.10 | 0.61 | 0.53 |
| Rims1 | NM_053270.1 | NM_053270.1:90 | 461.46 | 115.61 | 505.42 | 193.96 | -1.10 | 0.61 | -0.52 |
| Mecp2 | NM_010788.2 | NM_010788.2:755 | 287.88 | 63.86 | 270.37 | 61.57 | 1.06 | 0.61 | 0.52 |
| Efr3a | NM_133766.3 | NM_133766.3:1062 | 73.77 | 28.41 | 88.82 | 64.60 | -1.20 | 0.61 | -0.52 |
| Grik2 | NM_010349.2 | NM_010349.2:256 | 265.82 | 52.52 | 286.93 | 99.20 | -1.08 | 0.62 | -0.52 |
| Scn2a1 | NM_001099298.3 | NM_001099298.3:173 | 835.02 | 231.75 | 769.60 | 248.60 | 1.09 | 0.62 | 0.51 |
| Pls1 | NM_001033210.3 | NM_001033210.3:1815 | 21.04 | 1.77 | 20.56 | 1.62 | 1.02 | 0.63 | 0.50 |
| AI464131 | NM_001085515.2 | NM_001085515.2:1232 | 71.16 | 35.39 | 80.65 | 27.73 | -1.13 | 0.63 | -0.51 |
| Hexb | NM_010422.2 | NM_010422.2:805 | 57.58 | 24.79 | 63.02 | 10.80 | -1.09 | 0.63 | -0.51 |
| Spast | NM_016962.2 | NM_016962.2:1530 | 192.86 | 107.20 | 162.99 | 98.20 | 1.18 | 0.63 | 0.50 |
| Taf4b | NM_001100449.1 | NM_001100449.1:4090 | 28.48 | 14.20 | 25.70 | 7.32 | 1.11 | 0.64 | 0.50 |
| Actn1 | NM_134156.2 | NM_134156.2:2688 | 264.98 | 69.17 | 247.13 | 52.35 | 1.07 | 0.64 | 0.49 |
| Itgax | NM_021334.2 | NM_021334.2:327 | 21.43 | 3.71 | 20.65 | 1.90 | 1.04 | 0.64 | 0.49 |
| Adcy5 | NM_001012765.4 | NM_001012765.4:219 | 113.06 | 22.89 | 105.82 | 32.83 | 1.07 | 0.64 | 0.48 |
| Cacna1b | NM_001042528.1 | NM_001042528.1:4345 | 334.57 | 79.87 | 315.88 | 68.61 | 1.06 | 0.65 | 0.48 |
| Tnr | NM_022312.3 | NM_022312.3:3195 | 167.38 | 41.73 | 157.36 | 36.94 | 1.06 | 0.65 | 0.47 |
| Prf1 | NM_011073.2 | NM_011073.2:1350 | 26.49 | 11.49 | 28.80 | 6.95 | -1.09 | 0.66 | -0.46 |
| Slc1a1 | NM_009199.2 | NM_009199.2:869 | 147.90 | 27.23 | 156.26 | 35.96 | -1.06 | 0.66 | -0.45 |

| | | | | | | | | | |
|---|---|---|---|---|---|---|---|---|---|
| Egfl7 | NM_001164564.1 | NM_001164564.1:168 | 82.94 | 41.77 | 92.38 | 22.27 | -1.11 | 0.66 | -0.46 |
| Mmp2 | NM_008610.2 | NM_008610.2:2376 | 130.83 | 44.91 | 120.31 | 32.89 | 1.09 | 0.66 | 0.45 |
| Igf1r | NM_010513.2 | NM_010513.2:3390 | 109.24 | 36.08 | 101.23 | 18.60 | 1.08 | 0.67 | 0.46 |
| Ugt8a | NM_011674.4 | NM_011674.4:138 | 76.07 | 31.78 | 83.86 | 23.74 | -1.10 | 0.67 | -0.44 |
| Ptgs2 | NM_011198.3 | NM_011198.3:675 | 30.08 | 7.19 | 32.35 | 13.07 | -1.08 | 0.68 | -0.42 |
| Ntng1 | NM_001163351.1 | NM_001163351.1:1090 | 214.68 | 64.43 | 200.86 | 48.17 | 1.07 | 0.70 | 0.40 |
| Olfm3 | NM_153157.3 | NM_153157.3:888 | 322.33 | 61.49 | 304.83 | 95.22 | 1.06 | 0.70 | 0.40 |
| Epha7 | NM_001122889.1 | NM_001122889.1:844 | 488.86 | 89.12 | 458.06 | 174.52 | 1.07 | 0.70 | 0.40 |
| Ctse | NM_007799.3 | NM_007799.3:1290 | 41.09 | 25.07 | 45.62 | 15.63 | -1.11 | 0.71 | -0.39 |
| Nf1 | NM_010897.2 | NM_010897.2:2705 | 451.17 | 125.93 | 425.35 | 130.36 | 1.06 | 0.71 | 0.38 |
| Comt | NM_007744.3 | NM_007744.3:625 | 41.56 | 18.98 | 37.48 | 16.95 | 1.11 | 0.72 | 0.37 |
| Calb2 | NM_007586.1 | NM_007586.1:1250 | 88.35 | 33.22 | 82.23 | 18.61 | 1.07 | 0.72 | 0.37 |
| Mapkapk2 | NM_008551.1 | NM_008551.1:1991 | 107.82 | 32.02 | 101.17 | 32.32 | 1.07 | 0.73 | 0.35 |
| Gria2 | NM_001039195.1 | NM_001039195.1:300 | 1544.00 | 326.24 | 1637.67 | 621.47 | -1.06 | 0.73 | -0.35 |
| Epha3 | NM_010140.3 | NM_010140.3:1716 | 26.74 | 13.35 | 28.86 | 10.44 | -1.08 | 0.74 | -0.35 |
| Chd4 | NM_145979.2 | NM_145979.2:1090 | 141.81 | 53.04 | 131.72 | 41.01 | 1.08 | 0.74 | 0.35 |
| Arc | NM_018790.2 | NM_018790.2:2715 | 78.71 | 34.98 | 85.31 | 35.98 | -1.08 | 0.75 | -0.33 |
| Pink1 | NM_026880.2 | NM_026880.2:688 | 120.91 | 45.16 | 113.74 | 21.55 | 1.06 | 0.75 | 0.34 |
| Dbh | NM_138942.3 | NM_138942.3:254 | 23.04 | 9.28 | 24.38 | 7.20 | -1.06 | 0.75 | -0.33 |
| Lrp1 | NM_008512.2 | NM_008512.2:1310 | 190.32 | 41.40 | 182.14 | 51.99 | 1.04 | 0.76 | 0.31 |
| Efna1 | NM_010107.4 | NM_010107.4:437 | 20.72 | 1.49 | 20.47 | 1.33 | 1.01 | 0.76 | 0.31 |
| Cntnap2 | NM_001004357.2 | NM_001004357.2:3985 | 213.58 | 68.75 | 223.92 | 39.10 | -1.05 | 0.76 | -0.32 |
| Hpgds | NM_019455.4 | NM_019455.4:194 | 49.23 | 29.60 | 53.42 | 18.49 | -1.09 | 0.77 | -0.31 |
| Cln8 | NM_012000.3 | NM_012000.3:762 | 95.89 | 28.02 | 100.90 | 31.70 | -1.05 | 0.77 | -0.30 |

| | | | | | | | | | |
|---|---|---|---|---|---|---|---|---|---|
| Apc | NM_007462.3 | NM_007462.3:645 | 186.19 | 67.76 | 171.07 | 125.28 | 1.09 | 0.78 | 0.29 |
| Gria4 | NM_001113180.1 | NM_001113180.1:1274 | 119.61 | 57.69 | 131.81 | 77.92 | -1.10 | 0.79 | -0.27 |
| Cspg4 | NM_139001.2 | NM_139001.2:1530 | 132.30 | 35.62 | 136.84 | 24.58 | -1.03 | 0.80 | -0.26 |
| Creb1 | NM_001037726.1 | NM_001037726.1:2734 | 209.00 | 80.90 | 197.01 | 59.56 | 1.06 | 0.81 | 0.26 |
| Slc32a1 | NM_009508.2 | NM_009508.2:2616 | 789.30 | 468.76 | 859.68 | 650.13 | -1.09 | 0.81 | -0.25 |
| Gls | NM_001113383.1 | NM_001113383.1:976 | 1570.69 | 354.24 | 1521.58 | 397.01 | 1.03 | 0.81 | 0.24 |
| Camk2d | NM_001025439.1 | NM_001025439.1:1315 | 647.25 | 200.48 | 626.94 | 88.29 | 1.03 | 0.83 | 0.23 |
| Htra2 | NM_019752.3 | NM_019752.3:1088 | 182.96 | 42.28 | 188.13 | 43.49 | -1.03 | 0.83 | -0.22 |
| Cntf | NM_170786.2 | NM_170786.2:110 | 60.50 | 19.12 | 58.41 | 13.75 | 1.04 | 0.83 | 0.22 |
| Sp1 | NM_013672.2 | NM_013672.2:6580 | 36.63 | 17.79 | 38.76 | 18.96 | -1.06 | 0.84 | -0.21 |
| Lpar1 | NM_010336.2 | NM_010336.2:230 | 27.80 | 10.91 | 26.64 | 11.53 | 1.04 | 0.84 | 0.20 |
| Atp2b3 | NM_177236.3 | NM_177236.3:1485 | 98.15 | 29.01 | 95.33 | 18.52 | 1.03 | 0.84 | 0.20 |
| Hmox1 | NM_010442.2 | NM_010442.2:610 | 316.74 | 129.84 | 332.44 | 157.35 | -1.05 | 0.85 | -0.20 |
| Mfn2 | XM_006535920.1 | XM_006535920.1:692 | 444.16 | 86.90 | 452.96 | 65.98 | -1.02 | 0.85 | -0.20 |
| Prpf3 | NM_027541.4 | NM_027541.4:1486 | 183.33 | 50.37 | 188.45 | 44.44 | -1.03 | 0.85 | -0.19 |
| Ntf3 | NM_008742.2 | NM_008742.2:305 | 126.28 | 55.68 | 121.91 | 23.10 | 1.04 | 0.85 | 0.19 |
| Slc4a10 | NM_001242380.1 | NM_001242380.1:1118 | 382.88 | 88.56 | 393.76 | 110.87 | -1.03 | 0.86 | -0.18 |
| Nmnat2 | NM_175460.3 | NM_175460.3:67 | 228.02 | 85.61 | 218.89 | 94.65 | 1.04 | 0.86 | 0.18 |
| Col4a2 | NM_009932.3 | NM_009932.3:5600 | 210.62 | 58.22 | 215.66 | 39.11 | -1.02 | 0.87 | -0.17 |
| Ubqln1 | NM_152234.2 | NM_152234.2:3460 | 22.77 | 8.15 | 23.35 | 7.31 | -1.03 | 0.88 | -0.15 |
| Nos1 | NM_008712.2 | NM_008712.2:2985 | 30.02 | 5.65 | 30.85 | 15.25 | -1.03 | 0.88 | -0.15 |
| Wfs1 | NM_011716.2 | NM_011716.2:2975 | 52.31 | 24.79 | 54.48 | 22.24 | -1.04 | 0.88 | -0.15 |
| Cers1 | NM_138647.3 | NM_138647.3:414 | 34.75 | 11.12 | 33.73 | 15.21 | 1.03 | 0.89 | 0.15 |
| Sox10 | XM_128139.6 | XM_128139.6:2646 | 55.03 | 17.12 | 56.23 | 14.36 | -1.02 | 0.89 | -0.15 |

| | | | | | | | | | |
|---|---|---|---|---|---|---|---|---|---|
| Pla2g4a | NM_008869.2 | NM_008869.2:1525 | 31.54 | 18.92 | 30.58 | 10.92 | 1.03 | 0.90 | 0.13 |
| Hdac1 | NM_008228.2 | NM_008228.2:470 | 337.65 | 134.73 | 329.84 | 52.30 | 1.02 | 0.90 | 0.13 |
| Car2 | NM_009801.4 | NM_009801.4:437 | 89.17 | 50.00 | 91.87 | 19.86 | -1.03 | 0.90 | -0.13 |
| Col4a1 | NM_009931.2 | NM_009931.2:4116 | 21.96 | 3.80 | 21.71 | 3.81 | 1.01 | 0.90 | 0.13 |
| Slc2a1 | NM_011400.3 | NM_011400.3:2190 | 45.05 | 25.90 | 43.63 | 14.39 | 1.03 | 0.91 | 0.12 |
| Dot1l | NM_199322.1 | NM_199322.1:5490 | 126.03 | 26.70 | 128.03 | 31.56 | -1.02 | 0.91 | -0.12 |
| Ngfr | NM_033217.3 | NM_033217.3:1995 | 32.27 | 9.42 | 31.40 | 18.76 | 1.03 | 0.91 | 0.12 |
| Nos2 | NM_010927.3 | NM_010927.3:3715 | 22.22 | 3.39 | 21.99 | 4.12 | 1.01 | 0.91 | 0.12 |
| Emp2 | NM_007929.2 | NM_007929.2:3196 | 66.65 | 23.85 | 65.23 | 11.93 | 1.02 | 0.91 | 0.12 |
| Inpp4a | NM_172971.2 | NM_172971.2:1624 | 154.88 | 78.88 | 150.51 | 49.07 | 1.03 | 0.92 | 0.11 |
| Cacna1d | NM_028981.2 | NM_028981.2:2935 | 296.89 | 93.80 | 292.63 | 65.36 | 1.01 | 0.93 | 0.09 |
| Gabra1 | NM_010250.4 | NM_010250.4:905 | 634.68 | 144.66 | 642.69 | 152.28 | -1.01 | 0.93 | -0.09 |
| Pla2g4e | NM_177845.4 | NM_177845.4:1016 | 27.87 | 7.52 | 27.47 | 10.50 | 1.01 | 0.93 | 0.09 |
| Nostrin | NM_181547.3 | NM_181547.3:1452 | 21.43 | 3.71 | 21.28 | 4.10 | 1.01 | 0.94 | 0.08 |
| Lrrk2 | NM_025730.3 | NM_025730.3:4475 | 62.44 | 19.59 | 63.54 | 29.07 | -1.02 | 0.94 | -0.07 |
| Gria3 | NM_016886.3 | NM_016886.3:390 | 202.58 | 41.08 | 200.83 | 66.09 | 1.01 | 0.95 | 0.06 |
| Atp7a | NM_001109757.2 | NM_001109757.2:1200 | 106.62 | 47.08 | 105.34 | 23.70 | 1.01 | 0.95 | 0.06 |
| Ager | NM_007425.2 | NM_007425.2:361 | 21.62 | 4.26 | 21.73 | 3.30 | -1.00 | 0.96 | -0.05 |
| Cacna1a | NM_007578.3 | NM_007578.3:1655 | 391.80 | 107.55 | 394.71 | 112.42 | -1.01 | 0.96 | -0.05 |
| Adcy9 | NM_009624.1 | NM_009624.1:3640 | 143.97 | 40.08 | 143.02 | 29.24 | 1.01 | 0.97 | 0.04 |
| Ikbkb | NM_010546.2 | NM_010546.2:498 | 115.80 | 44.88 | 116.76 | 41.33 | -1.01 | 0.97 | -0.04 |
| Egfr | NM_207655.2 | NM_207655.2:1335 | 48.01 | 14.20 | 48.39 | 20.73 | -1.01 | 0.97 | -0.04 |
| Notch3 | NM_008716.2 | NM_008716.2:550 | 34.34 | 8.49 | 34.57 | 15.94 | -1.01 | 0.98 | -0.03 |
| Hdac7 | NM_019572.2 | NM_019572.2:3706 | 117.89 | 41.54 | 117.34 | 26.04 | 1.00 | 0.98 | 0.03 |
| Sla | NM_001029841.1 | NM_001029841.1:75 | 105.18 | 16.70 | 104.97 | 20.70 | 1.00 | 0.98 | 0.02 |

| | | | | | | | | | |
|---|---|---|---|---|---|---|---|---|---|
| Pcsk2 | NM_008792.3 | NM_008792.3:2915 | 35.92 | 12.33 | 35.74 | 15.32 | 1.00 | 0.98 | 0.02 |
| Npc1 | NM_008720.2 | NM_008720.2:2645 | 20.92 | 2.25 | 20.91 | 2.76 | 1.00 | 0.99 | 0.01 |
| Egr2 | NM_010118.2 | NM_010118.2:1785 | 27.33 | 11.72 | 27.34 | 11.46 | -1.00 | 1.00 | 0.00 |

Appendix table 2: Raw Nanostring nCounter data

# References


Abdollahi, M.R., Morrison, E., Sirey, T., Molnar, Z., Hayward, B.E., Carr, I.M., Springell, K., Woods, C.G., Ahmed, M. and Hattingh, L., 2009. Mutation of the variant α-tubulin TUBA8 results in polymicrogyria with optic nerve hypoplasia. *The American Journal of Human Genetics,* 85 (5), 737-744.

Abeles, M., 1991. *Corticonics: Neural circuits of the cerebral cortex.* Cambridge University Press.

Abeles, M., and Goldstein, M.H.,Jr, 1970. Functional architecture in cat primary auditory cortex: columnar organization and organization according to depth. *Journal of Neurophysiology,* 33 (1), 172-187.

Aboody, K.S., Brown, A., Rainov, N.G., Bower, K.A., Liu, S., Yang, W., Small, J.E., Herrlinger, U., Ourednik, V., Black, P.M., Breakefield, X.O. and Snyder, E.Y., 2000. Neural stem cells display extensive tropism for pathology in adult brain: Evidence from intracranial gliomas. *Proceedings of the National Academy of Sciences,* 97 (23), 12846-12851.

Abu-Rub, M.T., Billiar, K.L., Van Es, M.H., Knight, A., Rodriguez, B.J., Zeugolis, D.I., McMahon, S., Windebank, A.J. and Pandit, A., 2011. Nano-textured self-assembled aligned collagen hydrogels promote directional neurite guidance and overcome inhibition by myelin associated glycoprotein. *Soft Matter,* 7 (6), 2770-2781.

Adewole, D.O., Struzyna, L.A., Harris, J.P., Nemes, A.D., Burrell, J.C., Petrov, D., Kraft, R.H., Chen, H.I., Serruya, M.D. and Wolf, J.A., 2018. Optically-Controlled" Living Electrodes" with Long-Projecting Axon Tracts for a Synaptic Brain-Machine Interface. *Biorxiv,* , 333526.

Aebischer, P., Valentini, R.F., Dario, P., Domenici, C. and Galletti, P.M., 1987. Piezoelectric guidance channels enhance regeneration in the mouse sciatic nerve after axotomy. *Brain Research,* 436 (1), 165-168.

Agostini, M., Romeo, F., Inoue, S., Niklison-Chirou, M.V., Elia, A.J., Dinsdale, D., Morone, N., Knight, R.A., Mak, T.W. and Melino, G., 2016. Metabolic reprogramming during neuronal differentiation. *Cell Death and Differentiation,* 23 (9), 1502.

Ahmed, E.M., 2015. Hydrogel: Preparation, characterization, and applications: A review. *Journal of Advanced Research,* 6 (2), 105-121.

Aiello, N.M., Maddipati, R., Norgard, R.J., Balli, D., Li, J., Yuan, S., Yamazoe, T., Black, T., Sahmoud, A. and Furth, E.E., 2018. EMT subtype influences epithelial plasticity and mode of cell migration. *Developmental Cell,* 45 (6), 681-695. e4.

Albieri, G., Barnes, S.J., de Celis Alonso, B., Cheetham, C.E., Edwards, C.E., Lowe, A.S., Karunaratne, H., Dear, J.P., Lee, K.C. and Finnerty, G.T., 2014. Rapid bidirectional reorganization of cortical microcircuits. *Cerebral Cortex,* 25 (9), 3025-3035.

Ali, S., Wall, I.B., Mason, C., Pelling, A.E. and Veraitch, F.S., 2015. The effect of Young's modulus on the neuronal differentiation of mouse embryonic stem cells. *Acta Biomaterialia,* 25, 253-267.

Allen, E.A., Damaraju, E., Plis, S.M., Erhardt, E.B., Eichele, T. and Calhoun, V.D., 2014. Tracking whole-brain connectivity dynamics in the resting state. *Cerebral Cortex,* 24 (3), 663-676.

Alvarez, Z., Castaño, O., Castells, A.A., Mateos-Timoneda, M.A., Planell, J.A., Engel, E. and Alcántara, S., 2014. Neurogenesis and vascularization of the damaged brain using a lactate-releasing biomimetic scaffold. *Biomaterials,* 35 (17), 4769-4781.

Amin, H., Nieus, T., Lonardoni, D., Maccione, A. and Berdondini, L., 2017. High-resolution bioelectrical imaging of Aβ-induced network dysfunction on CMOS-MEAs for neurotoxicity and rescue studies. *Scientific Reports,* 7 (1), 2460.

Amin, H., Maccione, A., Marinaro, F., Zordan, S., Nieus, T. and Berdondini, L., 2016. Electrical Responses and Spontaneous Activity of Human iPS-Derived Neuronal Networks Characterized for 3-month Culture with 4096-Electrode Arrays. *Frontiers in Neuroscience,* 10, 121.

An, J., Zhang, Y., He, J., Zang, Z., Zhou, Z., Pei, X., Zheng, X., Zhang, W., Yang, H. and Li, S., 2017. Lactate dehydrogenase A promotes the invasion and proliferation of pituitary adenoma. *Scientific Reports,* 7 (1), 4734.

Anastassiou, C.A., Perin, R., Markram, H. and Koch, C., 2011. Ephaptic coupling of cortical neurons. *Nature Neuroscience,* 14 (2), 217.

Angel, T.E., Aryal, U.K., Hengel, S.M., Baker, E.S., Kelly, R.T., Robinson, E.W. and Smith, R.D., 2012. Mass spectrometry-based proteomics: existing capabilities and future directions. *Chemical Society Reviews,* 41 (10), 3912-3928.

Antoni, D., Burckel, H., Josset, E. and Noel, G., 2015. Three-dimensional cell culture: a breakthrough in vivo. *International Journal of Molecular Sciences,* 16 (3), 5517-5527.

Araya, R., 2014. Input transformation by dendritic spines of pyramidal neurons. *Frontiers in Neuroanatomy,* 8, 141.

Arcaute, K., Mann, B.K. and Wicker, R.B., 2006. Stereolithography of three-dimensional bioactive poly (ethylene glycol) constructs with encapsulated cells. *Annals of Biomedical Engineering,* 34 (9), 1429-1441.

Arias, V., Höglund, A., Odelius, K. and Albertsson, A., 2013. Tuning the degradation profiles of poly (l-lactide)-based materials through miscibility. *Biomacromolecules,* 15 (1), 391-402.

Arinstein, A., Burman, M., Gendelman, O. and Zussman, E., 2007. Effect of supramolecular structure on polymer nanofibre elasticity. *Nature Nanotechnology,* 2 (1), 59-62.

Attwell, S., Roskelley, C. and Dedhar, S., 2000. The integrin-linked kinase (ILK) suppresses anoikis. *Oncogene,* 19 (33), 3811-3815.

Baalman, K., Marin, M.A., Ho, T.S., Godoy, M., Cherian, L., Robertson, C. and Rasband, M.N., 2015. Axon initial segment-associated microglia. *The Journal of Neuroscience : The Official Journal of the Society for Neuroscience,* 35 (5), 2283-2292.

Baji, A., Mai, Y., Wong, S., Abtahi, M. and Chen, P., 2010. Electrospinning of polymer nanofibres: Effects on oriented morphology, structures and tensile properties. *Composites Science and Technology,* 70 (5), 703-718.

Baker, B.M., Shah, R.P., Silverstein, A.M., Esterhai, J.L., Burdick, J.A. and Mauck, R.L., 2012. Sacrificial nanofibrous composites provide instruction without impediment and enable functional tissue formation. *Proceedings of the National Academy of Sciences of the United States of America,* 109 (35), 14176-14181.

Ballester-Beltrán, J., Rico, P., Moratal, D., Song, W., Mano, J.F. and Salmerón-Sánchez, M., 2011. Role of superhydrophobicity in the biological activity of fibronectin at the cell–material interface. *Soft Matter,* 7 (22), 10803-10811.

Basu, A., Drame, A., Muñoz, R., Gijsbers, R., Debyser, Z., De Leon, M. and Casiano, C.A., 2012. Pathway specific gene expression profiling reveals oxidative stress genes potentially regulated by transcription co-activator LEDGF/p75 in prostate cancer cells. *The Prostate,* 72 (6), 597-611.

Baxter, P.S., and Hardingham, G.E., 2016. Adaptive regulation of the brain's antioxidant defences by neurons and astrocytes. *Free Radical Biology and Medicine,* 100, 147-152.

Beachley, V., and Wen, X., 2009. Effect of electrospinning parameters on the nanofiber diameter and length. *Materials Science and Engineering: C,* 29 (3), 663-668.

Bear, M.F., Connors, B.W. and Paradiso, M.A.,
2016. ***Neuroscience : exploring the brain.*** Fourth edition ed. Philadelphia: Lippincott Williams and Wilkins.

Bell, A.H., and Bultitude, J.H., 2018. Methods matter: A primer on permanent and reversible interference techniques in animals for investigators of human neuropsychology. *Neuropsychologia,* 115, 211-219.

Belyanskaya, L., Weigel, S., Hirsch, C., Tobler, U., Krug, H.F. and Wick, P., 2009. Effects of carbon nanotubes on primary neurons and glial cells. *Neurotoxicology,* 30 (4), 702-711.

Bennett, S.H., Kirby, A.J. and Finnerty, G.T., 2018. Rewiring the connectome: Evidence and effects. *Neuroscience & Biobehavioral Reviews,* .

Bentea, E., Moore, C., Deneyer, L., Verbruggen, L., Churchill, M.J., Hood, R.L., Meshul, C.K. and Massie, A., 2017. Plastic changes at corticostriatal synapses predict improved motor

function in a partial lesion model of Parkinson's disease. *Brain Research Bulletin,* 130, 257-267.

Bentley, B., 2017. *Connectomics of Extrasynaptic Signalling: Applications to the Nervous System of Caenorhabditis Elegans,* .

Biffi, E., Regalia, G., Menegon, A., Ferrigno, G. and Pedrocchi, A., 2013. The influence of neuronal density and maturation on network activity of hippocampal cell cultures: a methodological study. *PloS One,* 8 (12), e83899.

Biswas, S.K., 2016. Does the interdependence between oxidative stress and inflammation explain the antioxidant paradox? *Oxidative Medicine and Cellular Longevity,* 2016.

Bjugstad, K., Lampe, K., Kern, D. and Mahoney, M., 2010. Biocompatibility of poly (ethylene glycol)-based hydrogels in the brain: An analysis of the glial response across space and time. *Journal of Biomedical Materials Research Part A,* 95 (1), 79-91.

Blondel, O., Collin, C., McCarran, W.J., Zhu, S., Zamostiano, R., Gozes, I., Brenneman, D.E. and McKay, R.D., 2000. A glia-derived signal regulating neuronal differentiation. *The Journal of Neuroscience : The Official Journal of the Society for Neuroscience,* 20 (21), 8012-8020.

Blumenfeld-Katzir, T., Pasternak, O., Dagan, M. and Assaf, Y., 2011. Diffusion MRI of structural brain plasticity induced by a learning and memory task. *PloS One,* 6 (6), e20678.

Blumenthal, N.R., Hermanson, O., Heimrich, B. and Shastri, V.P., 2014. Stochastic nanoroughness modulates neuron-astrocyte interactions and function via mechanosensing cation channels. *Proceedings of the National Academy of Sciences of the United States of America,* 111 (45), 16124-16129.

Boehm-Sturm, P., Aswendt, M., Minassian, A., Michalk, S., Mengler, L., Adamczak, J., Mezzanotte, L., Löwik, C. and Hoehn, M., 2014. A multi-modality platform to image stem cell graft survival in the naïve and stroke-damaged mouse brain. *Biomaterials,* 35 (7), 2218-2226.

Boele, H.J., Koekkoek, S.K., De Zeeuw, C.I. and Ruigrok, T.J., 2013. Axonal sprouting and formation of terminals in the adult cerebellum during associative motor learning. *The Journal of Neuroscience : The Official Journal of the Society for Neuroscience,* 33 (45), 17897-17907.

Boes, A.D., Prasad, S., Liu, H., Liu, Q., Pascual-Leone, A., Caviness, V.S.,Jr and Fox, M.D., 2015. Network localization of neurological symptoms from focal brain lesions. *Brain : A Journal of Neurology,* 138 (Pt 10), 3061-3075.

Bonnamain, V., Neveu, I. and Naveilhan, P., 2012. Neural stem/progenitor cells as promising candidates for regenerative therapy of the central nervous system. *Frontiers of Cellular Neuroscience,* 6.

Bouyakdan, K., Taïb, B., Budry, L., Zhao, S., Rodaros, D., Neess, D., Mandrup, S., Faergeman, N.J. and Alquier, T., 2015. A novel role for central ACBP/DBI as a regulator of long-chain fatty acid metabolism in astrocytes. *Journal of Neurochemistry,* 133 (2), 253-265.

Boyke, J., Driemeyer, J., Gaser, C., Buchel, C. and May, A., 2008. Training-induced brain structure changes in the elderly. *The Journal of Neuroscience : The Official Journal of the Society for Neuroscience,* 28 (28), 7031-7035.

Brainbits, 2017. *Brainbits Primary Neuron Culture Protocol* [online]. Brainbits LLC. Available at: http://www.brainbits.co.uk/bb/Files/6550105.pdf [Accessed 10/23 2017].

Braitenberg, V., and Schüz, A., 1985. Cortex: Statistics and Geometry of Neuronal Connectivity. 1998. *New York: Berlin,* .

Breous, E., Somanathan, S., Bell, P. and Wilson, J.M., 2011. Inflammation Promotes the Loss of Adeno-Associated Virus–Mediated Transgene Expression in Mouse Liver. *Gastroenterology,* 141 (1), 348-357. e3.

Brevig, T., Holgersson, J. and Widner, H., 2000. Xenotransplantation for CNS repair: immunological barriers and strategies to overcome them. *Trends in Neurosciences,* 23 (8), 337-344.

Brilli, E., Reitano, E., Conti, L., Conforti, P., Gulino, R., Consalez, G.G., Cesana, E., Smith, A., Rossi, F. and Cattaneo, E., 2012. Neural stem cells engrafted in the adult brain fuse with endogenous neurons. *Stem Cells and Development,* 22 (4), 538-547.

Broeke, J.H., Roelandse, M., Luteijn, M.J., Boiko, T., Matus, A., Toonen, R.F. and Verhage, M., 2010. Munc18 and Munc13 regulate early neurite outgrowth. *Biology of the Cell,* 102 (8), 479-488.

Brosenitsch, T.A., and Katz, D.M., 2001. Physiological patterns of electrical stimulation can induce neuronal gene expression by activating N-type calcium channels. *The Journal of Neuroscience : The Official Journal of the Society for Neuroscience,* 21 (8), 2571-2579.

Brown, A.M., and Ransom, B.R., 2015. Astrocyte–Neuron Interactions. *Homeostatic Control of Brain Function,* 98.

Brownell, A., Livni, E., Galpern, W. and Isacson, O., 1998. In vivo PET imaging in rat of dopamine terminals reveals functional neural transplants. *Annals of Neurology,* 43 (3), 387-390.

Brudvig, J.J., Cain, J.T., Sears, R.M., Schmidt-Grimminger, G.G., Wittchen, E.S., Adler, K.B., Ghashghaei, H.T. and Weimer, J.M., 2018. MARCKS regulates neuritogenesis and interacts with a CDC42 signaling network. *Scientific Reports,* 8 (1), 13278-018-31578-0.

Brustle, O., Spiro, A., Karram, K., Choudhary, K., Okabe, S. and McKay, R., 1997. *In vitro*-generated neural precursors participate in mammalian brain development. *Proceedings of the National Academy of Sciences of the United States of America,* 94 (26), 14809-14814.

Bussmann, J., and Raz, E., 2015. Chemokine-guided cell migration and motility in zebrafish development. *The EMBO Journal,* 34 (10), 1309-1318.

Callahan, L.A.S., Xie, S., Barker, I.A., Zheng, J., Reneker, D.H., Dove, A.P. and Becker, M.L., 2013. Directed differentiation and neurite extension of mouse embryonic stem cell on

aligned poly (lactide) nanofibres functionalized with YIGSR peptide. *Biomaterials,* 34 (36), 9089-9095.

Carboni, A., Lavelle, W., Barnes, C. and Cipolloni, P., 1990. Neurons of the lateral entorhinal cortex of the rhesus monkey: a Golgi, histochemical, and immunocytochemical characterization. *Journal of Comparative Neurology,* 291 (4), 583-608.

Carunchio, I., Pieri, M., Ciotti, M.T., Albo, F. and Zona, C., 2007. Modulation of AMPA receptors in cultured cortical neurons induced by the antiepileptic drug levetiracetam. *Epilepsia,* 48 (4), 654-662.

Casasola, R., Thomas, N.L., Trybala, A. and Georgiadou, S., 2014. Electrospun poly lactic acid (PLA) fibres: effect of different solvent systems on fibre morphology and diameter. *Polymer,* 55 (18), 4728-4737.

Castro, A.G.B., Polini, A., Azami, Z., Leeuwenburgh, S.C.G., Jansen, J.A., Yang, F. and van den Beucken, J.J.J.P., 2017. Incorporation of PLLA micro-fillers for mechanical reinforcement of calcium-phosphate cement. *Journal of the Mechanical Behavior of Biomedical Materials,* 71, 286-294.

Cawley, N.X., Wetsel, W.C., Murthy, S.R., Park, J.J., Pacak, K. and Loh, Y.P., 2012. New roles of carboxypeptidase E in endocrine and neural function and cancer. *Endocrine Reviews,* 33 (2), 216-253.

Chan, S., Yang, H., Ko, F., Ayranci, C. and Basu, S., 2012. Tensile Stress-Strain Response of Small-diameter Electrospun Fibers. *Agil.Technol,* .

Chang, J., Dommer, M., Chang, C. and Lin, L., 2012. Piezoelectric nanofibres for energy scavenging applications. *Nano Energy,* 1 (3), 356-371.

Chao, T., Xiang, S., Chen, C., Chin, W., Nelson, A.J., Wang, C. and Lu, J., 2009. Carbon nanotubes promote neuron differentiation from human embryonic stem cells. *Biochemical and Biophysical Research Communications,* 384 (4), 426-430.

Chau, K.F., Shannon, M.L., Fame, R.M., Fonseca, E., Mullan, H., Johnson, M.B., Sendamarai, A.K., Springel, M.W., Laurent, B. and Lehtinen, M.K., 2018. Downregulation of ribosome biogenesis during early forebrain development. *Elife,* 7, e36998.

Chaubey, S., and Wolfe, J.H., 2013. Transplantation of CD15-enriched murine neural stem cells increases total engraftment and shifts differentiation toward the oligodendrocyte lineage. *Stem Cells Translational Medicine,* 2 (6), 444-454.

Chen, Z., Jalabi, W., Hu, W., Park, H., Gale, J.T., Kidd, G.J., Bernatowicz, R., Gossman, Z.C., Chen, J.T. and Dutta, R., 2014. Microglial displacement of inhibitory synapses provides neuroprotection in the adult brain. *Nature Communications,* 5, 4486.

Chen, Z., Lu, X.M., Shear, D.A., Dave, J.R., Davis, A.R., Evangelista, C.A., Duffy, D. and Tortella, F.C., 2011. Synergism of human amnion-derived multipotent progenitor (AMP) cells and a collagen scaffold in promoting brain wound recovery: pre-clinical studies in an experimental model of penetrating ballistic-like brain injury. *Brain Research,* 1368, 71-81.

Chen, J., and Su, C., 2011. Surface modification of electrospun PLLA nanofibres by plasma treatment and cationized gelatin immobilization for cartilage tissue engineering. *Acta Biomaterialia,* 7 (1), 234-243.

Chen, Z., Haegeli, V., Yu, H. and Strickland, S., 2009. Cortical deficiency of laminin γ1 impairs the AKT/GSK-3β signaling pathway and leads to defects in neurite outgrowth and neuronal migration. *Developmental Biology,* 327 (1), 158-168.

Cheng, K., Bai, L. and Belluscio, L., 2011. Fas-associated factor 1 as a regulator of olfactory axon guidance. *Journal of Neuroscience,* 31 (33), 11905-11913.

Chiurchiu, V., Maccarrone, M. and Orlacchio, A., 2014. The role of reticulons in neurodegenerative diseases. *Neuromolecular Medicine,* 16 (1), 3-15.

Choi, A., Kim, J.Y., Lee, J.E. and Jung, H., 2009. Effects of PDMS curing ratio and 3D micro-pyramid structure on the formation of an in vitro neural network. *Current Applied Physics,* 9 (4), e294-e297.

Chornyy, S., Parkhomenko, Y. and Chorna, N., 2017. Thiamine antagonists trigger p53-dependent apoptosis in differentiated SH-SY5Y cells. *Scientific Reports,* 7 (1), 10632.

Christopherson, G.T., Song, H. and Mao, H., 2009. The influence of fiber diameter of electrospun substrates on neural stem cell differentiation and proliferation. *Biomaterials,* 30 (4), 556-564.

Chung, L., 2015. A Brief Introduction to the Transduction of Neural Activity into Fos Signal. *Development & Reproduction,* 19 (2), 61-67.

Chung, W.S., Allen, N.J. and Eroglu, C., 2015. Astrocytes Control Synapse Formation, Function, and Elimination. *Cold Spring Harbor Perspectives in Biology,* 7 (9), a020370.

Cobley, J.N., 2018. Synapse pruning: mitochondrial ROS with their hands on the shears. *Bioessays,* 40 (7), 1800031.

Colello, R.J., Chow, W.N., Bigbee, J.W., Lin, C., Dalton, D., Brown, D., Jha, B.S., Mathern, B.E., Lee, K.D. and Simpson, D.G., 2016. The incorporation of growth factor and chondroitinase ABC into an electrospun scaffold to promote axon regrowth following spinal cord injury. *Journal of Tissue Engineering and Regenerative Medicine,* 10 (8), 656-668.

Collier, J.H., Camp, J.P., Hudson, T.W. and Schmidt, C.E., 2000. Synthesis and characterization of polypyrrole–hyaluronic acid composite biomaterials for tissue engineering applications. *Journal of Biomedical Materials Research,* 50 (4), 574-584.

Colognato, H., and Yurchenco, P.D., 2000. Form and function: the laminin family of heterotrimers. *Developmental Dynamics,* 218 (2), 213-234.

Colonna, M., and Butovsky, O., 2017. Microglia function in the central nervous system during health and neurodegeneration. *Annual Review of Immunology,* 35, 441-468.

Conde Guerri, B., Sinues Porta, E., Arrazola Schlamilch, M., Comunas Gonzalez, F. and Calatayud Maldonado, V., 1989. Effects of glia-conditioned medium on primary cultures of central neurons. *Histology and Histopathology,* 4 (2), 217-222.

Cooke, M., Vulic, K. and Shoichet, M., 2010. Design of biomaterials to enhance stem cell survival when transplanted into the damaged central nervous system. *Soft Matter,* 6 (20), 4988-4998.

Cooke, M., Zahir, T., Phillips, S., Shah, D., Athey, D., Lakey, J., Shoichet, M. and Przyborski, S., 2010. Neural differentiation regulated by biomimetic surfaces presenting motifs of extracellular matrix proteins. *Journal of Biomedical Materials Research Part A,* 93 (3), 824-832.

Cooper, J.A., 2008. A mechanism for inside-out lamination in the neocortex. *Trends in Neurosciences,* 31 (3), 113-119.

Corey, J.M., Gertz, C.C., Wang, B., Birrell, L.K., Johnson, S.L., Martin, D.C. and Feldman, E.L., 2008. The design of electrospun PLLA nanofiber scaffolds compatible with serum-free growth of primary motor and sensory neurons. *Acta Biomaterialia,* 4 (4), 863-875.

Corey, J.M., Lin, D.Y., Mycek, K.B., Chen, Q., Samuel, S., Feldman, E.L. and Martin, D.C., 2007. Aligned electrospun nanofibres specify the direction of dorsal root ganglia neurite growth. *Journal of Biomedical Materials Research Part A,* 83 (3), 636-645.

Cossetti, C., Alfaro-Cervello, C., Donegà, M., Tyzack, G. and Pluchino, S., 2012. New perspectives of tissue remodelling with neural stem and progenitor cell-based therapies. *Cell and Tissue Research,* 349 (1), 321-329.

Cowles, E.A., Brailey, L.L. and Gronowicz, G.A., 2000. Integrin-mediated signaling regulates AP-1 transcription factors and proliferation in osteoblasts. *Journal of Biomedical Materials Research Part A,* 52 (4), 725-737.

Coyle, D.E., Li, J. and Baccei, M., 2011. Regional differentiation of retinoic acid-induced human pluripotent embryonic carcinoma stem cell neurons. *PLoS One,* 6 (1), e16174.

Cunningham, D., Spychala, K., McLarren, K.W., Garza, L.A., Boerkoel, C.F. and Herman, G.E., 2009. Developmental expression pattern of the cholesterogenic enzyme NSDHL and negative selection of NSDHL-deficient cells in the heterozygous Bpa1H/+ mouse. *Molecular Genetics and Metabolism,* 98 (4), 356-366.

Cusulin, C., Monni, E., Ahlenius, H., Wood, J., Brune, J.C., Lindvall, O. and Kokaia, Z., 2012. Embryonic Stem Cell-Derived Neural Stem Cells Fuse with Microglia and Mature Neurons. *Stem Cells,* 30 (12), 2657-2671.

Daadi, M.M., Klausner, J.Q., Bajar, B., Goshen, I., Lee-Messer, C., Lee, S.Y., Winge, M.C., Ramakrishnan, C., Lo, M., Sun, G., Deisseroth, K. and Steinberg, G.K., 2016. Optogenetic Stimulation of Neural Grafts Enhances Neurotransmission and Downregulates the Inflammatory Response in Experimental Stroke Model. *Cell Transplantation,* 25 (7), 1371-1380.

D'Ambrosio, R., Maris, D.O., Grady, M.S., Winn, H.R. and Janigro, D., 1999. Impaired K(+) homeostasis and altered electrophysiological properties of post-traumatic hippocampal glia. *The Journal of Neuroscience : The Official Journal of the Society for Neuroscience,* 19 (18), 8152-8162.

Daoud, J., Petropavlovskaia, M., Rosenberg, L. and Tabrizian, M., 2010. The effect of extracellular matrix components on the preservation of human islet function in vitro. *Biomaterials,* 31 (7), 1676-1682.

Davanlou, M., and Smith, D.F., 2004. Unbiased stereological estimation of different cell types in rat cerebral cortex. *Image Analysis & Stereology,* 23 (1), 1-11.

Davis, O., Merrison-Hort, R., Soffe, S.R. and Borisyuk, R., 2017. Studying the role of axon fasciculation during development in a computational model of the Xenopus tadpole spinal cord. *Scientific Reports,* 7 (1), 13551.

De Zio, D., Ferraro, E., D'amelio, M., Simoni, V., Bordi, M., Soroldoni, D., Berghella, L., Meyer, B. and Cecconi, F., 2008. Faf1 is expressed during neurodevelopment and is involved in Apaf1-dependent caspase-3 activation in proneural cells. *Cellular and Molecular Life Sciences,* 65 (11), 1780-1790.

De Zio, D., Ferraro, E., D'amelio, M., Simoni, V., Bordi, M., Soroldoni, D., Berghella, L., Meyer, B. and Cecconi, F., 2008. Faf1 is expressed during neurodevelopment and is involved in Apaf1-dependent caspase-3 activation in proneural cells. *Cellular and Molecular Life Sciences,* 65 (11), 1780-1790.

Decourt, B., Bouleau, Y., Dulon, D. and Hafidi, A., 2005. Expression analysis of neuroleukin, calmodulin, cortactin, and Rho7/Rnd2 in the intact and injured mouse brain. *Developmental Brain Research,* 159 (1), 36-54.

Dhaliwal, J., Xi, Y., Bruel-Jungerman, E., Germain, J., Francis, F. and Lagace, D.C., 2016. Doublecortin (DCX) is not essential for survival and differentiation of newborn neurons in the adult mouse dentate gyrus. *Frontiers in Neuroscience,* 9, 494.

Di Angelantonio, S., Bertollini, C., Piccinin, S., Rosito, M., Trettel, F., Pagani, F., Limatola, C. and Ragozzino, D., 2015. Basal adenosine modulates the functional properties of AMPA receptors in mouse hippocampal neurons through the activation of A1R A2AR and A3R. *Frontiers in Cellular Neuroscience,* 9, 409.

Dodla, M.C., and Bellamkonda, R.V., 2006. Anisotropic scaffolds facilitate enhanced neurite extension in vitro. *Journal of Biomedical Materials Research Part A,* 78 (2), 213-221.

Ducheyne, P., Healy, K., Hutmacher, D.E., Grainger, D.W. and Kirkpatrick, C.J., 2015. *Comprehensive biomaterials.* Newnes.

Duffau, H., 2015. Stimulation mapping of white matter tracts to study brain functional connectivity. *Nature Reviews Neurology,* 11 (5), 255-265.

Dunnett, S.B., and Björklund, A., 2017. *Chapter 1 - Mechanisms and use of neural transplants for brain repair.* Elsevier.

Duverger, V., Sartorius, U., Klein-Bauernschmitt, P., Krammer, P.H. and Schlehofer, J.R., 2002. Enhancement of cisplatin-induced apoptosis by infection with adeno-associated virus type 2. *International Journal of Cancer,* 97 (5), 706-712.

Duxbury, M., Ito, H., Zinner, M., Ashley, S. and Whang, E., 2004. Focal adhesion kinase gene silencing promotes anoikis and suppresses metastasis of human pancreatic adenocarcinoma cells. *Surgery,* 135 (5), 555-562.

Edgar, N., and Sibille, E., 2012. A putative functional role for oligodendrocytes in mood regulation. *Translational Psychiatry,* 2 (5), e109.

Eide, L., and McMurray, C.T., 2005. Culture of adult mouse neurons. *Biotechniques,* 38 (1), 99-108.

Ero-Phillips, O., Jenkins, M. and Stamboulis, A., 2012. Tailoring crystallinity of electrospun plla fibres by control of electrospinning parameters. *Polymers,* 4 (3), 1331-1348.

Espuny-Camacho, I., Michelsen, K., Gall, D., Linaro, D., Hasche, A., Bonnefont, J., Bali, C., Orduz, D., Bilheu, A., Herpoel, A., Lambert, N., Gaspard, N., Péron, S., Schiffmann, S., Giugliano, M., Gaillard, A. and Vanderhaeghen, P., 2013. Pyramidal Neurons Derived from Human Pluripotent Stem Cells Integrate Efficiently into Mouse Brain Circuits In Vivo. *Neuron,* 77 (3), 440-456.

Estrada-Bernal, A., Gatlin, J.C., Sunpaweravong, S. and Pfenninger, K.H., 2009. Dynamic adhesions and MARCKS in melanoma cells. *Journal of Cell Science,* 122 (Pt 13), 2300-2310.

Evans, G., Brandt, K., Widmer, M., Lu, L., Meszlenyi, R., Gupta, P., Mikos, A., Hodges, J., Williams, J. and Gürlek, A., 1999. In vivo evaluation of poly (L-lactic acid) porous conduits for peripheral nerve regeneration. *Biomaterials,* 20 (12), 1109-1115.

Evans, G.R., Brandt, K., Niederbichler, A.D., Chauvin, P., Hermann, S., Bogle, M., Otta, L., Wang, B. and Patrick, C.W., 2000. Clinical long-term in vivo evaluation of poly (L-lactic acid) porous conduits for peripheral nerve regeneration. *Journal of Biomaterials Science, Polymer Edition,* 11 (8), 869-878.

Evsyukova, I., Plestant, C. and Anton, E., 2013. Integrative mechanisms of oriented neuronal migration in the developing brain. *Annual Review of Cell and Developmental Biology,* 29, 299-353.

Fairbanks, B.D., Schwartz, M.P., Bowman, C.N. and Anseth, K.S., 2009. Photoinitiated polymerization of PEG-diacrylate with lithium phenyl-2, 4, 6-trimethylbenzoylphosphinate: polymerization rate and cytocompatibility. *Biomaterials,* 30 (35), 6702-6707.

Falkner, S., Grade, S., Dimou, L., Conzelmann, K., Bonhoeffer, T., Götz, M. and Hübener, M., 2016. Transplanted embryonic neurons integrate into adult neocortical circuits. *Nature,* 539 (7628), 248.

Famulski, J.K., and Solecki, D.J., 2013. New spin on an old transition: epithelial parallels in neuronal adhesion control. *Trends in Neurosciences,* 36 (3), 163-173.

Fan, B., Kwon, K., Rechenberg, R., Khomenko, A., Haq, M., Becker, M.F., Weber, A.J. and Li, W., 2015. A polycrystalline diamond-based, hybrid neural interfacing probe for optogenetics. *In: Micro Electro Mechanical Systems (MEMS), 2015 28th IEEE International Conference on,* IEEE, pp. 616-619.

Fang, P., Schachner, M. and Shen, Y., 2012. HMGB1 in development and diseases of the central nervous system. *Molecular Neurobiology,* 45 (3), 499-506.

Fatehullah, A., Tan, S.H. and Barker, N., 2016. Organoids as an in vitro model of human development and disease. *Nature Cell Biology,* 18 (3), 246.

Faulkner, J., and Keirstead, H.S., 2005. Human embryonic stem cell-derived oligodendrocyte progenitors for the treatment of spinal cord injury. *Transplant Immunology,* 15 (2), 131-142.

Fennema, E., Rivron, N., Rouwkema, J., van Blitterswijk, C. and de Boer, J., 2013. Spheroid culture as a tool for creating 3D complex tissues. *Trends in Biotechnology,* 31 (2), 108-115.

Fields, R. ., Woo, D. and Basser, P., 2015. Glial Regulation of the Neuronal Connectome through Local and Long-Distant Communication. *Neuron,* 86 (2), 374-386.

Fine, E.G., Valentini, R.F., Bellamkonda, R. and Aebischer, P., 1991. Improved nerve regeneration through piezoelectric vinylidenefluoride-trifluoroethylene copolymer guidance channels. *Biomaterials,* 12 (8), 775-780.

Flanagan, L.A., Ju, Y.E., Marg, B., Osterfield, M. and Janmey, P.A., 2002. Neurite branching on deformable substrates. *Neuroreport,* 13 (18), 2411-2415.

Foong, J., Maier, M., Barker, G.J., Brocklehurst, S., Miller, D.H. and Ron, M.A., 2000. In vivo investigation of white matter pathology in schizophrenia with magnetisation transfer imaging. *Journal of Neurology, Neurosurgery, and Psychiatry,* 68 (1), 70-74.

Forbes, L.H., and Andrews, M.R., 2019. Grafted Human iPSC-Derived Neural Progenitor Cells Express Integrins and Extend Long-Distance Axons Within the Developing Corticospinal Tract. *Frontiers in Cellular Neuroscience,* 13.

French, H.M., Reid, M., Mamontov, P., Simmons, R.A. and Grinspan, J.B., 2009. Oxidative stress disrupts oligodendrocyte maturation. *Journal of Neuroscience Research,* 87 (14), 3076-3087.

Frimat, J., Xie, S., Bastiaens, A., Schurink, B., Wolbers, F., den Toonder, J. and Luttge, R., 2015. Advances in 3D neuronal cell culture. *Journal of Vacuum Science & Technology B, Nanotechnology and Microelectronics: Materials, Processing, Measurement, and Phenomena,* 33 (6), 06F902.

Friocourt, G.M., and Parnavelas, J.G., 2011. Identification of Arx targets unveils new candidates for controlling cortical interneuron migration and differentiation. *Frontiers in Cellular Neuroscience,* 5, 28.

Frisch, S.M., and Screaton, R.A., 2001. Anoikis mechanisms. *Current Opinion in Cell Biology,* 13 (5), 555-562.

Furtak, S.C., Moyer, J.R. and Brown, T.H., 2007. Morphology and ontogeny of rat perirhinal cortical neurons. *Journal of Comparative Neurology,* 505 (5), 493-510.

Gao, Y., Broussard, J., Haque, A., Revzin, A. and Lin, T., 2016. Functional imaging of neuron–astrocyte interactions in a compartmentalized microfluidic device. *Microsystems & Nanoengineering,* 2, 15045.

Garlotta, D., 2001. A literature review of poly (lactic acid). *Journal of Polymers and the Environment,* 9 (2), 63-84.

Gary, D.S., and Mattson, M.P., 2001. Integrin signaling via the PI3-kinase–Akt pathway increases neuronal resistance to glutamate-induced apoptosis. *Journal of Neurochemistry,* 76 (5), 1485-1496.

Gavalda, N., Gutierrez, H. and Davies, A.M., 2009. Developmental switch in NF-kappaB signalling required for neurite growth. *Development (Cambridge, England),* 136 (20), 3405-3412.

Geerken, M., Lammertink, R.G. and Wessling, M., 2007. Tailoring surface properties for controlling droplet formation at microsieve membranes. *Colloids and Surfaces A: Physicochemical and Engineering Aspects,* 292 (2-3), 224-235.

Georges, P.C., Miller, W.J., Meaney, D.F., Sawyer, E.S. and Janmey, P.A., 2006. Matrices with compliance comparable to that of brain tissue select neuronal over glial growth in mixed cortical cultures. *Biophysical Journal,* 90 (8), 3012-3018.

Georges, P.C., Miller, W.J., Meaney, D.F., Sawyer, E.S. and Janmey, P.A., 2006. Matrices with Compliance Comparable to that of Brain Tissue Select Neuronal over Glial Growth in Mixed Cortical Cultures. *Biophysical Journal,* 90 (8), 3012-3018.

Geranmayeh, M.H., Rahbarghazi, R. and Farhoudi, M., 2019. Targeting pericytes for neurovascular regeneration. *Cell Communication and Signaling,* 17 (1), 26.

Ghasemi-Mobarakeh, L., Prabhakaran, M.P., Morshed, M., Nasr-Esfahani, M.H., Baharvand, H., Kiani, S., Al-Deyab, S.S. and Ramakrishna, S., 2011. Application of conductive polymers, scaffolds and electrical stimulation for nerve tissue engineering. *Journal of Tissue Engineering and Regenerative Medicine,* 5 (4), e17-e35.

Ghasemi-Mobarakeh, L., Prabhakaran, M.P., Morshed, M., Nasr-Esfahani, M.H. and Ramakrishna, S., 2009. Electrical stimulation of nerve cells using conductive nanofibrous scaffolds for nerve tissue engineering. *Tissue Engineering Part A,* 15 (11), 3605-3619.

Ghasemi-Mobarakeh, L., Prabhakaran, M.P., Tian, L., Shamirzaei-Jeshvaghani, E., Dehghani, L. and Ramakrishna, S., 2015. Structural properties of scaffolds: crucial parameters towards stem cells differentiation. *World Journal of Stem Cells,* 7 (4), 728-744.

Ghosh, A., Carnahan, J. and Greenberg, M.E., 1994. Requirement for BDNF in activity-dependent survival of cortical neurons. *Science,* 263 (5153), 1618-1624.

Gilbert, P.M., Havenstrite, K.L., Magnusson, K.E., Sacco, A., Leonardi, N.A., Kraft, P., Nguyen, N.K., Thrun, S., Lutolf, M.P. and Blau, H.M., 2010. Substrate elasticity regulates skeletal muscle stem cell self-renewal in culture. *Science (New York, N.Y.),* 329 (5995), 1078-1081.

Goldman, S.A., Pulsinelli, W.A., Clarke, W.Y., Kraig, R.P. and Plum, F., 1989. The effects of extracellular acidosis on neurons and glia in vitro. *Journal of Cerebral Blood Flow & Metabolism,* 9 (4), 471-477.

Gomez, I.G., Roach, A.M., Nakagawa, N., Amatucci, A., Johnson, B.G., Dunn, K., Kelly, M.C., Karaca, G., Zheng, T.S., Szak, S., Peppiatt-Wildman, C.M., Burkly, L.C. and Duffield, J.S., 2016. TWEAK-Fn14 Signaling Activates Myofibroblasts to Drive Progression of Fibrotic Kidney Disease. *Journal of the American Society of Nephrology : JASN,* 27 (12), 3639-3652.

Gompf, H.S., Budygin, E.A., Fuller, P.M. and Bass, C.E., 2015. Targeted genetic manipulations of neuronal subtypes using promoter-specific combinatorial AAVs in wild-type animals. *Frontiers in Behavioral Neuroscience,* 9, 152.

Goodenough, D.A., and Paul, D.L., 2009. Gap junctions. *Cold Spring Harbor Perspectives in Biology,* 1 (1), a002576.

Gorman, A.M., 2008. Neuronal cell death in neurodegenerative diseases: recurring themes around protein handling. *Journal of Cellular and Molecular Medicine,* 12 (6a), 2263-2280.

Goyal, M., Hawrylycz, M., Miller, J., Snyder, A. and Raichle, M., 2014. *Aerobic Glycolysis in the Human Brain Is Associated with Development and Neotenous Gene Expression.*

Green, R.A., Hassarati, R.T., Goding, J.A., Baek, S., Lovell, N.H., Martens, P.J. and Poole-Warren, L.A., 2012. Conductive hydrogels: mechanically robust hybrids for use as biomaterials. *Macromolecular Bioscience,* 12 (4), 494-501.

Guillemot, F., Molnár, Z., Tarabykin, V. and Stoykova, A., 2006. Molecular mechanisms of cortical differentiation. *European Journal of Neuroscience,* 23 (4), 857-868.

Gunn, J.W., Turner, S.D. and Mann, B.K., 2005. Adhesive and mechanical properties of hydrogels influence neurite extension. *Journal of Biomedical Materials Research Part A,* 72 (1), 91-97.

Günther, M., Waxman, D., Wagner, E. and Ogris, M., 2006. Effects of hypoxia and limited diffusion in tumor cell microenvironment on bystander effect of P450 prodrug therapy. *Cancer Gene Therapy,* 13 (8), 771.

Gupta, D., Tator, C.H. and Shoichet, M.S., 2006. Fast-gelling injectable blend of hyaluronan and methylcellulose for intrathecal, localized delivery to the injured spinal cord. *Biomaterials,* 27 (11), 2370-2379.

Guru, A., Post, R.J., Ho, Y. and Warden, M.R., 2015. Making sense of optogenetics. *International Journal of Neuropsychopharmacology,* 18 (11).

Guy, J., and Staiger, J.F., 2017. The functioning of a cortex without layers. *Frontiers in Neuroanatomy,* 11, 54.

Haddad, G.G., and Yu, S.P., 2009. *Brain hypoxia and ischemia.* Springer.

Haenisch, C., Diekmann, H., Klinger, M., Gennarini, G., Kuwada, J.Y. and Stuermer, C.A., 2005. The neuronal growth and regeneration associated Cntn1 (F3/F11/Contactin) gene is duplicated in fish: expression during development and retinal axon regeneration. *Molecular and Cellular Neuroscience,* 28 (2), 361-374.

Hallett, P., Deleidi, M., Astradsson, A., Smith, G., Cooper, O., Osborn, T., Sundberg, M., Moore, M., Perez-Torres, E., Brownell, A., Schumacher, J., Spealman, R. and Isacson, O., 2015. *Successful Function of Autologous iPSC-Derived Dopamine Neurons following Transplantation in a Non-Human Primate Model of Parkinson's Disease.*

Hamada, N., Iwamoto, I., Tabata, H. and Nagata, K., 2017. MUNC18–1 gene abnormalities are involved in neurodevelopmental disorders through defective cortical architecture during brain development. *Acta Neuropathologica Communications,* 5 (1), 92.

Hammond, V.E., So, E., Cate, H.S., Britto, J.M., Gunnersen, J.M. and Tan, S., 2010. Cortical layer development and orientation is modulated by relative contributions of reelin-negative and-positive neurons in mouse chimeras. *Cerebral Cortex,* 20 (9), 2017-2026.

Han, Y., Li, H., Lang, Y., Zhao, Y., Sun, H., Zhang, P., Ma, X., Han, J., Wang, Q. and Zhou, J., 2017. The effects of acute GABA treatment on the functional connectivity and network topology of cortical cultures. *Neurochemical Research,* 42 (5), 1394-1402.

Han, X., Chen, M., Wang, F., Windrem, M., Wang, S., Shanz, S., Xu, Q., Oberheim, N., Bekar, L., Betstadt, S., Silva, A., Takano, T., Goldman, S. and Nedergaard, M., 2013. *Forebrain Engraftment by Human Glial Progenitor Cells Enhances Synaptic Plasticity and Learning in Adult Mice.*

Han, X., Qian, X., Bernstein, J.G., Zhou, H., Franzesi, G.T., Stern, P., Bronson, R.T., Graybiel, A.M., Desimone, R. and Boyden, E.S., 2009. Millisecond-Timescale Optical Control of Neural Dynamics in the Nonhuman Primate Brain. *Neuron,* 62 (2), 191-198.

Hanson, M.G., Aiken, J., Sietsema, D.V., Sept, D., Bates, E.A., Niswander, L. and Moore, J.K., 2016. Novel α-tubulin mutation disrupts neural development and tubulin proteostasis. *Developmental Biology,* 409 (2), 406-419.

Hargus, G., Cooper, O., Deleidi, M., Levy, A., Lee, K., Marlow, E., Yow, A., Soldner, F., Hockemeyer, D., Hallett, P.J., Osborn, T., Jaenisch, R. and Isacson, O., 2010. Differentiated Parkinson patient-derived induced pluripotent stem cells grow in the adult rodent brain and reduce motor asymmetry in Parkinsonian rats. *Proceedings of the National Academy of Sciences,* 107 (36), 15921-15926.

Harris, J., Hess, A.E., Rowan, S.J., Weder, C., Zorman, C., Tyler, D. and Capadona, J.R., 2011. In vivo deployment of mechanically adaptive nanocomposites for intracortical microelectrodes. *Journal of Neural Engineering,* 8 (4), 046010.

Harris, J., Struzyna, L., Murphy, P., Adewole, D., Kuo, E. and Cullen, D., 2016. Advanced biomaterial strategies to transplant preformed micro-tissue engineered neural networks into the brain. *Journal of Neural Engineering,* 13 (1), 016019.

Hattori, T., Orimo, S., Aoki, S., Ito, K., Abe, O., Amano, A., Sato, R., Sakai, K. and Mizusawa, H., 2012. Cognitive status correlates with white matter alteration in Parkinson's disease. *Human Brain Mapping,* 33 (3), 727-739.

Haycock, J.W., 2011. 3D cell culture: a review of current approaches and techniques. *In:* 3D cell culture: a review of current approaches and techniques. *3D cell culture.* Springer, 2011, pp. 1-15.

He, L., Liao, S., Quan, D., Ma, K., Chan, C., Ramakrishna, S. and Lu, J., 2010. Synergistic effects of electrospun PLLA fiber dimension and pattern on neonatal mouse cerebellum C17.2 stem cells. *Acta Biomaterialia,* 6 (8), 2960-2969.

Hedberg, M.L., Peyser, N.D., Bauman, J.E., Gooding, W.E., Li, H., Bhola, N.E., Zhu, T.R., Zeng, Y., Brand, T.M., Kim, M.O., Jordan, R.C.K., VandenBerg, S., Olivas, V., Bivona, T.G., Chiosea, S.I., Wang, L., Mills, G.B., Johnson, J.T., Duvvuri, U., Ferris, R.L., Ha, P., Johnson, D.E. and Grandis, J.R., 2019. Use of nonsteroidal anti-inflammatory drugs predicts improved patient survival for PIK3CA-altered head and neck cancer. *The Journal of Experimental Medicine,* 216 (2), 419-427.

Hekmati, A.H., Khenoussi, N., Nouali, H., Patarin, J. and Drean, J., 2014. Effect of nanofiber diameter on water absorption properties and pore size of polyamide-6 electrospun nanoweb. *Textile Research Journal,* 84 (19), 2045-2055.

Hihara, S., Notoya, T., Tanaka, M., Ichinose, S., Ojima, H., Obayashi, S., Fujii, N. and Iriki, A., 2006. *Extension of corticocortical afferents into the anterior bank of the intraparietal sulcus by tool-use training in adult monkeys.*

Hindley, C.J., Condurat, A.L., Menon, V., Thomas, R., Azmitia, L.M., Davis, J.A. and Pruszak, J., 2016. The Hippo pathway member YAP enhances human neural crest cell fate and migration. *Scientific Reports,* 6, 23208.

Hindriks, R., Adhikari, M.H., Murayama, Y., Ganzetti, M., Mantini, D., Logothetis, N.K. and Deco, G., 2016. Can sliding-window correlations reveal dynamic functional connectivity in resting-state fMRI? *Neuroimage,* 127, 242-256.

Hochberg, L., and Donoghue, J., 2006. Sensors for brain-computer interfaces. *IEEE Engineering in Medicine and Biology Magazine,* 25 (5), 32-38.

Hochberg, L., Serruya, M., Friehs, G., Mukand, J., Saleh, M., Caplan, A., Branner, A., Chen, D., Penn, R. and Donoghue, J., 2006. Neuronal ensemble control of prosthetic devices by a human with tetraplegia. *Nature,* 442 (7099), 164-171.

Hong, J.K., Xu, G., Piao, D. and Madihally, S.V., 2013. Analysis of void shape and size in the collector plate and polycaprolactone molecular weight on electrospun scaffold pore size. *Journal of Applied Polymer Science,* 128 (3), 1583-1591.

Hosseinkhani, M., Mehrabani, D., Karimfar, M.H., Bakhtiyari, S., Manafi, A. and Shirazi, R., 2014. Tissue engineered scaffolds in regenerative medicine. *World Journal of Plastic Surgery,* 3 (1), 3-7.

Howard, D.B., Powers, K., Wang, Y. and Harvey, B.K., 2008. Tropism and toxicity of adeno-associated viral vector serotypes 1, 2, 5, 6, 7, 8, and 9 in rat neurons and glia in vitro. *Virology,* 372 (1), 24-34.

Hu, C., Sun, Y., Liu, C., Zhou, B., Li, C., Xu, Q. and Xu, X., 2018. NSDHL-containing duplication at Xq28 in a male patient with autism spectrum disorder: a case report. *BMC Medical Genetics,* 19 (1), 192.

Hubel, D.H., and Wiesel, T.N., 1974. Uniformity of monkey striate cortex: a parallel relationship between field size, scatter, and magnification factor. *Journal of Comparative Neurology,* 158 (3), 295-305.

Hurelbrink, C., and Barker, R., 2005. Migration of cells from primary transplants of allo- and xenografted foetal striatal tissue in the adult rat brain. *The European Journal of Neuroscience,* 21 (6), 1503-1510.

Inatani, M., Honjo, M., Otori, Y., Oohira, A., Kido, N., Tano, Y., Honda, Y. and Tanihara, H., 2001. Inhibitory effects of neurocan and phosphacan on neurite outgrowth from retinal ganglion cells in culture. *Investigative Ophthalmology & Visual Science,* 42 (8), 1930-1938.

Inoue, S., Hayashi, K., Fujita, K., Tagawa, K., Okazawa, H., Kubo, K. and Nakajima, K., 2018. Drebrin-like (Dbnl) controls neuronal migration via regulating N-cadherin expression in the developing cerebral cortex. *Journal of Neuroscience,* , 1634-1618.

Ip, J.P., Fu, A.K. and Ip, N.Y., 2014. CRMP2: functional roles in neural development and therapeutic potential in neurological diseases. *The Neuroscientist,* 20 (6), 589-598.

Ishizaki, T., Saito, N. and Takai, O., 2010. Correlation of cell adhesive behaviors on superhydrophobic, superhydrophilic, and micropatterned superhydrophobic/superhydrophilic surfaces to their surface chemistry. *Langmuir,* 26 (11), 8147-8154.

Ivaska, J., Pallari, H., Nevo, J. and Eriksson, J.E., 2007. Novel functions of vimentin in cell adhesion, migration, and signaling. *Experimental Cell Research,* 313 (10), 2050-2062.

Jaglin, X.H., Poirier, K., Saillour, Y., Buhler, E., Tian, G., Bahi-Buisson, N., Fallet-Bianco, C., Phan-Dinh-Tuy, F., Kong, X.P. and Bomont, P., 2009. Mutations in the β-tubulin gene TUBB2B result in asymmetrical polymicrogyria. *Nature Genetics,* 41 (6), 746.

Jaiswal, A.K., Dhumal, R.V., Bellare, J.R. and Vanage, G.R., 2013. In vivo biocompatibility evaluation of electrospun composite scaffolds by subcutaneous implantation in rat. *Drug Delivery and Translational Research,* 3 (6), 504-517.

Jayachandran, P., Olmo, V.N., Sanchez, S.P., McFarland, R.J., Vital, E., Werner, J.M., Hong, E., Sanchez-Alberola, N., Molodstov, A. and Brewster, R.M., 2016. Microtubule-associated protein 1b is required for shaping the neural tube. *Neural Development,* 11 (1), 1.

Jgamadze, D., Bergen, J., Stone, D., Jang, J., Schaffer, D.V., Isacoff, E.Y. and Pautot, S., 2012. Colloids as mobile substrates for the implantation and integration of differentiated neurons into the mammalian brain. *PloS One,* 7 (1), e30293.

Jha, B.S., Colello, R.J., Bowman, J.R., Sell, S.A., Lee, K.D., Bigbee, J.W., Bowlin, G.L., Chow, W.N., Mathern, B.E. and Simpson, D.G., 2011. Two pole air gap electrospinning: fabrication of highly aligned, three-dimensional scaffolds for nerve reconstruction. *Acta Biomaterialia,* 7 (1), 203-215.

Ji, R., Berta, T. and Nedergaard, M., 2013. Glia and pain: is chronic pain a gliopathy? *Pain®,* 154, S10-S28.

Jiang, F.X., Yurke, B., Firestein, B.L. and Langrana, N.A., 2008. Neurite outgrowth on a DNA crosslinked hydrogel with tunable stiffnesses. *Annals of Biomedical Engineering,* 36 (9), 1565-1579.

Jin, X., and Yamashita, T., 2016. Microglia in central nervous system repair after injury. *The Journal of Biochemistry,* 159 (5), 491-496.

Jin, Y., Lee, D.H., Kim, H.Y., Cho, H.N., Chung, H.J., Park, Y., Youn, H., Lee, S.J., Lee, H.J. and Kim, S.U., 2014. In vivo bioluminescence imaging for prolonged survival of transplanted human neural stem cells using 3D biocompatible scaffold in corticectomized rat model. *PloS One,* 9 (9), e105129.

Jin, G., Kim, M., Shin, U.S. and Kim, H., 2011. Neurite outgrowth of dorsal root ganglia neurons is enhanced on aligned nanofibrous biopolymer scaffold with carbon nanotube coating. *Neuroscience Letters,* 501 (1), 10-14.

Johansson, F., Carlberg, P., Danielsen, N., Montelius, L. and Kanje, M., 2006. Axonal outgrowth on nano-imprinted patterns. *Biomaterials,* 27 (8), 1251-1258.

Johnson, R.H., Kho, D.T., O'Carroll, S.J., Angel, C.E. and Graham, E.S., 2018. The functional and inflammatory response of brain endothelial cells to Toll-Like Receptor agonists. *Scientific Reports,* 8 (1), 10102-018-28518-3.

Jones, D.T., Vemuri, P., Murphy, M.C., Gunter, J.L., Senjem, M.L., Machulda, M.M., Przybelski, S.A., Gregg, B.E., Kantarci, K. and Knopman, D.S., 2012. Non-stationarity in the "resting brain's" modular architecture. *PloS One,* 7 (6), e39731.

Jung, H.J., Ahn, K., Han, D.K. and Ahn, D., 2005. Surface characteristics and fibroblast adhesion behavior of RGD-immobilized biodegradable PLLA films. *Macromolecular Research,* 13 (5), 446-452.

Kadoshima, T., Sakaguchi, H., Nakano, T., Soen, M., Ando, S., Eiraku, M. and Sasai, Y., 2013. Self-organization of axial polarity, inside-out layer pattern, and species-specific progenitor dynamics in human ES cell-derived neocortex. *Proceedings of the National Academy of Sciences of the United States of America,* 110 (50), 20284-20289.

Kalluri, R., and Weinberg, R.A., 2009. The basics of epithelial-mesenchymal transition. *The Journal of Clinical Investigation,* 119 (6), 1420-1428.

Kandel, E., Schwartz, J. and Jessell, T., 2000. *Principles of Neural Science.* Fourth ed. China: McGraw-Hill.

Kandel, E., 2012. Principles of neural science, Fifth Editition, Kandel, ER; Schwartz, JH; Jessell TM and two more.

Kanemaru, K., Okubo, Y., Hirose, K. and Iino, M., 2007. Regulation of neurite growth by spontaneous Ca2+ oscillations in astrocytes. *The Journal of Neuroscience : The Official Journal of the Society for Neuroscience,* 27 (33), 8957-8966.

Kannan, V., Brouwer, N., Hanisch, U., Regen, T., Eggen, B.J. and Boddeke, H.W., 2013. Histone deacetylase inhibitors suppress immune activation in primary mouse microglia. *Journal of Neuroscience Research,* 91 (9), 1133-1142.

Kärkkäinen, V., Pomeshchik, Y., Savchenko, E., Dhungana, H., Kurronen, A., Lehtonen, S., Naumenko, N., Tavi, P., Levonen, A. and Yamamoto, M., 2014. Nrf2 regulates neurogenesis and protects neural progenitor cells against Aβ toxicity. *Stem Cells,* 32 (7), 1904-1916.

Kato-Negishi, M., Morimoto, Y., Onoe, H. and Takeuchi, S., 2013. Millimeter-Sized Neural Building Blocks for 3D Heterogeneous Neural Network Assembly. *Advanced Healthcare Materials,* 2 (12), 1564-1570.

Kawashima, T., Kitamura, K., Suzuki, K., Nonaka, M., Kamijo, S., Takemoto-Kimura, S., Kano, M., Okuno, H., Ohki, K. and Bito, H., 2013. Functional labeling of neurons and their projections using the synthetic activity–dependent promoter E-SARE. *Nature Methods,* 10 (9), 889.

Kelava, I., and Lancaster, M.A., 2016. Dishing out mini-brains: Current progress and future prospects in brain organoid research. *Developmental Biology,* 420 (2), 199-209.

Kiffin, R., Bandyopadhyay, U. and Cuervo, A.M., 2006. Oxidative stress and autophagy. *Antioxidants & Redox Signaling,* 8 (1-2), 152-162.

Kilberg, M.S., Terada, N. and Shan, J., 2016. Influence of amino acid metabolism on embryonic stem cell function and differentiation. *Advances in Nutrition,* 7 (4), 780S-789S.

Kim, C., and Kim, D., 2016. Self-healing Characteristics of Collagen Coatings with Respect to Surface Abrasion. *Scientific Reports,* 6, 20563.

Kim, H., Zahir, T., Tator, C.H. and Shoichet, M.S., 2011. Effects of dibutyryl cyclic-AMP on survival and neuronal differentiation of neural stem/progenitor cells transplanted into spinal cord injured rats. *PLoS One,* 6 (6), e21744.

Kim, S.H., Im, S., Oh, S., Jeong, S., Yoon, E., Lee, C.J., Choi, N. and Hur, E., 2017. Anisotropically organized three-dimensional culture platform for reconstruction of a hippocampal neural network. *Nature Communications,* 8, 14346.

Kim, I.A., Park, S.A., Kim, Y.J., Kim, S., Shin, H.J., Lee, Y.J., Kang, S.G. and Shin, J., 2006. Effects of mechanical stimuli and microfiber-based substrate on neurite outgrowth and guidance. *Journal of Bioscience and Bioengineering,* 101 (2), 120-126.

Kim, J.S., and Kaiser, M., 2014. From Caenorhabditis elegans to the human connectome: a specific modular organization increases metabolic, functional and developmental

efficiency. *Philosophical Transactions of the Royal Society of London.Series B, Biological Sciences,* 369 (1653), 10.1098/rstb.2013.0529.

Kim, Y., Haftel, V.K., Kumar, S. and Bellamkonda, R.V., 2008. The role of aligned polymer fiber-based constructs in the bridging of long peripheral nerve gaps. *Biomaterials,* 29 (21), 3117-3127.

Kirkham, G.R., Britchford, E., Upton, T., Ware, J., Gibson, G.M., Devaud, Y., Ehrbar, M., Padgett, M., Allen, S. and Buttery, L.D., 2015. Precision assembly of complex cellular microenvironments using holographic optical tweezers. *Scientific Reports,* 5, 8577.

Kleene, R., Mzoughi, M., Joshi, G., Kalus, I., Bormann, U., Schulze, C., Xiao, M.F., Dityatev, A. and Schachner, M., 2010. NCAM-induced neurite outgrowth depends on binding of calmodulin to NCAM and on nuclear import of NCAM and fak fragments. *The Journal of Neuroscience : The Official Journal of the Society for Neuroscience,* 30 (32), 10784-10798.

Kniss, D.A., and Burry, R.W., 1988. Serum and fibroblast growth factor stimulate quiescent astrocytes to re-enter the cell cycle. *Brain Research,* 439 (1), 281-288.

Knoblich, J. and Lancester, M.A., 2015. *Three dimensional heterogeneously differentiated tissue culture.* United States US20150330970A1. 2014-06-18.

Koene, R.A., Tijms, B., van Hees, P., Postma, F., de Ridder, A., Ramakers, G.J., van Pelt, J. and van Ooyen, A., 2009. NETMORPH: a framework for the stochastic generation of large scale neuronal networks with realistic neuron morphologies. *Neuroinformatics,* 7 (3), 195-210.

Koh, H.S., Yong, T., Chan, C.K. and Ramakrishna, S., 2008. Enhancement of neurite outgrowth using nano-structured scaffolds coupled with laminin. *Biomaterials,* 29 (26), 3574-3582.

Köse-Dunn, M., Fricker, R. and Roach, P., 2017. Tissue Engineered Organoids for Neural Network Modelling. *Adv Tissue Eng Regen Med Open Access,* 3 (3), 00066.

Koser, D.E., Thompson, A.J., Foster, S.K., Dwivedy, A., Pillai, E.K., Sheridan, G.K., Svoboda, H., Viana, M., da F Costa, L. and Guck, J., 2016. Mechanosensing is critical for axon growth in the developing brain. *Nature Neuroscience,* 19 (12), 1592-1598.

Kovács, K.J., 1998. Invited review c-Fos as a transcription factor: a stressful (re)view from a functional map. *Neurochemistry International,* 33 (4), 287-297.

Kovalevich, J., and Langford, D., 2013. Considerations for the use of SH-SY5Y neuroblastoma cells in neurobiology. *Neuronal Cell Culture: Methods and Protocols,* , 9-21.

Kowno, M., Watanabe-Susaki, K., Ishimine, H., Komazaki, S., Enomoto, K., Seki, Y., Wang, Y.Y., Ishigaki, Y., Ninomiya, N. and Taka-aki, K.N., 2014. Prohibitin 2 regulates the proliferation and lineage-specific differentiation of mouse embryonic stem cells in mitochondria. *PLoS One,* 9 (4), e81552.

Kuang, Y., and Xu, B., 2013. Disruption of the dynamics of microtubules and selective inhibition of glioblastoma cells by nanofibres of small hydrophobic molecules. *Angewandte Chemie,* 125 (27), 7082-7086.

Kügler, S., Lingor, P., Schöll, U., Zolotukhin, S. and Bähr, M., 2003. Differential transgene expression in brain cells in vivo and in vitro from AAV-2 vectors with small transcriptional control units. *Virology,* 311 (1), 89-95.

Kulkarni, M.M., 2011. Digital multiplexed gene expression analysis using the NanoString nCounter system. *Current Protocols in Molecular Biology,* 94 (1), 25B. 10.1-25B. 10.17.

Kwon, K.Y., Lee, H., Ghovanloo, M., Weber, A. and Li, W., 2015. Design, fabrication, and packaging of an integrated, wirelessly-powered optrode array for optogenetics application. *Frontiers in Systems Neuroscience,* 9, 69.

Lagenaur, C., and Lemmon, V., 1987. An L1-like molecule, the 8D9 antigen, is a potent substrate for neurite extension. *Proceedings of the National Academy of Sciences of the United States of America,* 84 (21), 7753-7757.

Lambert, J., Ivosev, G., Couzens, A.L., Larsen, B., Taipale, M., Lin, Z., Zhong, Q., Lindquist, S., Vidal, M. and Aebersold, R., 2013. Mapping differential interactomes by affinity purification coupled with data-independent mass spectrometry acquisition. *Nature Methods,* 10 (12), 1239.

Lamouille, S., Xu, J. and Derynck, R., 2014. Molecular mechanisms of epithelial–mesenchymal transition. *Nature Reviews Molecular Cell Biology,* 15 (3), 178.

Lancashire, L.J., Lemetre, C. and Ball, G.R., 2009. An introduction to artificial neural networks in bioinformatics—application to complex microarray and mass spectrometry datasets in cancer studies. *Briefings in Bioinformatics,* 10 (3), 315-329.

Lancaster, M.A., and Knoblich, J.A., 2014. Generation of cerebral organoids from human pluripotent stem cells. *Nature Protocols,* 9 (10), 2329.

Laplaca, M.C., Lee, V.M. and Thibault, L.E., 1997. An in vitro model of traumatic neuronal injury: loading rate-dependent changes in acute cytosolic calcium and lactate dehydrogenase release. *Journal of Neurotrauma,* 14 (6), 355-368.

LaPlaca, M.C., Prado, G.R., Cullen, D.K. and Irons, H.R., 2006. High rate shear insult delivered to cortical neurons produces heterogeneous membrane permeability alterations. *In: Engineering in Medicine and Biology Society, 2006. EMBS'06. 28th Annual International Conference of the IEEE,* IEEE, pp. 2384-2387.

Latremoliere, A., Cheng, L., DeLisle, M., Wu, C., Chew, S., Hutchinson, E.B., Sheridan, A., Alexandre, C., Latremoliere, F. and Sheu, S., 2018. Neuronal-Specific TUBB3 Is Not Required for Normal Neuronal Function but Is Essential for Timely Axon Regeneration. *Cell Reports,* 24 (7), 1865-1879. e9.

Laverty, P.H., Leskovar, A., Breur, G.J., Coates, J.R., Bergman, R.L., Widmer, W.R., Toombs, J.P., Shapiro, S. and Borgens, R.B., 2004. A preliminary study of intravenous surfactants in paraplegic dogs: polymer therapy in canine clinical SCI. *Journal of Neurotrauma,* 21 (12), 1767-1777.

Le Friec, A., Salabert, A., Davoust, C., Demain, B., Vieu, C., Vaysse, L., Payoux, P. and Loubinoux, I., 2017. Enhancing plasticity of the central nervous system: drugs, stem cell therapy, and neuro-implants. *Neural Plasticity,* 2017.

Leach, M.K., Feng, Z., Tuck, S.J. and Corey, J.M., 2011. Electrospinning fundamentals: optimizing solution and apparatus parameters. *JoVE (Journal of Visualized Experiments),* (47), e2494.

Lee, J.H., Kim, H., Kim, J.H. and Lee, S., 2016. Soft implantable microelectrodes for future medicine: prosthetics, neural signal recording and neuromodulation. *Lab on a Chip,* 16 (6), 959-976.

Lee, Y., and Arinzeh, T.L., 2012. The influence of piezoelectric scaffolds on neural differentiation of human neural stem/progenitor cells. *Tissue Engineering Part A,* 18 (19-20), 2063-2072.

Lee, Y., Collins, G. and Livingston Arinzeh, T., 2011. Neurite extension of primary neurons on electrospun piezoelectric scaffolds. *Acta Biomaterialia,* 7 (11), 3877-3886.

Leondaritis, G., and Eickholt, B.J., 2015. Short lives with long-lasting effects: filopodia protrusions in neuronal branching morphogenesis. *PLoS Biology,* 13 (9), e1002241.

Leong, M.F., Rasheed, M.Z., Lim, T.C. and Chian, K.S., 2009. In vitro cell infiltration and in vivo cell infiltration and vascularization in a fibrous, highly porous poly (d, l-lactide) scaffold fabricated by cryogenic electrospinning technique. *Journal of Biomedical Materials Research Part A: An Official Journal of the Society for Biomaterials, the Japanese Society for Biomaterials, and the Australian Society for Biomaterials and the Korean Society for Biomaterials,* 91 (1), 231-240.

Lesuisse, C., and Martin, L.J., 2002. Long-term culture of mouse cortical neurons as a model for neuronal development, aging, and death. *Developmental Neurobiology,* 51 (1), 9-23.

Leung, B.K., Biran, R., Underwood, C.J. and Tresco, P.A., 2008. Characterization of microglial attachment and cytokine release on biomaterials of differing surface chemistry. *Biomaterials,* 29 (23), 3289-3297.

Li, W., Shanti, R.M. and Tuan, R.S., 2006. Electrospinning technology for nanofibrous scaffolds in tissue engineering. *Nanotechnologies for the Life Sciences,* .

Li, W., Fan, B., Yong, K. and Weber, A., 2015. Microfabricated optoelectronic neural implants for optogenetics. *In: SENSORS, 2015 IEEE,* IEEE, pp. 1-4.

Liang, C., Carrel, D., Omelchenko, A., Kim, H., Patel, A., Fanget, I. and Firestein, B.L., 2018. Cortical neuron migration and dendrite morphology are regulated by carboxypeptidase E. *Cerebral Cortex,* .

Liao, H., Bu, W.Y., Wang, T.H., Ahmed, S. and Xiao, Z.C., 2005. Tenascin-R plays a role in neuroprotection via its distinct domains that coordinate to modulate the microglia function. *The Journal of Biological Chemistry,* 280 (9), 8316-8323.

Liedtke, W., Yeo, M., Zhang, H., Wang, Y., Gignac, M., Miller, S., Berglund, K. and Liu, J., 2013. Highly conductive carbon nanotube matrix accelerates developmental chloride extrusion in central nervous system neurons by increased expression of chloride transporter KCC2. *Small,* 9 (7), 1066-1075.

Liljelund, P., Ghosh, P. and van den Pol, A.N., 1994. Expression of the neural axon adhesion molecule L1 in the developing and adult rat brain. *The Journal of Biological Chemistry,* 269 (52), 32886-32895.

Limongi, T., Cesca, F., Gentile, F., Marotta, R., Ruffilli, R., Barberis, A., Dal Maschio, M., Petrini, E.M., Santoriello, S. and Benfenati, F., 2013. Nanostructured superhydrophobic substrates trigger the development of 3D neuronal networks. *Small,* 9 (3), 402-412.

Lindvall, O., and Kokaia, Z., 2010. Stem cells in human neurodegenerative disorders - time for clinical translation? *The Journal of Clinical Investigation,* 120 (1), 29-40.

Liu, J., Appaix, F., Bibari, O., Marchand, G., Benabid, A., Sauter-Starace, F. and De Waard, M., 2011. Control of neuronal network organization by chemical surface functionalization of multi-walled carbon nanotube arrays. *Nanotechnology,* 22 (19), 195101.

Liu, K., Lu, Y., Lee, J.K., Samara, R., Willenberg, R., Sears-Kraxberger, I., Tedeschi, A., Park, K.K., Jin, D. and Cai, B., 2010. PTEN deletion enhances the regenerative ability of adult corticospinal neurons. *Nature Neuroscience,* 13 (9), 1075-1081.

Liu, Y., Joo, K. and Wang, P., 2013. Endocytic processing of adeno-associated virus type 8 vectors for transduction of target cells. *Gene Therapy,* 20 (3), 308.

Liu, Y.C., and Lu, D.N., 2006. Surface energy and wettability of plasma-treated polyacrylonitrile fibers. *Plasma Chemistry and Plasma Processing,* 26 (2), 119.

Liu, C., Mei, M., Li, Q., Roboti, P., Pang, Q., Ying, Z., Gao, F., Lowe, M. and Bao, S., 2017. Loss of the golgin GM130 causes Golgi disruption, Purkinje neuron loss, and ataxia in mice. *Proceedings of the National Academy of Sciences of the United States of America,* 114 (2), 346-351.

Liu, Y., Kim, Y.J., Ji, M., Fang, J., Siriwon, N., Zhang, L.I. and Wang, P., 2014. Enhancing gene delivery of adeno-associated viruses by cell-permeable peptides. *Molecular Therapy - Methods & Clinical Development,* 1, 12.

Lively, S., and Schlichter, L.C., 2013. The microglial activation state regulates migration and roles of matrix-dissolving enzymes for invasion. *Journal of Neuroinflammation,* 10 (1), 843.

Loh, Q.L., and Choong, C., 2013. Three-dimensional scaffolds for tissue engineering applications: role of porosity and pore size. *Tissue Engineering Part B: Reviews,* 19 (6), 485-502.

Lopes, M.S., Jardini, A. and Maciel Filho, R., 2012. Poly (lactic acid) production for tissue engineering applications. *Procedia Engineering,* 42, 1402-1413.

Lopes, F.M., Schröder, R., Júnior,Mário Luiz Conte da Frota, Zanotto-Filho, A., Müller, C.B., Pires, A.S., Meurer, R.T., Colpo, G.D., Gelain, D.P., Kapczinski, F., Moreira, J.C.F., Fernandes,

M.D.C. and Klamt, F., 2010. Comparison between proliferative and neuron-like SH-SY5Y cells as an in vitro model for Parkinson disease studies. *Brain Research,* 1337, 85-94.

Lo, C.W., 1999. Genes, gene knockouts, and mutations in the analysis of gap junctions. *Developmental Genetics,* 24 (1-2), 1-4.

Lovat, V., Pantarotto, D., Lagostena, L., Cacciari, B., Grandolfo, M., Righi, M., Spalluto, G., Prato, M. and Ballerini, L., 2005. Carbon nanotube substrates boost neuronal electrical signaling. *Nano Letters,* 5 (6), 1107-1110.

Lu, Y.B., Iandiev, I., Hollborn, M., Korber, N., Ulbricht, E., Hirrlinger, P.G., Pannicke, T., Wei, E.Q., Bringmann, A., Wolburg, H., Wilhelmsson, U., Pekny, M., Wiedemann, P., Reichenbach, A. and Kas, J.A., 2011. Reactive glial cells: increased stiffness correlates with increased intermediate filament expression. *FASEB Journal : Official Publication of the Federation of American Societies for Experimental Biology,* 25 (2), 624-631.

Lundberg, C., Englund, U., Trono, D., Bjorklund, A. and Wictorin, K., 2002. Differentiation of the RN33b cell line in to forebrain projection neurons after transplantation in to the neonatal rat brain. *Experimental Neurology,* 175, 370-387.

Lyman, K.A., and Chetkovich, D.M., 2015. Cortical compass: EML1 helps point the way in neuronal migration. *Epilepsy Currents,* 15 (1), 43-44.

Ma, Z., Cao, Q., Zhang, L., Hu, J., Howard, R.M., Lu, P., Whittemore, S.R. and Xu, X., 2009. Oligodendrocyte precursor cells differentially expressing Nogo-A but not MAG are more permissive to neurite outgrowth than mature oligodendrocytes. *Experimental Neurology,* 217 (1), 184-196.

Ma, J., Gao, J., Hou, B., Liu, J., Chen, S., Yan, G. and Ren, H., 2015. Neural stem cell transplantation promotes behavioral recovery in a photothrombosis stroke model. *International Journal of Clinical and Experimental Pathology,* 8 (7), 7838-7848.

Mackenzie, F., and Ruhrberg, C., 2012. Diverse roles for VEGF-A in the nervous system. *Development (Cambridge, England),* 139 (8), 1371-1380.

Maclean, F., 2017. Biomaterials to change astrocyte behaviour and morphology for brain repair.

Maere, S., Heymans, K. and Kuiper, M., 2005. BiNGO: a Cytoscape plugin to assess overrepresentation of gene ontology categories in biological networks. *Bioinformatics,* 21 (16), 3448-3449.

Mailander, V., and Landfester, K., 2009. Interaction of nanoparticles with cells. *Biomacromolecules,* 10 (9), 2379-2400.

Manoharan, S., Guillemin, G.J., Abiramasundari, R.S., Essa, M.M., Akbar, M. and Akbar, M.D., 2016. The role of reactive oxygen species in the pathogenesis of Alzheimer's disease, Parkinson's disease, and Huntington's disease: a mini review. *Oxidative Medicine and Cellular Longevity,* 2016.

Mao, Z., Bonni, A., Xia, F., Nadal-Vicens, M. and Greenberg, M.E., 1999. Neuronal activity-dependent cell survival mediated by transcription factor MEF2. *Science (New York, N.Y.),* 286 (5440), 785-790.

Mario Cheong, G.L., Lim, K.S., Jakubowicz, A., Martens, P.J., Poole-Warren, L.A. and Green, R.A., 2014. Conductive hydrogels with tailored bioactivity for implantable electrode coatings. *Acta Biomaterialia,* 10 (3), 1216-1226.

Markram, H., Lübke, J., Frotscher, M., Roth, A. and Sakmann, B., 1997. Physiology and anatomy of synaptic connections between thick tufted pyramidal neurones in the developing rat neocortex. *The Journal of Physiology,* 500 (2), 409-440.

Marote, A., Barroca, N., Vitorino, R., Silva, R.M., Fernandes, M.H., Vilarinho, P.M., e Silva, Odete AB da Cruz and Vieira, S.I., 2016. A proteomic analysis of the interactions between poly (L-lactic acid) nanofibres and SH-SY5Y neuronal-like cells. *AIMS Molecular Science,* 3 (4), 661-682.

Martinez-Banaclocha, M., 2018. Ephaptic Coupling of Cortical Neurons: Possible Contribution of Astroglial Magnetic Fields? *Neuroscience,* 370, 37-45.

Martínez-Serrano, A., and Björklund, A., 1997. Immortalized neural progenitor cells for CNS gene transfer and repair. *Trends in Neurosciences,* 20 (11), 530-538.

Mason, S., 2017. Lactate shuttles in neuroenergetics—homeostasis, allostasis and beyond. *Frontiers in Neuroscience,* 11, 43.

Matthews, J.A., Wnek, G.E., Simpson, D.G. and Bowlin, G.L., 2002. Electrospinning of collagen nanofibres. *Biomacromolecules,* 3 (2), 232-238.

Matute, C., 2017. Chapter 44 - Mechanisms of Glial Death and Protection. *In:* L.R. Caplan, J. Biller, M.C. Leary, E.H. Lo, A.J. Thomas, M. Yenari and J.H. Zhang, eds., *Primer on Cerebrovascular Diseases (Second Edition).* San Diego: Academic Press, 2017, pp. 215-219.

McCain, M.L., Lee, H., Aratyn-Schaus, Y., Kleber, A.G. and Parker, K.K., 2012. Cooperative coupling of cell-matrix and cell-cell adhesions in cardiac muscle. *Proceedings of the National Academy of Sciences of the United States of America,* 109 (25), 9881-9886.

McConnell, G.C., Rees, H.D., Levey, A.I., Gutekunst, C., Gross, R.E. and Bellamkonda, R.V., 2009. Implanted neural electrodes cause chronic, local inflammation that is correlated with local neurodegeneration. *Journal of Neural Engineering,* 6 (5), 056003.

McMurtrey, R.J., 2016. Analytic models of oxygen and nutrient diffusion, metabolism dynamics, and architecture optimization in three-dimensional tissue constructs with applications and insights in cerebral organoids. *Tissue Engineering Part C: Methods,* 22 (3), 221-249.

McMurtrey, R.J., 2014. Patterned and functionalized nanofiber scaffolds in three-dimensional hydrogel constructs enhance neurite outgrowth and directional control. *Journal of Neural Engineering,* 11 (6), 066009.

Melak, T., and Gakkhar, S., 2015. Comparative genome and network centrality analysis to identify drug targets of mycobacterium tuberculosis h37rv. *BioMed Research International,* 2015.

Mele, L., Paino, F., Papaccio, F., Regad, T., Boocock, D., Stiuso, P., Lombardi, A., Liccardo, D., Aquino, G. and Barbieri, A., 2018. A new inhibitor of glucose-6-phosphate dehydrogenase blocks pentose phosphate pathway and suppresses malignant proliferation and metastasis in vivo. *Cell Death & Disease,* 9 (5), 572.

Mena, M.A., Casarejos, M.J., Carazo, A., Paino, C.L. and de Yébenes García, J., 1996. Glia conditioned medium protects fetal rat midbrain neurones in culture from L-DOPA toxicity. *Neuroreport,* 7 (2), 441-445.

Meng, S., Rouabhia, M. and Zhang, Z., 2011. *Electrical stimulation in tissue regeneration.* INTECH Open Access Publisher.

Mezzanotte, L., Aswendt, M., Tennstaedt, A., Hoeben, R., Hoehn, M. and Löwik, C., 2013. Evaluating reporter genes of different luciferases for optimized in vivo bioluminescence imaging of transplanted neural stem cells in the brain. *Contrast Media & Molecular Imaging,* 8 (6), 505-513.

Michelsen, K., Acosta-Verdugo, S., Benoit-Marand, M., Espuny-Camacho, I., Gaspard, N., Saha, B., Gaillard, A. and Vanderhaeghen, P., 2015. Area-Specific Reestablishment of Damaged Circuits in the Adult Cerebral Cortex by Cortical Neurons Derived from Mouse Embryonic Stem Cells. *Neuron,* 85 (5), 982-997.

Millet, L.J., and Gillette, M.U., 2012. New perspectives on neuronal development via microfluidic environments. *Trends in Neurosciences,* 35 (12), 752-761.

Minary-Jolandan, M., and Yu, M., 2009. Nanoscale characterization of isolated individual type I collagen fibrils: polarization and piezoelectricity. *Nanotechnology,* 20 (8), 085706.

Missaire, M., and Hindges, R., 2015. The role of cell adhesion molecules in visual circuit formation: from neurite outgrowth to maps and synaptic specificity. *Developmental Neurobiology,* 75 (6), 569-583.

Miyashita, T., Shao, Y.R., Chung, J., Pourzia, O. and Feldman, D., 2013. Long-term channelrhodopsin-2 (ChR2) expression can induce abnormal axonal morphology and targeting in cerebral cortex. *Frontiers in Neural Circuits,* 7, 8.

Moffat, K.L., Kwei, A.S., Spalazzi, J.P., Doty, S.B., Levine, W.N. and Lu, H.H., 2008. Novel nanofiber-based scaffold for rotator cuff repair and augmentation. *Tissue Engineering Part A,* 15 (1), 115-126.

Moffett, J.R., Ross, B., Arun, P., Madhavarao, C.N. and Namboodiri, A.M., 2007. N-Acetylaspartate in the CNS: from neurodiagnostics to neurobiology. *Progress in Neurobiology,* 81 (2), 89-131.

Moreb, J.S., 2008. Aldehyde dehydrogenase as a marker for stem cells. *Current Stem Cell Research & Therapy,* 3 (4), 237-246.

Mountcastle, V.B., 1957. Modality and topographic properties of single neurons of cat's somatic sensory cortex. *Journal of Neurophysiology,* 20 (4), 408-434.

Musyanovych, A., Dausend, J., Dass, M., Walther, P., Mailänder, V. and Landfester, K., 2011. Criteria impacting the cellular uptake of nanoparticles: A study emphasizing polymer type and surfactant effects. *Acta Biomaterialia,* 7 (12), 4160-4168.

Myers, J.P., Santiago-Medina, M. and Gomez, T.M., 2011. Regulation of axonal outgrowth and pathfinding by integrin–ECM interactions. *Developmental Neurobiology,* 71 (11), 901-923.

Nakayama, H., Abe, M., Morimoto, C., Iida, T., Okabe, S., Sakimura, K. and Hashimoto, K., 2018. Microglia permit climbing fiber elimination by promoting GABAergic inhibition in the developing cerebellum. *Nature Communications,* 9 (1), 2830-018-05100-z.

Naso, M.F., Tomkowicz, B., Perry, W.L. and Strohl, W.R., 2017. Adeno-associated virus (AAV) as a vector for gene therapy. *Biodrugs,* 31 (4), 317-334.

Nasrabady, S.E., Rizvi, B., Goldman, J.E. and Brickman, A.M., 2018. White matter changes in Alzheimer's disease: a focus on myelin and oligodendrocytes. *Acta Neuropathologica Communications,* 6 (1), 22.

Nathanson, J.L., Yanagawa, Y., Obata, K. and Callaway, E.M., 2009. Preferential labeling of inhibitory and excitatory cortical neurons by endogenous tropism of adeno-associated virus and lentivirus vectors. *Neuroscience,* 161 (2), 441-450.

Nedergaard, M., Goldman, S.A., Desai, S. and Pulsinelli, W.A., 1991. Acid-induced death in neurons and glia. *The Journal of Neuroscience : The Official Journal of the Society for Neuroscience,* 11 (8), 2489-2497.

Neves, H.P., 2013. 1 - Materials for implantable systems. *In:* A. Inmann, and D. Hodgins, eds., *Implantable Sensor Systems for Medical Applications.* Woodhead Publishing, 2013, pp. 3-38.

Nho, Y., Kim, J.Y., Khang, D., Webster, T.J. and Lee, J.E., 2010. Adsorption of mesenchymal stem cells and cortical neural stem cells on carbon nanotube/polycarbonate urethane. *Nanomedicine,* 5 (3), 409-417.

Nisbet, D.R., Rodda, A.E., Horne, M.K., Forsythe, J.S. and Finkelstein, D.I., 2009. Neurite infiltration and cellular response to electrospun polycaprolactone scaffolds implanted into the brain. *Biomaterials,* 30 (27), 4573-4580.

Nisbet, D., Pattanawong, S., Ritchie, N., Shen, W., Finkelstein, D., Horne, M.K. and Forsythe, J.S., 2007. Interaction of embryonic cortical neurons on nanofibrous scaffolds for neural tissue engineering. *Journal of Neural Engineering,* 4 (2), 35.

Nisbet, D., Yu, L., Zahir, T., Forsythe, J.S. and Shoichet, M., 2008. Characterization of neural stem cells on electrospun poly (ε-caprolactone) submicron scaffolds: evaluating their potential in neural tissue engineering. *Journal of Biomaterials Science, Polymer Edition,* 19 (5), 623-634.

Nonnenmacher, M., and Weber, T., 2012. Intracellular transport of recombinant adeno-associated virus vectors. *Gene Therapy,* 19 (6), 649.

Noren, N.K., Liu, B.P., Burridge, K. and Kreft, B., 2000. p120 catenin regulates the actin cytoskeleton via Rho family GTPases. *The Journal of Cell Biology,* 150 (3), 567-580.

Nosonovsky, M., and Bhushan, B., 2005. Roughness optimization for biomimetic superhydrophobic surfaces. *Microsystem Technologies,* 11 (7), 535-549.

Nowicki, K.W., and Sekula Jr, R.F., 2018. Pericytes Protect White-Matter Structure and Function. *Neurosurgery,* 83 (3), E103-E104.

Oberlaender, M., Ramirez, A. and Bruno, R.M., 2012. Sensory experience restructures thalamocortical axons during adulthood. *Neuron,* 74 (4), 648-655.

O'Connor, S.M., Stenger, D.A., Shaffer, K.M. and Ma, W., 2001. Survival and neurite outgrowth of rat cortical neurons in three-dimensional agarose and collagen gel matrices. *Neuroscience Letters,* 304 (3), 189-193.

Oki, K., Tatarishvili, J., Wood, J., Koch, P., Wattananit, S., Mine, Y., Monni, E., Tornero, D., Ahlenius, H. and Ladewig, J., 2012. Human-induced pluripotent stem cells form functional neurons and improve recovery after grafting in stroke-damaged brain. *Stem Cells,* 30 (6), 1120-1133.

Ono, S., Baux, G., Sekiguchi, M., Fossier, P., Morel, N.F., Nihonmatsu, I., Hirata, K., Awaji, T., Takahashi, S. and Takahashi, M., 1998. Regulatory roles of complexins in neurotransmitter release from mature presynaptic nerve terminals. *European Journal of Neuroscience,* 10 (6), 2143-2152.

Orza, A., Soritau, O., Olenic, L., Diudea, M., Florea, A., Rus Ciuca, D., Mihu, C., Casciano, D. and Biris, A.S., 2011. Electrically conductive gold-coated collagen nanofibres for placental-derived mesenchymal stem cells enhanced differentiation and proliferation. *ACS Nano,* 5 (6), 4490-4503.

Oswald, M.C., Garnham, N., Sweeney, S.T. and Landgraf, M., 2018. Regulation of neuronal development and function by ROS. *FEBS Letters,* 592 (5), 679-691.

Ottoboni, L., Merlini, A. and Martino, G., 2017. Neural stem cell plasticity: advantages in therapy for the injured central nervous system. *Frontiers in Cell and Developmental Biology,* 5, 52.

Ovsianikov, A., Malinauskas, M., Schlie, S., Chichkov, B., Gittard, S., Narayan, R., Löbler, M., Sternberg, K., Schmitz, K. and Haverich, A., 2011. Three-dimensional laser micro-and nano-structuring of acrylated poly (ethylene glycol) materials and evaluation of their cytoxicity for tissue engineering applications. *Acta Biomaterialia,* 7 (3), 967-974.

Packer, A.M., Peterka, D.S., Hirtz, J.J., Prakash, R., Deisseroth, K. and Yuste, R., 2012. Two-photon optogenetics of dendritic spines and neural circuits. *Nature Methods,* 9 (12), 1202.

Panduranga Rao, K., 1996. Recent developments of collagen-based materials for medical applications and drug delivery systems. *Journal of Biomaterials Science, Polymer Edition,* 7 (7), 623-645.

Pang, X., and Panee, J., 2014. Roles of glutathione in antioxidant defense, inflammation, and neuron differentiation in the thalamus of HIV-1 transgenic rats. *Journal of Neuroimmune Pharmacology,* 9 (3), 413-423.

Panyam, J., and Labhasetwar, V., 2003. Biodegradable nanoparticles for drug and gene delivery to cells and tissue. *Advanced Drug Delivery Reviews,* 55 (3), 329-347.

Park, J., Yoo, J., Jeong, S., Choi, J., Lee, M., Lee, M., Hwa Lee, J., Kim, H.C., Jo, H. and Yu, D., 2011. Peroxiredoxin 2 deficiency exacerbates atherosclerosis in apolipoprotein E–deficient mice. *Circulation Research,* 109 (7), 739-749.

Park, K.I., Teng, Y.D. and Snyder, E.Y., 2002. The injured brain interacts reciprocally with neural stem cells supported by scaffolds to reconstitute lost tissue. *Nature Biotechnology,* 20 (11), 1111-1117.

Paşca, A.M., Sloan, S.A., Clarke, L.E., Tian, Y., Makinson, C.D., Huber, N., Kim, C.H., Park, J., O'rourke, N.A. and Nguyen, K.D., 2015. Functional cortical neurons and astrocytes from human pluripotent stem cells in 3D culture. *Nature Methods,* 12 (7), 671.

Pastuzyn, E.D., Day, C.E., Kearns, R.B., Kyrke-Smith, M., Taibi, A.V., McCormick, J., Yoder, N., Belnap, D.M., Erlendsson, S., Morado, D.R., Briggs, J.A.G., Feschotte, C. and Shepherd, J.D., 2018. The Neuronal Gene Arc Encodes a Repurposed Retrotransposon Gag Protein that Mediates Intercellular RNA Transfer. *Cell,* 172 (1), 275-288.e18.

Pathak, M.M., Nourse, J.L., Tran, T., Hwe, J., Arulmoli, J., Le, D.T., Bernardis, E., Flanagan, L.A. and Tombola, F., 2014. Stretch-activated ion channel Piezo1 directs lineage choice in human neural stem cells. *Proceedings of the National Academy of Sciences of the United States of America,* 111 (45), 16148-16153.

Pearce, J.M., 2009. Marie-Jean-Pierre Flourens (1794-1867) and cortical localization. *European Neurology,* 61 (5), 311-314.

Peković, S., Filipović, R., Šubašić, S., Lavrnja, I., Stojkov, D., Nedeljković, N., Rakić, L. and Stojiljković, M., 2005. Downregulation of glial scarring after brain injury: the effect of purine nucleoside analogue ribavirin. *Annals of the New York Academy of Sciences,* 1048 (1), 296-310.

Perin, R., Berger, T.K. and Markram, H., 2011. A synaptic organizing principle for cortical neuronal groups. *Proceedings of the National Academy of Sciences of the United States of America,* 108 (13), 5419-5424.

Peschanski, M., Cesaro, P. and Hantraye, P., 1995. Rationale for intrastriatal grafting of striatal neuroblasts in patients with Huntington's disease. *Neuroscience,* 68 (2), 273-285.

Peters, A., and Feldman, M.L., 1976. The projection of the lateral geniculate nucleus to area 17 of the rat cerebral cortex. I. General description. *Journal of Neurocytology,* 5 (1), 63-84.

Pettikiriarachchi, J.T., Parish, C.L., Shoichet, M.S., Forsythe, J.S. and Nisbet, D.R., 2010. Biomaterials for brain tissue engineering. *Australian Journal of Chemistry,* 63 (8), 1143-1154.

Pfrieger, F.W., and Ungerer, N., 2011. Cholesterol metabolism in neurons and astrocytes. *Progress in Lipid Research,* 50 (4), 357-371.

Philips, M., Vikeså, J., Luuk, H., Jønson, L., Lilleväli, K., Rehfeld, J.F., Vasar, E., Kõks, S. and Nielsen, F.C., 2009. Characterization of MYG1 gene and protein: subcellular distribution and function. *Biology of the Cell,* 101 (6), 361-377.

Pires, L.R., Rocha, D.N., Ambrosio, L. and Pêgo, A.P., 2014. Effect of surface topography on microglia-implications for central nervous tissue engineering. *Bridging the Lesion–Engineering a Permissive Substrate Towards Nerve Regeneration,* , 51.

Popiolek-Barczyk, K., and Mika, J., 2016. Targeting the microglial signaling pathways: new insights in the modulation of neuropathic pain. *Current Medicinal Chemistry,* 23 (26), 2908-2928.

Postler, E., Rimner, A., Beschorner, R., Schluesener, H. and Meyermann, R., 2000. Allograft-inflammatory-factor-1 is upregulated in microglial cells in human cerebral infarctions. *Journal of Neuroimmunology,* 104 (1), 85-91.

Pothayee, N., Maric, D., Sharer, K., Tao-Cheng, J., Calac, A., Bouraoud, N., Pickel, J., Dodd, S. and Koretsky, A., 2018. Neural precursor cells form integrated brain-like tissue when implanted into rat cerebrospinal fluid. *Communications Biology,* 1 (1), 114.

Prabhakaran, M.P., Ghasemi-Mobarakeh, L., Jin, G. and Ramakrishna, S., 2011. Electrospun conducting polymer nanofibres and electrical stimulation of nerve stem cells. *Journal of Bioscience and Bioengineering,* 112 (5), 501-507.

Purves, D., Augustine, G., Fitzpatrick, D., Katz, L., LaMantia, A., McNamara, J. and Williams, S., 2001. Neuroscience 2nd Edition. Sunderland (MA) Sinauer Associates.

Raizada, R.D., and Grossberg, S., 2003. Towards a theory of the laminar architecture of cerebral cortex: Computational clues from the visual system. *Cerebral Cortex,* 13 (1), 100-113.

Rajagopal, P., Duraiswamy, S., Sethuraman, S., Giridhara Rao, J. and Krishnan, U.M., 2018. Polymer-coated viral vectors: hybrid nanosystems for gene therapy. *The Journal of Gene Medicine,* 20 (4), e3011.

Ramsden, J., 2015. *Bioinformatics: an introduction.* Springer.

Ravi, M., Paramesh, V., Kaviya, S., Anuradha, E. and Solomon, F.P., 2015. 3D cell culture systems: advantages and applications. *Journal of Cellular Physiology,* 230 (1), 16-26.

Recknor, J.B., Sakaguchi, D.S. and Mallapragada, S.K., 2006. Microenvironmental Regulation of Neural Progenitor Cell Outgrowth and Differentiation. *Directed Growth and Selective Differentiation of Neural Progenitor Cells using a Synergistic Combination of Topographical and Soluble Cues,* 1050, 147.

Recknor, J.B., 2006. Directed growth and selective differentiation of neural progenitor cells using a synergistic combination of topographical and soluble cues.

Rees, C.L., Moradi, K. and Ascoli, G.A., 2017. Weighing the Evidence in Peters' Rule: Does Neuronal Morphology Predict Connectivity? *Trends in Neurosciences,* 40 (2), 63-71.

Riccomagno, M.M., and Kolodkin, A.L., 2015. Sculpting neural circuits by axon and dendrite pruning. *Annual Review of Cell and Developmental Biology,* 31, 779-805.

Rieckmann, A., Van Dijk, K.R.A., Sperling, R.A., Johnson, K.A., Buckner, R.L. and Hedden, T., 2016. Accelerated decline in white matter integrity in clinically normal individuals at risk for Alzheimer's disease. *Neurobiology of Aging,* 42, 177-188.

Riemann, A., Schneider, B., Ihling, A., Nowak, M., Sauvant, C., Thews, O. and Gekle, M., 2011. Acidic environment leads to ROS-induced MAPK signaling in cancer cells. *PloS One,* 6 (7), e22445.

Rivet, C.J., Zhou, K., Gilbert, R.J., Finkelstein, D.I. and Forsythe, J.S., 2015. Cell infiltration into a 3D electrospun fiber and hydrogel hybrid scaffold implanted in the brain. *Biomatter,* 5 (1), e1005527.

Rogers, S.L., Letourneau, P.C., Palm, S.L., McCarthy, J. and Furcht, L.T., 1983. Neurite extension by peripheral and central nervous system neurons in response to substratum-bound fibronectin and laminin. *Developmental Biology,* 98 (1), 212-220.

Rojas, A., Wetherington, J., Shaw, R., Serrano, G., Swanger, S. and Dingledine, R., 2013. Activation of group I metabotropic glutamate receptors potentiates heteromeric kainate receptors. *Molecular Pharmacology,* 83 (1), 106-121.

Roth, F.C., and Draguhn, A., 2012. GABA metabolism and transport: effects on synaptic efficacy. *Neural Plasticity,* 2012.

Rotty, J.D., Brighton, H.E., Craig, S.L., Asokan, S.B., Cheng, N., Ting, J.P. and Bear, J.E., 2017. Arp2/3 complex is required for macrophage integrin functions but is dispensable for FcR phagocytosis and in vivo motility. *Developmental Cell,* 42 (5), 498-513. e6.

Roy, N.S., Cleren, C., Singh, S.K., Yang, L., Beal, M.F. and Goldman, S.A., 2006. Functional engraftment of human ES cell–derived dopaminergic neurons enriched by coculture with telomerase-immortalized midbrain astrocytes. *Nature Medicine,* 12 (11), 1259.

Royo, N.C., Vandenberghe, L.H., Ma, J., Hauspurg, A., Yu, L., Maronski, M., Johnston, J., Dichter, M.A., Wilson, J.M. and Watson, D.J., 2008. Specific AAV serotypes stably transduce primary hippocampal and cortical cultures with high efficiency and low toxicity. *Brain Research,* 1190, 15-22.

Royo-Gascon, N., Wininger, M., Scheinbeim, J.I., Firestein, B.L. and Craelius, W., 2013. Piezoelectric substrates promote neurite growth in rat spinal cord neurons. *Annals of Biomedical Engineering,* 41 (1), 112-122.

Ruardy, T.G., Moorlag, H.E., Schakenraad, J.M., Van Der Mei, H.C. and Busscher, H.J., 1997. Growth of Fibroblasts and Endothelial Cells on Wettability Gradient Surfaces. *Journal of Colloid and Interface Science,* 188 (1), 209-217.

Russo, I., 2019. The role of LRRK2 on PKA-NFkappaB pathway in microglia cells: implications for Parkinson's disease. *Neural Regeneration Research,* 14 (10), 1713-1714.

Rustenhoven, J., Jansson, D., Smyth, L.C. and Dragunow, M., 2017. Brain Pericytes As Mediators of Neuroinflammation. *Trends in Pharmacological Sciences,* 38 (3), 291-304.

Saha, K., Keung, A.J., Irwin, E.F., Li, Y., Little, L., Schaffer, D.V. and Healy, K.E., 2008. Substrate modulus directs neural stem cell behavior. *Biophysical Journal,* 95 (9), 4426-4438.

Sakuma, R., Kawahara, M., Nakano-Doi, A., Takahashi, A., Tanaka, Y., Narita, A., Kuwahara-Otani, S., Hayakawa, T., Yagi, H. and Matsuyama, T., 2016. Brain pericytes serve as microglia-generating multipotent vascular stem cells following ischemic stroke. *Journal of Neuroinflammation,* 13 (1), 57.

Santoro, M., Shah, S.R., Walker, J.L. and Mikos, A.G., 2016. Poly(lactic acid) nanofibrous scaffolds for tissue engineering. *Advanced Drug Delivery Reviews,* 107, 206-212.

Sanz, R., Ferraro, G.B. and Fournier, A.E., 2015. IgLON cell adhesion molecules are shed from the cell surface of cortical neurons to promote neuronal growth. *The Journal of Biological Chemistry,* 290 (7), 4330-4342.

Satoh, J., Kino, Y., Asahina, N., Takitani, M., Miyoshi, J., Ishida, T. and Saito, Y., 2016. TMEM119 marks a subset of microglia in the human brain. *Neuropathology,* 36 (1), 39-49.

Schaub, N.J., Le Beux, C., Miao, J., Linhardt, R.J., Alauzun, J.G., Laurencin, D. and Gilbert, R.J., 2015. The effect of surface modification of aligned poly-l-lactic acid electrospun fibers on fiber degradation and neurite extension. *PLoS One,* 10 (9), e0136780.

Scholz, J., Klein, M.C., Behrens, T.E. and Johansen-Berg, H., 2009. Training induces changes in white-matter architecture. *Nature Neuroscience,* 12 (11), 1370.

Schultz, C., Mühleisen, T., Nenadic, I., Koch, K., Wagner, G., Schachtzabel, C., Siedek, F., Nöthen, M., Rietschel, M. and Deufel, T., 2014. Common variation in NCAN, a risk factor for bipolar disorder and schizophrenia, influences local cortical folding in schizophrenia. *Psychological Medicine,* 44 (4), 811-820.

Seddiki, R., Narayana, Gautham Hari Narayana Sankara, Strale, P., Balcioglu, H.E., Peyret, G., Yao, M., Le, A.P., Teck Lim, C., Yan, J. and Ladoux, B., 2018. Force-dependent binding of vinculin to α-catenin regulates cell–cell contact stability and collective cell behavior. *Molecular Biology of the Cell,* 29 (4), 380-388.

Seddiki, R., Narayana, Gautham Hari Narayana Sankara, Strale, P., Balcioglu, H.E., Peyret, G., Yao, M., Le, A.P., Teck Lim, C., Yan, J. and Ladoux, B., 2018. Force-dependent binding of vinculin to α-catenin regulates cell–cell contact stability and collective cell behavior. *Molecular Biology of the Cell,* 29 (4), 380-388.

Segev, R., Benveniste, M., Shapira, Y. and Ben-Jacob, E., 2003. Formation of electrically active clusterized neural networks. *Physical Review Letters,* 90 (16), 168101.

Semple, B.D., Blomgren, K., Gimlin, K., Ferriero, D.M. and Noble-Haeusslein, L.J., 2013. Brain development in rodents and humans: Identifying benchmarks of maturation and vulnerability to injury across species. *Progress in Neurobiology,* 106, 1-16.

Seong, S., and Matzinger, P., 2004. Hydrophobicity: an ancient damage-associated molecular pattern that initiates innate immune responses. *Nature Reviews Immunology,* 4 (6), 469.

Serruya, M.D., Harris, J.P., Adewole, D.O., Struzyna, L.A., Burrell, J.C., Nemes, A., Petrov, D., Kraft, R.H., Chen, H.I. and Wolf, J.A., 2017. Engineered Axonal Tracts as "Living Electrodes" for Synaptic-Based Modulation of Neural Circuitry. *Advanced Functional Materials,* .

Shah, R.R., 2018. *Human Neuronal LUHMES Cell Line as a Model System for Studying Rett Syndrome,* .

Shamseldin, H.E., Bennett, A.H., Alfadhel, M., Gupta, V. and Alkuraya, F.S., 2016. GOLGA2, encoding a master regulator of golgi apparatus, is mutated in a patient with a neuromuscular disorder. *Human Genetics,* 135 (2), 245-251.

Shih, R., Wang, C. and Yang, C., 2015. NF-kappaB signaling pathways in neurological inflammation: a mini review. *Frontiers in Molecular Neuroscience,* 8, 77.

Shima, Y., Kawaguchi, S., Kosaka, K., Nakayama, M., Hoshino, M., Nabeshima, Y., Hirano, T. and Uemura, T., 2007. Opposing roles in neurite growth control by two seven-pass transmembrane cadherins. *Nature Neuroscience,* 10 (8), 963.

Shparberg, R.A., 2017. L-proline-mediated neural differentiation of mouse embryonic stem cells.

Silver, J., Schwab, M.E. and Popovich, P.G., 2014. Central nervous system regenerative failure: role of oligodendrocytes, astrocytes, and microglia. *Cold Spring Harbor Perspectives in Biology,* 7 (3), a020602.

Singh, S., and Solecki, D.J., 2015. Polarity transitions during neurogenesis and germinal zone exit in the developing central nervous system. *Frontiers in Cellular Neuroscience,* 9, 62.

Slepička, P., Michaljaničová, I., Sajdl, P., Fitl, P. and Švorčík, V., 2013. Surface ablation of PLLA induced by KrF excimer laser. *Applied Surface Science,* 283, 438-444.

Sohal, H.S., Vassilevski, K., Jackson, A., Baker, S.N. and O'Neill, A., 2016. Design and Microfabrication considerations for reliable Flexible intracortical implants. *Frontiers in Mechanical Engineering,* 2, 5.

Son, J.H., Shim, J.H., Kim, K., Ha, J. and Han, J.Y., 2012. Neuronal autophagy and neurodegenerative diseases. *Experimental & Molecular Medicine,* 44 (2), 89.

Son, W.K., Youk, J.H. and Park, W.H., 2006. Antimicrobial cellulose acetate nanofibres containing silver nanoparticles. *Carbohydrate Polymers,* 65 (4), 430-434.

Sortwell, C.E., Pitzer, M.R. and Collier, T.J., 2000. Time course of apoptotic cell death within mesencephalic cell suspension grafts: implications for improving grafted dopamine neuron survival. *Experimental Neurology,* 165 (2), 268-277.

Spencer, K.C., Sy, J.C., Ramadi, K.B., Graybiel, A.M., Langer, R. and Cima, M.J., 2017. Characterization of mechanically matched hydrogel coatings to improve the biocompatibility of neural implants. *Scientific Reports,* 7 (1), 1952.

Sridharan, A., Nguyen, J.K., Capadona, J.R. and Muthuswamy, J., 2015. Compliant intracortical implants reduce strains and strain rates in brain tissue in vivo. *Journal of Neural Engineering,* 12 (3), 036002.

Stahnke, S., Lux, K., Uhrig, S., Kreppel, F., Hösel, M., Coutelle, O., Ogris, M., Hallek, M. and Büning, H., 2011. Intrinsic phospholipase A2 activity of adeno-associated virus is involved in endosomal escape of incoming particles. *Virology,* 409 (1), 77-83.

Stapor, P.C., Sweat, R.S., Dashti, D.C., Betancourt, A.M. and Murfee, W.L., 2014. Pericyte dynamics during angiogenesis: new insights from new identities. *Journal of Vascular Research,* 51 (3), 163-174.

Steel, E.M., and Sundararaghavan, H.G., 2016. Electrically Conductive Materials for Nerve Regeneration. *In:* Electrically Conductive Materials for Nerve Regeneration. *Neural Engineering.* Springer, 2016, pp. 145-179.

Stefen, H., Chaichim, C., Power, J. and Fath, T., 2016. Regulation of the postsynaptic compartment of excitatory synapses by the actin cytoskeleton in health and its disruption in disease. *Neural Plasticity,* 2016.

Steinbeck, J., Choi, S., Mrejeru, A., Ganat, Y., Deisseroth, K., Sulzer, D., Mosharov, E. and Studer, L., 2015. Optogenetics enables functional analysis of human embryonic stem cell-derived grafts in a Parkinson's disease model. *Nature Biotechnology,* 33 (2), 204-209.

Steinbeck, J.A., Koch, P., Derouiche, A. and Brüstle, O., 2012. Human embryonic stem cell-derived neurons establish region-specific, long-range projections in the adult brain. *Cellular and Molecular Life Sciences,* 69 (3), 461-470.

STEMCELL Technologies, 2017. *NeuroCult™ Neuronal Basal Medium and NeuroCult™ SM1 Neuronal Supplement* [online]. STEMCELL Technologies. Available at: https://cdn.stemcell.com/media/files/pis/29918-PIS_2_7_0.pdf [Accessed 12/19 2017].

Stevenson, G., Moulton, S.E., Innis, P.C. and Wallace, G.G., 2010. Polyterthiophene as an electrostimulated controlled drug release material of therapeutic levels of dexamethasone. *Synthetic Metals,* 160 (9–10), 1107-1114.

Stichel, C.C., Hermanns, S., Luhmann, H.J., Lausberg, F., Niermann, H., D'urso, D., Servos, G., Hartwig, H. and Müller, H.W., 1999. Inhibition of collagen IV deposition promotes regeneration of injured CNS axons. *European Journal of Neuroscience,* 11 (2), 632-646.

Storchel, P.H., Thummler, J., Siegel, G., Aksoy-Aksel, A., Zampa, F., Sumer, S. and Schratt, G., 2015. A large-scale functional screen identifies Nova1 and Ncoa3 as regulators of neuronal miRNA function. *The EMBO Journal,* 34 (17), 2237-2254.

Stout, D.A., and Webster, T.J., 2012. Carbon nanotubes for stem cell control. *Materials Today,* 15 (7–8), 312-318.

Struzyna, L.A., Adewole, D.O., Gordián-Vélez, W.J., Grovola, M.R., Burrell, J.C., Katiyar, K.S., Petrov, D., Harris, J.P. and Cullen, D.K., 2017. Anatomically Inspired Three-dimensional Micro-tissue Engineered Neural Networks for Nervous System Reconstruction, Modulation, and Modeling. *JoVE (Journal of Visualized Experiments),* (123), e55609-e55609.

Struzyna, L.A., Browne, K.D., Brodnik, Z.D., Burrell, J.C., Harris, J.P., Isaac Chen, H., Wolf, J.A., Panzer, K.V., Lim, J. and Duda, J.E., 2018. Tissue engineered nigrostriatal pathway for treatment of Parkinson's disease. *Journal of Tissue Engineering and Regenerative Medicine,* 12, 1702-1706.

Struzyna, L.A., Wolf, J.A., Mietus, C.J., Adewole, D.O., Chen, H.I., Smith, D.H. and Cullen, D.K., 2015. Rebuilding brain circuitry with living micro-tissue engineered neural networks. *Tissue Engineering Part A,* 21 (21-22), 2744-2756.

Su, C., Menuz, K., Reisert, J. and Carlson, J.R., 2012. Non-synaptic inhibition between grouped neurons in an olfactory circuit. *Nature,* 492 (7427), 66.

Sun, S., Li, H., Chen, J. and Qian, Q., 2017. Lactic acid: no longer an inert and end-product of glycolysis. *Physiology,* 32 (6), 453-463.

Sun, L., Xie, P., Wada, J., Kashihara, N., Liu, F.Y., Zhao, Y., Kumar, D., Chugh, S.S., Danesh, F.R. and Kanwar, Y.S., 2008. Rap1b GTPase ameliorates glucose-induced mitochondrial dysfunction. *Journal of the American Society of Nephrology : JASN,* 19 (12), 2293-2301.

Sung, S., Min, S.H., Cho, K.Y., Lee, S., Min, Y., Yeom, Y.I. and Park, J., 2003. Effect of polyethylene glycol on gene delivery of polyethylenimine. *Biological and Pharmaceutical Bulletin,* 26 (4), 492-500.

Swanson, L.W., and Lichtman, J.W., 2016. From Cajal to connectome and beyond. *Annual Review of Neuroscience,* 39, 197-216.

Szmydynger-Chodobska, J., Zink, B.J. and Chodobski, A., 2011. Multiple sites of vasopressin synthesis in the injured brain. *Journal of Cerebral Blood Flow & Metabolism,* 31 (1), 47-51.

Tai, H., Besche, H., Goldberg, A.L. and Schuman, E.M., 2010. Characterization of the brain 26S proteasome and its interacting proteins. *Frontiers in Molecular Neuroscience,* 3, 12.

Takenaka, K., Fukami, K., Otsuki, M., Nakamura, Y., Kataoka, Y., Wada, M., Tsuji, K., Nishikawa, S., Yoshida, N. and Takenawa, T., 2003. Role of phospholipase C-L2, a novel phospholipase C-like protein that lacks lipase activity, in B-cell receptor signaling. *Molecular and Cellular Biology,* 23 (20), 7329-7338.

Tamaki, S., Eckart, K., Dongping, H., Sutton, R., Doshe, M., Jain, G., Tushinski, R., Reitsma, M., Harris, B., Tsukamoto, A., Gage, F., Weissman, I. and Uchida, N., 2002. Engraftment of sorted/expanded human central nervous system stem cells from fetal brain. *Journal of Neuroscience Research,* 69, 976-986.

Tan, E., and Lim, C., 2005. Nanoindentation study of nanofibres. *Applied Physics Letters,* 87 (12), 123106.

Tan, E., and Lim, C., 2004. Physical properties of a single polymeric nanofiber. *Applied Physics Letters,* 84 (9), 1603-1605.

Tang, X.Q., Heron, P., Mashburn, C. and Smith, G.M., 2007. Targeting sensory axon regeneration in adult spinal cord. *The Journal of Neuroscience : The Official Journal of the Society for Neuroscience,* 27 (22), 6068-6078.

Tang-Schomer, M.D., Hu, X., Hronik-Tupaj, M., Tien, L.W., Whalen, M.J., Omenetto, F.G. and Kaplan, D.L., 2014. Film-Based Implants for Supporting Neuron–Electrode Integrated Interfaces for The Brain. *Advanced Functional Materials,* 24 (13), 1938-1948.

Tang-Schomer, M.D., White, J.D., Tien, L.W., Schmitt, L.I., Valentin, T.M., Graziano, D.J., Hopkins, A.M., Omenetto, F.G., Haydon, P.G. and Kaplan, D.L., 2014. Bioengineered functional brain-like cortical tissue. *Proceedings of the National Academy of Sciences of the United States of America,* 111 (38), 13811-13816.

Teschemacher, A., Gourine, A. and Kasparov, S., 2015. A role for astrocytes in sensing the brain microenvironment and neuro-metabolic integration. *Neurochemical Research,* 40 (12), 2386-2393.

Thakur, R., Florek, C., Kohn, J. and Michniak, B., 2008. Electrospun nanofibrous polymeric scaffold with targeted drug release profiles for potential application as wound dressing. *International Journal of Pharmaceutics,* 364 (1), 87-93.

Thei, L., Imm, J., Kaisis, E., Dallas, M.L. and Kerrigan, T.L., 2018. Microglia in alzheimer's disease: a role for ion channels. *Front.Neurosci,* 12 (676), 10.3389.

Thievessen, I., Fakhri, N., Steinwachs, J., Kraus, V., McIsaac, R.S., Gao, L., Chen, B., Baird, M.A., Davidson, M.W. and Betzig, E., 2015. Vinculin is required for cell polarization, migration, and extracellular matrix remodeling in 3D collagen. *The FASEB Journal,* 29 (11), 4555-4567.

Thompson, L.H., and Björklund, A., 2015. Reconstruction of brain circuitry by neural transplants generated from pluripotent stem cells. *Neurobiology of Disease,* 79, 28-40.

Tischer, D., and Weiner, O.D., 2014. Illuminating cell signalling with optogenetic tools. *Nature Reviews Molecular Cell Biology,* 15 (8), 551.

Tong, D.L., Boocock, D.J., Dhondalay, G.K.R., Lemetre, C. and Ball, G.R., 2014. Artificial neural network inference (ANNI): a study on gene-gene interaction for biomarkers in childhood sarcomas. *PloS One,* 9 (7), e102483.

Tornero, D., Wattananit, S., Grønning Madsen, M., Koch, P., Wood, J., Tatarishvili, J., Mine, Y., Ge, R., Monni, E. and Devaraju, K., 2013. Human induced pluripotent stem cell-derived cortical neurons integrate in stroke-injured cortex and improve functional recovery. *Brain,* 136 (12), 3561-3577.

Tortosa, E., Montenegro-Venegas, C., Benoist, M., Härtel, S., González-Billault, C., Esteban, J.A. and Avila, J., 2011. Microtubule-associated protein 1B (MAP1B) is required for dendritic spine development and synaptic maturation. *Journal of Biological Chemistry,* 286 (47), 40638-40648.

Traub, R.D., Whittington, M.A., Gutiérrez, R. and Draguhn, A., 2018. Electrical coupling between hippocampal neurons: contrasting roles of principal cell gap junctions and interneuron gap junctions. *Cell and Tissue Research,* , 1-21.

Triyoso, D.H., and Good, T.A., 1999. Pulsatile shear stress leads to DNA fragmentation in human SH-SY5Y neuroblastoma cell line. *The Journal of Physiology,* 515 (2), 355-365.

Tseng, Y., Kao, Y., Liao, J., Chen, W. and Liu, S., 2013. Biodegradable drug-eluting poly [lactic-co-glycol acid] nanofibres for the sustainable delivery of vancomycin to brain tissue: in vitro and in vivo studies. *ACS Chemical Neuroscience,* 4 (9), 1314-1321.

Tseng, Y., Wang, Y., Su, C. and Liu, S., 2015. Biodegradable vancomycin-eluting poly [(d, l)-lactide-co-glycolide] nanofibres for the treatment of postoperative central nervous system infection. *Scientific Reports,* 5, 7849.

Tseng, Y., Wang, Y., Su, C., Yang, T., Chang, T., Kau, Y. and Liu, S., 2015. Concurrent delivery of carmustine, irinotecan, and cisplatin to the cerebral cavity using biodegradable nanofibres: In vitro and in vivo studies. *Colloids and Surfaces B: Biointerfaces,* 134, 254-261.

Tymanskyj, S.R., Scales, T.M. and Gordon-Weeks, P.R., 2012. MAP1B enhances microtubule assembly rates and axon extension rates in developing neurons. *Molecular and Cellular Neuroscience,* 49 (2), 110-119.

Vaidya, A.R., Pujara, M.S., Petrides, M., Murray, E.A. and Fellows, L.K., 2019. Lesion studies in contemporary neuroscience. *Trends in Cognitive Sciences.*

Valamehr, B., Jonas, S.J., Polleux, J., Qiao, R., Guo, S., Gschweng, E.H., Stiles, B., Kam, K., Luo, T.J., Witte, O.N., Liu, X., Dunn, B. and Wu, H., 2008. Hydrophobic surfaces for enhanced differentiation of embryonic stem cell-derived embryoid bodies. *Proceedings of the National Academy of Sciences of the United States of America,* 105 (38), 14459-14464.

van Gemert, M.J., and Welch, A., 1989. Clinical use of laser-tissue interactions. *IEEE Engineering in Medicine and Biology Magazine,* 8 (4), 10-13.

Van Hée, V.F., Pérez-Escuredo, J., Cacace, A., Copetti, T. and Sonveaux, P., 2015. Lactate does not activate NF-κB in oxidative tumor cells. *Frontiers in Pharmacology,* 6, 228.

van Ooyen, A., Carnell, A., de Ridder, S., Tarigan, B., Mansvelder, H.D., Bijma, F., de Gunst, M. and van Pelt, J., 2014. Independently outgrowing neurons and geometry-based synapse formation produce networks with realistic synaptic connectivity. *PloS One,* 9 (1), e85858.

Vaysse, L., Beduer, A., Sol, J.C., Vieu, C. and Loubinoux, I., 2015. Micropatterned bioimplant with guided neuronal cells to promote tissue reconstruction and improve functional recovery after primary motor cortex insult. *Biomaterials,* 58, 46-53.

Vidal, M., Maniglier, M., Deboux, C., Bachelin, C., Zujovic, V. and Baron-Van Evercooren, A., 2015. Adult DRG stem/progenitor cells generate pericytes in the presence of central nervous system (CNS) developmental cues, and Schwann cells in response to CNS demyelination. *Stem Cells,* 33 (6), 2011-2024.

Vogel, C., and Marcotte, E.M., 2012. Insights into the regulation of protein abundance from proteomic and transcriptomic analyses. *Nature Reviews Genetics,* 13 (4), 227.

Walker, F.R., Beynon, S.B., Jones, K.A., Zhao, Z., Kongsui, R., Cairns, M. and Nilsson, M., 2014. Dynamic structural remodelling of microglia in health and disease: A review of the models, the signals and the mechanisms. *Brain, Behavior, and Immunity,* 37, 1-14.

Wang, T., Forsythe, J.S., Nisbet, D.R. and Parish, C.L., 2012. Promoting engraftment of transplanted neural stem cells/progenitors using biofunctionalised electrospun scaffolds. *Biomaterials,* 33 (36), 9188-9197.

Wang, X., Kluge, J.A., Leisk, G.G. and Kaplan, D.L., 2008. Sonication-induced gelation of silk fibroin for cell encapsulation. *Biomaterials,* 29 (8), 1054-1064.

Wang, T., Bruggeman, K.F., Kauhausen, J.A., Rodriguez, A.L., Nisbet, D.R. and Parish, C.L., 2016. Functionalized composite scaffolds improve the engraftment of transplanted dopaminergic progenitors in a mouse model of Parkinson's disease. *Biomaterials,* 74, 89-98.

Wanner, I.B., Anderson, M.A., Song, B., Levine, J., Fernandez, A., Gray-Thompson, Z., Ao, Y. and Sofroniew, M.V., 2013. Glial scar borders are formed by newly proliferated, elongated astrocytes that interact to corral inflammatory and fibrotic cells via STAT3-dependent mechanisms after spinal cord injury. *The Journal of Neuroscience : The Official Journal of the Society for Neuroscience,* 33 (31), 12870-12886.

Waterham, H.R., Koster, J., van Roermund, C.W., Mooyer, P.A., Wanders, R.J. and Leonard, J.V., 2007. A lethal defect of mitochondrial and peroxisomal fission. *New England Journal of Medicine,* 356 (17), 1736-1741.

Weber, G.F., Bjerke, M.A. and DeSimone, D.W., 2011. Integrins and cadherins join forces to form adhesive networks. *Journal of Cell Science,* 124 (Pt 8), 1183-1193.

Webster, T.J., 2010. *Nanotechnology enabled in situ sensors for monitoring health.* Springer Science & Business Media.

Weerakkody, T., 2014. Cellular and circuit level responses to neural stem cell transplantation in the rodent cortex.

Weerakkody, T.N., Patel, T.P., Yue, C., Takano, H., Anderson, H.C., Meaney, D.F., Coulter, D.A. and Wolfe, J.H., 2013. Engraftment of nonintegrating neural stem cells differentially perturbs cortical activity in a dose-dependent manner. *Molecular Therapy,* 21 (12), 2258-2267.

Wei, W., Sethuraman, A., Jin12, C., Monteiro-Riviere24, N. and Narayan12, R., 2007. Biological Properties of Carbon Nanotubes. *Nanoscience and Nanotechnology,* 7, 1-14.

Weimer, J.M., Yokota, Y., Stanco, A., Stumpo, D.J., Blackshear, P.J. and Anton, E.S., 2009. MARCKS modulates radial progenitor placement, proliferation and organization in the developing cerebral cortex. *Development (Cambridge, England),* 136 (17), 2965-2975.

Weir, N., Buchanan, F., Orr, J. and Dickson, G., 2004. Degradation of poly-L-lactide. Part 1: in vitro and in vivo physiological temperature degradation. *Proceedings of the Institution of Mechanical Engineers, Part H: Journal of Engineering in Medicine,* 218 (5), 307-319.

Weiss, P., 1934. In vitro experiments on the factors determining the course of the outgrowing nerve fiber. *Journal of Experimental Zoology Part A: Ecological Genetics and Physiology,* 68 (3), 393-448.

Wernig, M., Zhao, J.P., Pruszak, J., Hedlund, E., Fu, D., Soldner, F., Broccoli, V., Constantine-Paton, M., Isacson, O. and Jaenisch, R., 2008. Neurons derived from reprogrammed fibroblasts functionally integrate into the fetal brain and improve symptoms of rats with Parkinson's disease. *Proceedings of the National Academy of Sciences of the United States of America,* 105 (15), 5856-5861.

West, A.E., and Greenberg, M.E., 2011. Neuronal activity-regulated gene transcription in synapse development and cognitive function. *Cold Spring Harbor Perspectives in Biology,* 3 (6), 10.1101/cshperspect.a005744.

White, M., Whittaker, R., Gandara, C. and Stoll, E.A., 2017. A guide to approaching regulatory considerations for lentiviral-mediated gene therapies. *Human Gene Therapy Methods,* 28 (4), 163-176.

Willerth, S.M., and Sakiyama-Elbert, S.E., 2007. Approaches to neural tissue engineering using scaffolds for drug delivery. *Advanced Drug Delivery Reviews,* 59 (4), 325-338.

Woerly, S., Doan, V.D., Sosa, N., de Vellis, J. and Espinosa-Jeffrey, A., 2004. Prevention of gliotic scar formation by NeuroGel™ allows partial endogenous repair of transected cat spinal cord. *Journal of Neuroscience Research,* 75 (2), 262-272.

Wu, F., Tien, L.W., Chen, F., Berke, J.D., Kaplan, D.L. and Yoon, E., 2015. Silk-backed structural optimization of high-density flexible intracortical neural probes. *Journal of Microelectromechanical Systems,* 24 (1), 62-69.

Wu, Q., Sun, X., Yue, W., Lu, T., Ruan, Y., Chen, T. and Zhang, D., 2016. RAB18, a protein associated with Warburg Micro syndrome, controls neuronal migration in the developing cerebral cortex. *Molecular Brain,* 9 (1), 19.

Wu, Q., Sun, X., Yue, W., Lu, T., Ruan, Y., Chen, T. and Zhang, D., 2016. RAB18, a protein associated with Warburg Micro syndrome, controls neuronal migration in the developing cerebral cortex. *Molecular Brain,* 9 (1), 19.

Xiao, P.J., and Samulski, R.J., 2012. Cytoplasmic trafficking, endosomal escape, and perinuclear accumulation of adeno-associated virus type 2 particles are facilitated by microtubule network. *Journal of Virology,* 86 (19), 10462-10473.

Xie, Y., Yang, S. and Kniss, D.A., 2001. Three-dimensional cell-scaffold constructs promote efficient gene transfection: implications for cell-based gene therapy. *Tissue Engineering,* 7 (5), 585-598.

Xin, Y., Li, Z., Zheng, H., Ho, J., Chan, M.T. and Wu, W.K., 2017. Neuro-oncological ventral antigen 1 (NOVA 1): Implications in neurological diseases and cancers. *Cell Proliferation,* 50 (4), e12348.

Xu, X.M., Guénard, V., Kleitman, N. and Bunge, M.B., 1995. Axonal regeneration into Schwann cell-seeded guidance channels grafted into transected adult rat spinal cord. *Journal of Comparative Neurology,* 351 (1), 145-160.

y Cajal, S.R., 1888. *Estructura de los centros nerviosos de las aves.*

Yaguchi, K., Nishimura-Akiyoshi, S., Kuroki, S., Onodera, T. and Itohara, S., 2014. Identification of transcriptional regulatory elements for Ntng1 and Ntng2 genes in mice. *Molecular Brain,* 7 (1), 19.

Yamada, J., Sawada, M. and Nakanishi, H., 2006. Cell cycle-dependent regulation of kainate-induced inward currents in microglia. *Biochemical and Biophysical Research Communications,* 349 (3), 913-919.

Yamada, M., and Sekiguchi, K., 2015. Chapter Six - Molecular Basis of Laminin–Integrin Interactions. *Current Topics in Membranes,* 76, 197-229.

Yamagishi, S., Yamada, K., Sawada, M., Nakano, S., Mori, N., Sawamoto, K. and Sato, K., 2015. Netrin-5 is highly expressed in neurogenic regions of the adult brain. *Frontiers in Cellular Neuroscience,* 9, 146.

Yang, C., Tibbitt, M.W., Basta, L. and Anseth, K.S., 2014. Mechanical memory and dosing influence stem cell fate. *Nature Materials,* 13 (6), 645.

Yang, J., Oza, J., Bridges, K., Chen, K.Y. and Liu, A.Y., 2008. Neural differentiation and the attenuated heat shock response. *Brain Research,* 1203, 39-50.

Yang, Z., Liu, Z., Allaker, R., Reip, P., Oxford, J., Ahmad, Z. and Ren, G., 2010. A review of nanoparticle functionality and toxicity on the central nervous system. *Journal of the Royal Society Interface,* 7 (suppl_4), S411-S422.

Yang, C., Tibbitt, M.W., Basta, L. and Anseth, K.S., 2014. Mechanical memory and dosing influence stem cell fate. *Nature Materials,* 13 (6), 645-652.

Yang, F., Murugan, R., Wang, S. and Ramakrishna, S., 2005. Electrospinning of nano/micro scale poly(l-lactic acid) aligned fibers and their potential in neural tissue engineering. *Biomaterials,* 26 (15), 2603-2610.

Yao, L., O'Brien, N., Windebank, A. and Pandit, A., 2009. Orienting neurite growth in electrospun fibrous neural conduits. *Journal of Biomedical Materials Research Part B: Applied Biomaterials,* 90 (2), 483-491.

Yata, T., Nishikawa, M., Nishizaki, C., Oku, M., Yurimoto, H., Sakai, Y. and Takakura, Y., 2009. Control of hypoxia-induced tumor cell adhesion by cytophilic human catalase. *Free Radical Biology and Medicine,* 47 (12), 1772-1778.

Ye, J., Das, S., Roy, A., Wei, W., Huang, H., Lorenz-Guertin, J.M., Xu, Q., Jacob, T.C., Wang, B. and Sun, D., 2019. Ischemic injury-induced CaMKIIδ and CaMKIIγ confer neuroprotection through the NF-κB signaling pathway. *Molecular Neurobiology,* 56 (3), 2123-2136.

Yin, Z., Chen, X., Chen, J.L., Shen, W.L., Nguyen, T.M.H., Gao, L. and Ouyang, H.W., 2010. The regulation of tendon stem cell differentiation by the alignment of nanofibres. *Biomaterials,* 31 (8), 2163-2175.

Yip, P.K., Wong, L., Sears, T.A., Yáñez-Muñoz, R.J. and McMahon, S.B., 2010. Cortical overexpression of neuronal calcium sensor-1 induces functional plasticity in spinal cord following unilateral pyramidal tract injury in rat. *PLoS Biol,* 8 (6), e1000399.

Yoon, S.D., Kwon, Y.S. and Lee, K.S., 2017. Biodegradation and Biocompatibility of Poly L-lactic Acid Implantable Mesh. *International Neurourology Journal,* 21 (Suppl 1), S48-54.

Zeisberg, M., and Neilson, E.G., 2009. Biomarkers for epithelial-mesenchymal transitions. *The Journal of Clinical Investigation,* 119 (6), 1429-1437.

Zeisel, A., Munoz-Manchado, A.B., Codeluppi, S., Lonnerberg, P., La Manno, G., Jureus, A., Marques, S., Munguba, H., He, L., Betsholtz, C., Rolny, C., Castelo-Branco, G., Hjerling-Leffler, J. and Linnarsson, S., 2015. Brain structure. Cell types in the mouse cortex and hippocampus revealed by single-cell RNA-seq. *Science (New York, N.Y.),* 347 (6226), 1138-1142.

Zhan, M., Zhao, H. and Han, Z.C., 2004. Signalling mechanisms of anoikis. *Histology and Histopathology,* 19 (3), 973-983.

Zhang, L., Stauffer, W.R., Jane, E.P., Sammak, P.J. and Cui, X.T., 2010. Enhanced differentiation of embryonic and neural stem cells to neuronal fates on laminin peptides doped polypyrrole. *Macromolecular Bioscience,* 10 (12), 1456-1464.

Zhang, P., Ma, X., Song, E., Chen, W., Pang, H., Ni, D., Gao, Y., Fan, Y., Ding, Q. and Zhang, Y., 2013. Tubulin cofactor A functions as a novel positive regulator of ccRCC progression, invasion and metastasis. *International Journal of Cancer,* 133 (12), 2801-2811.

Zhang, Y., Chen, Y., Wu, J., Manaenko, A., Yang, P., Tang, J., Fu, W. and Zhang, J.H., 2015. Activation of dopamine D2 receptor suppresses neuroinflammation through αB-crystalline by inhibition of NF-κB nuclear translocation in experimental ICH mice model. *Stroke,* 46 (9), 2637-2646.

Zhang, Y., Qin, N., Diao, Y., Guan, Y., Fan, L., Crair, M.C. and Zhang, J., 2012. Optogenetic tools for in vivo applications in neonatal mice. *In: SPIE Nanosystems in Engineering Medicine,* International Society for Optics and Photonics, pp. 854842-854842-9.

Zhang, Y.Z., Su, B., Venugopal, J., Ramakrishna, S. and Lim, C.T., 2007. Biomimetic and bioactive nanofibrous scaffolds from electrospun composite nanofibres. *International Journal of Nanomedicine,* 2 (4), 623-638.

Zheng, X., Boyer, L., Jin, M., Mertens, J., Kim, Y., Ma, L., Hamm, M., Gage, F.H. and Hunter, T., 2016. Metabolic reprogramming during neuronal differentiation from aerobic glycolysis to neuronal oxidative phosphorylation. *Elife,* 5, e13374.

Zhong, J., Chan, A., Morad, L., Kornblum, H.I., Fan, G. and Carmichael, S.T., 2010. Hydrogel matrix to support stem cell survival after brain transplantation in stroke. *Neurorehabilitation and Neural Repair,* 24 (7), 636-644.

Zhu, Y., Murali, S., Cai, W., Li, X., Suk, J.W., Potts, J.R. and Ruoff, R.S., 2010. Graphene and graphene oxide: synthesis, properties, and applications. *Advanced Materials,* 22 (35), 3906-3924.

Zincarelli, C., Soltys, S., Rengo, G. and Rabinowitz, J.E., 2008. Analysis of AAV Serotypes 1–9 Mediated Gene Expression and Tropism in Mice After Systemic Injection. *Molecular Therapy,* 16 (6), 1073-1080.

Zou, Y., Kottmann, A.H., Kuroda, M., Taniuchi, I. and Littman, D.R., 1998. Function of the chemokine receptor CXCR4 in haematopoiesis and in cerebellar development. *Nature,* 393 (6685), 595-599.